

**Design, Development and Fabrication of Gallium Nitride
(GaN) High Electron Mobility Transistor (HEMT) based
terahertz devices for Space Applications**

*A thesis submitted
in partial fulfillment for the degree of*

Doctor of Philosophy

by

RAKESHKUMAR KANERIYA



**Department of Physics
INDIAN INSTITUTE OF SPACE SCIENCE AND
TECHNOLOGY**

Thiruvananthapuram – 695547

March - 2023

ॐ प्रज्ञानं ब्रह्म ।

Dedicated to my beloved family

Hridved, Gyana and Mira

CERTIFICATE

This is to certify that the thesis titled **Design, Development and Fabrication of Gallium Nitride (GaN) High Electron Mobility Transistor (HEMT) based terahertz devices for Space Applications** submitted by Mr. Rakeshkumar Kaneriya to the Indian Institute of Space Science and Technology, Thiruvananthapuram, for the award of the degree of Doctor of Philosophy is a bonafide record of the research work done by him under my supervision. The contents of this thesis, in full, or in parts, have not been submitted to any other Institute or University for the award of any degree or diploma.

Dr. Palashkumar Basu

Co-Supervisor

Professor, Department of Avionics

IIST

Dr. Solomon Ivan

Supervisor

Professor, Department of Physics

IIST

Place: Thiruvananthapuram

March 2023

Counter signature of HoD with seal.

DECLARATION

I declare that this thesis titled **Design, Development and Fabrication of Gallium Nitride (GaN) High Electron Mobility Transistor (HEMT) based terahertz devices for Space Applications** submitted in fulfillment of the Degree of Doctor of Philosophy is a record of original work carried out by me under the supervision of **Dr. Solomon Ivan** and **Dr. Palashkumar Basu** has not formed the basis for the award of any degree, diploma, associateship, fellowship or other titles in this or any other Institution or University of higher learning. In keeping with the ethical practice in reporting scientific information, due acknowledgments have been made wherever the findings of others have been cited.

Mr. Rakeshkumar Kaneriya
SC16D050

Place: Thiruvananthapuram
March 2023

ACKNOWLEDGEMENTS

*In the beginning, I would like to take this opportunity to thank and express my gratitude towards my organization **Space Applications Centre (SAC) ISRO**, for allowing me to pursue my doctoral studies in Department of Physics, Indian Institute of Space Science and Technology.*

*The work would not have been a success without the expert supervision and guidance from my supervisors, **Prof. Soloman Ivan** from Department of Physics and **Prof Palashkumar Basu** from Department of Avionics, Indian Institute of Space Science and Technology. I would like to thank them for equipping me with valuable knowledge in the field of THz sciences through Semiconductor technology. They are very kind and wonderful persons. I would like to thank them for giving me an opportunity to work with them. I have learned a lot from them about the THz GaN HEMTs, which can be considered as an extension of my thesis with regard to the applications.*

*Another two persons whose contributions are equally valuable are **Gunjan Rastogi** and **Chiranjit Karmakar**. Both have helped me throughout with their experimental skills. Gunjan has helped me a lot in setting up the experimental set-up. It was and still is nice working with her and I hope we continue our collaborations and deals in future too. Special thanks to Chiranjit Karmakar for extensive characterization of the samples for me. I sincerely thank my organization's internal guide **Dr Naresh Babu Pendyala** for many valuable suggestions and constant guidance throughout the project.*

*I am also thankful to **Microelectronics Group** of my organization for providing fabrication and characterization support. I also thank **CeNSE, Indian Institute of Science (IISc)**, Bangalore, for providing Si_3N_4 deposition and characterization support.*

*I would also like to thank my organization, two most important persons, **Dr R B Upadhyay** and **Santanu Sinha** for their valuable scientific discussions. Gratitude is extended to DD, ESSA, **Shri A N Bhattacharya** and GH, MEG **Smt Punam P Kumar** for many helpful discussions and monitoring of the project. I am thankful to **Director, SAC** for giving me an opportunity to work on this challenging project and for continued encouragement during this study.*

*Last, but not the least, My Family, who believed in me, supported me and motivated me all through my life. I would like to thank my loving wife **Mira Kaneriya** and my cute daughter **Gyana Kaneriya**, for their unconditional support and trust in me completely, all colleagues from SAC, ISRO as well as IIST and anyone who has played any role during these years.*

Rakeshkumar Kaneriya

Thiruvananthapuram

ABSTRACT

Terahertz (THz) technology has attracted tremendous attention recently due to its promising applications in various domains such as medical, biological, industrial imaging, broadband, safety, communication, radar, space science, etc. Due to non-availability of powerful sources and highly sensitive & efficient detectors, the so called “THz gap” remains largely unfilled. Despite seamless efforts from electronics and photonics technology researchers, the desired level of technology development to fill the THz gap still remains a challenge. In the present thesis, a very new and versatile mechanism for electrical tuning of intersubband transitions (ISBT) is presented in Gallium Nitride (GaN) high electron mobility transistor (HEMT) device. ISBT phenomena is usually demonstrated in the photonic device like quantum cascade laser (QCL). This dissertation is explored the photonics ISBT phenomenon in an electronics GaN HEMT device. Conventional photonic devices are operated at cryogenic temperatures to minimize the thermal effect. The reported maximum operating temperature of THz QCL is in the range of 150-200 K which is too low for general applications. The conduction band tuning through external gate bias makes advantage of HEMT device for room temperature (RT) terahertz applications.

The theoretical models for electrically tuneable plasmonic metamaterials-assisted ISBT have been developed. Experimental demonstration of electrical tuning of ISBT in a GaN HEMT device at room temperature has not only provided a novel mechanism but also discriminates ISBT from other transitions induced by deep-level traps and defects in the 100 nm GaN HEMT device. The intersubband energy levels are extracted by using low temperature Photoluminescence (PL) measurement. The PL emission peaks data are also supported by a simulation based on a self-consistent solution of Schrodinger and Poisson equations. It is possible to tune the subband energy level inside triangular quantum well of GaN HEMT by applying gate voltage. The GaN HEMT device responds toward incident terahertz radiation due to inherent advantage of conduction subband tuning through external bias. The presented novel approach for ISBT in GaN HEMT has the potential possibilities in the context of overcome the THz gap in the electromagnetic spectrum at ambient temperature.

Contents

CERTIFICATE.....	iii
DECLARATION.....	v
ACKNOWLEDGEMENTS.....	vii
ABSTRACT	xi
LIST OF FIGURES	xvii
LIST OF TABLES	xxiii
ABBREVIATIONS	xxv
PHYSICAL CONSTANTS.....	xxix
SYMBOLS	xxxi
1. Introduction.....	1
1.1 Field of Study and Objectives	1
1.2 Terahertz Gap	2
1.3 Gallium Nitride: The wide bandgap semiconductor	4
1.4 Problem statement and its possible solution.....	6
1.5 Structure of the thesis	7
2. Polarization and ISBT in III-Nitride Semiconductor	11
2.1 Basic Physical properties of III-nitride semiconductor	11
2.1.1 Polarization in III-nitride semiconductor.....	12
2.1.2 Polarization effect on energy band	15
2.1.3 Quantum confinement in GaN Heterostructure	17
2.1.4 Electron-Photon interaction and transition rate	22
2.2 Fundamentals of Metamaterials	25
2.3 Fundamentals of Plasmonics	28

2.3.1 Surface plasmons polaritons	28
2.3.2 Localized surface plasmons	30
2.4 Plasmonics Metamaterials in Terahertz region	31
3. Theoretical Modelling and Simulation.....	33
3.1 GaN Heterostructure and Device description.....	33
3.2 Semiconductor ISBT Modelling	35
3.3. Metamaterial embedded ISBT Modelling	43
3.4. Plasmonic assisted ISBT	47
4. GaN Heterostructure Growth and Characterization	51
4.1 Heterostructure growth.....	51
4.2 Heterostructure characterization.....	54
4.2.1 Visual Inspection.....	58
4.2.2 Sheet Resistivity measurement	59
4.2.3 Surface morphology	59
4.2.4 Photoluminescence (PL) Spectroscopy.....	60
4.2.5 Hall measurement.....	61
4.2.6 High Resolution X-Ray Diffraction	68
4.2.7 Raman Spectroscopy	72
4.2.8 Measurement Correlation.....	75
5. GaN HEMT Device Fabrication	81
5.1 Device Fabrication	81
5.1.1 Layout Design	84
5.1.2 Alignment marker Scheme & Mask Preparation	85
5.1.3 Mesa Lithography & Etching.....	86
5.1.4 Ohmic Contact Fabrication	89
5.1.4.1 Electron beam Lithography for Ohmic contact.....	91

5.1.4.2 Recess Etching using ICP RIE.....	92
5.1.4.3 Metal stack deposition and Annealing process:	93
5.1.4.4 Ohmic Contact Characterization	95
5.1.5 Schottky Contact Fabrication	100
5.1.6 Device Passivation Process	107
5.1.6.1 Passivation Layer Deposition.....	108
5.1.6.2 Passivation Layer Etching.....	114
5.1.7 Contact Thickening and Air Bridge Fabrication	115
6. Device DC and RF Measurements.....	120
6.1 DC Measurement.....	120
6.2 Breakdown Voltage Measurement	121
6.3 RF Measurement	124
6.3 Power Measurement	129
7. Terahertz Intersubband Transition Measurement	133
7.1 Introduction	133
7.2 Rule out Plasma wave mechanism	134
7.3 Defects/traps-based transitions	134
7.4 Thermal energy assisted transitions	135
7.5 Optical transitions in GaN	141
7.5 Optical transitions in GaN Heterostructure	145
8. Conclusion and Future Work	155
REFERENCES	158
LIST OF PUBLICATIONS BASED ON THESIS	177
Book Chapter	177
Papers in peer reviewed international journals.....	177
Conference Proceedings	178

LIST OF FIGURES

1.1	(a) Terahertz region in the electromagnetic spectrum and (b) terahertz gap.....	3
2.1	The schematic of the band diagram for the heterojunction (a) before charge transfer and (b) band diagram after charge transfer for Al _{0.3} Ga _{0.7} N/GaN heterostructure	15
2.2	(a) The schematic cross-section of GaN HEMT and (b) its band diagram.....	16
2.3	(a) The absorption and (b) the emission of photon with corresponding to electron transition	23
2.4	Representation of natural materials (top) and metamaterials (bottom). The natural materials composed by atoms, while the metamaterials composed by meta-atoms	27
2.5	(a) Electric field for SPP propagation at a dielectric metal interface and (b) Dispersion relation	29
2.6	(a) Polarizability and (b) extinction cross section of a gold nanosphere of radius 50 nm in two media along with two different permittivity ϵ_m	31
3.1	a) GaN Heterostructure, (b) HEMT cross-sectional view and (c) HEMT Mesh structure	34
3.2	Typical configurations of GaN HEMT (a) 2 gate fingers with 150 micron gate width (2x150) (zoom image for gate fingers visualization and (b) 8 gate fingers with 150 micron gate width (8x150).	35
3.3	(a) Output characteristics (I_d - V_d), (b) transfer characteristics (I_d - V_g) and (c) Transconductance of the simulated device	36
3.4	Extracted (a) CV profile and (b) 2DEG profile with applied Gate voltage	36
3.5	Current gain and power gain of the simulated device	37
3.6	(a) Conduction band energy profile with different applied gate voltage and Fermi Energy level with filled subband inside Triangular Quantum well with different applied Gate biasing (b) $V_g > 0 > V_t$, (c) $V_g = 0 > V_t$ and (d) $0 > V_t > V_g$	41
3.7	Intersubband Resonance Frequency as a function of the applied field (a) Calculated using eq (3.3) and (b) By solving self-consistency Schrodinger-Poisson solver	42
3.8	2DEG carrier concentration of AlGa _N /AlN/GaN heterostructure for (a) different AlGa _N thickness and (b) different Al composition in AlGa _N layer ...	43

3.9	Three different configuration (a) 2x50, (b) 2x100 and (c) 2x150 of GaN HEMT and (d) GaN HEMT meshing	44
3.10	Electrical field enhancement for 0.4 THz incident radiation on (a) 2x50, (b) 2x100 and (c) 2x150 of GaN HEMT devices. Electrical field enhancement for 2x100 GaN HEMT device at (d) 0.3 THz, (e) 0.7 THz and (f) 1.75 THz incident radiation	46
3.11	Electrical field enhancement due to illumination of terahertz radiation on GaN HEMT devices	47
3.12	Electrical field enhancement for 0.4 THz incident radiation on GaN HEMT device using a finite element method-based electromagnetic solver (COMSOL)	48
3.13	Induced Electrical field due to terahertz radiation illumination on GaN HEMT device using a finite element method-based electromagnetic solver (COMSOL)	49
4.1	Schematic of Metal Organic Chemical Vapor Deposition (MOCVD) reactor ...	51
4.2	Thickness, composition and layers sequence of investigated three GaN heterostructure grown on 6H-SiC having (a) Sample A: AlGa _N /Ga _N , (b) Sample B: Ga _N /AlGa _N /Al _N /Ga _N and (c) Sample C: AlGa _N /Al _N /Ga _N heterostructure	52
4.3	Nine points measurement over 4" GaN heterostructure on 6H-SiC wafer.....	53
4.4	Surface morphology measured by AFM for AlGa _N /Ga _N (samples A), Ga _N /AlGa _N /Al _N /Ga _N (Sample B) and AlGa _N /Al _N /Ga _N (Sample C)	58
4.5	(a) Schematic representation of typical PL set up and (b) DongWoo Optron PL set up including excitation source, a grating monochromator, PMT detector, cryostat, filters and collecting lenses.....	59
4.6	The room temperature PL spectra measured from AlGa _N /Ga _N (samples A), Ga _N /AlGa _N /Al _N /Ga _N (Sample B) and AlGa _N /Al _N /Ga _N (Sample C)	60
4.7	(a) Schematic representation of typical Hall Measurement set up and (b) different geometry used for Hall measurement	62
4.8	Hall Measurement set up	63
4.9	(a) Hall mobility and (b) 2DEG carrier concentration with respect to temperature for Samples A, B and C.....	64
4.10	(a) Magnetoresistance up to 14 T at a set of temperatures and (b) Shubnikov–de Haas oscillations after subtracting the background.....	65
4.11	(a) Effective mass plot at 13.9 T, where the data are best fit to Eq. (4.11) and (b) the field dependence of the Landau-level spacing.....	66
4.12	High Resolution XRD (HR-XRD) system.....	67

4.13	XRD scan towards (a) (0002) and (b) (10-14) of samples A, B, and C are used to determine thickness, composition and lattice constants a and c	68
4.14	Symmetric (0002) and asymmetric (10-14) rocking scan of samples A, B, and C are used to determine the crystalline quality and dislocation defects.....	69
4.15	The room temperature Raman spectra measured from AlGaIn/GaN (samples A), GaN/AlGaIn/AlN/GaN (Sample B), AlGaIn/AlN/GaN (Sample C) and Etched GaN buffer layer (Sample D).....	72
4.16	Measurement methodology for depth profiling Raman measurement	73
4.17	(a) Raman E2-high peak spectra for GaN Heterostructure, (b) change in Raman E2-high peak in depth profiling, (c) Raman E2-high peak shifting in depth profiling, (d) Calculated stress.....	74
4.18	The conduction band profile calculated using semiconductor device physics based simulation for (a) AlGaIn/GaN (samples A), (b) GaN/AlGaIn/AlN/GaN (Sample B) and (c) AlGaIn/AlN/GaN (Sample C).....	75
4.19	The measurement correlation among HR-XRD, Raman and PL data of AlGaIn/GaN (samples A), GaN/AlGaIn/AlN/GaN (Sample B), AlGaIn/AlN/GaN (Sample C) and Etched GaN buffer layer (Sample D).....	76
4.20	The room-temperature band gaps of the AlGaIn/GaN (samples A), GaN/AlGaIn/AlN/GaN (Sample B) and AlGaIn/AlN/GaN (Sample C) vs the corresponding stresses measured by HRXRD and Raman. The solid line represents a linear fitting result to the experimental data.....	77
5.1	Schematic of GaN HEMT Fabrication flow.....	80
5.2	GaN HEMT Fabrication process flow along with used semiconductor fab equipments and the view of the fabricated device.....	81
5.3	(a) GaN HEMT fabricated wafer and (b) 100 nm 2x100 GaN HEMT device...	82
5.4	(a) Layout designing on 1"x1" and (b) zoom one device image.....	83
5.5	Varieties of process control monitors (PCM) for short, open and through the structure for RF measurement.....	84
5.6	Dicing Line (Blue) and Alignment Markers (Red) Layout.....	85
5.7	(a) Photolithography Marker Placed on Wafer, (b) Arrangement of Global (yellow) and Local (Red) Electron Beam Markers and (c) Vernier Scale marker used to determine alignment Error.....	85
5.8	Schematic cross-sectional and top view of mesa Isolation process.....	86
5.9	ICP-RIE Sentech SI-500 system.....	87

5.10	(a) Top view of etched mesa structures taken using confocal microscope on 1"x1" sample, (b) Cross-sectional SEM image of etched mesa structure and (c) Etch depth measurement using stylus profiler.....	88
5.11	Flowchart showing process flow for ohmic contact fabrication.....	89
5.12	Raith Electron Beam Patter Generation (EBPG) 5200 system.....	90
5.13	Source/Drain Resist Profile after Development Process.....	91
5.14	Dual gun Electron Beam evaporation system.....	93
5.15	Annealsys AS-One 150 Rapid Thermal Processing system.....	93
5.16	Source-Drain (a) resist profile after lithography, (b) metal deposition after lift-off process and (c) ohmic contact after annealing process.....	94
5.17	Schematic cross-sectional and top view of Ohmic contact fabrication.....	94
5.18	(a) Optical image of TLM patterns after metal lift-off and (b) SEM image of TLM pattern.....	95
5.19	(a) AFM image of Bare Heterostructure and (b) Ohmic Contact Sample.....	96
5.20	(a) HAADF TEM image of metal/semiconductor interface before annealing, (b) EDS analysis across white line shown in figure 6a before annealing.....	97
5.21	Post annealing (a) AFM image of ohmic contact sample and (b) HRTEM image of metal/semiconductor interface of ohmic contact sample.....	98
5.22	(a) I-V measurement of ohmic contact sample and (b) Total resistance vs. pad spacing for ohmic contact sample.....	98
5.23	Cross Sectional View of T-gate	99
5.24	Flowchart showing process steps for Fabrication of Gate Contact.....	100
5.25	(a) Resist profile for mushroom gate, (b) Resist profile after SiN etching (c) Fabricated Mushroom gate, (d) 2 finger device and (e) cross sectional schematic of Gate fabrication Schematic cross-sectional view of Gate fabrication.....	101
5.26	Optical image of Schottky test patterns after metal lift-off.....	103
5.27	AFM image of (a) Bare Heterostructure, (b) Ohmic contact and (c) Schottky contact.....	103
5.28	(a) Reverse biased Schottky diode characteristics and (b) C-V characteristics before and after annealing.....	105
5.29	Typical image of wafer taken by confocal microscopy (a) before SiN deposition and (b) after SiN deposition.....	109
5.30	(a) XPS spectra before wet chemical & N ₂ Plasma treatment and (b) XPS spectra after wet chemical & N ₂ Plasma treatment.....	109

5.31	XPS spectra post NP Si ₃ N ₄ deposition.....	110
5.32	HR-XRD pattern before and after NP Si ₃ N ₄ deposition.....	111
5.33	FTIR spectra of NP Si ₃ N ₄ film.....	112
5.34	Part of Air Bridge connecting Source Terminals.....	114
5.35	Cross sectional view of Air Bridge fabrication process flow.....	115
5.36	Air Bridge Fabrication Process Steps.....	116
5.37	Typical image of wafer taken by confocal microscopy (a) before air-bridge fabrication and (b) after air-bridge fabrication.....	117
5.38	Typical portion of fabricated wafer along with zoom image of two finger and multi-finger GaN HEMT devices.....	117
6.1	Semiconductor Device characterization set up for GaN HEMT DC and Breakdown measurement.....	120
6.2	Measured 100 nm GaN HEMT (a) output characteristics (Id-Vd), (b) transfer characteristics (Id-Vg) and (c) transconductance.....	120
6.3	Breakdown voltage measurement on 100 nm GaN HEMT devices.....	121
6.4	Optical image of HEMT before and after destructive breakdown of (a) Device 1 and (b) Device 4.....	122
6.5	GaN HEMT RF and power measurement set-up.....	124
6.6	The two-port network indicating the incident and reflected voltages at the input and output, reflection coefficients at the input and output port, and s-parameters.....	124
6.7	Measured current gain h ₂₁ parameters at different biasing conditions	126
6.8	Measured current gain and power gain.....	127
6.9	(a) GaN HEMT 1"x1" wafer mounted on measurement setup and (b) 10x100 GaN HEMT Device.....	128
6.10	On device large signal gain and power measurement.....	129
7.1	Effect of 90°AOI illumination with Blue LED (a) on Id-Vd characteristics of 100 nm GaN HEMT Device (b) change in drain current.....	135
7.2	Effect of 45°AOI illumination with SWIR led (a) on Id-Vd characteristics of 100 nm GaN HEMT Device (b) zoom portion of Id-Vd characteristics for drain current change visualization and (c) change in drain current.....	136
7.3	(a) Band-schematic of the first two subbands in a 2DEG with respect to the Fermi level (b) carrier distribution in two subband and (c) absorption in the subband	137
7.4	Low-temperature PL measurement of GaN heterostructure.....	138

7.5	Change in drain current due to 45° AOI and 30 second illumination with SWIR LED at temperature (a) 200 K and (b) 100 K.....	139
7.6	Temperature dependent GaN bandgap and change in drain current ($V_g=0V$ and $V_d=8V$) due to illumination.....	139
7.7	Band structure for wurtzite (WZ) bulk semiconductor with Conduction band (CB), heavy-hole (HH), light-hole (LH) and crystal field split off band (SO)...	141
7.8	Schematic of (a) the neutral donor ground state, (b) neutral donor bound exciton state, (c) the neutral acceptor ground state and (d) the neutral acceptor bound exciton state	142
7.9	Intrinsic and extrinsic optical transitions that occur in response to an above bandgap excitation in GaN.....	142
7.10	Low temperature (5K) PL measurement of 2.0 micron GaN buffer layer grown on SiC wafer.....	143
7.11	(a) GaN heterostructure, (b) Simulated Band structure of AlGaIn/AlN/GaN heterostructure, (c) zoom portion of triangular quantum well in conduction band and (d) zoom portion of valance band with light & heavy holes (HH, LH) splitting.....	144
7.12	Temperature dependent PL spectra of GaN heterostructure from ambient to 5K.	146
7.13	Low temperature (5K) PL spectra of AlGaIn/GaN heterostructure on SiC wafer.	147
7.14	(a) triangular quantum well of CB & VB and (b) 5K PL spectra of GaN HEMT structures as well as corresponding D°X, FX and 2DEG band structure.....	148
7.15	Low temperature (5K) PL measurement of (a) only buffer GaN layer grown heterostructure and (b) top etched (~220 nm) GaN heterostructure on SiC wafer.....	149
7.16	Electrons and holes are separated near the interface to form the quasi-two-dimensional excitons.....	150
7.17	5K PL spectra of GaN HEMT structures with increase of excitation power (inset zoom portion of Peak #2 showing blue shift and stronger PL intensity as increase the excitation laser power).....	151
7.18	(a) 5K PL spectra of GaN HEMT structures with increase of excitation power and (b) Excitation intensity dependent peak shift for peak 1 to peak 6.....	151
7.19	(a) PL spectra of AlGaIn/GaN Heterostructure with increase of temperature and (b) temperature dependent peak shift for peak 1 to peak 6.....	152

LIST OF TABLES

1.1	Properties of Semiconductor materials	4
1.2	Renowned GaN Foundries along with its process and capabilities	5
2.1	III-N Semiconductor materials properties	12
3.1	Summary of simulated device DC and RF Parameters	37
3.2	Different devices configurations used in metamaterial simulations	45
4.1	GaN Heterostructure properties over 4" wafer for Sample A	54
4.2	GaN Heterostructure properties over 4" wafer for Sample B	55
4.3	GaN Heterostructure properties over 4" wafer for Sample C	56
4.4	Summary of measured heterostructure properties using standard semiconductor characterization equipment	57
4.5	Extracted/calculated heterostructure properties	70
5.1	Summary of AFM characterization for Ohmic Contact	96
5.2	Schottky contact geometry parameters	99
5.3	Summary of AFM characterization of Schottky contact	104
5.4	Summary of extracted parameters from I-V data	105
5.5	Summary of extracted parameters from C-V data	106
5.6	SiN passivation experiments details	107
5.7	Optimized process parameters for SiN deposition	108
6.1	Summary of breakdown voltage measurement on 100 nm GaN HEMT devices	123
6.2	Summary of DC and RF properties of device before passivation, after passivation and after pad thickening	127
6.3	100nm GaN HEMTs Power measurement Results (Two-fingers devices)	129
6.4	100nm GaN HEMTs Power measurement Results (Multi-fingers devices)	130
6.5	Summary Simulated and measured DC, breakdown, RF and power device parameters	130
7.1	Measurement methods and excitation sources used to confirm ISBT	134
7.2	Simulated and measured Energy subband levels inside triangular quantum well	153

ABBREVIATIONS

2DEG	Two Dimensional Electron Gas
ABEs	Acceptor Bound Excitons
AC	Alternating Current
ADS	Advanced Design System
AFM	Atomic Force Microscopy
AlN	Aluminium Nitride
AOI	Angle Of Incident
BEs	Bound Excitons
BN	Boron Nitride
CAN	Ceric Ammonium Nitrate
CL	CathodoLuminescence
CR	Cyclotron Resonance
CV	Capacitance Voltage
DBEs	Doner Bound Excitons
DC	Direct Current
DI	Deionized Water
DIC	Differential Interference Contrast
DLTS	Deep-Level Transient Spectroscopy
DOS	Density Of States
eb	electron beam
EDS	Energy Dispersive Spectroscopy
EFA	Envelope Function Approximation
EL	ElectroLuminescence
FET	Field Effect Transistor

FTIR	F ourier T ransform I nfra R ed spectroscopy
FWHM	F ull W idth at H alf M aximum
GaN	G allium N itride
GaAs	G allium A rsenic
GSG	G round S ource G round
HCl	H ydro C hloric
HEMT	H igh E lectron M obility T ransistor
HH	H eavy H ole
HRXRD	H igh R esolution X - R ay D iffraction
ICP-RIE	I nductive C oupled P lasma R eactive I on E tching
InN	I ndium N itride
IPA	I so P ropyl A lcohol
ISR	I nter S ubband R esonance
ISBT	I nter S ub B and T ransition
LED	L ight E mitting D iode
LH	L ight H ole
LO	L ongitudinal O ptical
LSPs	L ocalized S urface P lasmons
MBE	M olecular B eam E pitaxy
MOCVD	M etal- O rganic C hemical V apour D eposition
MOVPE	M etal- O rganic V apour P hase E pitaxy
MODFET	M ODulation D oped F ield E ffect T ransistor
MUG	M aximum U nilateral G ain
NIR	N ear I nfra R ed
NP	N itrogen P retreated
PA	P ower A mplifier

PAE	P ower A dded E fficiency
PCM	P rocess C ontrol M onitor
PDK	P rocess D esign K it
PE	P iezoelectric P olarization
PECVD	P lasma E nhanced C hemical V apor D eposition
PL	P hoto L uminescence
PLE	P hoto L uminescence E xcitation
PMMA	P oly M ethyl M ethacrylate
PNA	P arametric N etwork A nalysers
QCLs	Q uantum C ascade L asers
QDMR	O ptically D etected M agnetic R esonance
QW	Q uantum W ell
RHEED	R eflected H igh E lectron E nergy D iffraction
RF	R adio F requency
RSM	R eciprocal S pace M ap
RTA	R apid T hermal A nneling
SBH	S chottky B arrier H eight
SCCM	S tandard C ubic C entimetres per M inute
SEM	S canning E lectron M icroscopy
Si	S ilicon
SiC	S ilicon C arbide
SiPDR	S ingle P ost D ielectric R esonators
SMU	S ource M easurement U nit
SO	S plit O ff band
SP	S pontaneous P olarization
SPPs	S urface P lasmon P olaritons

SSPL	S teady S tate P hoto L uminescence
SWIR	S hort W ave I nfra R ed
TCAD	T echnology C omputer A ided D esign
TEM	T ransmission E lectron M icroscopy
THz	T erahertz
TLM	T ransmission L ine M odel
TMAI	T iri M ethyl A luminium
TMGa	T iri M ethyl G allium
TRPL	T ime R esolved P hoto L uminescence
UHV	U ltra H igh V acuum
UV	U ltraviolet
VNA	V ector N etwork A nalysers
WBG	W ide B and G ap
XPS	X -Ray P hotoelectron S pectroscopy

PHYSICAL CONSTANTS

Speed of light,	$c = 2.997\,924\,58 \times 10^8 \text{ m/sec}$
Boltzmann constant,	$k_B = 1.380\,650\,32 \times 10^{-23} \text{ J/K}$
Planck's constant,	$h = 6.626\,068\,76 \times 10^{-34} \text{ Js}$
Reduced Planck's constant,	$\hbar = 1.054\,571\,59 \times 10^{-34} \text{ Js}$
Absolute permeability,	$\mu_0 = 1.256\,637\,06 \times 10^{-6} \text{ H/m}$
Absolute permittivity,	$\epsilon_0 = 8.854\,187\,82 \times 10^{-12} \text{ F/m}$
Charge of an electron,	$e = 1.602\,176\,46 \times 10^{-19} \text{ C}$
Mass of an electron,	$m_e = 9.109\,381\,88 \times 10^{-31} \text{ kg}$
Avogadro number,	$N_A = 6.022\,141\,99 \times 10^{23} \text{ /mol}$
Pi,	$\pi = 3.141\,592\,65$

SYMBOLS

k	Wavevector
β	Propagation Constant
λ	Wavelength, Perturbation Parameter
ω	Angular frequency
Ψ, ψ	Wavefunction
μ	Chemical Potential, Mobility
φ, ε	Energy
ε, ϵ	Dielectric constant
σ	Conductivity
α	Absorption Coefficient
Γ	FWHM
δ	Phase Difference
τ	Relaxation Time
z	Transition Matrix Elements
l_e, l_h	Effective Lengths
\hat{p}	Momentum Operator
χ	Susceptibility
Ω	Coupling Strength
t	Time
m	Mass
g	Density of States
f	Boltzmann Function, Fermi-Dirac Function, Oscillator Strength
ν	Filling Factor, Frequency
h_{21}	Current Gain
A	Vector Potential
C	Capacitance
E	Electric field, Piezoelectric coefficient
E_n	Energy
F	Electric field
G	Gain
H, B	Magnetic field, Hamiltonian
H_n	Hermite Functions

I	Intensity, Current
N_A	Acceptor Density
P	Polarization
S_{11}	Reflection Coefficient at Port 1
S_{12}	Forward voltage transfer ratio from Port 1 to Port 2
S_{21}	Reverse transfer ratio from Port 1 to Port 2
S_{22}	Reflection Coefficient at Port 2
T	Temperature, Transmission
V	Potential, Voltage
W	Transition Rate
V_b	Breakdown Voltage
V_d	Drain Voltage
V_g	Gate Voltage
V_{th}	Threshold Voltage
V_r	Reference Voltage

Introduction

This thesis describes the research work performed under the doctorate program “Terahertz Technology” from Indian Institute of Space Science and Technology (IIST), for the degree of Doctor of Philosophy (PhD) in Physics. The guidance and supervision of this doctoral thesis has been conducted by Prof Soloman Ivan Department of Physics and Prof Palashkumar Basu Department of Avionics from Indian Institutes of Space Science and Technology (IIST) as well as Dr Naresh Babu Pendyala from Space Applications Centre, ISRO. The GaN HEMT device design, fabrication and its characterization work have been developed at Microelectronics Group, Space Applications Centre, ISRO Ahmedabad.

1.1 Field of Study and Objectives

The research presented in this manuscript falls under the framework of light-matter interaction in Quantum structure. It is mainly focused on applications at terahertz (THz) frequencies, a spectral band lying between microwaves and infrared. A new and versatile mechanism studied in which photonics phenomena **intersubband transitions** (ISBT) is explored in electronics device structure of **high electron mobility transistor** (HEMT).

The objective of this thesis is to design, development, fabrication and measurement of GaN HEMT devices for terahertz applications. Particularly, concentrated on the utilization of the current state of art GaN HEMT devices for operation at much higher frequencies up to the terahertz beyond its conventional transit-time limitations. The contributions presented here start from the specific theory of the

field and the results are supported by numerical simulations, analytical calculations and measurements of real prototypes device.

1.2 Terahertz Gap

Terahertz radiation is a small portion of the electromagnetic spectrum lying between the microwave and infrared regions. There is no precise range defining THz band, but it is most often be considered as frequencies in the range of 0.3 –3.0 THz. Although sometimes it refers to 0.1–10.0 THz also. The terahertz spectral range has drawn tremendous attention recently due to its promising applications in varied domains. For example, in the field of biomedical, THz radiation has been explored to detect various biomaterials like nucleic acids, proteins, cells and tissue applications [1, 2]. In the field of medical applications, the THz system has been demonstrated as a highly effective technique in cancer imaging, particularly for skin cancer [3, 4]. A portable real-time THz imaging system could be used to assist the early detection of diseases in routine health check-up. Since many non-metallic, non-polar materials are transparent to THz radiation, scanning of humans is feasible with no health hazard. Due to this, THz radiation has great potential for security and public safety applications. THz radiation can detect concealed weapons, explosives (for example C-4, HMX, RDX and TNT), illicit drugs (for example methamphetamine and heroin), etc. [1]. THz imaging has become a valuable characterization tool for non-destructive testing, process control and quality inspection for example inspection of silicon solar cells, nanocomposites, polymer films and dielectric films [1, 5, 6]. Space and ground-based THz instruments have been explored significantly in the field of astronomy. For example, the terahertz system is extensively used to study the origin of the universe, formation of stars and galaxies, composition of planets and planetary atmospheres, the climate and environmental balance of our planet Earth, etc. [7, 8].

Despite this tremendous applications potential, the so-called “THz Gap” is not fulfilled to required level due to technology requirements of high-power sources as well as efficient and sensitive detectors in THz range as shown in Figure 1.1. Semiconductor devices and circuits like transistor and frequency multiplier work well toward low terahertz frequency end, but their power level drops off precipitously as the frequency

increases. These devices can be operated up to ~ 1 THz with very low power. On another side, semiconductor photonic devices like lasers can be utilized for high frequency terahertz range. Again, lasers are limited due to the non-availability of lower bandgap semiconductor materials towards low-frequency terahertz. The THz Quantum Cascade Lasers (QCLs) showed promising results to fill this terahertz gap from 1 to 10 terahertz. However, QCLs required bulky cooling requirements and reported maximum operating temperature is in the range of 150-200K which is too low for general applications [9, 10]. The demand for a compact, efficient, high-speed THz detector and source operating at room temperature has increased drastically. The non-availability of room temperature terahertz source and detector is a prime limitation of modern terahertz systems.

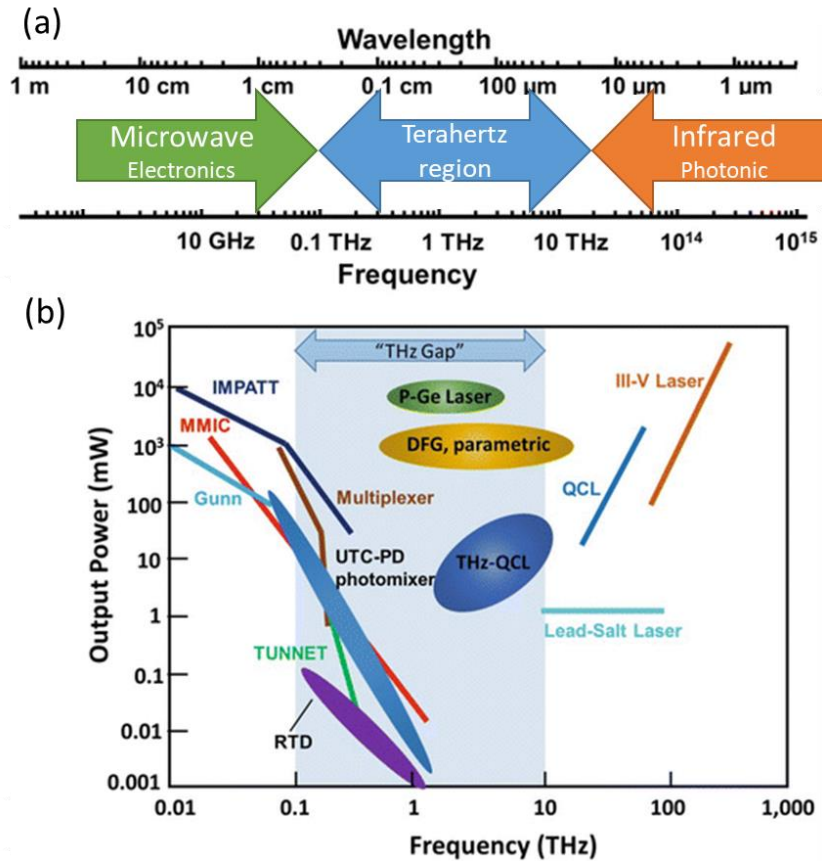


Figure 1.1: (a) terahertz region in the electromagnetic spectrum and (b) terahertz gap

1.3 Gallium Nitride: The wide bandgap semiconductor

Wide bandgap (WBG) semiconductor devices are highly dominant in today's advanced power, RF, optoelectronic and photonic devices due to their outstanding material properties. Silicon carbide (SiC), Gallium Nitride (GaN), Aluminum Nitride (AlN), diamond etc. are renowned WBG materials. Table 1.1 listed a few WBG materials

Table 1.1: Properties of Semiconductor materials

Properties	Conventional Semiconductor		Wide Bandgap Semiconductor		
	Si	GaAs	6H-SiC	4H-SiC	GaN
Band Gap (eV)	1.12	1.43	3.03	3.26	3.45
Dielectric constant	11.9	13.1	9.66	10.1	9.0
Electric breakdown field (kV/cm)	300	400	2500	2200	2000
electron mobility (cm ² /V.s)	1500	8500	500	1000	1250
Thermal conductivity (W/cm.K)	1.5	0.46	4.9	4.9	1.3
Electron saturation velocity (cm/s)	1	1	2	2	2.2

properties along with conventional semiconductors Silicon (Si) and Gallium Arsenic (GaAs). GaN is a very promising material for high power and high frequency devices due to WBG, high thermal stability and high breakdown voltage. Gallium Nitride semiconductors and heterostructure devices are prime contenders for advanced electronics systems including space hardware due to their outstanding material properties especially with reference to speed, power, efficiency and linearity. GaN based devices found a special place in the communication area due to above distinct advantages, at the same time the fabrication technology offers numbers of challenges. There are several renowned GaN foundries that provide power, RF and Microwave GaN devices and circuits for commercial, military and space applications in Europe, America and Taiwan [11]. Table 1.2 shows a full listing of the processes offered by international GaN foundries to the customer.

Table 1.2: Renowned GaN Foundries along with its Process and capabilities

Company	Process	Gate length (μm)	Drain Bias (V)	Breakdown Voltage (V)	Power Density (W/mm)	Max Frequency (GHz)	Wafer size (Inch)	Substrate
GCS	0.5 μm GaN	0.5	48	200	12	3.5	4	SiC
	0.4 μm GaN	0.4	48	200	12	6	4	SiC
	0.25 μm GaN	0.25	48	200	12	12	4	SiC
	0.15 μm GaN	0.15	28	100	5	40	4	SiC
	0.4 μm GaN	0.4	28	200	10	6	4, 6	Si
	0.25 μm GaN	0.25	28	200	10	10	4, 6	Si
	0.4 μm GaN	0.4	48	200	25	6	4	Diamond
	0.25 μm GaN	0.25	48	200	25	10	4	Diamond
HRL Laboratories	T2 GaN	0.15	12	>50	1.8	110	4	SiC
	T3 GaN	0.04	12	>50	1.5	140	4	SiC
	T4a GaN	0.04	4	15	1	200+	4	SiC
	T3L GaN	0.06	>14	>50	>2	110	4	SiC
NXP	0.4 μm GaN	0.4	50	>150	10	5	6	SiC
	0.25 μm GaN	0.25	50	>150	10	10	6	SiC
	0.2 μm GaN	0.2	32-40	>120	6	15	6	SiC
	0.15 μm GaN	0.15	20-28	>100	5	30	6	SiC
Qorvo	QGaN50	0.50	65	>190	10	8	4	SiC
	QGaN25HV	0.25	48	>150	8	12	4,6	SiC
	QGaN25	0.25	40	>100	8	25	4	SiC
	QGaN15	0.15	28	>60	4	50	4,6	SiC
	QGaN15THN	0.15	28	>60	4	60	4,6	SiC
OMMIC	D01GH	0.1	12	40	4.5	110	6	Si
	D006GH	0.06	12	25	3	150	6	Si
UMS	GH50	0.5	50	> 200	> 5	6	4	SiC
	GH25	0.25	30	> 120	> 4.5	20	4	SiC
	GH15	0.15	20-25	>80	>3.5	38	4	SiC
	GH10	0.1	15	>60	>3.0	50	4	SiC
	GH10-20	<0.1	10-12	>40	>2.5	90	4	SiC
WIN	NP45-11	0.45	50	160	10	6	4	SiC
	NP25-02	0.25	28	120	6	18	4	SiC
	NP-15-00	0.15	28	120	3	35	4	SiC
Wolfspeed	G28V3	0.4	28	120	4.5	18	4	SiC
	G28V4	0.25	28	120	4.5	8	4	SiC
	G28V5	0.15	28	84	3.75	40	4	SiC

	G40V4	0.25	40	120	6	18	4	SiC
	G50V3	0.4	50	150	8	6	4	SiC

1.4 Problem statement and its possible solution

The cut-off frequency of field effect transistor (FET) including HEMT is defined by,

$$f_T = \frac{v}{2\pi L} = \frac{1}{2\pi\tau} \quad (1.1)$$

where v is carrier velocity, L is gate length and τ is electron transit time under the gate. For a very small 30 nm gate length up to 300-350 GHz cut-off frequency operation has been demonstrated [12]. However, beyond conventional transit-time limitations, these FET devices can be operated at much higher frequencies up to the terahertz. Dyakonov–Shur proposed the plasma wave theory to describe THz behavior in FET devices [13, 14]. The basic of plasma wave theory is the instability of two-dimensional electron gas (2DEG) which has a resonant response to incident electromagnetic radiation in short channel FET. The size and shape of the FET channel are used to govern the resonant response of plasma frequency to electromagnetic radiation. The tuning of plasmon frequency by external biasing has been used for detectors, mixers and multipliers [14]. There are several reports available in which the plasma wave theory is used to describe the THz behavior of devices. Plasma wave theory concept has been widely demonstrated from conventional semiconductors like Si [15], GaAs [13], GaN [16], InP [17] to new two-dimensional material system like Graphene [18], Black Phosphorus [19], etc. There are also few literatures available in which GaN HEMT device working mechanism is also explained through plasma wave theory [16, 20-23].

In this dissertation, we have demonstrated for the first-time, that **Intersubband transition (ISBT)** mechanism, in addition to established Plasma wave theory, can describe the terahertz behavior of the GaN HEMT device. ISBT theory is based on carrier transitions within a conduction band which is entirely different from plasma wave theory. The possibility of electrical tuning the intersubband resonances (ISBR) in GaN HEMT device by external gate biased is explored. Moreover, these resonances

are strongly coupled to the HEMT device geometry. Standard GSG HEMT device geometry act as a metamaterial, while the nanometric gate of HEMT device generates surface plasmon. The overall terahertz performance of GaN HEMT is governed by aggregate effects of ISBT, plasmonic structure and metamaterial behavior. GaN HEMT devices are fabricated on the SiC wafer by a standard semiconductor fabrication process. The results of this dissertation can be taken further to other material system heterostructure along with different plasmonic metamaterial designs to tune and study light-matter interactions. This dissertation makes effective contributions towards fundamental investigations in quantum mechanics and electrodynamics as a whole.

1.5 Structure of the thesis

Chapter 1 of the manuscript begins with this introduction where the research line and objectives are defined. The brief literature survey illustrates the outreach and prospects of terahertz technology, substantiating the motivation to explore and understand the underlying fundamental physical phenomena. This section is followed by seven chapters, which describe the main contents of the thesis.

In Chapter 2 the fundamentals of polarization and intersubband transition in III-Nitride heterostructure are described in order to present the foundations for the rest of the thesis. ISBT in GaN heterostructure is presented as a core mechanism able to achieve intriguing terahertz interaction in GaN heterostructure. The fundamentals of plasmonics and metamaterials are described in order to explore plasmonic metamaterial contribution in terahertz interaction with GaN HEMT.

Chapter 3 introduces theoretical modeling and simulation starting from with role of polarization in wurtzite semiconductor followed by the self-consistent solution of Schrodinger and Poisson equations, k.p model and Fermi Golden rule are used to compute ISBT in GaN HEMT structure. Next, the modeling of HEMT structure and nanometric gate contact putting emphasis on the metamaterials and plasmonics effects respectively are shown. Extraordinary enhancement of terahertz interaction in GaN HEMT, a phenomenon connected to plasmonic metamaterials is presented at the end.

- **Paper 1:** “Intersubband Device Modeling of Gallium Nitride High Electron Mobility Transistor for Terahertz Applications” Journal of Radio Science, 54, 1172-1180, 2019. <https://doi.org/10.1029/2019RS006844>
- **Paper 2:** “Physics based Modeling of Gallium Nitride High Electron Mobility Transistor for Terahertz Applications” URSI AP-RASC 2019, IEEE Xplore, DOI: 10.23919/URSIAP-RASC.2019.8738691
- **Paper 3:** “Physics Based Simulation for Studying the Impact of Contact Resistance on DC and RF Characteristics of AlGa_N/Al_N/Ga_N HEMT” URSI AP-RASC 2019, IEEE Xplore, DOI: 10.23919/URSIAP-RASC.2019.8738496 (2019).
- **Paper 4:** “Physics Based Simulation for Studying the Impact of Contact Resistance on DC and RF Characteristics of AlGa_N/Al_N/Ga_N HEMT” Journal of Radio Science, 54, 904-909, 2019. <https://doi.org/10.1029/2019RS006855>
- **Paper 5:** “Modeling of electrically tunable metamaterial embedded intersubband transitions in Gallium Nitride (Ga_N) High Electron Mobility Transistor (HEMT) for terahertz applications” URSI RCRS 2020, IEEE Xplore, DOI: 10.23919/URSIRCRS4921.2020.9113510

Chapter 4 describes Ga_N heterostructure growth and characterization. The collective correlation among structural, mechanical, electrical and optical properties in Ga_N heterostructure is described here.

- **Paper 6:** “Suppression of weak localization due to Al_N interlayer in AlGa_N/Ga_N 2DEG”, Physics Letter A, 417 127693, (2021). <https://doi.org/10.1016/j.physleta.2021.127693>
- **Paper 7:** “Influence of Al_N spacer and Ga_N cap layer in Ga_N Heterostructure for RF HEMT Applications”, Microelectronic Engineering 255 111724 (2022). <https://doi.org/10.1016/j.mee.2022.111724>
- **Paper 8:** “Investigation of inherent stress using confocal Micro Raman in Ga_N Heterostructure for RF HEMT Applications”, International Raman summit 2020, WiTec, Germany.

In the 5th chapter, the technology for the fabrication of GaN HEMT devices on silicon carbide (SiC) wafer is described. Starting with layout design, masks fabrication, ohmic contact, Schottky contact, passivation to ending with the technology of air-bridges describes in this chapter.

- **Paper 9:** “Optimization of ohmic contact fabrication for $\text{Al}_{0.3}\text{Ga}_{0.7}\text{N}/\text{AlN}/\text{GaN}$ HEMTs on 6H-SiC using recess etching and surface plasma treatment processes” J Nanomater Mol Nanotechnol of SciTechnol 2019, 8:2. doi: 10.4172/2324-8777.1000267
- **Paper 10:** “Optimization of Ni/Au Schottky contacts on $\text{Al}_{0.3}\text{Ga}_{0.7}\text{N}/\text{AlN}/\text{GaN}$ heterostructure for RF applications”, International Journal of Nanotechnology and Nanoscience, 6, 8-15, (2020)

Chapter 6 presents the GaN HEMTs device performances of on SiC. The influence of the different process parameters on the device performances is studied in this chapter. The DC, small signal and the large signal characterization of optimized devices is described.

- **Paper 11:** “Performance improvement of $\text{Al}_{0.3}\text{Ga}_{0.7}\text{N}/\text{AlN}/\text{GaN}$ HEMTs using Nitrogen pre-treated Si_3N_4 passivation”, Microelectronic Engineering 249, 111617 (2021). <https://doi.org/10.1016/j.mee.2021.111617>
- **Paper 12:** “Characterization of GaN HEMT at Cryogenic Temperatures” IEEE MTT-S International Microwave and RF Conference 2021, IMaRC2021 (2021). doi: 10.1109/IMRC49196.2021.9714643.

Chapter 7 is devoted to experimental investigation of room temperature photon-induced electrical tuning of ISB transition in GaN HEMT which extends the device operating frequency well beyond its present cut-off frequency. Non-destructive low temperature photoluminescence (PL) method for extracting the true signatures of intersubband energy levels in AlGa_{0.3}N/GaN heterostructure is presented.

- **Paper 13:** “Room temperature photon induced electrical tuning of intersubband transition in GaN HEMT for terahertz applications”, *Microelectronic Engineering*, 233, 111433 (2020). <https://doi.org/10.1016/j.mee.2020.111433>
- **Paper 14:** “Low temperature photoluminescence study for identification of Intersubband energy levels inside triangular quantum well of AlGaIn/GaN Heterostructure”, *Microelectronics Journal*, 131, 105660 (2023).
- **Book Chapter 15:** “A Novel approach for Room-Temperature Intersubband Transition in GaN HEMT for terahertz Applications; Terahertz Technology, IntechOpen, doi: 10.5772/intechopen.98435 (2021); ISBN 978-1-83962-684-5

The summarized conclusion with an outlook to future work is presented in Chapter 8. At the end of the thesis, the references section lists all works that are cited throughout the text. Subsequently, the complete list of the Author’s merits is given, including the main contributions to international book chapter [Book Chapter 01], the main contributions to international journals [Journal Paper 01-04], the additional contributions to international journals [Journal Paper 05-09] and the conference proceedings resulting from invited oral and poster presentations [Conference Paper 01 - 05]

Polarization and ISBT in III-Nitride Semiconductor

This chapter is an overview of Intersubband transition (ISBT) in III-N semiconductor heterostructure. Starting from the basis of polarization in wurtzite semiconductor, we will see how polarization play a role to generate two-dimensional electron gas (2DEG) in III-Nitride heterostructure followed by the self-consistent solution of Schrodinger and Poisson equations, $k.p$ model and Fermi Golden rule are used to compute ISBT. We will also see how metamaterials can be seen as effective media that exhibit enthralling interaction of terahertz radiation with 2DEG. Secondly, plasmonics effects play a key role, and thus, a detailed description of them will be given. Finally, extraordinary electromagnetic interaction in quantum structure, a phenomenon connected to both metamaterials and plasmonics, is described to show different theoretical explanations and experimental demonstrations that have flourished over more than a decade to describe it.

2.1 Basic Physical properties of III-Nitride semiconductor

Gallium Nitride (GaN) is binary compound semiconductors of the III-Nitride material system, which includes other members, are Aluminium Nitride (AlN), Indium Nitride (InN) and Boron Nitride (BN). Wurtzite and zinc-blende are two types of crystal structures are found for III-Nitride semiconductors among them wurtzite is a very stable phase. III-Nitride materials have excellent optical and electrical properties. For this reason, III-Nitrides materials are receiving attention as a decisive element for next generation electronics and photonics devices like lasers, detectors, LEDs, high-power amplifiers, etc. The III-Nitride material system covers a broad range of bandgap energies, starting from infrared (0.7 eV for InN) to ultraviolet (6.2 eV for AlN). The large electronic polarization field which is a combination of spontaneous and

piezoelectric in the III-Nitride semiconductors affects the electronic properties in terms of band diagrams, charge distributions of layered structures in many ways. Table 2.1 summarize the lattice constants, bandgap, elastic constants (c_{ij}), piezoelectric moduli (e_{ij}) and spontaneous polarization (P_{SP}) of III-Nitride semiconductors.

Table 2.1: III-Nitride Semiconductor materials properties

	III-Nitride Semiconductor			
Properties	GaN	InN	AlN	BN
Lattice Constant a_0 (Å)	3.189	3.544	3.111	2.504
Lattice Constant c_0 (Å)	5.185	5.718	4.978	6.661
Bandgap (eV)	3.4	0.7	6.2	5.95
P_{SP} (C/m²)	-0.029	-0.032	-0.081	-
e_{33} (C/m²)	0.73	0.97	1.46	-
e_{31} (C/m²)	-0.49	-0.57	-0.60	-
C_{13} (Gpa)	103	92	108	-
C_{33} (GPa)	405	224	473	-

2.1.1 Polarization in III-Nitride semiconductor

The nitride semiconductor materials exhibit inherent polarization properties. Having the large ionicity of the nitride bond (Ga-N, Al-N, In-N, etc.), it possesses a piezoelectric polarization (P_{PE}) component. While the absence of the center of inversion symmetry and uniaxial nature of the crystal structure produces spontaneous polarization (P_{SP}). Total polarization (P_T) in the nitride semiconductor heterostructure is a combination of spontaneous polarization (P_{SP}) and piezoelectric polarization (P_{PE}) as shown in equation (2.1) [24].

$$P_T = P_{SP} + P_{PE} \quad (2.1)$$

Furthermore, the strain-induced effect at the interface between two nitride semiconductors enhances piezoelectric polarization in the heterostructure. Piezoelectric polarization of the crystal is generally defined in terms of strain (ϵ) and stress (σ) components. Stress and strain are correlated in a crystal by elastic coefficient $\epsilon_{ij}=C_{ij}\sigma_{ij}$. The piezoelectric polarization in heterostructure grown along z-axis (0001) is given by [24],

$$P_{PE} = E_{33}\epsilon_z + E_{31}(\epsilon_x + \epsilon_y) \quad (2.2)$$

where, E_{33} and E_{31} are piezoelectric coefficients, ϵ_x , ϵ_y and ϵ_z are strain in x, y and z-direction respectively. The crystal edge length and height are represented as a_0 and c_0 respectively in a hexagonal crystal lattice. The strain along the x, y and z-axis is given by (in-plane strain along x and y-axis are assumed to be isotropic),

$$\epsilon_z = \frac{c - c_0}{c_0}, \quad \epsilon_x = \epsilon_y = \frac{a - a_0}{a_0} \quad (2.3)$$

where, a_0 and c_0 are the equilibrium or unstrained values of lattice constants and a and c are the strain lattice constant due to growth of heterostructure. For hexagonal lattice crystal, the strain components along ϵ_z and ϵ_x are related with elastic coefficients as per the following equation,

$$\epsilon_z = -2 \frac{c_{13}}{c_{33}} \epsilon_x; \quad \frac{c - c_0}{c_0} = -2 \frac{c_{13}}{c_{33}} \frac{a - a_0}{a_0} \quad (2.4)$$

where, C_{13} and C_{33} are the elastic constants. Substituting equation (2.3) and (2.4) in equation (2.2),

$$P_{PE} = 2 \frac{a - a_0}{a_0} \left(E_{31} - E_{33} \frac{c_{13}}{c_{33}} \right) \quad (2.5)$$

The macroscopic piezoelectric polarization is defined by variations of the lattice constants a and c . The microscopic piezoelectric polarization is expressed in terms of an internal parameter u , defined as the anion-cation bond length along the z -axis (0001) [24]. Substituting elastic constant values for AlN and GaN in equation (2.5), one gets piezoelectric polarization of AlN greater than GaN. Spontaneous polarization closely depends upon crystal structure c/a ratio. The ideal c/a ratio in the hexagonal closed pack crystal structure is 1.633. The spontaneous polarization is found to be higher in actual crystal structure as the c/a ratio is different from its ideal value [24]. This nonideality of c/a ratio in AlN is also higher than GaN, leading the higher spontaneous polarization. The spontaneous and piezoelectric polarization for alloy i.e. AlGa_N is obtained by linear interpolation of the binary constituents (Vegard's law) [25]. In summary, the spontaneous and piezoelectric polarizations for AlGa_N over the whole range of compositions are larger than that of a GaN buffer layer.

The polarization induced charge density and sheet density in the heterostructure is given by [24, 26],

$$\rho = -\nabla \cdot P \quad (2.6)$$

$$\sigma = P_{T(Layer1)} - P_{T(Layer2)}$$

$$\sigma = [P_{SP(Layer1)} + P_{PE(Layer1)}] - [P_{SP(Layer2)} + P_{PE(Layer2)}] \quad (2.7)$$

The polarization induced charge density and sheet density for the case of AlGa_N/GaN heterostructure given by [24, 26],

$$\sigma = [P_{SP(GaN)} + P_{PE(GaN)}] - [P_{SP(AlGa_N)} + P_{PE(AlGa_N)}] \quad (2.8)$$

2.1.2 Polarization effect on energy band

When two different semiconductors (in the present case $\text{Al}_{0.3}\text{Ga}_{0.7}\text{N}/\text{GaN}$) are in contact with each other, due to their difference of the Fermi level with respect to the vacuum level, there will be net charge transfer from one material to the other. The Fermi level lines up on both sides of the junction at equilibrium. The key issue in dealing with heterojunctions is band alignment. The band alignment is how the respective conduction band edges and valance band edges of the two semiconductors line up relative to each other at the interface. $\text{Al}_{0.3}\text{Ga}_{0.7}\text{N}$ has a wider band gap than GaN, as illustrated in Figure 2.1 (a), energy band offsets arise at the AlGaN/GaN interface. The conduction band offset (ΔE_c) becomes an electron containment barrier. The schematic of the band diagram for the heterojunction before charge transfer and band diagram after charge transfer for $\text{Al}_{0.3}\text{Ga}_{0.7}\text{N}/\text{GaN}$ heterostructure are shown in Figure 2.1

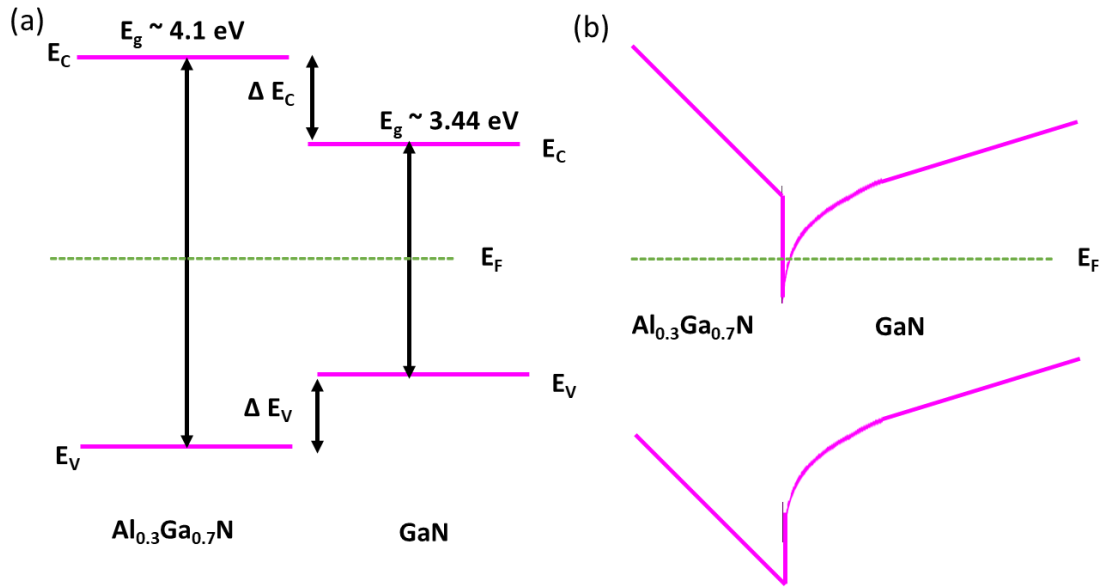


Figure 2.1: The schematic of the band diagram for the heterojunction (a) before charge transfer and (b) band diagram after charge transfer for $\text{Al}_{0.3}\text{Ga}_{0.7}\text{N}/\text{GaN}$ heterostructure

There is no doubt about the 2DEG generation ($\sim 10^{13} \text{ cm}^{-2}$ order) for undoped Nitride heterostructures. Hence, unlike GaAs MODFET heterostructures, no doping is required in Nitride heterostructures to generate 2DEG concentration which is a great advantage of these structures. However, the origin of the carriers in AlGaN/GaN

heterostructures is debatable. Some of the researcher claim the generation of carriers is due to surface state, while other reported unintentionally doped GaN exhibits n-type conduction with a typical electron concentration of $\sim 10^{17}\text{cm}^{-3}$. Even intentionally undoped AlGaIn/GaN heterostructures with high structural quality the formation of a 2DEG can be expected because of the free carrier background concentration in the active GaN layer. The 2DEG density dependence on the thickness and composition of the active GaN layer. The 2DEG density dependence on the thickness and composition of the AlGaIn barrier has been linked to surface donor states. The debate on the origin of the carriers in both the cases end up with polarization induced carriers at the interface due to either surface states or free background electrons concentration.

The positive polarization charge at the interface and the negative polarization charge at the top of the AlGaIn layer induce an electric field in AlGaIn barrier layer. The resultant energy band along with the Fermi level tilt toward the interface. Under the force of the electric field, the surface conducting electrons in AlGaIn move to the positive electrode and accumulate in the conduction band of GaN region because of low potential energy. The extracted 2DEG concentration, purely due to polarization effects, is the order of $\sim 10^{13}\text{cm}^{-2}$ for Nitride heterostructures.

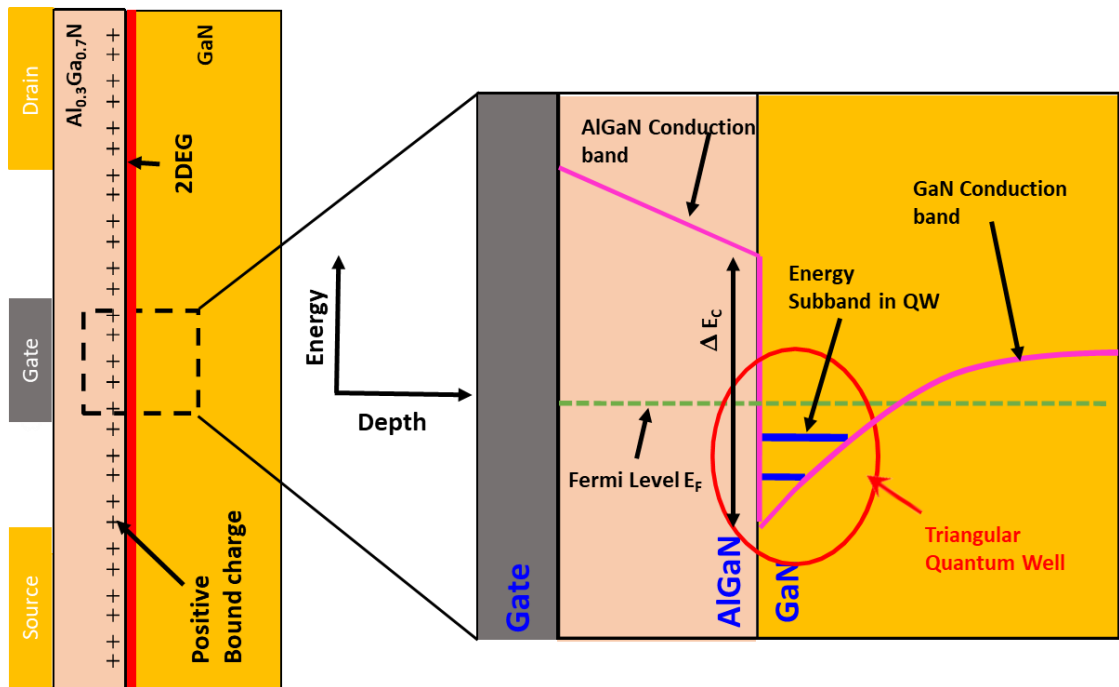


Figure 2.2: (a) The schematic cross-section of GaN HEMT and (b) its band diagram

In the GaN HEMT device, gate Schottky contact control the carrier inside channel through Fermi energy level pinning. The conduction band at the gate/AlGaIn interface is pinned to the Schottky barrier Φ_B can be calculated as, $\Phi_B = \Phi_M - \chi_{AlGaIn}$ where, Φ_M is work function of metal, χ_{AlGaIn} is the electron affinity of AlGaIn. The schematic cross-section of GaN HEMT and its band diagram are shown in Figure 2.2.

2.1.3 Quantum confinement in GaN Heterostructure

The interaction between photons and electrons in the semiconductor can be expressed by the Hamiltonian,

$$H = \frac{1}{2m_0}(\mathbf{p} - e\mathbf{A})^2 + V(\mathbf{r}) \quad (2.9)$$

where m_0 is the free electron mass, $V(\mathbf{r})$ is the periodic crystal potential in the present case it is the triangular potential function given by, $V(z) = eF_z z$, where e is the charge of electron and F_z is the electric field, \mathbf{A} is vector potential of applied electromagnetic field. Hamilton can be expanded into,

$$H = \frac{p^2}{2m_0} + V(r) - \frac{e}{2m_0}(\mathbf{p} \cdot \mathbf{A} + \mathbf{A} \cdot \mathbf{p}) + \frac{e^2 A^2}{2m_0} \quad (2.10)$$

Since, $\mathbf{p} \cdot \mathbf{A} = \mathbf{A} \cdot \mathbf{p}$. Also, $H = \hbar k = \frac{\hbar \pi}{a_0}$, where a_0 is lattice constant. Hence, for most practical cases $|eA| \ll |p|$. This leads to the last term in equation (2.10) $\frac{e^2 A^2}{2m_0}$ is much smaller than the terms linear in \mathbf{A} .

$$H = \frac{p^2}{2m_0} + V(r) - \frac{e}{m_0} \mathbf{A} \cdot \mathbf{p} \quad (2.11)$$

$$H \approx H_0 + H'$$

Here H_0 is unperturbed Hamiltonian and H' is perturbed Hamiltonian due to the interaction of electromagnetic wave:

$$H_0 = \frac{p^2}{2m_0} + V(\mathbf{r}) \quad (2.12)$$

$$H' = -\frac{e}{m_0} \mathbf{A} \cdot \mathbf{p} \quad (2.13)$$

The vector potential of the electric field can be expressed as,

$$\mathbf{A} = \hat{e} A_0 \cos(\mathbf{k} \cdot \mathbf{r} - \omega t)$$

$$\mathbf{A} = \hat{e} \frac{A_0}{2} e^{i\mathbf{k} \cdot \mathbf{r}} e^{-i\omega t} + \hat{e} \frac{A_0}{2} e^{-i\mathbf{k} \cdot \mathbf{r}} e^{i\omega t} \quad (2.14)$$

where \mathbf{k} is the wave vector, ω is the angular frequency and \hat{e} is a unit vector in the direction of the electric field, we have

$$\mathbf{E}(\mathbf{r}, t) = -\frac{\partial \mathbf{A}}{\partial t} = -\hat{e} \omega A_0 \sin(\mathbf{k} \cdot \mathbf{r} - \omega t) \quad (2.15)$$

$$\mathbf{H}(\mathbf{r}, t) = \frac{1}{\mu} \nabla \times \mathbf{A} = \frac{1}{\mu} \mathbf{k} \times \hat{e} A_0 \sin(\mathbf{k} \cdot \mathbf{r} - \omega t) \quad (2.16)$$

The Schrödinger equation can be expressed as,

$$H \psi(\mathbf{r}, t) = -\frac{\hbar}{i} \frac{\partial}{\partial t} \psi(\mathbf{r}, t) \quad (2.17)$$

where the Hamiltonian H consists of time independent an unperturbed part H_0 and a small time depends perturbation $H'(r, t)$ as per equations (2.12)-(2.13)

The solution to the unperturbed part is given by,

$$H \phi(r, t) = -\frac{\hbar}{i} \frac{\partial}{\partial t} \phi(r, t) \quad (2.18)$$

$$\phi(\mathbf{r}, t) = \phi(\mathbf{r}) e^{-iE_n t/\hbar} \quad (2.19)$$

The time-dependent perturbation part is given by,

$$H'(r, t) = H'(\mathbf{r}) e^{-i\omega t} + H'(\mathbf{r}) e^{i\omega t}; \quad t \geq 0 \quad (2.20)$$

$$H'(r, t) = 0; \quad t < 0$$

We expand the wave function in terms of the unperturbed solutions as,

$$\psi(\mathbf{r}, t) = \sum_n a_n(t) \phi_n(\mathbf{r}) e^{-iE_n t/\hbar} \quad (2.21)$$

where, $|a_n|^2$ gives the probability that the electron in the n^{th} state at time t . By substituting the equation (2.21) in equation (2.18) we get,

$$\sum_n \frac{da_n(t)}{dt} \phi_n(\mathbf{r}) e^{-iE_n t/\hbar} = -\frac{i}{\hbar} \sum_n H'(\mathbf{r}, t) a_n(t) \phi_n(\mathbf{r}) e^{-iE_n t/\hbar} \quad (2.22)$$

Using the orthonormal property, $\int d^3\mathbf{r} \phi_m^*(\mathbf{r}) \phi_n(\mathbf{r}) = \delta_{mn}$, we find

$$\frac{da_n(t)}{dt} = -\frac{i}{\hbar} \sum_n a_n(t) H'_{mn} \phi_n(t) e^{i\omega_{mn}t} \quad (2.23)$$

Where,

$$\begin{aligned} H'_{mn}(t) &= \langle m | H'(\mathbf{r}, t) | n \rangle \pi r^2 \\ &= \int \phi_m^*(\mathbf{r}) H'(\mathbf{r}, t) \phi_n(\mathbf{r}) d^3\mathbf{r} \\ &= H'_{mn} e^{-i\omega t} + H'^{\dagger}_{mn} e^{i\omega t} \end{aligned} \quad (2.24)$$

$$\omega_{mn} = (E_m - E_n)/\hbar \quad (2.25)$$

The matrix element is defined as,

$$H'_{mn} = \int \phi_m^*(\mathbf{r}) H'(\mathbf{r}) \phi_n(\mathbf{r}) d^3\mathbf{r} \quad (2.26)$$

By introducing the perturbation parameter λ ,

$$H = H_0 + \lambda H'(\mathbf{r}, t) \quad (2.27)$$

And,

$$a_n(t) = a_n^{(0)} + \lambda a_n^{(1)}(t) + \lambda^2 a_n^{(2)}(t) + \dots \quad (2.28)$$

We get,

$$\frac{da_m^{(0)}}{dt} = 0 \quad (2.29)$$

$$\frac{da_m^{(1)}}{dt} = -\frac{i}{\hbar} \sum_n a_n^{(0)}(t) H'_{mn}(t) e^{i\omega_{mn}t} \quad (2.30)$$

$$\frac{da_m^{(2)}}{dt} = -\frac{i}{\hbar} \sum_n a_n^{(1)}(t) H'_{mn}(t) e^{i\omega_{mn}t} \quad (2.31)$$

The zeroth order solution of equation (2.29) is constant. Let consider the electron to be at the state i initially

$$a_i^{(0)}(t) = 1, \quad (2.32)$$

$$a_i^{(0)}(t) = 0, \quad m \neq i$$

The first order solution,

$$\frac{da_m^{(1)}}{dt} = -\frac{i}{\hbar} H'_{mi}(t) e^{i\omega_{mi}t}$$

$$\frac{da_m^{(1)}}{dt} = -\frac{i}{\hbar} [H'_{mi}(t) e^{i(\omega_{mi}-\omega)t} + H'_{mi}(t) e^{i(\omega_{mi}+\omega)t}] \quad (2.33)$$

Let us consider a final state $m=f$; the above equation (2.33) can be solved directly by integration

$$a_f^{(1)}(t) = -\frac{1}{\hbar} \left[H'_{fi} \frac{e^{i(\omega_{fi}-\omega)t} - 1}{\omega_{fi} - \omega} + H'_{fi} \frac{e^{i(\omega_{fi}+\omega)t} - 1}{\omega_{fi} + \omega} \right] \quad (2.34)$$

When photon energy to be near resonance i.e. $\omega \sim \pm \omega_{fi}$, we get

$$\left| a_f^{(1)}(t) \right|^2 = \frac{4|H'_{fi}|^2 \sin^2 \frac{t}{2} (\omega_{fi} - \omega)}{\hbar^2 (\omega_{fi} - \omega)^2} + \frac{4|H'^{\dagger}_{fi}|^2 \sin^2 \frac{t}{2} (\omega_{fi} + \omega)}{\hbar^2 (\omega_{fi} + \omega)^2} \quad (2.35)$$

When interaction time is long enough, we find,

$$\frac{\sin^2 \left(\frac{xt}{2} \right)}{x^2} \rightarrow \frac{\pi t}{2} \delta(x)$$

We find

$$\left| a_f^{(1)}(t) \right|^2 = \frac{2\pi t}{\hbar^2} |H'_{fi}|^2 \delta(\omega_{fi} - \omega) + \frac{2\pi t}{\hbar^2} |H'^{\dagger}_{fi}|^2 \delta(\omega_{fi} + \omega) \quad (2.36)$$

The transition rate is given by,

$$W_{if} = \frac{d}{dt} \left| a_f^{(1)}(t) \right|^2$$

$$W_{if} = \frac{2\pi}{\hbar} |H'_{fi}|^2 \delta(E_f - E_i - \hbar\omega) + \frac{2\pi}{\hbar} |H'^{\dagger}_{fi}|^2 \delta(E_f - E_i + \hbar\omega) \quad (2.37)$$

2.1.4 Electron-Photon interaction and transition rate

Let us consider initially electron is at energy state E_i . The electron interacts with the incident photon, which allows it to enter an excited energy state E_f . Similarly, after sometime electron transit from higher energy E_f state to lower energy E_i state by emitting the photon. The absorption and emission of photon corresponding to electron transitions is shown in Figure 2.3.

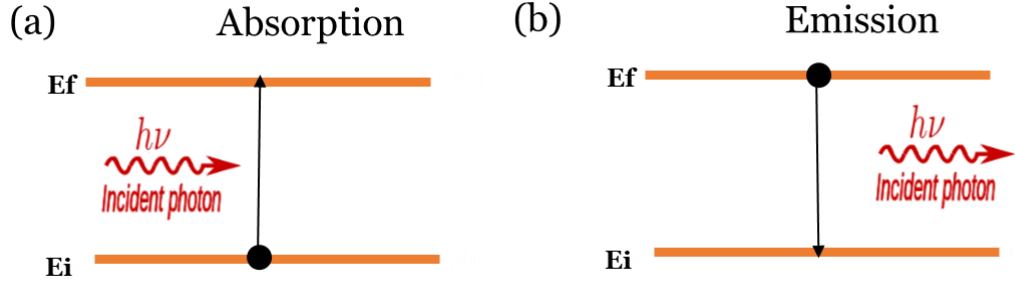


Figure 2.3: (a) the absorption and (b) the emission of photon with corresponding to electron transition

By applying Fermi's golden rule and using section 2.1.2 time dependent perturbation theory, the absorption and emission coefficient given by,

$$W_{if} = W_{abs} = \frac{2\pi}{\hbar} |H'_{fi}|^2 \delta(E_f - E_i - \hbar\omega) \quad (2.38)$$

$$W_{fi} = W_{ems} = \frac{2\pi}{\hbar} |H'_{fi}^\dagger|^2 \delta(E_f - E_i + \hbar\omega) \quad (2.39)$$

The interacting Hamiltonian from equations (2.13) and (2.14), we get

$$W_{if} = W_{abs} = \frac{2\pi}{\hbar} \frac{e^2 E_0^2}{4m_0^2 \omega^2} |\langle i | e \cdot \mathbf{p} | f \rangle|^2 \delta(E_f - E_i - \hbar\omega) \quad (2.40)$$

The matrix element in the above equation can be expanded in terms of interband and intersubband transitions as following,

$$\langle i | e \cdot \mathbf{p} | f \rangle = e \cdot \langle u_v | \mathbf{p} | u_{v'} \rangle \langle f_n | f_{n'} \rangle + e \cdot \langle u_v | u_{v'} \rangle \langle f_n | \mathbf{p} | f_{n'} \rangle \quad (2.41)$$

Where v and v' and n and n' are the band and subband indices of the initial and final states, respectively. The first term describes interband transitions, i.e. transitions from the valence band to the conduction band that are accompanied by a change of the band index v . In the case of intersubband transitions, the initial and the final bands are the same, the first term in equation (2.41) vanishes. The second term, which describes transitions within the same band between subbands. Hence, in the one-band model, which consists of overlap integral of the Bloch function and a dipole matrix element of the envelope function. Further decomposition of the matrix elements of the envelope function given by,

$$\langle f_{nk_{\perp}} | e \cdot \mathbf{p} | f_{n'k'_{\perp}} \rangle = \frac{1}{A} \int d^3r e^{-ik_{\perp} \cdot r} \phi_n^*(z) [e_x p_x + e_y p_y + e_z p_z] e^{ik_{\perp} \cdot r} \phi_{n'}(z) \quad (2.42)$$

Only the third term $e_z p_z$ yields a contribution at finite frequency. The first and second terms $e_x p_x$ and $e_y p_y$ vanish, except when initial and final states are identical i.e., $n=n'$ and $k_{\perp}=k'_{\perp}$. The physical interpretation of these terms is the free-carrier absorption in the two-dimensional electron gas, which is finite only at zero frequency when no scattering processes are included. Hence, the matrix element determines the intersubband absorption in the one-band model is given by,

$$\langle n | p_z | n' \rangle = \int dz \phi_n^*(z) p_z \phi_{n'}(z) \quad (2.43)$$

The electric field of the incident radiation must have a component perpendicular to the semiconductor layers (parallel to the growth direction) in order to couple to the intersubband transitions. This is the famous polarization selection rule for the intersubband transitions. As a result, the sample is tilted at an angle to obey the selection rule, which is discussed later in Chapter 7. Another important quantity defines the dimensionless oscillator strength by,

$$f_{nn'} = \frac{2}{m^* \hbar \omega_{nn'}} \langle n | p_z | n' \rangle^2 = \frac{2m^* \hbar \omega_{nn'}}{\hbar} \langle n | z | n' \rangle^2 \quad (2.44)$$

The above quantity gives the strengths of the transitions in different physical systems, and obey the Thomas-Reiche-Kuhn sum rule

$$\sum_{n'} f_{nn'} = 1 \quad (2.45)$$

For symmetric quantum well, only parity changing transitions (odd-even or even-odd) are allowed due to the inversion symmetry of the potential. But for asymmetric quantum wells, like that of the triangular potential well, the inversion symmetry with respect to the quantum well center is broken. Hence, the transitions between all the subbands are allowed.

2.2 Fundamentals of Metamaterials

Metamaterials define as artificially made materials which exhibit engineered electromagnetic properties that do not occur or may not be readily available in nature or in their constituent materials. There has been great interest in developing materials, which could control the flow of electromagnetic waves in unprecedented ways. Marvelling engineering has provided means to create artificial materials that are difficult to find in naturally appearing and earlier-known, classical materials. Metamaterials are composed of their elements in the same sense as matter consists of atoms. Metamaterial represents the next level of structural organization of matter, hence the prefix 'meta'. The structural elements known as artificial molecules are building blocks or unit cells in large 1D, 2D or 3D arrays. There are various inclusion shapes, such as spheres, ellipses, helices, bent wires have been employed to achieve possibilities for the artificial material behavior [27]. Metamaterials are an arrangement of artificial structural elements, designed to achieve advantageous and unusual electromagnetic properties. When the wavelength of the electromagnetic wave is larger

than 10 nm i.e., between ultraviolet and X-rays in the electromagnetic spectrum, quantum effects can be neglected and the response is governed by macroscopic Maxwell's equations as following [28]

$$\nabla \times \mathbf{E}(\mathbf{r}, t) = -\frac{\partial \mathbf{B}(\mathbf{r}, t)}{\partial t} \quad (2.46)$$

$$\nabla \times \mathbf{H}(\mathbf{r}, t) = -\frac{\partial \mathbf{D}(\mathbf{r}, t)}{\partial t} + \mathbf{J}(\mathbf{r}, t) \quad (2.47)$$

$$\nabla \cdot \mathbf{B}(\mathbf{r}, t) = 0 \quad (2.48)$$

$$\nabla \cdot \mathbf{D}(\mathbf{r}, t) = \rho(\mathbf{r}, t) \quad (2.49)$$

All quantities are functions of space (\mathbf{r}) and time (t). The spatial and temporal differentiations are denoted as ∇ and $\partial/\partial t$. \mathbf{E} is the electric field vector (V/m), \mathbf{H} the magnetic field vector (A/m), \mathbf{D} the electric flux density (displacement) vector (As/m²), \mathbf{B} the magnetic flux density (displacement) vector (Vs/m²) or tesla (T). \mathbf{J} the current density vector (A/m²), and ρ the scalar charge density (As/m²). \mathbf{H} and \mathbf{D} are auxiliary fields defined as:

$$\mathbf{D} = \epsilon_0 \mathbf{E} + \mathbf{P} \quad (2.50)$$

$$\mathbf{H} = \frac{1}{\mu_0} \mathbf{B} - \mathbf{M} \quad (2.51)$$

where ϵ_0 and μ_0 are the electric permittivity and magnetic permeability of vacuum respectively. For a linear media, the above equations can be written in terms of ϵ and μ , the constitutive parameters of the material, as follows

$$\mathbf{D} = \epsilon \mathbf{E} \quad (2.52)$$

$$H = \frac{1}{\mu} B \quad (2.53)$$

According to the above equations, the permittivity ϵ and permeability μ define all electromagnetic properties of the material. The materials are generally dispersive, so ϵ and μ depend on the frequency of the incident electromagnetic wave.

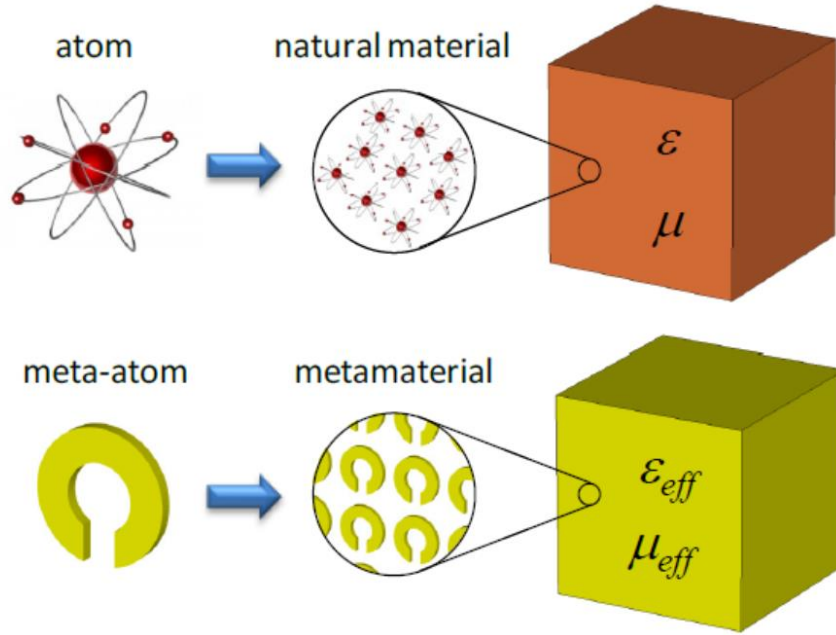


Figure 2.4: Representation of natural materials (top) and metamaterials (bottom). The natural materials composed by atoms, while the metamaterials composed by meta-atoms (Reprinted with permission from thesis Plasmonics and Metamaterials at Terahertz Frequencies by Víctor Landivar (2014))

The basic of Metamaterials are the idea of engineering artificial elementary particles in order to achieve a certain desired electromagnetic response. The operation wavelength should be larger than the size of these meta-atoms, also called unit cells, so that homogenization of the macroscopic fields inside the metamaterial is valid [28]. The meta-atoms have a specific geometry and they are made of natural materials with certain ϵ and μ . However, a periodic disposition of the meta-atoms allows

characterizing the whole structure with an effective permittivity ϵ_{eff} and permeability μ_{eff} . These effective parameters are quite different from the original ϵ and μ because the unit cell produces a specific electric and magnetic response where its geometry plays a role as important as the constituent materials. This way, it can be possible to achieve desire values of ϵ and μ not available in nature and design tailor-made medium properties. Figure 2.4 illustrates these basic ideas.

2.3 Fundamentals of Plasmonics

Plasmonics is concerned with the investigation of the interaction between electromagnetic radiation and conduction electrons oscillation in metallic nanostructures and nanoparticles. When the confinement of electromagnetic fields over dimensions on the order of or smaller than the wavelength of incident radiation, plasmonics effects comes in the picture. In the THz band, metals behave as good conductors since electrons can follow easily the driving electromagnetic field. However, the free electrons in metals can be excited to have collective oscillations at higher frequencies. Plasmonics is the field of nanophotonics which explains this phenomenon. There are two main parts in the field of plasmonics: surface plasmons polaritons and localized surface plasmons.

2.3.1 Surface Plasmons Polaritons

Surface Plasmons Polaritons (SPPs) are electromagnetic excitations propagating at the interface between a dielectric and a conductor [29]. The electric field component is enhanced near the surface and decays exponentially in the direction normal to the interface due to the rapid variation of the electromagnetic field at optical frequencies as shown in Figure 2.5 (a). Under certain conditions, a self-sustained excitation can be induced near the surface which may propagate closely confined to the metal. Research on SPPs has been initiated dates back to 1902 when Wood's studied the spectrum of light diffracted by diffraction gratings [30]. This study is called Wood's anomalies in

which the rapid variations in the intensity of the diffracted spectral in narrow frequency bands. Almost one century later Wood's discovery, plasmonics has considerable attention and nowadays it is considered as a vital part of nanophotonics.

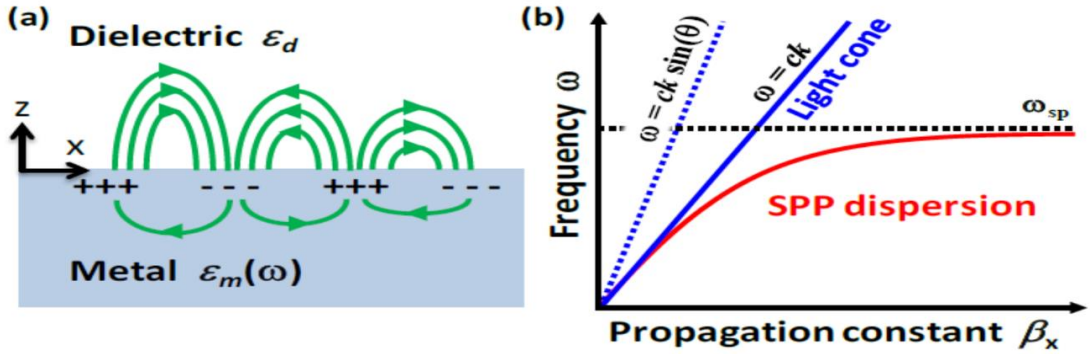


Figure 2.5: (a) electric field for SPP propagation at a dielectric metal interface and (b) Dispersion relation (Reprinted with permission from thesis Plasmonics and Metamaterials at Terahertz Frequencies by Víctor Landivar (2014))

The flat interface between a dielectric with real positive constant permittivity and metal is the simplest geometry sustaining SPPs. The derived dispersion relation of SPPs starting from Maxwell's equations through Helmholtz equation given by, [31],

$$\beta_x = k_0 \sqrt{\frac{\epsilon_d \epsilon_m(\omega)}{\epsilon_d + \epsilon_m(\omega)}} \quad (2.54)$$

where β_x is the propagation constant, k_0 is the wave vector of the propagating wave in vacuum and ϵ_d and $\epsilon_m(\omega)$ are the permittivity of the dielectric and the metal, respectively. The dispersion relation is shown in Figure 2.5 along with the representation of the geometry. The bound nature of the SPP can be deduced from Eq. (2.54) and Figure 2.5 (b). β_x is larger than dielectric's wave vector k and hence, the dispersion curve lies to the right side of the dielectric's light cone. The resultant evanescent decay on both sides of the interface is represented in Figure 2.5 (a). Since the wave impinging with an incident angle θ to the interface will never excite a SPP as

the projection of its wave vector $k_x = k \sin \theta$ is always smaller than β_x . In order to excite a SPP, phase-matching techniques should be applied to provide additional momentum to the impinging light [29]. Excitation upon charged particle impact, prism coupling, grating coupling, excitation using highly focused optical beams or near field excitations are the most common techniques for SPP excitations

2.3.2 Localized Surface Plasmons

Localized Surface Plasmons (LSPs) are non-propagating excitations of the conduction electrons of metallic nanostructures coupled to the electromagnetic field. This resonance arises from effective restoring forces on the driven electrons to the geometry of the nanostructure which allows the suitable scattering condition [28]. The main difference from SPP is that LSP can be excited by direct light illumination without the need of phase-matching techniques.

When a particle of size is much smaller than the wavelength of excitation in the surrounding medium, a quasi-static approximation can be done since over the volume of the particle, the phase of the oscillating electromagnetic field is practically constant under this electrostatic approach and after some algebra [29] we arrive to an expression for the dipole moment for a small nanosphere

$$p = \varepsilon_0 \varepsilon_m 4\pi a^3 \frac{\varepsilon - \varepsilon_m}{\varepsilon + 2\varepsilon_m} E \quad (2.55)$$

$$p = \varepsilon_0 \varepsilon_m \alpha E \quad (2.56)$$

Where,

$$\alpha = 4\pi a^3 \frac{\varepsilon - \varepsilon_m}{\varepsilon + 2\varepsilon_m} \quad (2.57)$$

Here, α is the electric polarizability of a small sphere of subwavelength diameter a , permittivity ε within a medium while under the excitation of an electric field E permittivity ε_m .

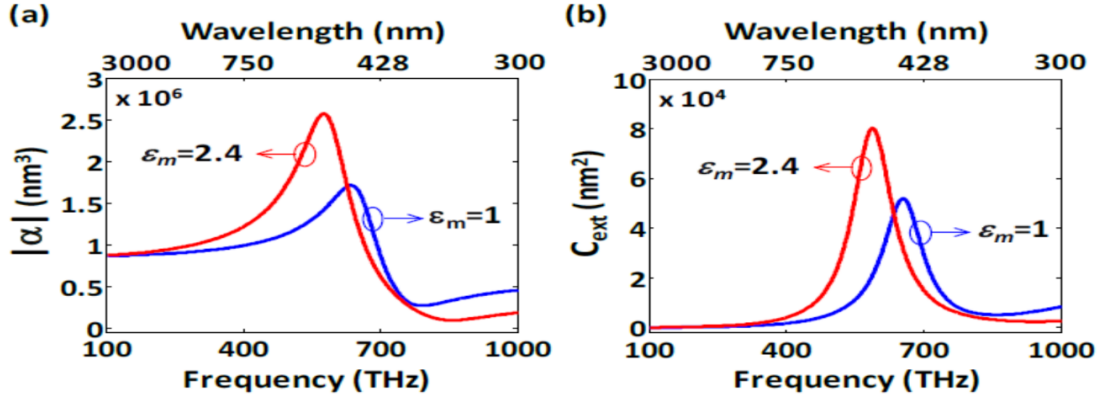


Figure 2.6: (a) Polarizability and (b) extinction cross section of a gold nanosphere of radius 50 nm in two media along with two different permittivity ϵ_m (Reprinted with permission from thesis Plasmonics and Metamaterials at Terahertz Frequencies by Víctor Landivar (2014))

The polarizability experiences a resonant enhancement under the condition that $|\epsilon + 2\epsilon_m|$ is a minimum according to Eq. (2.57). When $\text{Re}[\epsilon] = -2\epsilon_m$, the resonance takes place for the case of small or slowly-varying imaginary part of ϵ which is known as the Fröhlich condition. Metal nanoparticles are ideal elements for optical sensing of changes in the index of refraction as there is a strong dependence of the resonant frequency on the surrounding medium. Figure 2.6 (a) shows the polarizability of a gold sphere within two different media is depicted.

2.4 Plasmonics Metamaterials in Terahertz region

At dielectric-metal interface, strong electromagnetic field confinement can occur over length scales smaller than the incident wavelength as long as the fields oscillate at frequencies close to the plasma frequency of the metal. Hence, the SPPs are limited to the visible and near-infrared range since noble metals find their plasma frequency close to only that part of the spectrum. At lower frequencies, permittivity of metals is very large leading to negligible field penetration in the conductor and SPPs are highly

delocalized. The existence of SPPs for perfect electrical conductors is forbidding due to the electric field has not resided inside the metal. The resultant potential applications of SPP such as localized waveguiding and optical sensing cannot be achieved for the THz band and below frequency. However, this limitation can be overcome with metamaterials. The tailoring the effective permittivity and the effective plasma frequency to lower frequencies is possible by means of engineering the metal surface geometry. Pendry and co-workers demonstrated that metallic surfaces periodically arrangement are able to support bounded surface waves, even if the metal is a perfect conductor, copying the behavior of SPPs [32].

The combination of ISBT in semiconductor quantum-wells and metamaterials shows the great potential to operate in terahertz regime [33-39]. Depending upon the application and operating frequency, a large number of metamaterials and metasurface structure have been utilized to enhancement of the device performance in terahertz region [40-44]. Dimension and geometry depended antenna couple terahertz source and detector showing great enhance in the performance of devices [45-49]. Another area of significant research is plasmonic nanostructure which has been provided unique opportunities for manipulating electromagnetic waves in the terahertz range. Many novel terahertz devices such as photoconductor antenna [49, 50], detector [51], plasmonic photomixer [52], QCLs [53] in which plasmonic nanostructure significantly improve the devices performance.

Theoretical Modelling and Simulation

In this chapter we focus the attention on Plasmonics Metamaterials based Intersubband transition (ISBT) able to enhance efficiently the light-matter interactions putting emphasis in their theoretical modelling and simulation work. Theoretical modelling and simulation started from with role of polarization in wurtzite semiconductor followed by the self-consistent solution of Schrodinger and Poisson equations, $k.p$ model and Fermi Golden rule are used to compute ISBT in GaN HEMT structure. Furthermore, the Ground-source-ground (GSG) HEMT device configuration is presented as metamaterial configuration whose design is not only inspired by classic RF measurement geometries but also high-frequency metamaterial effects must be taken into account. Additionally, the nanometric gate structure of HEMT generates the terahertz plasmonic effect at the interface. Built upon the semiconductor ISBT model for III-Nitride semiconductor heterostructure and GaN HEMT. Two other aggregate effects contributions are presented (i) metamaterial embedded and (ii) plasmonic assisted ISBT in 100 nm GaN HEMT.

3.1 GaN Heterostructure and Device description

GaN heterostructure is generally grown on sapphire or silicon carbide (SiC) substrate. Figure 3.1(a) shows most widely used GaN heterostructure consisting of 60 nm AlN nucleation layer, 2 μm thick undoped GaN layer, 0.8 nm AlN spacer layer, 20 nm undoped $\text{Al}_{0.3}\text{Ga}_{0.7}\text{N}$ barrier layer and 3 nm Si_3N_4 passivation layer. Introducing a thin 0.8 nm AlN interlayer between AlGa N and Ga N plays a crucial role. Better carrier confinement, reduced alloy scattering and enhanced conductivity are achieved by inserting a thin AlN layer [54, 55]. The cross-sectional view of the simulated GaN HEMT device by Silvaco® TCAD is shown in Figure 3.1 (b). Computation mesh to simulate the device structure is shown in Figure 3.1 (c). In the regions, like beneath the

gate, at the edges of the source and drain contacts and at AlGaN/AlN/GaN interface, fine meshing is done in order to achieve the convergence and accuracy of the calculations. The spacing between different electrodes viz source to gate, gate to drain and source to drain are set to 0.9, 2.0 and 3.0 μm respectively. Gate length is kept as 100 nm. In order to get lower gate resistance, gate geometry is selected as T-gate in simulation as well as in fabrication.

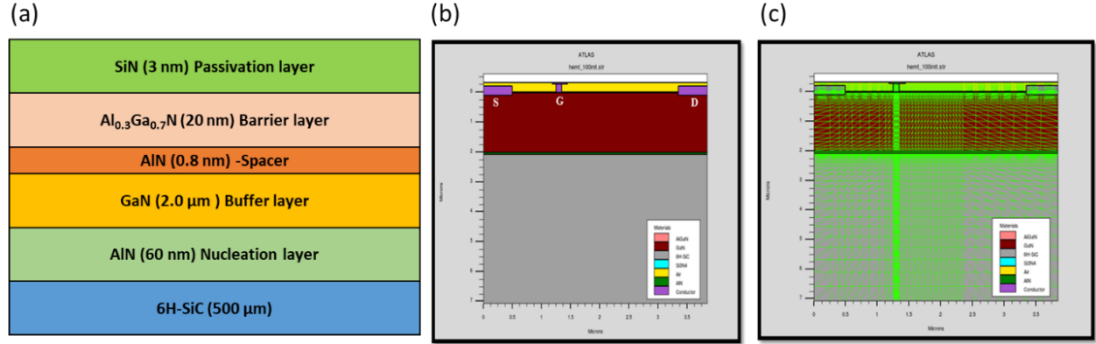


Figure 3.1: (a) GaN Heterostructure, (b) HEMT cross-sectional view and (c) HEMT Mesh structure

Generally, high-power RF GaN HEMT is fabricated in a multi-finger configuration. Two ground-source-ground (GSG) configurations namely 2x150 and 8x150 are shown in Figure 3.2. To measure the RF performance of the device GSG configuration is widely used for HEMT fabrication. 2x150 configuration contains 2 gate fingers with 150 micron unit gate width of the device. Similarly, 8x150 configuration contains 8 gate fingers with 150 micron unit gate width. In order to expand the device length for high-power applications, a higher number of gate fingers are used. For example, if the power handling capability of fabricated GaN HEMT is 5 W/mm, the 2x150 = 0.3 mm device can be used for 1.5 W RF power. Similarly, 8x150 = 1.2 mm device can be used for 6.0 W RF power. Before further discussion on Plasmonic metamaterial assisted ISBT, following section discussed the semiconductor ISBT modelling in III-Nitride semiconductors.

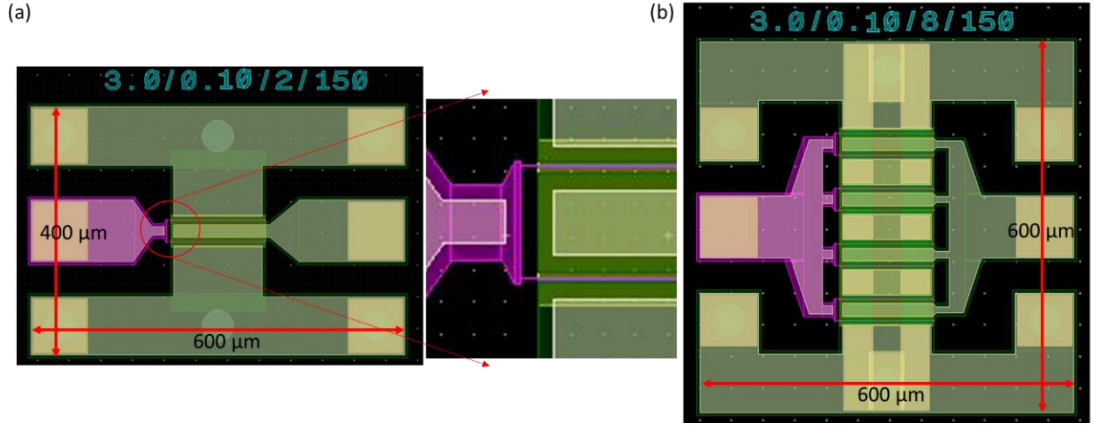


Figure 3.2: Typical configurations of GaN HEMT (a) 2 gate fingers with 150 micron gate width (2x150) (zoom image for gate fingers visualization and (b) 8 gate fingers with 150 micron gate width (8x150) [Representation 3.0/0.10/8/150 indicates Source to Drain distance 3.0 μm , 0.1 μm (100 nm) gate length, 8 fingers device with 150 μm gate width].

3.2 Semiconductor ISBT Modelling

The basic equations of physical processes are solved for every grid point in the simulation. These equations include Poisson's equation, continuity equations and transport equations, derived from Maxwell's equations [49]. The computation of 2DEG properties due to spontaneous and piezoelectric polarization effects is performed using the polarization model [57, 58]. An induced strong polarization field is introduced to calculate band diagrams. To increase the reliability of simulation, measurement-based ohmic contact resistance and Schottky barrier height data are incorporated in simulation in order to define source, drain and gate contacts. Low field mobility model is used to account the temperature dependent drift of electrons and holes separately [59]. While Shockley-Read-Hall recombination model is used to estimate the statistics of holes, electrons and their recombination rate. The traps/defects in the heterostructure play a crucial role in the performance of GaN devices. Accordingly, we also introduced interface traps energy level and density in the modeling. Output results are extracted by solving the basic equations for every grid point with the different biasing conditions.

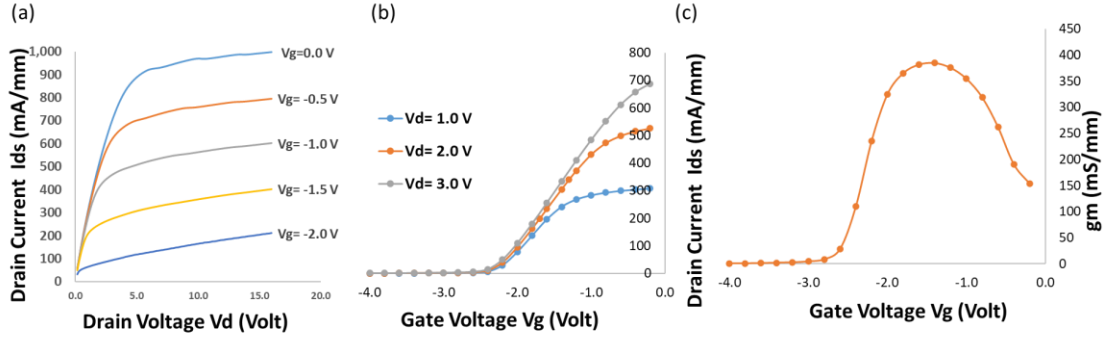


Figure 3.3: (a) output characteristics (I_d - V_d), (b) transfer characteristics (I_d - V_g) and (c) Transconductance of the simulated device

The variation of the drain current with respect to applied drain (V_d) and gate (V_g) biasing voltage is plotted in Figure 3.3. The simulated output characteristics (I_d - V_d) and transfer characteristics (I_d - V_g) are shown in Figure 3.3 (a) and (b) respectively. The extracted transconductance is > 350 mS/mm as shown in Figure 3.3 (c). The extracted Capacitance-Gate voltage (V_g) and 2DEG density with applied gate bias are depicted in Figure 3.4 (a) and (b) respectively.

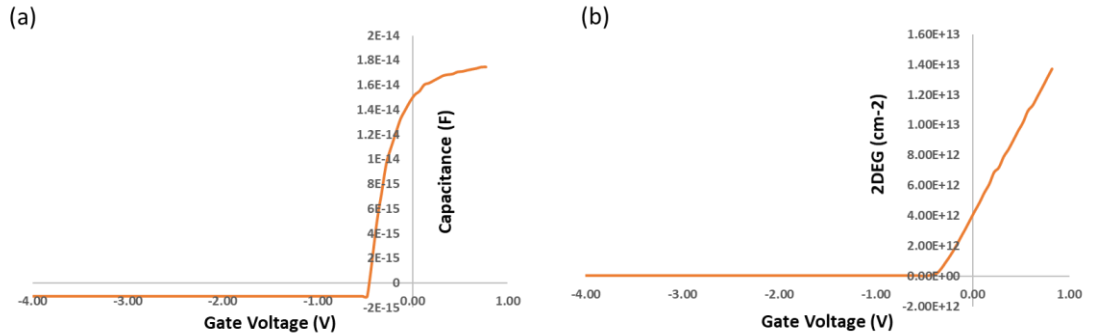


Figure 3.4: Extracted (a) CV profile and (b) 2DEG profile with applied Gate voltage

The current gain cut-off frequency (f_t) and maximum frequency of oscillations (f_{max}) are the two most pertinent parameters for high-speed device application. f_t and f_{max} are extracted from small signal RF simulation. Current gain (h_{21}) and maximum available power gain (G_a) are simulated at bias conditions $V_d = 7$ V; $V_g = -1.5$ V and plotted with respect to frequency in Figure 3.5. Summary of simulated DC and RF

device parameters are given in Table 3.1 which is closely matching with the corresponding process design kit (PDK) datasheet of renowned international GaN foundries [11].

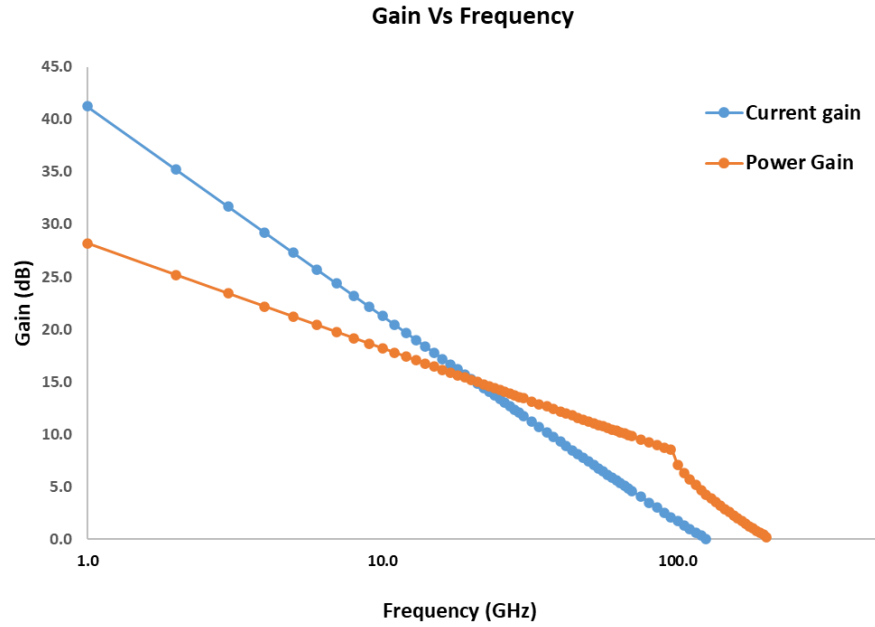


Figure 3.5: Current gain and power gain of the simulated device

Table 3.1: Summary of simulated device DC and RF Parameters

Sr No	Parameters	Simulated Result
1	Idss (A/mm)	0.995
2	Vknee (V)	5
3	Ron (ohm*mm)	3.5
4	Vth (V)	-3.0
5	gm (mS/mm)	384
6	ft (GHz)	110
7	fmax (GHz)	180

The cut-off frequency of field effect transistor (FET) including HEMT is defined by $f_T = v/2\pi L = 1/2\pi\tau$, where v is carrier velocity, L is gate length and τ is electron transit time under the gate. For a very small 30 nm gate length up to 300-350 GHz cut-off frequency operation has been demonstrated [12]. However, beyond conventional transit-time limitations, these FET devices can be operated at much higher frequencies up to the terahertz. Dyakonov–Shur proposed the plasma wave theory to describe THz behavior in FET devices [13, 14]. The basic of plasma wave theory is the instability of 2DEG which has a resonant response to incident electromagnetic radiation in short channel FET. The size and shape of the FET channel are used to govern the resonant response of plasma frequency to electromagnetic radiation. The tuning of plasmon frequency by external biasing has been used for detectors, mixers and multipliers [14]. There are several reports available in which the plasma wave theory is used to describe the THz behavior of devices. Plasma wave theory concept has been widely demonstrated from conventional semiconductors like Si [15], GaAs [13], GaN [16], InP [17] to new two-dimensional materials system like Graphene [18], Black Phosphorus [19], etc. There are few literatures available in which GaN HEMT device working mechanism is explained through plasma wave theory [16, 20-23].

In this chapter, it is demonstrated that in the addition to established Plasma wave theory, the Intersubband transition (ISBT) mechanism can also describe the terahertz behavior of the GaN HEMT device. ISBT theory is based on carrier transitions within a conduction band which is entirely different from plasma wave theory. The possibility of electrical tuning the intersubband resonances (ISBR) in GaN HEMT device by external gate biased is explored as follows.

The strain effects consideration for extraction of effective-mass Hamiltonian is of prime importance for wurtzite semiconductors. This Hamiltonian is used to derive the electronic band structures of bulk and quantum-well wurtzite semiconductors. Kane’s model is applied to derive the band-edge energies and the optical momentum-matrix elements for strained wurtzite semiconductors. We then derive the effective-mass Hamiltonian by using the k.p perturbation theory. The developed k.p model is applied to our heterostructures structures, especially quantum well via envelope function approximation (EFA) method [60, 61]. An envelope function model is derived

for electrons in a semiconductor heterostructure. The materials dependent Hamiltonian extraction by EFA method is most suitable for abrupt semiconductor junction [62]. The finite element method [63] is used to solve the coupled multi-band Schrödinger Poisson's equation [64] numerically. As discussed in section 2.1.2, when wide band gap material AlGaIn grow on lesser band material GaN, a triangular quantum well is formed at the interface. Under triangular quantum well the solution of the wave function is given by [65, 66],

$$\Psi(z) = Ai \left[\frac{2m_z^* e F_z}{\hbar^2} \left(z - \frac{E_i}{e F_z} \right) \right] \quad (3.1)$$

where m_z^* is the effective mass of electron in the GaN, F_z is the electric field in the z-direction, E_i is the eigenvalues of energy with $i=0,1,2,\dots$ for the ground state, 1st excited state and so on. Ai Airy function is given by

$$Ai(z) = \frac{1}{\pi} \int_0^\infty \cos \left(\frac{t^3}{3} + zt \right) dt \quad (3.2)$$

The eigen value is given by [69, 70],

$$E_i \approx \left(\frac{\hbar^2}{2m_z^*} \right)^{1/3} \left[\frac{3\pi e F_z}{2} \left(i + \frac{3}{4} \right) \right]^{2/3} \quad (3.3)$$

When an incident terahertz radiation illuminates the GaN HEMT, electrons may absorb the photon energy and jump to a higher energy subband. Carriers below Fermi energy levels are collected by drain electrode, when we applied voltage between source and drain. Using Fermi's golden rule for the transition from i state to j state, we can calculate the absorption coefficient by [61, 67],

$$W_{ij} = \frac{2\pi}{\hbar} < \Psi_i | H' | \Psi_j >^2 \delta(E_j - E_i - \hbar\omega) \quad (3.4)$$

where, H' is interaction Hamiltonian. By applying the dipole approximation, we obtain [61, 67],

$$W_{ij} = \frac{2\pi}{\hbar} \frac{e^2 E_0^2}{4m_z^2 \omega^2} \langle i | e \cdot p | j \rangle^2 \delta(E_j - E_i - \hbar\omega) \quad (3.5)$$

The matrix element in the above equation can be expanded in terms of interband and intersubband transitions as following,

$$\langle i | e \cdot p | f \rangle = e \cdot \langle u_v | p | u_{v'} \rangle \langle f_n | f_{n'} \rangle + e \cdot \langle u_v | u_{v'} \rangle \langle f_n | p | f_{n'} \rangle \quad (3.6)$$

Applying the envelope function matrix element in the z-direction can be written as,

$$\langle i | p_z | j \rangle = \int \Psi_i^*(z) p_z \Psi_j(z) dz \quad (3.7)$$

The dimensionless optical field strength between the two-energy state is given by [60, 65],

$$f_{ij} = \frac{2}{m_z^* \hbar \omega_{ij}} \langle i | p_z | j \rangle^2 = \frac{2m_0^* \omega_{ij}}{\hbar} \langle i | z | j \rangle^2 \quad (3.8)$$

Where,

$$\omega_{ij} = (E_j - E_i)/\hbar$$

And

$$\langle i | z | j \rangle = z_{ji} = \frac{2L}{(t_i - t_j)^2} \quad (3.9)$$

With, t_i and L are electric length express as,

$$t_i = \left[\frac{3\Pi}{2} \left(i + \frac{3}{4} \right) \right]^{2/3} \quad (3.10)$$

$$L = \left(\frac{\hbar^2}{2m_z^* e F_z} \right)^3 \quad (3.11)$$

By substituting equations (3.9)-(3.11) in equation (3.8) we get,

$$f_{ij} = \frac{8.32}{(t_i - t_j)^4} \left(\frac{\Pi}{2} \right)^{2/3} \left[\left(j + \frac{3}{4} \right)^{2/3} - \left(i + \frac{3}{4} \right)^{2/3} \right] \quad (3.12)$$

By substituting $i=0$ and $j= 1,2,3,\dots$ oscillation strength for transition can be calculated as $f_{01}=0.73$, $f_{02}=0.12$, $f_{03}=0.045$, etc. The oscillator strength of all the transitions is sum up to 1. Calculated transition indicates that the probability for higher levels transitions is very weak

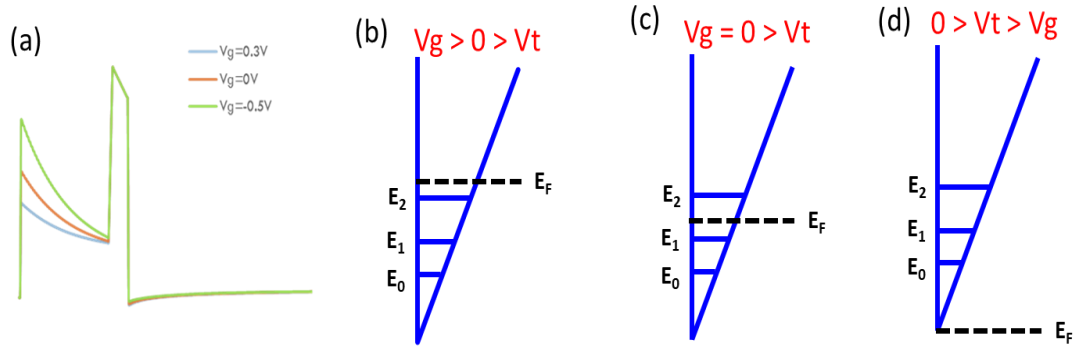


Figure 3.6: (a) Conduction band energy profile with different applied gate voltage and Fermi Energy level with filled subband inside Triangular Quantum well with different applied Gate biasing (b) $V_g > 0 > V_t$, (c) $V_g = 0 > V_t$ and (d) $0 > V_t > V_g$

The gradual pinning of the Fermi level inside the quantum well is possible by increasing gate voltage. When gate voltage is sufficiently negative ($0 > V_t > V_g$), the conduction band is above the Fermi level [Figure 3.6 (d)]. In this case, the channel is completely depleted of 2DEG. When the gate voltage is greater than the threshold

voltage ($V_g > V_t$), charges start filling the channel [Figure 3.6 (c)]. As the gate voltage increased, the fermi level gradually pins inside the quantum well and 2DEG carriers are filled among allowed subband in the channel. When gate voltage is sufficiently higher ($V_g > 0 > V_t$), carrier occupies all allowed subband below the fermi energy level [Figure 3.6 (b)]. For this case, total 2DEG charges are distributed in the allowed energy subband and take participation in channel conduction. The triangular quantum well conduction band energy profile for GaN HEMT with different gate biasing conditions is shown in Figure 3.6 (a). Fermi Energy level pinning inside the subband of triangular quantum well with different applied gate biasing is shown in Figure 3.6 (b)-(d). The spacing and charge filling inside the subband strongly depends upon gate biasing voltage. In other words, the gate biasing-assisted tuning of inter subband resonance (ISR) frequency is possible in HEMT structure.

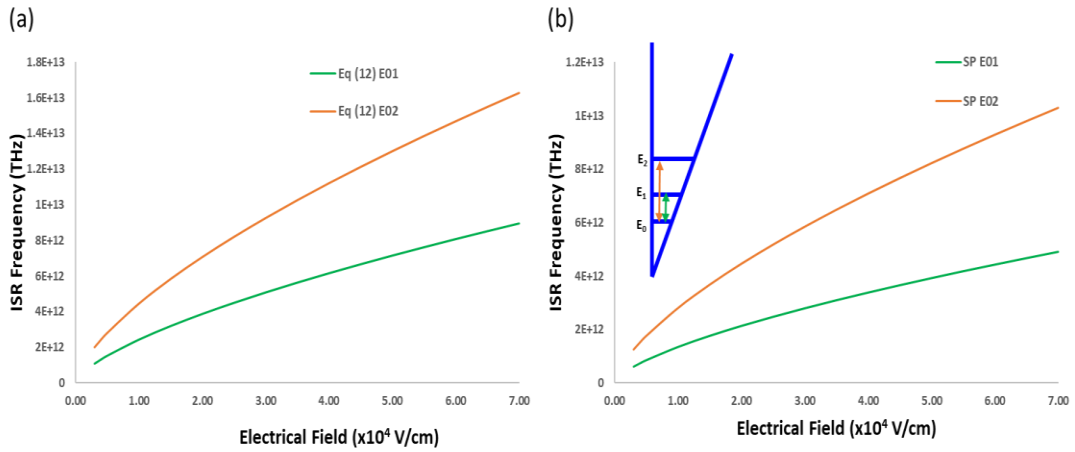


Figure 3.7: Intersubband Resonance Frequency as a function of the applied field (a) Calculated using eq (3.3) and (b) By solving self-consistency Schrodinger-Poisson solver.

In the simulation, we extracted up to three ISB energy levels inside the triangular quantum well. The ISR frequency as a function of applied gate biasing field is calculated using equation (3.3) and by solving self-consistency Schrodinger-Poisson solver for different gate bias voltages. The Intersubband Resonance frequency as a function of the applied field is shown in Figure 3.7 (a) and (b). The ISB tuning is one order higher in asymmetric triangular well potential as compared to the conventional

square well potential. Moreover, 2DEG carrier concentration inside the GaN HEMT channel also depends upon Al composition and AlGaN barrier layer thickness. Figure 3.8 (a) and (b) are shown the simulated 2DEG carrier concentration variation with AlGaN thickness and Al composition respectively. It clearly indicates that increment in barrier layer thickness and Al composition enhances the 2DEG density inside the channel. It further implies that manipulation in ISR is possible in GaN HEMT devices based on variation in 2DEG density, which provides tuning in the THz region.

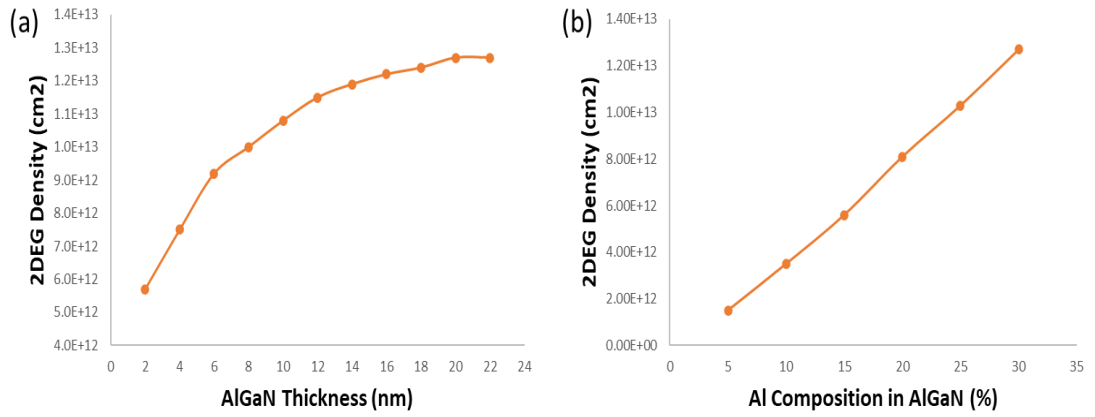


Figure 3.8: 2DEG carrier concentration of AlGaN/AlN/GaN heterostructure for (a) different AlGaN thickness and (b) different Al composition in AlGaN layer

3.3. Metamaterial embedded ISBT Modelling

The combination of ISBT in semiconductor quantum-wells with metamaterials shows great potential in the terahertz region [33-39]. There are large numbers of metamaterial and metasurface structures have been employed and demonstrated enhance performance in the terahertz region [40-44]. Based on the propagation phase constant (β) of the current flowing through the antenna element, one can classified the natural and metamaterials [68]. If the value of β is greater than zero ($\beta > 0$), the material is classified as natural materials. The material is classified as metamaterial if the value of β is less than zero ($\beta < 0$) for a particular frequency band or zero at the nonzero frequency ($\beta = 0$).

In the present modelling work, we are reporting that the standard GSG device geometry of HEMT which itself acts as a metamaterial structure ($\beta < 0$). The enhancement of terahertz interaction with 2DEG inside the triangular quantum well is reported for GaN HEMT. The resonance mode in metamaterial structure is dynamically manipulating the carrier distribution inside the quantum well.

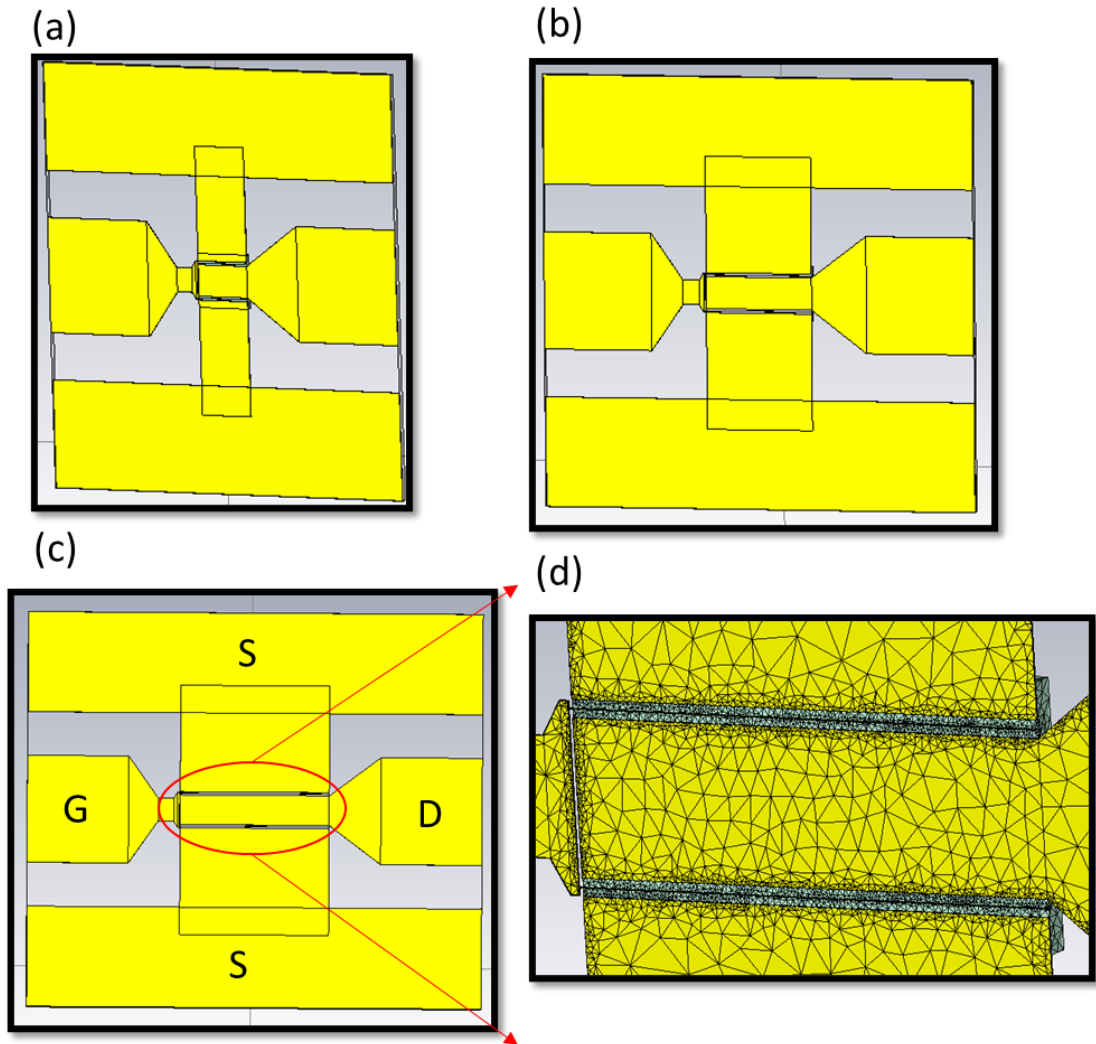


Figure 3.9: Three different configuration (a) 2x50, (b) 2x100 and (c) 2x150 of GaN HEMT and (d) GaN HEMT meshing

For the metamaterial modelling work, the GaN heterostructure and device geometry are kept identical as shown in Figure 3.1. Finite difference frequency domain CST Microwave Studio® simulator has been used to simulate the entire device configuration which acts as terahertz metamaterial. Standard GSG configuration along

with 50 to 150 micron gate width has been used for 3D electromagnetic modelling as shown in Figure 3.9 (a)-(c). Very fine localized tetrahedral sub-meshing has been used in the active source to drain region to enhance the accuracy of calculations as shown in Figure 3.9 (d). Terahertz radiation (0.3-3 THz) is illuminated on the entire GSG device configuration which includes the active GaN HEMT region also. Table 3.2 shows the dimension used in 3D EM simulation work. Three different geometries, viz 2x50, 2x100 and 2x150 have been used in the present study. The E-field of the incident THz plane wave is kept at 1 V/m for all three devices.

Table 3.2: Different devices configurations used in metamaterial simulations

Device configuration	Distance between S and D (μm)	Gate width (μm)	Gate length (nm)	Total device dimension ($\mu\text{m} \times \mu\text{m}$)
Device A (2x50)	3.0	50	100	350x400
Device B (2x100)	3.0	100	100	400x400
Device C (2x150)	3.0	150	100	450x400

The wavelength corresponding to entire terahertz spectrum (0.3 to 10 THz) is about 30-1000 micron. If the device dimension is the order of incident radiation, it acts as an antenna. Antenna size and shape largely determine the frequency it can handle. Antenna coupled terahertz source and detector are showing a potential advantage in the performance of devices for the terahertz region [38-42]. The dimensions of the devices as listed in Table 3.2 are of the order of illuminated terahertz radiation wavelength. These devices act as an antenna which leads to convergence of incident radiations toward the active channel region. Moreover, inside device microstructures like source-drain spacing, gate etc. are on the scale much less than the wavelength of incident radiation. The source drain configuration of HEMT resembles parallel plate capacitors, hence the electromagnetic energy is being stored. The E-field is trapped in the GaN heterostructure. The equivalent circuit of a GaN HEMT device is simplified as capacitance and resistance. The relationship between the THz power and the circuit capacitance is given by,

$$P_{THZ}(\omega) \propto \frac{1}{1 + (\omega R_C C)^2} \quad (3.13)$$

where P_{THZ} is the mean power of THz, ω is the frequency, R_C is the HEMT channel resistance and C is the capacitance of the HEMT structure. The resultant electric field intensity inside the active channel region between source and drain is greatly enhanced. The enhancement of the field due to illumination strongly depends on the frequency of incident radiation and device dimension. For example, the electric field intensity distribution for 0.4 THz incident radiation is shown in Figure 3.10 (a)-(c) for different

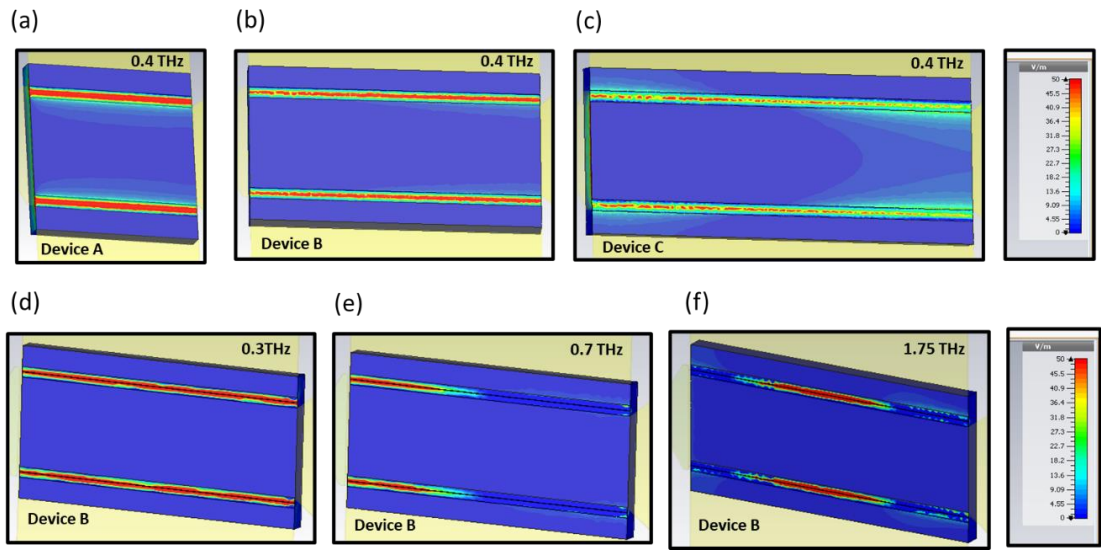


Figure 3.10: Electrical field enhancement for 0.4 THz incident radiation on (a) 2x50, (b) 2x100 and (c) 2x150 of GaN HEMT devices. Electrical field enhancement for 2x100 GaN HEMT device at (d) 0.3 THz, (e) 0.7 THz and (f) 1.75 THz incident radiation

three GaN HEMT devices namely 2x50, 2x100 and 2x150. Each device structure has a unique resonance response towards incident terahertz radiation. Similarly, the resonance response of 2x100 GaN HEMT device towards incident terahertz radiations namely 0.3, 0.7 and 1.75 terahertz are shown in Figure 3.10 (d)-(f). Moreover, the illumination-dependent enhancement of the field is not distributed uniformly throughout the channel. The highest field distribution found at the center of 2x100 device for 1.75 THz illuminations is shown in Figure 3.10 (f). The summary for average

field enhancement inside the channel region due to illumination is illustrated in Figure 3.11. GaN HEMT device itself acts as metamaterial which further influences the overall terahertz performance of the GaN HEMT device.

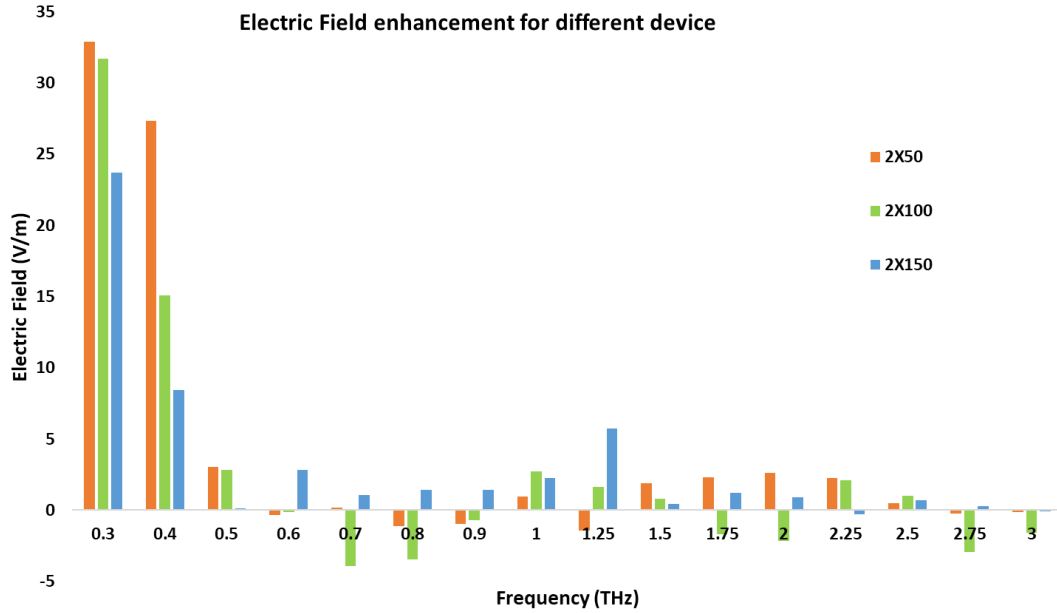


Figure 3.11: Electrical field enhancement due to illumination of terahertz radiation on GaN HEMT devices

3.4. Plasmonic assisted ISBT

Plasmonic nanostructure provides unique opportunities for manipulating electromagnetic waves in the terahertz range. Recently many novel plasmonic nanostructure-based devices such as photoconductor antenna [48, 50], detector [58], plasmonic photomixer [52], QCLs [53] showed significant improvement in devices performance.

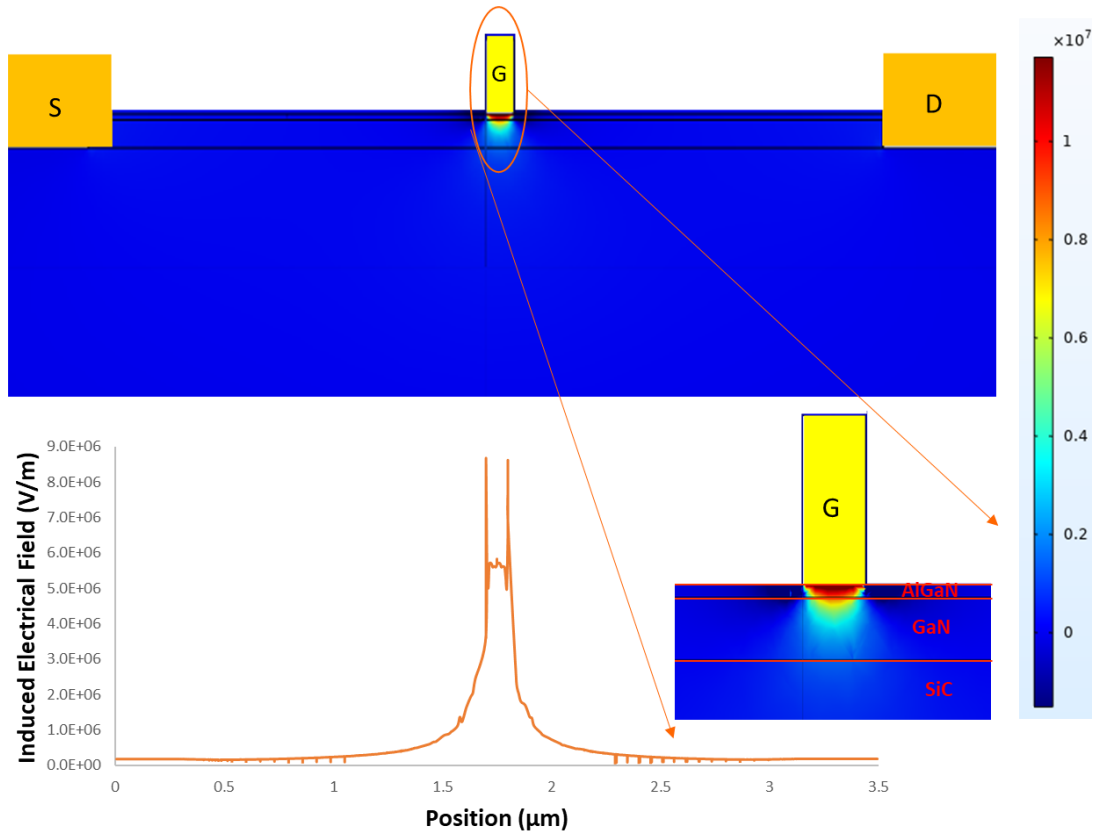


Figure 3.12: Electrical field enhancement for 0.4 THz incident radiation on GaN HEMT device using a finite element method-based electromagnetic solver (COMSOL)

For plasmonic structure simulation, finite element frequency domain COMSOL Multiphysics® numerical method has been used to solve Maxwell's equation in order to predict electromagnetic interaction in each layer of semiconductor heterostructure. Heterostructure stack, device geometry and device structure are kept identical as used in semiconductor modelling shown in Figure 3.1. The incident terahertz plane wave radiation is kept 1 V/m from 0.3 to 3 THz to interact with GaN heterostructure. The surface plasmon is generated at the interface between nanometric gate contact and heterostructure.

The field in the vicinity of the fine gate structure is drastically increased due to surface plasmon generation. Subsequently, the terahertz incident wave is coupled to

2DEG inside the channel. The concentration of the induced electric field is considerably enhanced in close proximity to the device gate contact electrodes. The induced electric field is approximately $5.5\text{E}+06$ on the gate and $8.5\text{E}+06$ V/m on the gate edge for 0.4 terahertz due to plasmonic structure as shown in Figure 3.12. As the incident frequency increases, the plasmonic induced electric field also increases and saturate towards higher frequency as depicted in Figure 3.13. It was interesting to find that the plasmonic enhanced field ($\sim 10^7$ V/m) is approximately one order higher than the externally applied bias field ($\sim 10^4$ V/cm= 10^6 V/m) at the gate (Figure 3.7).

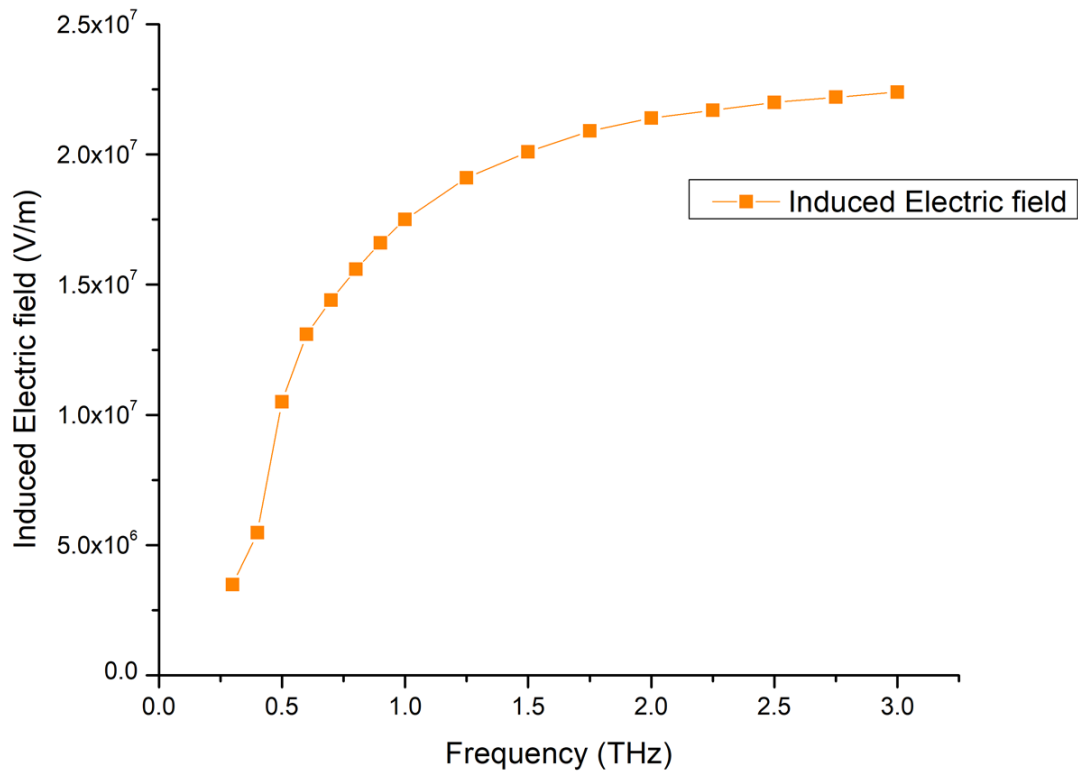


Figure 3.13: Induced Electrical field due to terahertz radiation illumination on GaN HEMT device using a finite element method-based electromagnetic solver (COMSOL)

The outcome of the entire simulation activities clearly demonstrates GaN HEMT devices operation exhibiting into THz range beyond its cut-off frequency. It is also manifested from simulation results that overall performance of GaN HEMT is governed by aggregate effects of ISBT, plasmonic structure and metamaterial behaviour.

GaN Heterostructure Growth and Characterization

This chapter introduces the semiconductor heterostructure fabrication and characterization technology in the context of III-Nitride GaN based HEMT device fabrication. The chapter lists the experimental techniques used in this dissertation, beginning with the GaN Heterostructure growth to the purpose of characterization of grown GaN heterostructure to assess quality and properties. Highly precise standard semiconductor characterization tools like Hall measurement, High-resolution XRD, Photoluminescence (PL) system, Atomic Force Microscope, Micro Raman Spectroscopy, etc. are not only used for structural, mechanical, electrical and optical properties extraction in GaN heterostructure, but also a collective correlation among all these properties is discussed.

4.1 Heterostructure growth

Molecular Beam Epitaxy (MBE) and Metal organic vapor phase epitaxy growth (MOVPE) are principal growth techniques for III-Nitride semiconductor. MOVPE and MBE growth are distinguished from the perspective of source materials, growth mechanism and growth pressure. In MBE growth, the source materials are evaporated in effusion cell by heating high purity elements and produced as a beam of atoms/molecular. Interaction within the evaporated atoms/molecules is prohibited in MBE growth, this technique needs growth vacuum as low as 10^{-11} torr. The growth temperature is usually 500-700 °C for MBE growth. Atoms react on a heated substrate surface and layers grow two dimensionally. In III-Nitride heterostructure growth, the ammonia cracking efficiency is quite low at the growth temperatures used in MBE system. Hence, nitrogen plasma is often used for supplying atomic source of nitrogen in MBE growth of III-Nitride heterostructure. The possibility to control the interface at

monolayer level is a great advantage of this growth technique through Reflected High Electron Energy Diffraction (RHEED) types of in-situ characterization tools.

MOVPE growth is also known as Metal organic chemical vapor deposition (MOCVD) in which metal organics ingredients are used in the growth. Generally, trimethylgallium (TMGa), trimethylindium (TMIn) and trimethylaluminum (TMAI) based metal organics are used for group III (alkyl) source and ammonia is used as a group V (hydride) source in MOVPE based III-Nitride growth. The carrier gases like hydrogen and nitrogen are used to transport the III-N sources to a heated substrate. Since ultra-high vacuum (UHV) does not require in MOCVD growth, it can become a mass production tool. GaN growth temperatures are usually above 1000 °C due to the low cracking efficiency of ammonia in MOCVD process. The substrate is heated using of Radio Frequency (RF), resistive or infrared lamp heating. The various type of reactors has been employed for MOCVD reactor in order to achieve high uniformity and stability of growth.

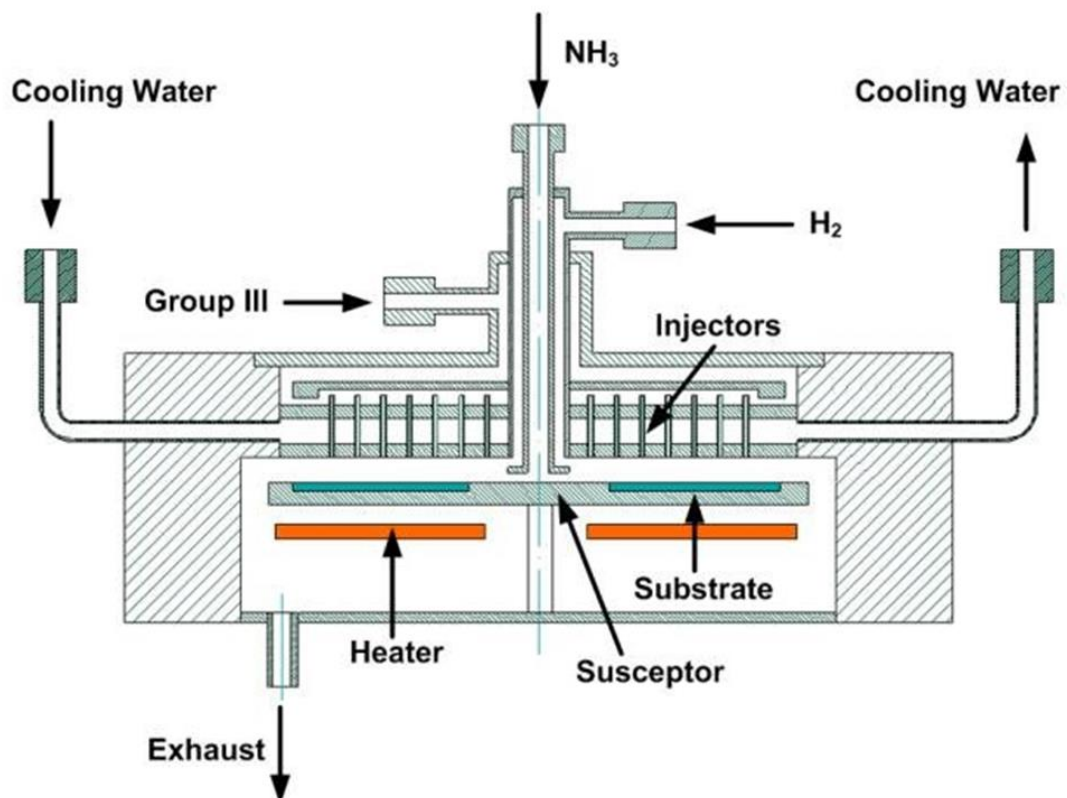


Figure 4.1: Schematic of Metal Organic Chemical Vapor Deposition (MOCVD)

MOCVD growth has been used to grow GaN heterostructure. The schematic of MOCVD reactor is shown in Figure 4.1. The ultrapure gases are inserted into a reactor and finely dosed to deposit a very thin layer of atoms onto a semiconductor wafer. Surface reaction of organic compounds or metalorganics and hydrides containing the required chemical elements creates conditions for crystalline growth. The layers are grown by transporting different precursors or reactants in the vapor phase, under controlled pressure, into a reactor chamber that holds the semi-insulating SiC wafer.

SiN (3 nm) Passivation layer	GaN (2 nm) Passivation layer	SiN (3 nm) Passivation layer
Al _{0.3} Ga _{0.7} N (20 nm) Barrier layer	Al _{0.3} Ga _{0.7} N (20 nm) Barrier layer	Al _{0.3} Ga _{0.7} N (20 nm) Barrier layer
	AlN (0.8 nm) -Spacer	AlN (0.8 nm) -Spacer
GaN (2.0 μm) Buffer layer	GaN (2.0 μm) Buffer layer	GaN (2.0 μm) Buffer layer
AlN (60 nm) Nucleation layer	AlN (60 nm) Nucleation layer	AlN (60 nm) Nucleation layer
6H-SiC (500 μm)	6H-SiC (500 μm)	6H-SiC (500 μm)
(a) Sample A	(b) Sample B	(c) Sample C

Figure 4.2: Thickness, composition and layers sequence of investigated three GaN heterostructure grown on 6H-SiC having (a) Sample A: AlGaN/GaN, (b) Sample B: GaN/AlGaN/AlN/GaN and (c) Sample C: AlGaN/AlN/GaN heterostructure

Three different optimized GaN heterostructures have been grown by MOCVD techniques on c-plane 4" diameter 6H-SiC wafer. The 60 nm AlN nucleation layer, 2 μm thick unintentional doped GaN buffer layer and 20 nm undoped Al_{0.3}Ga_{0.7}N layer kept identical in all three samples with less than 1% standard deviation in the growth process. Layer sequence, thickness and composition for grown three heterostructure is depicted in Figure 4.2. Sample B and C have 0.8 nm AlN spacer layer between AlGaN/GaN heterostructure, while Sample A is grown without AlN spacer layer. Sample B has 2 nm GaN cap layer at top of AlGaN/AlN/GaN heterostructure, while samples A and C have 3 nm Si₃N₄ passivation as shown in Figure 4.2. The highly uniform grown heterostructures are the primary requirement in order to investigate the light-matter interaction among specified three heterostructures. The fabricated heterostructures have been evaluated by using standard highly accurate semiconductor characterization techniques including atomic-force microscopy (AFM; Model: Keysight SPM 5420), Micro Raman Spectroscopy (Horiba; Model: LaBRAM HR) and

photoluminescence (PL) spectroscopy (DongWoo Optron), High resolution X-ray diffraction (HR-XRD; Bruker Model: D8 Discover), Hall measurements system (Nanomagnetic Instruments).

4.2 Heterostructure characterization

Structural, electrical, optical etc. properties of GaN heterostructure have been extracted by using standard highly accurate semiconductor characterization techniques. The characterization results show less than 1% standard deviation in the growth process which is extracted through nine measurement locations over 4" diameter GaN heterostructures as shown in Figure 4.3.

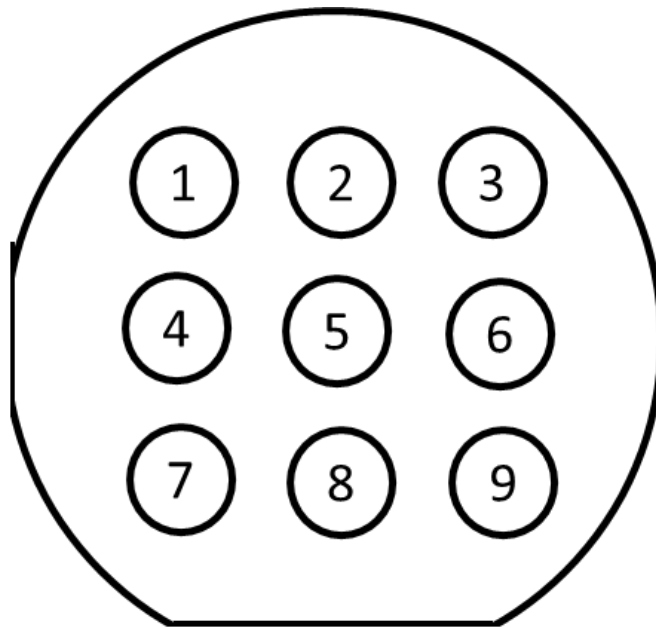


Figure 4.3: Nine points measurement over 4" GaN heterostructure on 6H-SiC wafer

The detailed each point measurement results are found in Tables 4.1 to 4.3 for each heterostructure. The summary of results extracted by using various characterization techniques (over nine locations average) are listed in Table 4.4. The discussion on the measurement results along with correlation among the optical, electrical, mechanical and structural properties in the following subsequence sections.

Table 4.1: GaN Heterostructure properties over 4” wafer for Sample A

Sr No	Measurement technique →	SiPDR	Hall	Hall	Hall	HR-XRD	HR-XRD	PL
	Measurement position ↓	Sheet Resistivity (Ω/\square)	Sheet Resistivity (Ω/\square)	2DEG (cm^{-2})	Mobility ($\text{cm}^2/\text{V.s}$)	AlGaIn thickness (nm)	Al content in AlGaIn (%)	GaN band gap (eV)
1	Position 1	498	546	6.55E+12	1283	19.3	30.1	3.436
2	Position 2	493	529	6.63E+12	1250	19.7	29.8	3.423
3	Position 3	494	533	6.69E+12	1312	19.3	29.7	3.419
4	Position 4	495	556	6.56E+12	1303	19.4	30.2	3.426
5	Position 5	491	519	6.58E+12	1276	19.5	30.1	3.401
6	Position 6	492	529	6.63E+12	1316	19.6	30.2	3.403
7	Position 7	485	541	6.65E+12	1321	19.7	30.3	3.426
8	Position 8	492	528	6.62E+12	1285	19.3	30.1	3.417
9	Position 9	499	549	6.55E+12	1268	19.3	29.9	3.407
	Mean	493.22	537	6.61E+12	1290	19.46	30.04	3.41759
	Std Deviation	3.88	11.30	4.64E+10	22.71	0.16	0.190	0.01
	Std Deviation (%)	0.79	2.11	0.70	1.76	0.84	0.63	0.33

Table 4.2: GaN Heterostructure properties over 4” wafer for Sample B

Sr No	Measurement technique →	SiPDR	Hall	Hall	Hall	HR-XRD	HR-XRD	PL
	Measurement position ↓	Sheet Resistivity (Ω/\square)	Sheet Resistivity (Ω/\square)	2DEG (cm^{-2})	Mobility ($\text{cm}^2/\text{V.s}$)	AlGaIn thickness (nm)	Al content in AlGaIn (%)	GaN band gap (eV)
1	Position 1	296	343	1.03E+13	1786	20.2	29.8	3.431
2	Position 2	293	325	1.04E+13	1751	19.7	29.8	3.418
3	Position 3	290	347	1.05E+13	1808	19.6	29.7	3.423
4	Position 4	294	337	1.02E+13	1805	19.9	30.4	3.393
5	Position 5	293	330	1.03E+13	1765	19.7	30.1	3.427
6	Position 6	294	351	1.04E+13	1821	19.8	29.9	3.412
7	Position 7	294	342	1.03E+13	1831	19.8	30.1	3.423
8	Position 8	293	311	1.03E+13	1786	19.9	29.4	3.404
9	Position 9	297	326	1.05E+13	1761	19.8	30.1	3.401
	Mean	293.78	335	1.04E+13	1790	19.82	29.92	3.41465
	Std Deviation	1.87	12.01	9.56E+10	26.26	0.16	0.27	0.012
	Std Deviation (%)	0.64	3.59	0.92	1.47	0.82	0.92	0.36

Table 4.3: GaN Heterostructure properties over 4” wafer for Sample C

Sr No	Measurement technique →	SiPDR	Hall	Hall	Hall	HR-XRD	HR-XRD	PL
	Measurement position ↓	Sheet Resistivity (Ω/\square)	Sheet Resistivity (Ω/\square)	2DEG (cm^{-2})	Mobility ($\text{cm}^2/\text{V.s}$)	AlGaIn thickness (nm)	Al content in AlGaIn (%)	GaN band gap (eV)
1	Position 1	333	327	1.08E+13	1644	19.8	30.3	3.429
2	Position 2	330	341	1.09E+13	1603	19.6	29.8	3.42
3	Position 3	330	355	1.10E+13	1655	19.2	29.7	3.403
4	Position 4	328	355	1.08E+13	1678	19.5	30.1	3.405
5	Position 5	327	347	1.08E+13	1629	19.5	30.4	3.421
6	Position 6	333	350	1.09E+13	1666	19.6	30.2	3.402
7	Position 7	333	359	1.08E+13	1665	19.7	30.3	3.413
8	Position 8	328	344	1.07E+13	1622	19.5	30.2	3.397
9	Position 9	333	361	1.10E+13	1690	19.5	30.1	3.401
	Mean	330.56	349	1.09E+13	1650	19.54	30.12	3.41012
	Std Deviation	2.36	9.96	9.56E+10	26.58	0.16	0.22	0.010
	Std Deviation (%)	0.72	2.86	0.88	1.61	0.80	0.73	0.31

Table 4.4: Summary of measured heterostructure properties using standard semiconductor characterization equipment

Sr No	Heterostructure properties	Characterization techniques	Sample A	Sample B	Sample C
1	SR (ohm/sq)	SiPDR	493.22	293.78	330.56
		Hall	537	335	349
2	Mobility (cm ² /V.s)	Hall	1290	1790	1650
3	2DEG (cm ⁻²)	Hall	6.61E+12	1.04E+13	1.09E+13
4	GaN band gap (eV)	PL	3.41759	3.41465	3.41012
5	Surface roughness (nm)	AFM	0.97	0.20	0.92
6	AlGaN composition (%)	HR-XRD	30.04	29.92	30.12
7	AlGaN thickness (nm)	HR-XRD	19.46	19.82	19.54

4.2.1 Visual Inspection

A powerful visual inspection tool is an optical (Olympus; Model: DSX 510) as well as Laser scanning microscope (Olympus Model: OLS 4100) has been used to inspect the grown heterostructure. It can provide surface morphologies defects like scratches, pits and particles. In particular, when optical microscope is equipped with a differential interference contrast mode like darkfield, differential interference contrast (DIC), fluorescence contrast, white light polarization etc. the surface feature contrast of the layer is enhanced further. 3D laser confocal Laser microscopy has been used to evaluate submicron size the small defects. The Laser Microscope OLS 4100 consist of a LED illumination as well as a short-wavelength 405 nm laser source so that standard optical images as well as confocal height images can be observed. System shall permit precise measurements like surface measurement, profile measurement, step height measurement, line/plane roughness measurement, Geometric/Area/Volume measurements.

4.2.2 Sheet Resistivity measurement

Post growth investigation started with sheet resistance mapping measurement by using Single Post Dielectric Resonators (SiPDR) method. Sheet resistivity map in Ohm/sq at different locations over 12mm diameter has been extracted using SiPDR method. The average sheet resistivity over nine measurement locations of samples A, B and C are founded 493, 294 and 330 Ohm/sq respectively.

4.2.3 Surface morphology

Surface probe microscopy (Agilent SPM 5420) has been extensively used to extract the surface morphology of growth heterostructure. Contact mode atomic force microscopy (AFM) is capable of forming high-resolution images of three-dimensional shape (topography) of sample surface. Along with topographic imaging of samples, AFM is also used for measuring local properties of surfaces like conductivity measurement, electromechanical properties measurement, dislocations, thin films grain size etc. Figure 4.4 shows the surface morphology scanning of samples by AFM. The average root mean square (RMS) roughness of samples A and C are identical around 9.7 \AA and 9.2 \AA respectively due to Si_3N_4 passivation layer, while sample B has a very low roughness 2 \AA due to top atomic flat GaN cap layer.

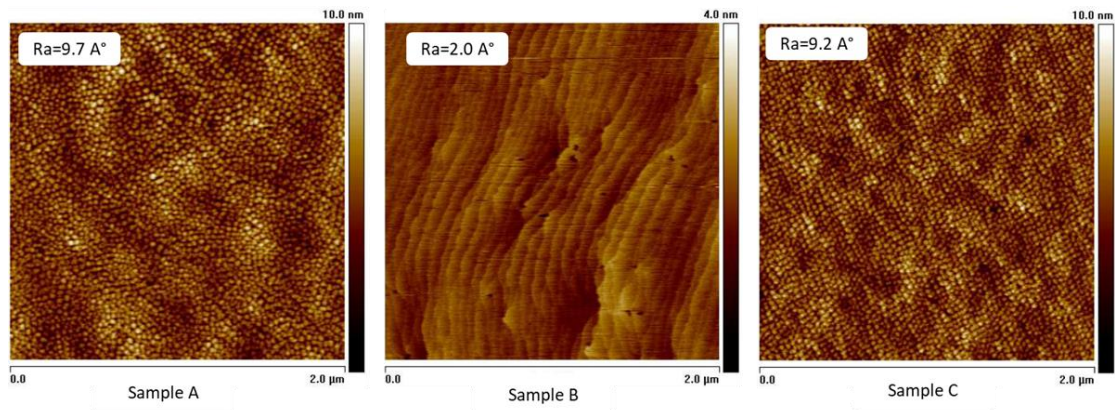


Figure 4.4: Surface morphology measured by AFM for AlGaN/GaN (samples A), GaN/AlGaN/AlN/GaN (Sample B) and AlGaN/AlN/GaN (Sample C).

4.2.4 Photoluminescence (PL) Spectroscopy

Luminescence is the light emission through any process other than blackbody radiation. A detailed description of the process and its use in evaluating GaN, particularly the defects, is referred to a comprehensive review [69]. As luminescence is a nonequilibrium process, it requires external excitation. When the used excitation source is optical, the process is called photoluminescence (PL). Electrical injection induced luminescence and electron beam induced luminescence are called electroluminescence (EL) and cathodoluminescence (CL) respectively. PL, EL and CL are the commonly used luminescence methods [70]. Both PL and CL have been the most widely used experimental methods used for wide bandgap materials. In addition, steady-state PL (SSPL) spectra, time-resolved PL (TRPL) spectra, or PL excitation (PLE) spectra are widely used very effectively for band edge luminescence, transitions associated with impurities and defects in semiconductors. Optically detected magnetic resonance (ODMR), a variant of the PL technique, is also a very effective method; especially in identifying the nature of the defects involved.

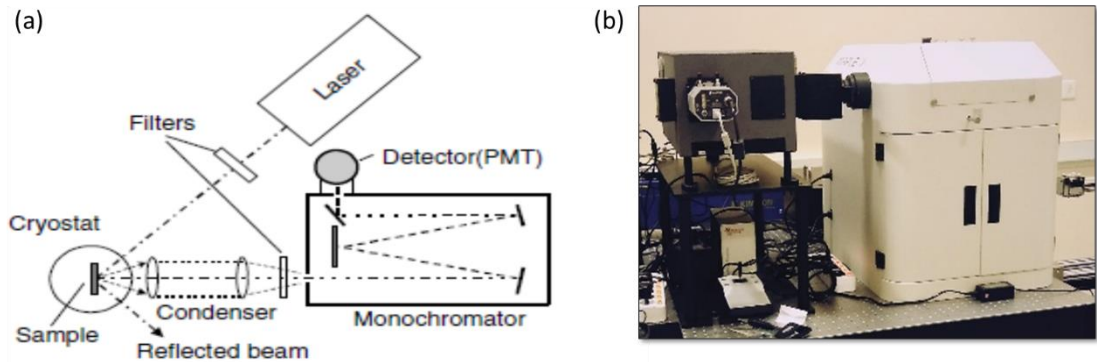


Figure 4.5: (a) Schematic representation of typical PL set up and (b) DongWoo Optron PL set up including excitation source, a grating monochromator, PMT detector, cryostat, filters and collecting lenses

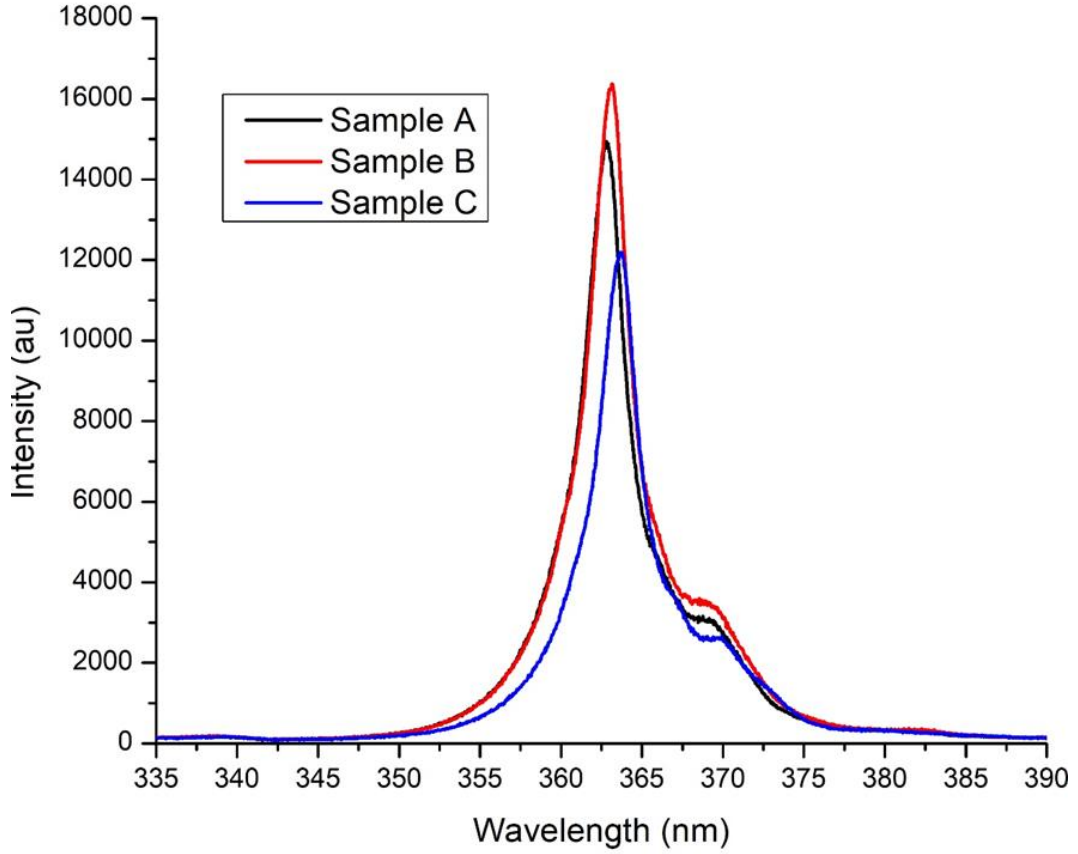


Figure 4.6: The room temperature PL spectra measured from AlGaIn/GaN (samples A), GaN/AlGaIn/AlN/GaN (Sample B) and AlGaIn/AlN/GaN (Sample C).

A typical schematic representation of PL set up is shown in Figure 4.5 (a), along with picture of DongWoo Optron PL set up in Figure 4.5 (b). It consists of light sources for excitation (325 nm He–Cd and 532 nm diode lasers), a sample holder, a dispersive element (grating), an optical detector that is sensitive to the dispersed light and closed cycle He cryostat along with temperature controller. The room temperature GaN bandgap and PL spectra of samples A, B and C are shown in Figure 4.6. Furthermore, non-destructive low temperature photoluminescence (PL) measurement to extract the true signatures of intersubband energy levels states is discussed in detail in Chapter 7.

4.2.5 Hall measurement

Hall Effect measurement is a method commonly used to characterize semiconductor materials. It provides information about the carrier types, concentration and mobility. Carrier concentration (2DEG) in the grown HEMT heterostructure is commonly

extracted by using this method. The basic principle for Hall Effect is Lorentz Force which is a combination of two separate forces: the electric force and the magnetic force. When an electron moves along the electric field direction, if applied magnetic field perpendicular, electron experiences a magnetic force $q(\mathbf{v} \times \mathbf{B})$ acting normal to both directions. The resultant Lorentz force given is by,

$$\mathbf{F} = q[(\mathbf{E} + \mathbf{v} \times \mathbf{B})] \quad (4.1)$$

Where q is electric charge, \mathbf{E} is an electric field, \mathbf{B} is a magnetic field and \mathbf{v} is velocity. Let us assume that a constant current I flows along the x -axis from left to right in the presence of a z -directed magnetic field as shown in Figure 4.7. Electrons subject to the Lorentz force initially drift away from the current direction toward the negative y -axis, resulting in an excess negative surface electrical charge on this side of the sample. This charge results in a potential drop across the two sides of the sample known as the Hall voltage and its magnitude is equal to IB/qnd , where I is current, B is the magnetic field, d is the sample thickness, and q is electric charge. Hence, by measuring the Hall voltage V_H and from the known values of I , B , and q , we can determine the sheet density n_s of charge carriers in semiconductors. Hall voltage is negative for n -type semiconductors and positive for p -type semiconductors.

van der Pauw method is widely used to estimate the Hall voltage and hence the mobility and the carrier density [71]. There are a few important prerequisite conditions that must be satisfied for this technique: (a) The sample must be uniform thickness, homogeneous and isotropic. (b) The four contacts must be at the corners of the sample and (c) The area of the contacts must be at least an order of magnitude smaller than the sample. The four contacts are marked 1 to 4 in Figure 4.7 (b) for different commonly used geometry for Hall measurement.

The average vertical and horizontal resistances are given by,

$$R_v = \frac{R_{12,34} + R_{34,12} + R_{21,43} + R_{43,21}}{4} \quad (4.2)$$

$$R_h = \frac{R_{23,41} + R_{41,23} + R_{32,14} + R_{14,32}}{4} \quad (4.3)$$

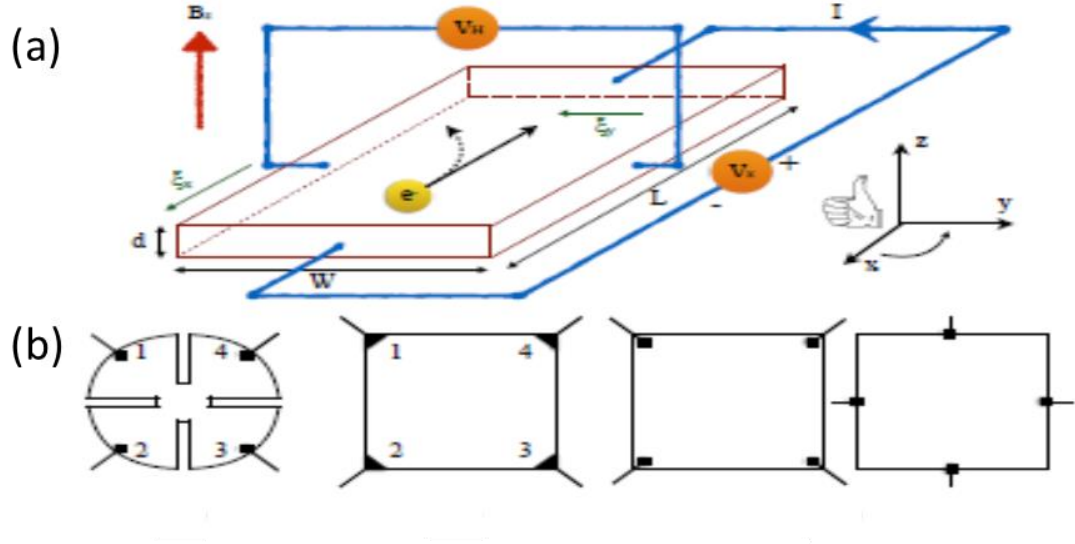


Figure 4.7: (a) Schematic representation of typical Hall Measurement set up and (b) different geometry used for Hall measurement (Reprinted with permission from thesis THz Transmission Spectroscopy of Charge Carriers in Semiconductor Heterostructures under Surface Electric Fields by Shovon Pal (2015))

The differences of the voltages for the positive and negative magnetic fields are calculated

$$V_{13} = V_{13,P} - V_{13,N} \quad (4.4a)$$

$$V_{24} = V_{24,P} - V_{24,N} \quad (4.4b)$$

$$V_{31} = V_{31,P} - V_{31,N} \quad (4.4c)$$

$$V_{42} = V_{42,P} - V_{42,N} \quad (4.4d)$$

The mean hall voltage is given by,

$$V_H = \frac{V_{13} + V_{24} + V_{31} + V_{42}}{8} \quad (4.5)$$

The sign of V_H determines the nature of the charge carriers i.e., either positive or negative. The sheet density can be calculated from the following relation:

$$n_s = \frac{IB}{q|V_H|} \quad (4.6)$$

The mobility is calculated from the sheet resistance is given by,

$$\mu_e = \frac{1}{qn_s R_s} \quad (4.7)$$



Figure 4.8: Hall Measurement set up

Figure 4.8 shows the M/s Nano-magnetics make Hall measurement system (HMS). The System is equipped low temperature close cycle cryostat (M/s Sumitomo, Model: SRP-082), PID temperature controller range from 2K to 1300K with display (M/s Oxford

Instruments, Model: Mercury ITC), 4 numbers Keithley make SMUs, Electromagnet (0 to 1.5 Tesla) with controller and Turbomolecular pump along with dry scroll pump as a vacuum system.

Standard van der paw geometry is fabricated by photolithography technique on all samples A, B and C. Contacts are formed by evaporating Ti/Al/Ni/Au films in sequence using e-beam deposition and then annealing at 900 °C for 30 secs in N₂ ambient in order to make low contact resistance. Electrical and magneto transport measurements are conducted with an applied current of 100μA. The experiments are conducted from ambient temperature to low as 2 K and magnetic field up to 1.5 Tesla. Figure 4.9 shows the carrier concentration and mobility measurements of samples A, B and C from ambient temperature to low temperature 2K.

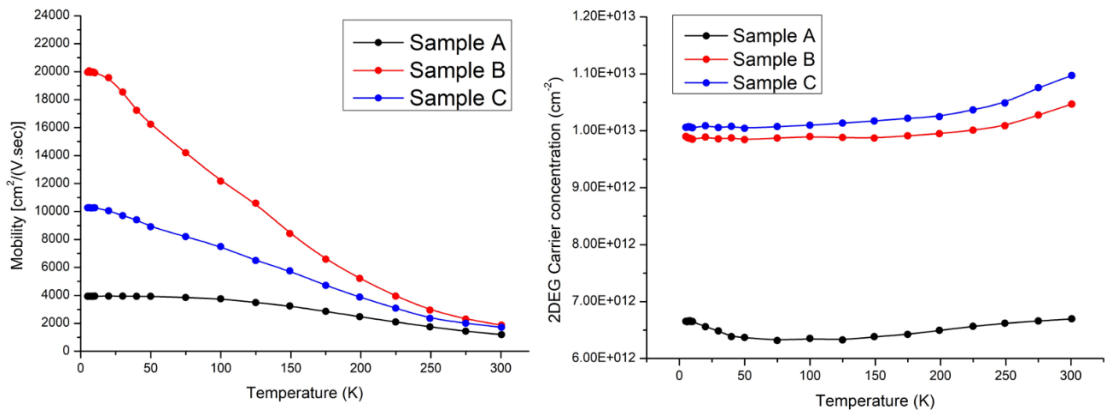


Figure 4.9: (a) Hall mobility and (b) 2DEG carrier concentration with respect to temperature for Samples A, B and C

Shubnikov–de Haas (SdH) oscillation is useful to investigate the quantum scattering mechanism and analyze the heterostructure properties including prime parameter effective mass to study intersubband transition. A high magnetic field with low temperature measurement is required to extract the SdH oscillation [72, 73, 74, 75]. At high magnetic fields, the carriers at interface of the GaN heterostructure execute cyclotron motion. But the Landau motion has disrupted the carriers which get scattered forward along the edge. This leads to a “superhigh current” that adds to the current flow and increases conductance. As the magnetic field increase, the system traverses through

the quantized Landau levels and the resistance oscillates periodically as a function of $1/B$, a behavior known as Shubnikov–de Haas (SdH) oscillation.

The longitudinal resistance R_{xx} as a function of applied magnetic field B up to 14 T is shown in Figure 4.10 (a). SdH oscillations appear as the magnetic field is increased. The peaks of the oscillations are dominated at low temperatures and damped with increasing temperature. Figure 4.10 (b) shows the ΔR_{xx} versus magnetic field after subtracting the background.

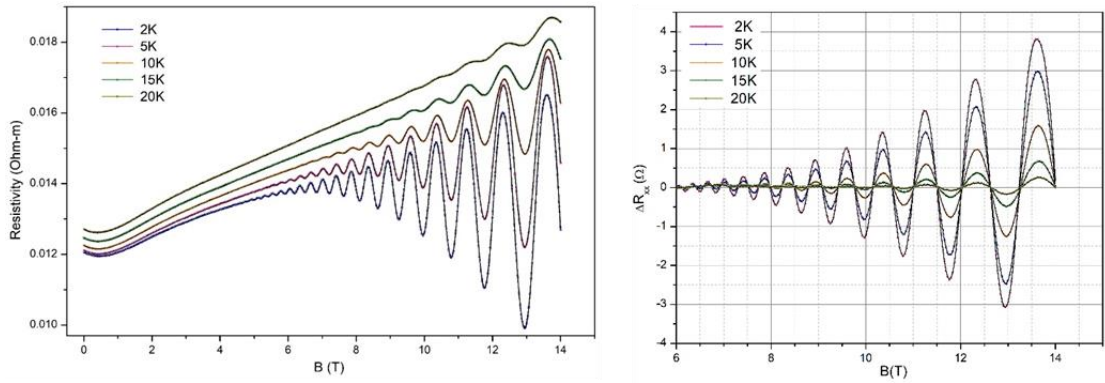


Figure 4.10: (a) Magnetoresistance up to 14 T at a set of temperatures and (b) Shubnikov–de Haas oscillations after subtracting the background

The amplitude of the SdH oscillation is given by [66, 68],

$$\Delta R_{xx} = 4R_0 \left[\frac{\chi}{\sinh h\chi} \right] e^{\left(\frac{-\pi}{\omega_c \tau q} \right)} \quad (4.8)$$

Where,

$$\chi = \left[\frac{2\pi^2 k_B T}{\Delta E} \right] \quad (4.9)$$

Here, ΔE is Landau level energy gap given by

$$\Delta E = \hbar \omega_c = \frac{heB}{m^*} \quad (4.10)$$

k_B is the Boltzmann constant, \hbar is the reduced Planck constant, e is the electron charge and m^* is effective mass of electrons.

The effective mass of electrons m^* can be extracted from the temperature dependence of the SdH amplitude at a constant magnetic field by [75]

$$\frac{\Delta R_{XX}(T, B)}{\Delta R_{XX}(T_0, B)} = \frac{T \sinh[\chi(T_0)]}{T_0 \sinh[\chi(T)]} = \frac{T \sinh\left[\frac{2\pi^2 k_B T_0}{\Delta E(B)}\right]}{T_0 \sinh\left[\frac{2\pi^2 k_B T}{\Delta E(B)}\right]} \quad (4.11)$$

The lowest temperature measurement is 2 K as T_0 . Figure 4.11 (a) shows the $\frac{\Delta R_{XX}(T, B)}{\Delta R_{XX}(T_0, B)}$ ratio of amplitude at $T_0 = 2.0$ K and $B = 13.9$ T.

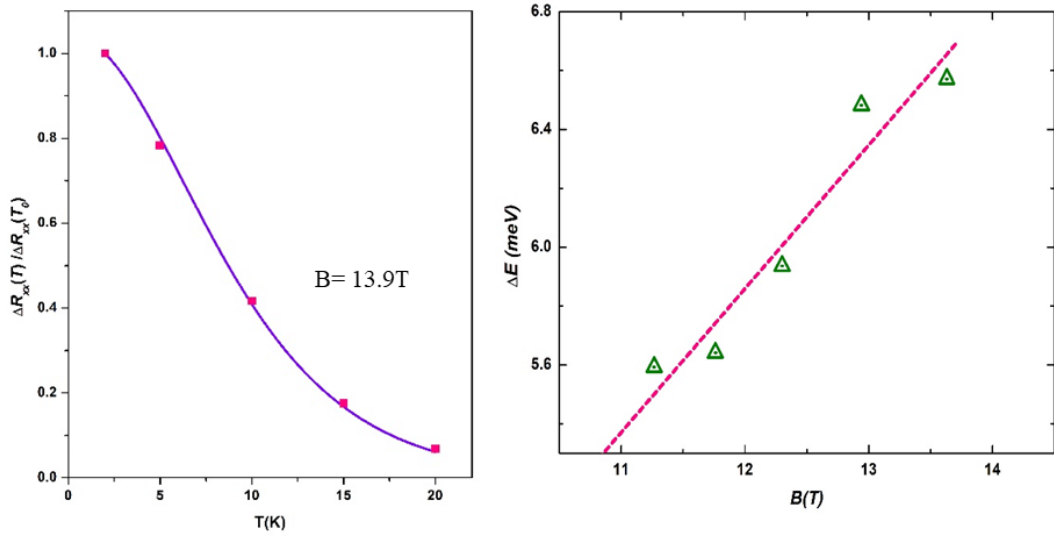


Figure 4.11: (a) Effective mass plot at 13.9 T, where the data are best fit to Eq. (4.11) and (b) the field dependence of the Landau-level spacing

Analyzing data using Eq. 4.11 we can extract $\Delta E(B)$. The field dependence of the Landau-level energy gap is shown in the inset of Figure 4.11(a). The corresponding effective mass m^* is $0.233 m_e$.

4.2.6 High Resolution X-Ray Diffraction

High resolution X-ray diffraction (HR-XRD) is an ex-situ characterization method and it is the core tool to analyze nano-scale epitaxial structures. X-rays are produced from a source where electrons are ejected from a cathode, collide on a metal plate (in the present case copper) and excite inner-shell electrons in the metal, resulting in the emission of strong spectral lines. The output is conditioned as a Cu K α quasi-parallel beam, strikes on the crystalline sample at different incidence angles. A detector collects the scattering signal. The working principle behind HR-XRD is Bragg's law, which states that when the x-ray incident onto a crystal surface with angle of incidence, θ , it will reflect back with the same angle of scattering.

$$2d \sin \theta = n\lambda \quad (4.12)$$

When the path difference is equal to an integral multiple of wavelength, constructive interference will occur. The path difference is the separation between the crystal planes that caused the reflection.



Figure 4.12: High Resolution XRD (HR-XRD) system

Figure 4.12 shows the Bruker D8 Discover HRXRD system which is extensively used to extract the crystalline and physical properties of all three GaN heterostructure samples A, B and C.

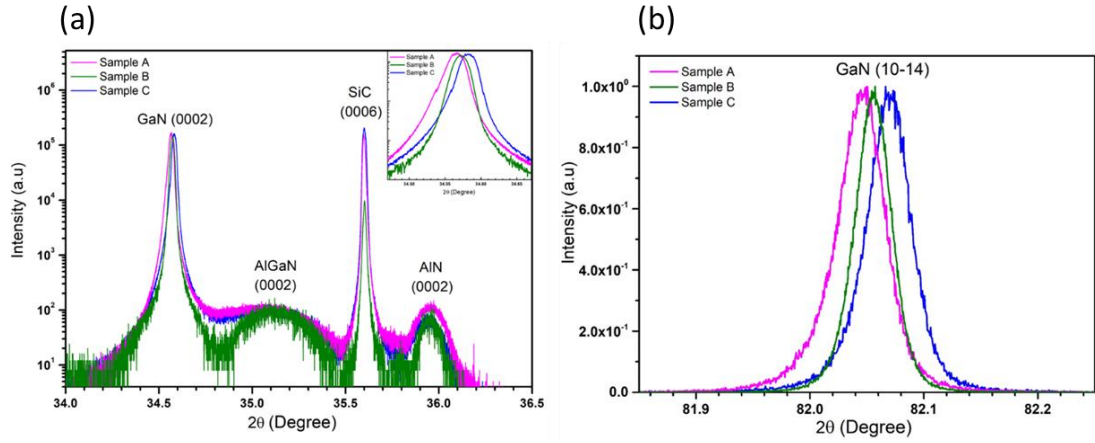


Figure 4.13: HR-XRD scan towards (a) (0002) and (b) (10-14) of samples A, B, and C are used to determine thickness, composition and lattice constants a and c

The system can be operated in different scanning modes:

- omega scan (rocking curve),
- detector scan (2θ),
- coupled scan (θ - 2θ) and
- reciprocal space map (RSM)

The measured data is used to analyze by a powerful software built with dynamic x-ray scattering models, where useful parameters such as layer thicknesses & composition, lattice parameters, stress etc. can be extracted.

The HR-XRD system is used to evaluate the crystal structure, composition, thickness and in-plane and out-plane stress measurement. Symmetric and asymmetric scan towards (0002) and (10-14) plane is used to extract lattice parameters c and a of epitaxial films. Figure 4.13 shows the comparative HR-XRD scan toward (0002) and (10-14) for all three samples. AlGaIn thickness and composition are extracted and found

identical for all three samples. A symmetric (0002) and asymmetric (10-14) rocking ω scan as shown in Figure 4.14 in order to extract the crystalline quality (FWHM) of heterostructure. In plane and out of plane strain ε and stress σ are calculated by using the following equations (4.13) and (4.14) [77, 78, 79]

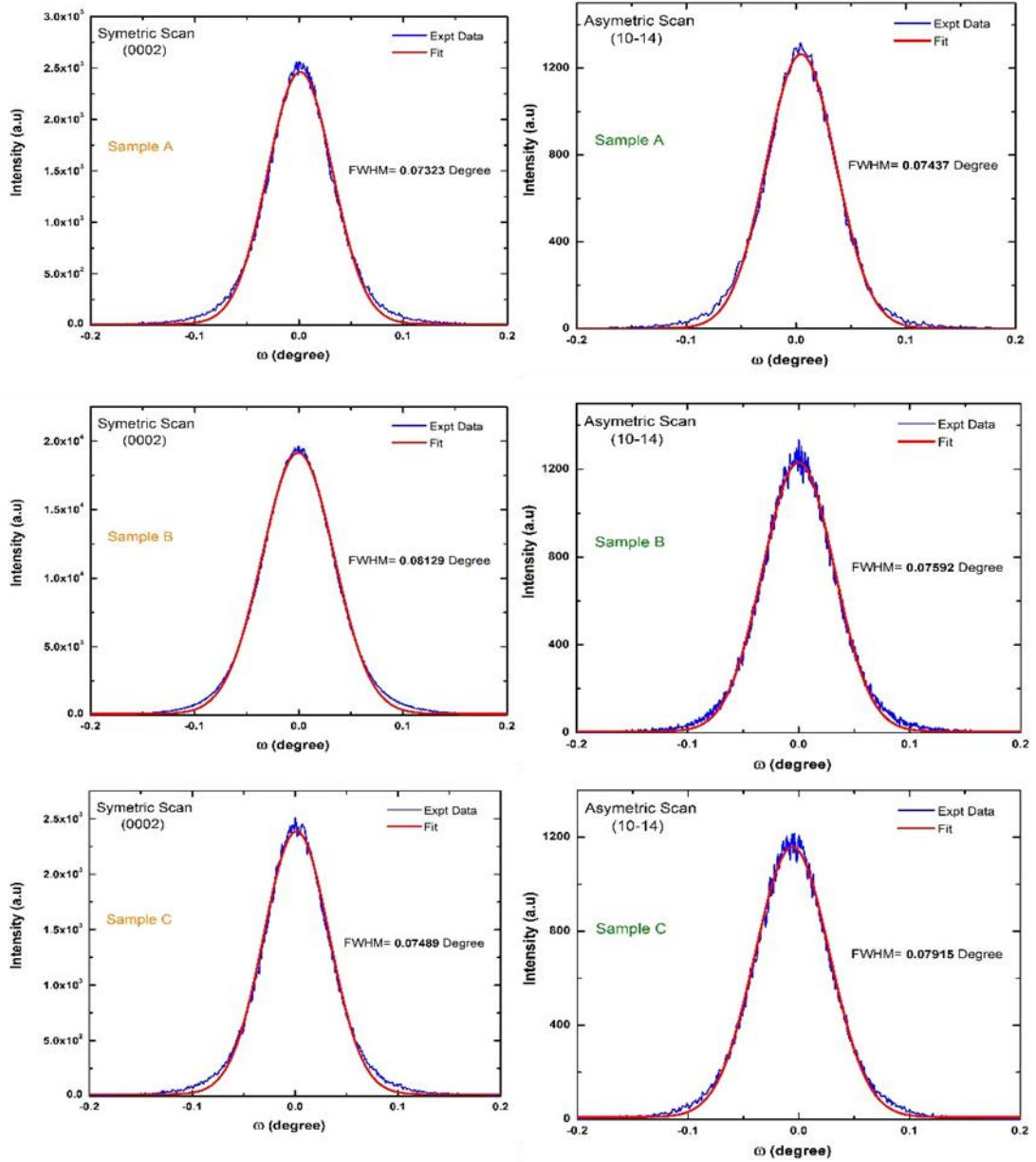


Figure 4.14: Symmetric (0002) and asymmetric (10-14) rocking scan of samples A, B, and C are used to determine the crystalline quality and dislocation defects.

$$\varepsilon_{xx} = \frac{a - a_0}{a_0}; \varepsilon_{zz} = \frac{c - c_0}{c_0} \quad (4.13)$$

Where, a, and c are measured strained lattice parameters, while $a_0=3.189$, $c_0=5.1852$, [78, 80] are equilibrium (unstrained) values of lattice constants.

$$\sigma_{xx} = \left[(C_{11} + C_{12}) - 2 \frac{C_{13}^2}{C_{33}} \right] \varepsilon_{xx} \quad (4.14)$$

With C_{ij} is elastic constants for GaN, ($C_{11}= 390$ GPa, $C_{12}=145$ GPa, $C_{13}=106$ GPa, $C_{33}=398$ GPa) [81, 82]. By using FWHM of GaN peak in symmetric (0002) and asymmetric (10-14) (i.e. $\beta(0002)$ and $\beta(10-14)$) direction, the screw and edge dislocation density estimated by using equations (4.15) [78]

$$D_{screw} = \frac{\beta_{(0002)}^2}{4.35b_{screw}^2}; D_{edge} = \frac{\beta_{(10-14)}^2}{4.35b_{edge}^2} \quad (4.15)$$

Where, $b_{screw}=5.185 \text{ \AA}$ and $b_{edge}=3.189 \text{ \AA}$ are Burger vectors. The results extracted by using HR-XRD characterization techniques are summarized in Table 4.5.

Table 4.5: Extracted/calculated heterostructure properties

Sr No	Properties	c (Å°)	a (Å°)	c/a	ε_{xx} (%)	ε_{zz} (%)	σ_{xx} (GPa)	σ_{zz} (GPa)	D_{screw}^{-2} (cm ⁻²)	D_{edge}^{-2} (cm ⁻²)
	Measurement Technique	HR-XRD	HR-XRD	HR-XRD	HR-XRD	HR-XRD	HR-XRD	Raman	HR-XRD	HR-XRD
1	Sample A	5.1860631	3.1887855	1.626344	0.0067 (Compressive)	0.020 (Tensile)	0.032 (Compressive)	0.070 (Compressive)	1.39E+08	3.80E+08
2	Sample B	5.1851323	3.1898775	1.625496	0.0275 (Tensile)	0.0026 (Tensile)	0.132 (Tensile)	0.026 (Tensile)	1.72E+08	3.96E+08
3	Sample C	5.1836787	3.1913704	1.624280	0.0743 (Tensile)	0.025 (Compressive)	0.356 (Tensile)	0.193 (Tensile)	1.46E+08	4.31E+08
4	Sample D (Etched)	5.1868	3.1870	1.627487	0.0627 (Compressive)	0.0347 (Tensile)	0.300 (Compressive)	0.185 (Compressive)	1.65E+08	4.38E+08

4.2.7 Raman Spectroscopy

The spontaneous and piezoelectric polarization induced two-dimensional electron gas (2DEG) formed at interface of c-axis grown AlGa_N/Ga_N heterostructure is the key attribute for generation carriers in channel. The inherent strain in growth plays a crucial role in the generation of carriers, especially piezoelectric polarization strongly depends upon in-plane strain. The inherent stress and corresponding generated 2DEG and its transport mechanism are significant influence by growth methodology and heterostructure stack. To improved device performance, extensive research and development are going on during the last few years to improve various growth methodologies as well as the selection of layer sequence, thickness and composition in heterostructure. The inherent strain and stress profile in Ga_N heterostructure can be extracted through non-destructive confocal micro Raman microscopy.

Room temperature micro Raman scattering experiments are carried out using Horiba LabRAM HR Raman spectrometer equipped with the 532 nm laser as the excitation light source, 1800 lines/mm grating, 100X objective lens is in confocal microscope configuration.

Both the E₂-high and A₁-LO modes are observed as reported in the literature. The respective E₂-high Raman peak positions are heterostructure dependent, which implies different stress levels in the samples. The biaxial stress σ_{xx} can be expressed in terms of linear deviation in phonon frequency by [77, 83, 84]

$$\Delta\omega = K\sigma_{xx} \quad (4.15)$$

The biaxial stress can be calculated from the measured Raman frequency shift of a given phonon mode if the linear stress coefficient K is known. The E₂ (high) phonon peak in Ga_N is used to extract the stress due to its sensitivity to strain/stress. A typical strain-free Ga_N shows E₂ (high) phonon peak at 567.5 cm⁻¹ [85, 88]. Peak shifting toward a lower wavenumber value is related to tensile stress, while toward a higher wavenumber shift is related to compressive stress. The reported stress coefficient

2.7 cm⁻¹/GPa for the GaN/6H-SiC sample [82, 83] is used for the calculation of stress value. Figure 4.15 shows the room temperature Raman spectra of samples A, B, C and 230 nm top etched GaN buffer sample D.

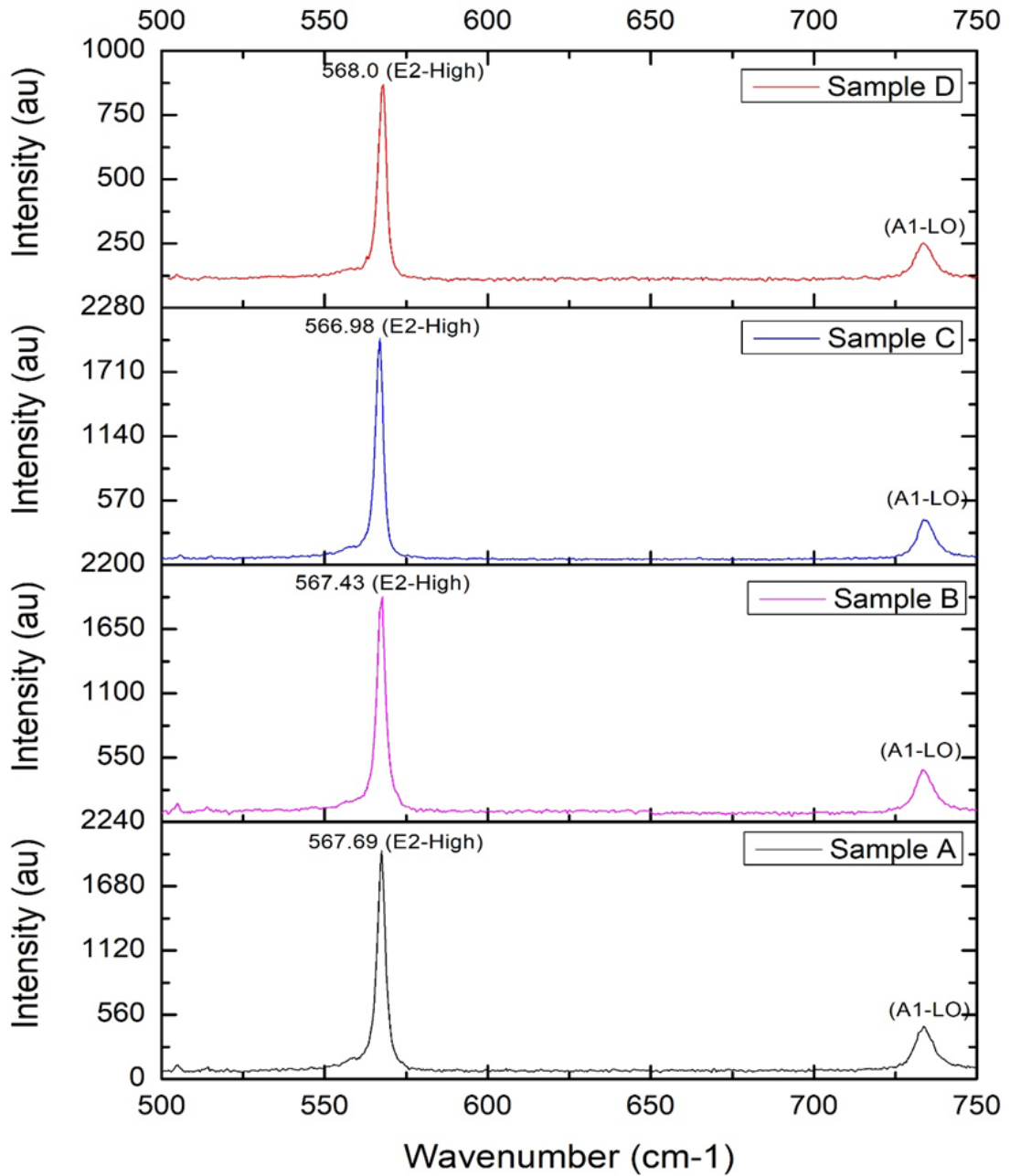


Figure 4.15: The room temperature Raman spectra measured from AlGaIn/GaN (samples A), GaN/AlGaIn/AlN/GaN (Sample B), AlGaIn/AlN/GaN (Sample C) and Etched GaN buffer layer (Sample D)

Measurement condition

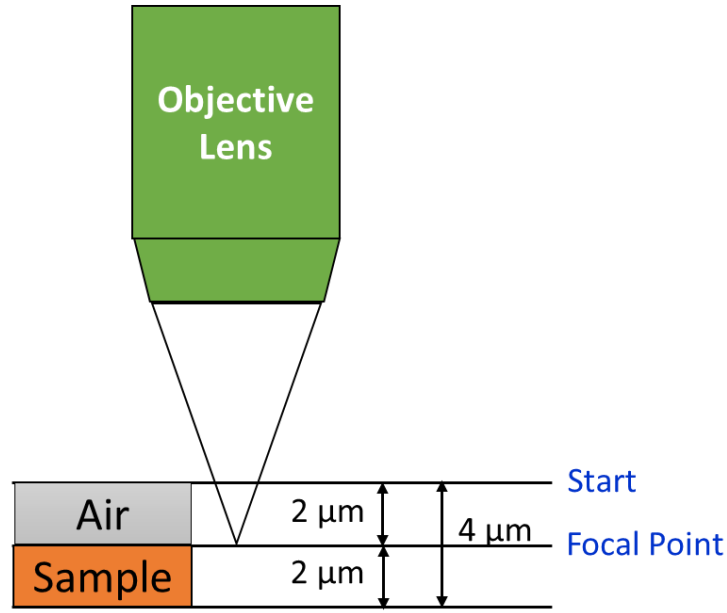


Figure 4.16: Measurement methodology for depth profiling Raman measurement

The Raman spectra give the information about lattice vibration of material. It is the integral information for the particular location with few nanometer depth, when laser light interacts with the material. Depending upon used laser wavelength and material characterization the depth penetration varies. The adopted measurement methodology is depicted in Figure 4.16 in order to extract the true nature of stress in depth profiling. The involved major steps are as per following

- Step 1: Focus the laser on GaN heterostructure surface
- Step 2: Lift the focus 2 micron above the surface
- Step 3: Start measurement
- Step 4: Depth profiling with 20 nm steps
- Step 5: Measure up to 4 micron (i.e. 2 micron depth from surface)

Room temperature Raman spectra of the GaN heterostructure is shown in Figure 4.17 (a). The variation in E_2 (high) peak throughout 4-micron depth measurement is shown Figure 4.17 (b), while the shift in the peak position with depth profiling is shown in Figure 4.17 (c). The shift in E_2 (high) phonon peak in GaN is used to extract the stress by using equation (4.16). The Raman E_2 -high peak shifting and calculated stress

is depicted in Figure 4.17 (d). The influence of AlGaN barrier layer and 6H-SiC substrate on inherent strain and stress in GaN heterostructure has been clearly identified in depth profiling Raman measurement.

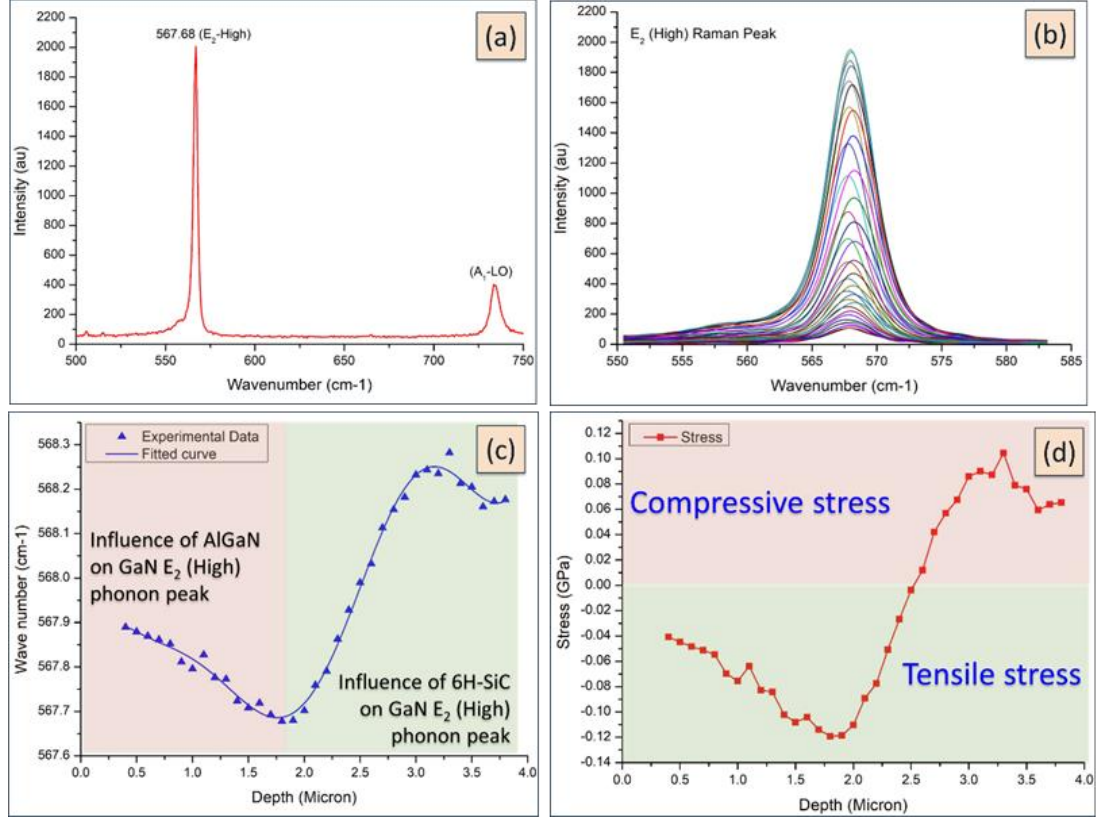


Figure 4.17: (a) Raman E2-high peak spectra for GaN Heterostructure, (b) change in Raman E2-high peak in depth profiling, (c) Raman E2-high peak shifting in depth profiling, (d) Calculated stress

4.2.8 Measurement Correlation

All three heterostructure has been simulated using Advanced SILVACO Atlas device simulation software by solving semiconductor device physics equations for every grid point. These equations include Schrodinger Poisson self-consistent equation, continuity equations and transport equations. Polarization in heterostructure is computed by two components, spontaneous polarization and piezoelectric polarization using polarization model. Mobility, carrier concentration and band diagram are extracted for all three heterostructures through simulation. Simulated band diagrams for all three

heterostructures using Silvaco Atlas TCAD are shown in Fig. 4.18. The higher conduction band offset for AlN/GaN interface is clearly observed for samples B and C. The conduction band offset (E_c) is ~ 0.59 eV for AlGaIn/GaN interface (Sample A) and ~ 2.09 eV for AlN/GaN interface (Sample B and C). The probability of electron penetration into the AlGaIn layer decreases as the rise in band offset, which further reduced alloy scattering, better carrier confinement, enhanced conductivity and mobility.

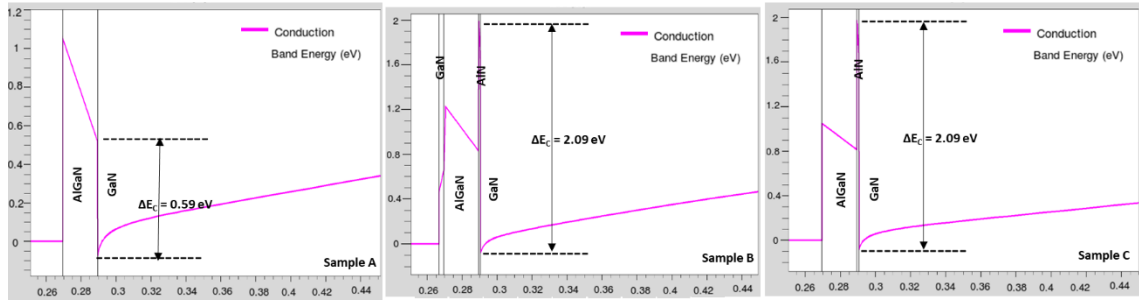


Figure 4.18: The conduction band profile calculated using semiconductor device physics-based simulation for (a) AlGaIn/GaN (samples A), (b) GaN/AlGaIn/AlN/GaN (Sample B) and (c) AlGaIn/AlN/GaN (Sample C).

It is almost impossible to correlate among all heterostructures if highly controlled grown samples are not used. In the present study, used grown heterostructures are having less than 1% standard deviation in the process as reported in Table 4.1 to 4.3 for each heterostructure samples A, B and C. The results extracted by using various characterization techniques (over nine locations average) are summarized in Table 4.4. To confirm the generated inherent stress due to the layer stacking effect in heterostructure i.e., by introducing the SiN cap, GaN cap and AlN spacer layer, HR-XRD measurement has been carried out after etching of 230 nm from top of all three heterostructure. This measurement provided the bare GaN buffer layer crystal structure and stress information without considering the influence of AlGaIn/GaN quantum well, SiN cap, GaN cap as well as AlN spacer. The crystal structure of GaN buffer layer is founded identical for all samples with lattice constant $a=3.1870\pm0.0002$ and $c=5.1868\pm0.0002$ after etching. This measurement clearly extracted the deformation in crystal structure due to the introduction of SiN cap, GaN cap layer and AlN space layer which leads to a change in the inherent stress and strain in the heterostructure.

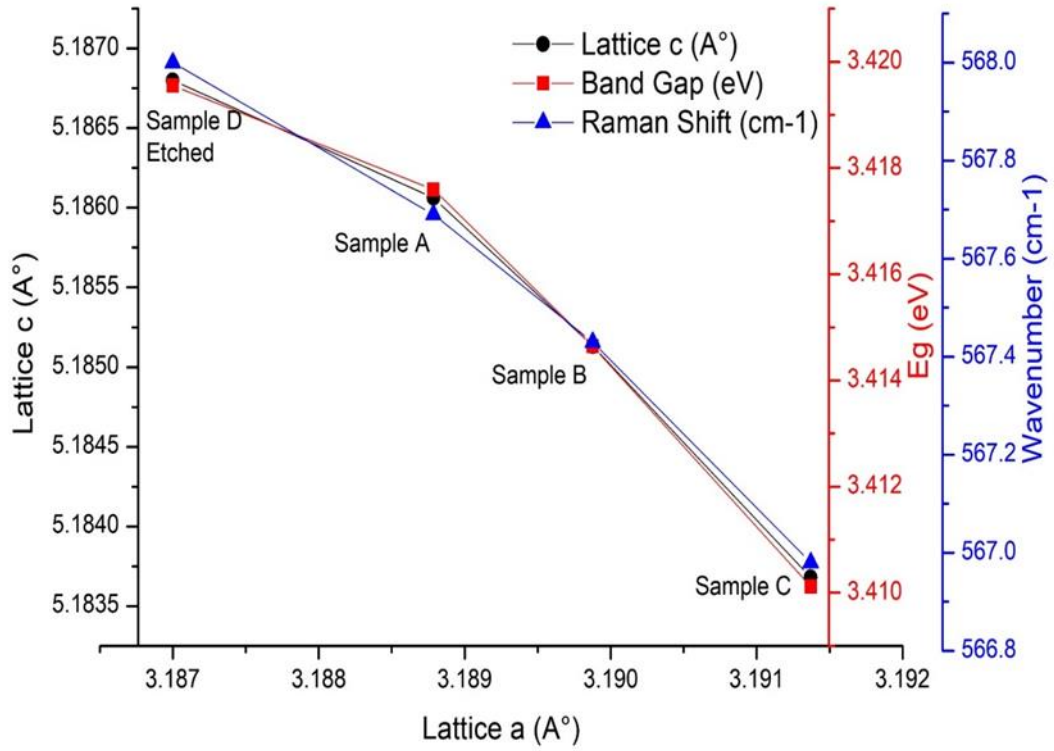


Figure 4.19: The measurement correlation among HR-XRD, Raman and PL data of AlGaN/GaN (samples A), GaN/AlGaN/AlN/GaN (Sample B), AlGaN/AlN/GaN (Sample C) and Etched GaN buffer layer (Sample D)

The energy bandgap of a semiconductor is affected by the residual stress in film. Generally tensile stress is increased and compressive stress has decreased the bandgap. The measurement correlation among all four samples (samples A, B and C having different GaN heterostructure on 6H-SiC as shown in Figure 4.2 and sample D is after etching of 230 nm from the top of all heterostructure) has been carried out.

The lattice constants versus luminescent bandgap and Raman E_2 peak are depicted in Figure 4.19. Extracted heterostructure properties for samples A, B, C and D are summarized in Table 4.5.

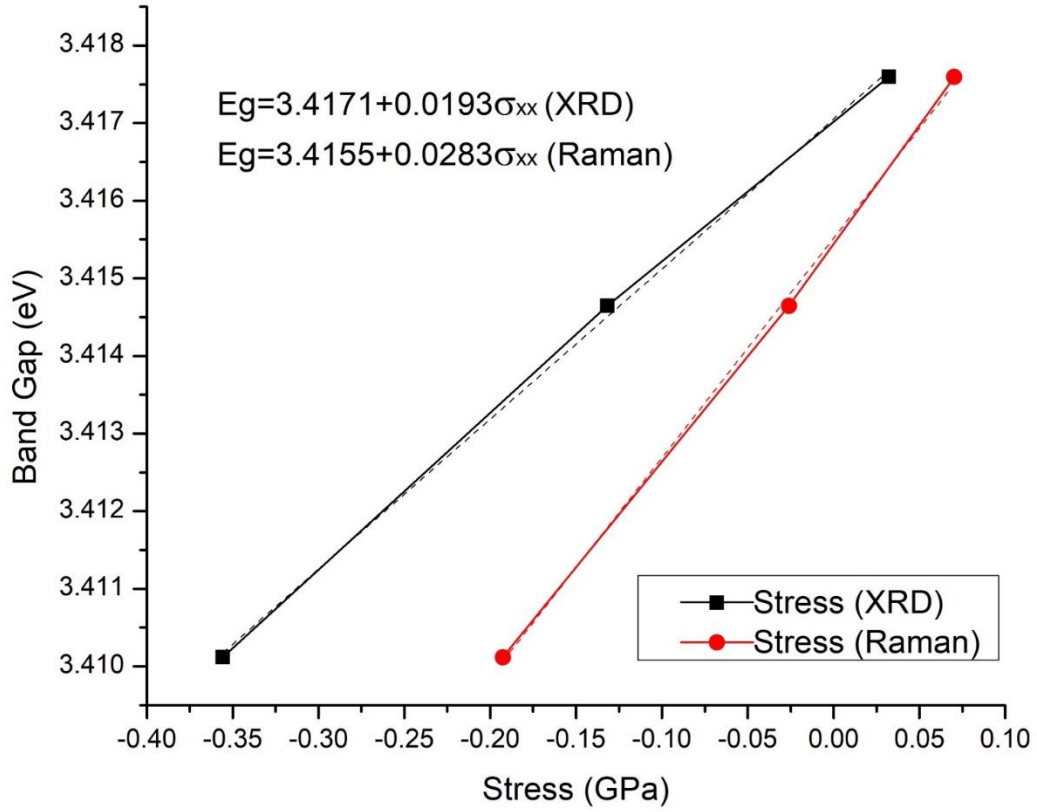


Figure 4.20: The room-temperature band gaps of the AlGaIn/GaN (samples A), GaN/AlGaIn/AlN/GaN (Sample B) and AlGaIn/AlN/GaN (Sample C) vs the corresponding stresses measured by HRXRD and Raman. The solid line represents a linear fitting result to the experimental data

The in-plane lattice constant and thermal expansion coefficient of GaN is larger than that of 6H-SiC. Both lattice and thermal mismatches lead to the compressive in-plane stress in the GaN epilayer. After 230 nm etching from top, the inherent in plane compressive stress in GaN buffer layer on 6H-SiC is measured around 0.300 and 0.185 GPa using Raman and XRD respectively. AlN has a small in-plane lattice constant a with compare to GaN, while AlGaIn has an intermediate composite dependent in-plane lattice constant. When epitaxial growth of AlGaIn and AlN over GaN gives in-plane tensile strain and while compressive strain in out-plane [0001] direction [87]. The inherent biaxial tensile stress due to AlGaIn on GaN is comparatively small to that of AlN on GaN. Sample A has compressive stress 0.032 (XRD) and 0.070 (Raman) GPa which is smaller as compared to buffer GaN/SiC, while tensile stress in sample C is measured 0.356 (XRD) and 0.193 (Raman) GPa. Having a 2 nm GaN cap layer on top

in sample B further results in relaxing the inherent tensile stress and found 0.132 (XRD) and 0.026 (Raman) GPa.

An excellent correlation and approximate linear dependence are observed in XRD, PL and Raman measurements for three heterostructures, except the etched sample as shown in Figure 4.18. Room temperature bandgap (E_g -RT) of GaN can be expressed in terms of biaxial stress measured by XRD and Raman. The least-square fitting of the data represented in Figure 4.20 matches with the literature [77, 82, 84, 88]

$$E_g = 3.4171 + 0.0193\sigma_{xx} \quad (4.16a)$$

$$E_g = 3.4155 + 0.0283\sigma_{xx} \quad (4.16b)$$

Carrier mobility is found highest in sample B i.e. with GaN cap layer, while lowest for sample A i.e. without a spacer. Mobility of carriers at AlGaIn/GaN (sample A) interface is limited by short-range scattering due to alloy disorder and interface roughness [89-91]. Sample B and C both have AlGaIn/AlN/GaN layers sequence implies transport mechanism inside 2DEG channel are same, but introduction of 2 nm GaN cap layer increases the mobility in sample B [92]. Sheet resistance is found highest in sample A, while lowest in sample B. In general, the sheet resistance is inversely related to 2DEG concentration, but this chronology breaks in our samples. In spite of having the lowest sheet resistance, 2DEG carrier concentration of sample B is not found highest. The presence of GaN cap layer caused a decrease in charge [92], while the top SiN layer in sample C saturated the surface traps resultant increase in 2DEG [93]. Keeping a GaN cap layer to the AlGaIn/AlN/GaN structure (Sample B) is introduced a negative polarization charge at the upper heterointerface, causing increased electric fields in the AlGaIn, and a decrease in 2DEG density. The reason for not getting the highest 2DEG concentration in GaN cap sample is also lying in the crystal structure of sample B heterostructure. Spontaneous and piezoelectric polarization is the basic source of 2DEG in GaN heterostructure [26, 94]. The crystal structure and inherent strain in growth play a crucial role in the generation of carriers. Spontaneous polarization is associated with crystal structure c/a ratio. The idea c/a ratio in the

hexagonal crystal structure is 1.633. The difference from the ideal values leads to the highest spontaneous polarization. c/a ratio depicted in Table 4.5 clearly indicates the spontaneous polarization is highest in Sample C. Spontaneous polarization is independent upon the strain, whether as piezoelectric polarization strongly depends upon in-plane strain by

$$P_{PE} = 2 \frac{a - a_0}{a_0} \left(e_{31} - e_{33} \frac{C_{13}}{C_{33}} \right) \quad (4.17)$$

where a_0 is ideal relaxed lattice constant and a is measured strained lattice constant, (C_{13} , C_{33}) are elastic constant and (e_{31} , e_{33}) are piezoelectric coefficients. Lattice constant a of sample B is smaller than sample C which is likely to favour the increased piezoelectric polarization at interface. Both spontaneous and piezoelectric polarization were found highest in Sample C which leads to resultant higher 2DEG concentration.

GaN HEMT Device Fabrication

This chapter introduces the device fabrication technology in the context of GaN HEMT fabrication. The standard fabrication process flow is adopted for GaN HEMT device fabrication. Integration of unit processes like mesa isolation, Ohmic contact, Schottky contact, device passivation, contact pad thickening, air-bridge fabrication etc. along with its in-line process characterization to assess the quality of each individual process are discussed.

5.1 Device Fabrication

The samples are grown by MOCVD technique and after growth, the samples are processed for the electrical transport and optical measurements, which is explained in

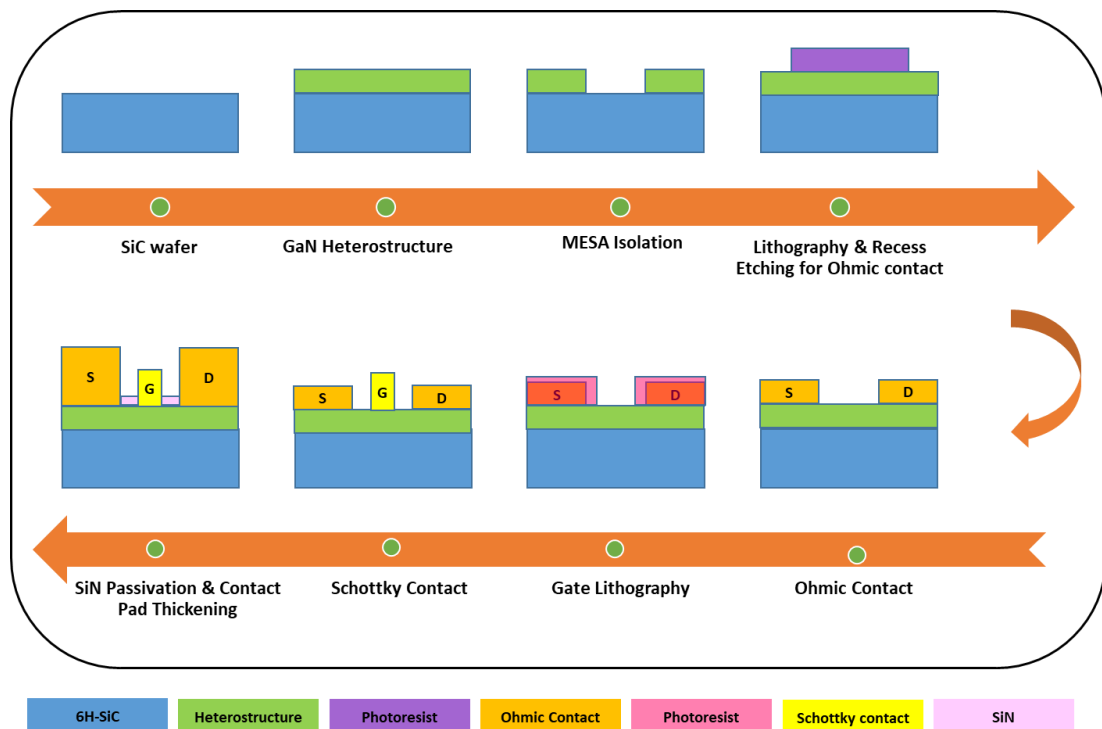


Figure 5.1: Schematic of GaN HEMT Fabrication flow

Chapter 4. The MOCVD grown samples containing the details of the epitaxial layer sequence are also depicted in Figure 4.2 of Chapter 4. HEMT device fabrication involved combinations of various processes. Standard fabrication process flow as shown in Figure 5.1 has been adopted for GaN HEMT device fabrication.

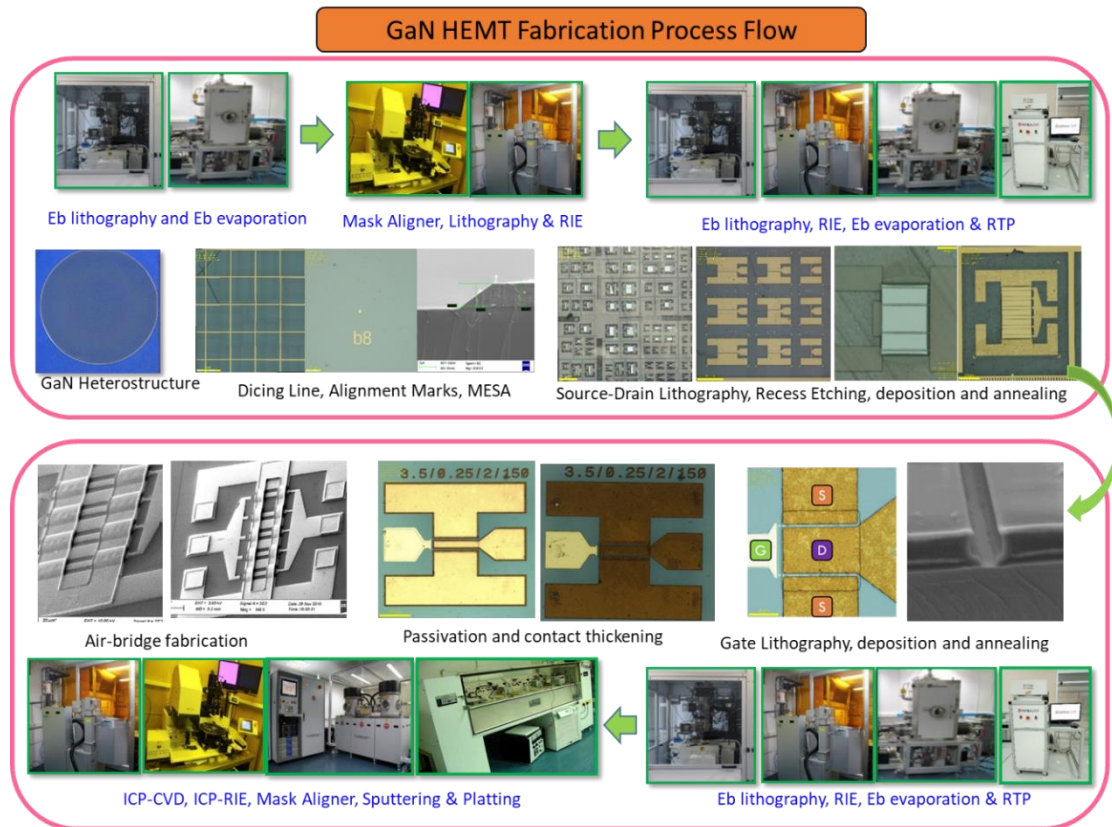


Figure 5.2: GaN HEMT Fabrication process flow along with used semiconductor fab equipments and the view of the fabricated device

Figure 5.2 depicts the GaN HEMT fab process flow along with used semiconductor fab equipments and the view of the fabricated device. Device-to-device isolation is performed by mesa etching using $\text{BCl}_3/\text{Cl}_2/\text{Ar}$ dry plasma. ICP-RIE (Inductively Coupled Plasma-Reactive Ion Etching) system is used for HEMT devices isolation. Source-drain spacing is kept 3.0 micron and electron beam lithography is used for ohmic contact (source and drain) patterning. Recess etching of barrier AlGaN layer is required to fabricate the good ohmic contacts. Optimize recessed etching process is

followed to etch ~ 10 nm of the AlGaN layer using $\text{BCl}_3/\text{Cl}_2/\text{Ar}$ plasma. Post recess, the sample is undergone for chemical treatment in order to minimize the impact of oxidation on the surface. The electron beam (eb) evaporation lift-off thin film deposition process is selected for ohmic contact. The sample is annealed under N_2 atmosphere using rapid thermal annealing (RTA) to form ohmic contact. The ohmic contact resistance is measured using standard transmission line model (TLM) with the

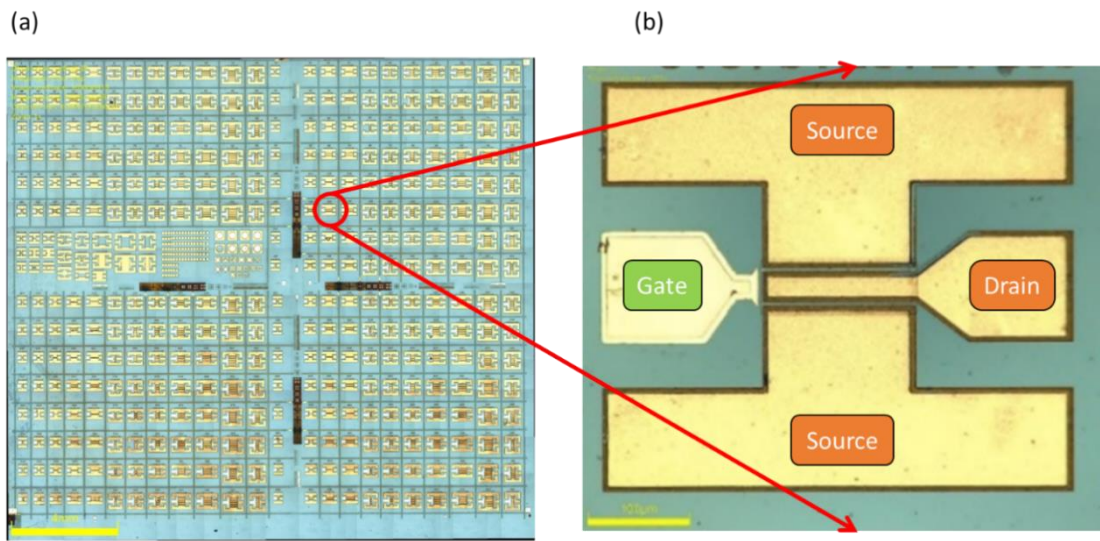


Figure 5.3: (a) GaN HEMT fabricated wafer and (b) 100 nm 2x100 GaN HEMT device

help of semiconductor characterization system (Model Keithley 4200). Electron beam lithography is used to form a mushroom gate contact. Again, eb evaporation lift off and post deposition RTA techniques are selected for gate contact in order to achieve high Schottky barrier height. In order to address the DC-RF dispersion issue, the Si_3N_4 passivation layer is deposited using PECVD. Contact pad thickening is formed in order to reduce resistive loss. Fabricated GaN HEMT wafer (1 square inch) having more than 300 GaN HEMT devices is shown in Figure 5.3. The detailed discussion about each process is explained in the following sections.

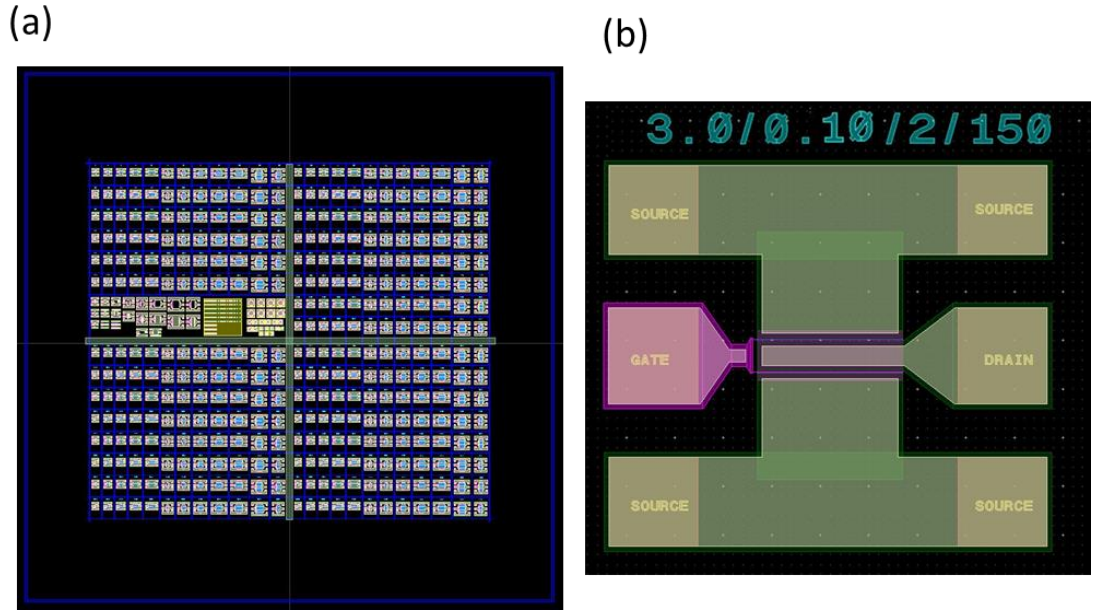


Figure 5.4: (a) layout designing on 1"x1" and (b) zoom one device image

5.1.1 Layout Design

The layout for GaN HEMT devices fabrication is done using Advanced Design System (ADS) software. The layout is designed for 1 square-inch wafer size. A sufficient number of variants are kept in layout in terms of device length and number of device fingers for wider statistical data. Device length varies from 50 to 300 micron (50, 100, 150, 200, 300), while number of fingers varies from 2 to 12 (2, 4, 6, 8, 10, 12). All devices have 100 nm mushroom gate structure. For each fabrication step, different layers are defined in the layout design as shown in Figure 5.4. The layout also contains varieties of process control monitors (PCM) for ohmic contact, Schottky contact etc. The RF measurement test structures like short, open and through are also kept in the layout as shown in Figure 5.5.

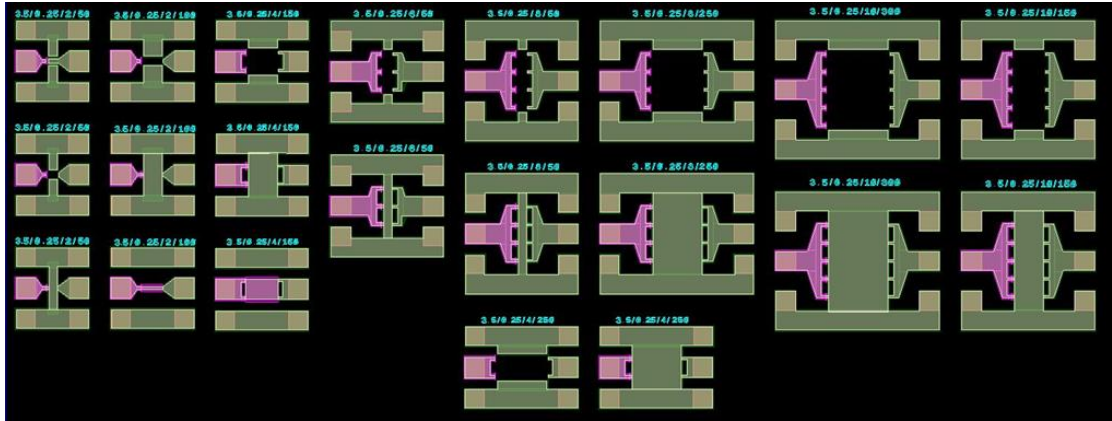


Figure 5.5: Varieties of process control monitors (PCM) for short, open and through the structure for RF measurement

5.1.2 Alignment marker Scheme & Mask Preparation

The first steps in the fabrication flow are dicing lines and reference alignment markers fabrication for photolithography as well as electron beam lithography process. Electron beam lithography-based lift off eb evaporation process is used for alignment markers and dicing line layer fabrication. NiCr/Au lift-off metallization is used for fabrication. The fabrication is carried out on a 4" GaN wafer, which is later diced into 1" x 1" samples for the fabrication of the subsequential further layers process. Figure 5.6 shows the layout of 1" x 1" wafer.

For the success of multilayer lithography, alignment markers are very crucial. Numbers of alignment markers are required to align one layer to another. It becomes highly important that markers are well designed and placed accurately. The complete GaN HEMT front-side fabrication process is consisting of eight layers and each layer shall be properly aligned with the reference layer for successful device fabrication. There are following three kinds of eb and photolithography alignment markers are used in GaN HEMT fabrication as shown in Figure 5.7

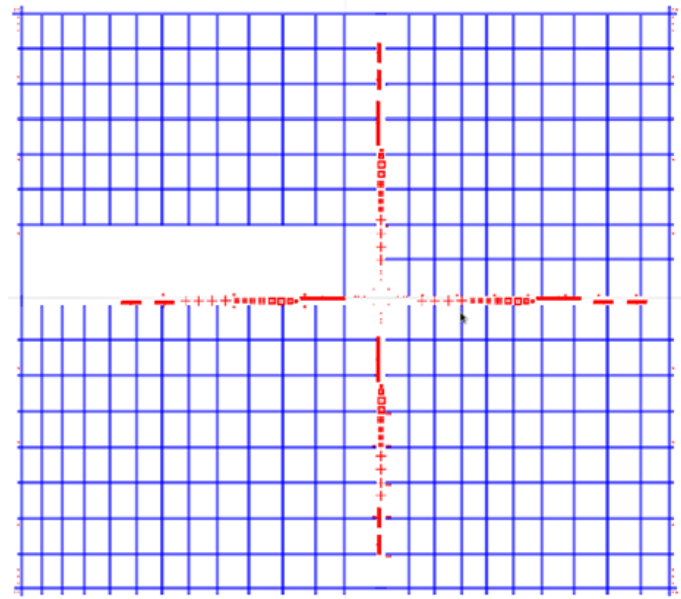


Figure 5.6: Dicing Line (Blue) and Alignment Markers (Red) Layout

Mask Fabrication for Photolithography Processes

Cr-mask is required for mask-based photolithography. Mask based photolithography is used for mesa isolation, SiN passivation layer etching and contact pad thickening process. The separate Cr- mask masks for each process are fabricated using Electron Beam Lithography based wet etching process

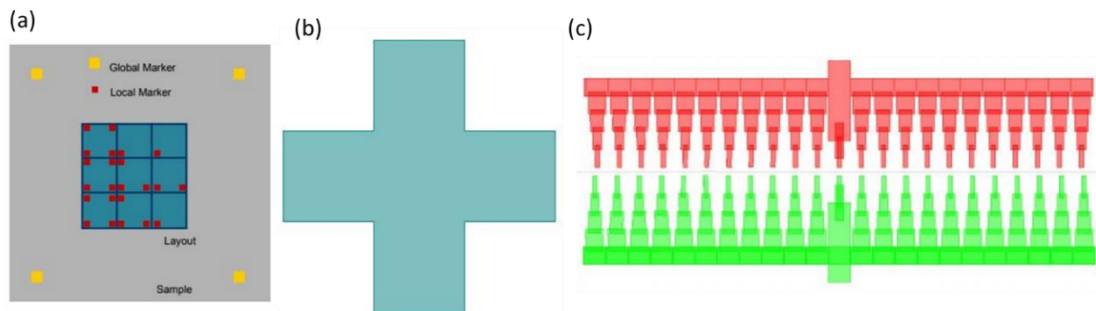


Figure 5.7: (a) Arrangement of Global (yellow) and Local (Red) Electron Beam Markers, (b) Photolithography Marker Placed on Wafer and (c) Vernier Scale marker used to determine alignment Error

5.1.3 Mesa Lithography & Etching

Electrical isolation between two neighbouring devices is prime requirement for wafer level fabrication. Schematic cross-section and top view of mesa isolation process represented in Figure 5.8 is used for devices isolation. The standard photolithography followed by dry etching process are used for mesa isolation.

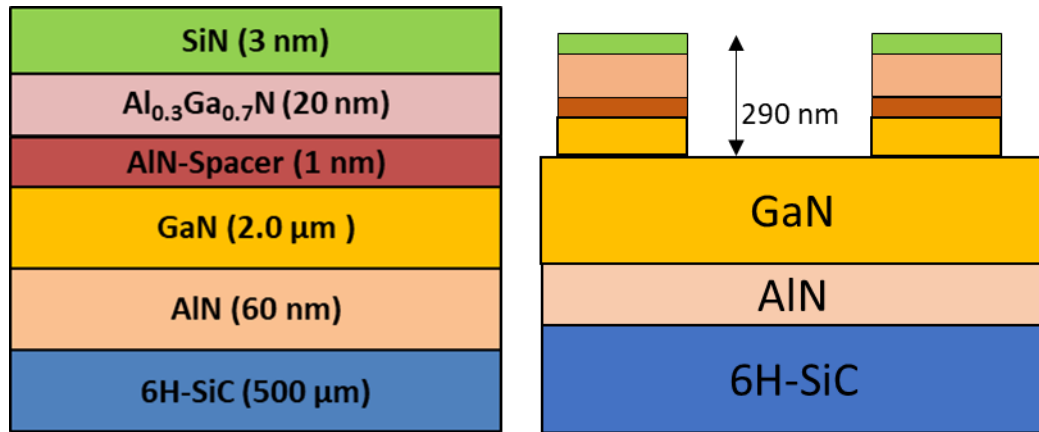


Figure 5.8: Schematic cross-sectional and top view of mesa Isolation process

Mask based Photolithography:

Mask based contact photolithography method is used for patterning of the mesa. AZ 4620 photo-resist is coated on the substrate using spin coating. Immediately after resist, coating a soft bake at 100 °C for 3 minutes has been carryout. The alignment accuracy for lithography is measured $\leq \pm 250$ nm and verified using confocal microscope. After proper alignment, the sample is exposed by UV radiation with i-line (365 nm) radiation. The substrate is developed to get the resist pattern. A hard-baking is done at temperature 100 °C for 8 minutes using a hot plate in order to stabilize and harden the photoresist.

Dry Etching using ICP RIE:

The mesa structures are etched by ICP RIE (Inductively Coupled Plasma Reactive Ion Etching) process using Sentech chlorine-based plasma system shown in Figure 5.9. The mesa dry etching process includes three steps. In the first step, the sample is processed in oxygen plasma to remove resist residue and active the sample surface for mesa etching. In this process 50 SCCM Oxygen, 10 SCCM Argon gases have been used. ICP power and RF power are set at 600 W and 50 W respectively. In the second step AlGaIn/GaN layer etching is initialized after a time delay of 3 minutes in order to cool

the sample. $\text{BCl}_3/\text{Cl}_2/\text{Ar}$ dry plasma is used to dry etch the AlGaIn and GaN layers. The flow rate of 10, 30 and 5 SCCM is set for BCl_3 , Cl_2 and Ar respectively, with an ICP power of 550W and RF power of 40 W. The etch rate has been achieved ~ 180 nm/min through this process. The recipe is optimized to minimize the roughness by varying ICP & RF powers, gas flow rates and electrode temperatures. After etching process, the remaining resist is removed by oxygen plasma ashing in the third step.



Figure 5.9: ICP-RIE Sentech SI-500 system

Characterization after mesa Etching:

The characterization of the mesa etched sample is done using confocal microscopy, SEM and stylus Profiler. A typical image taken by confocal microscope is shown in Figure 5.10 (a). The confocal microscope image can be used to understand the micro-roughness. The black spots in the images denote the peaks of the GaN substrate which are not etched. SEM and Stylus Profiler is used to measure the etch depth and roughness. Typical images of the etch depth measurement are shown in Figure 5.10 (b) and (c). The etch depth is achieved ~ 280 -300 nm with roughness is 2-3 nm.

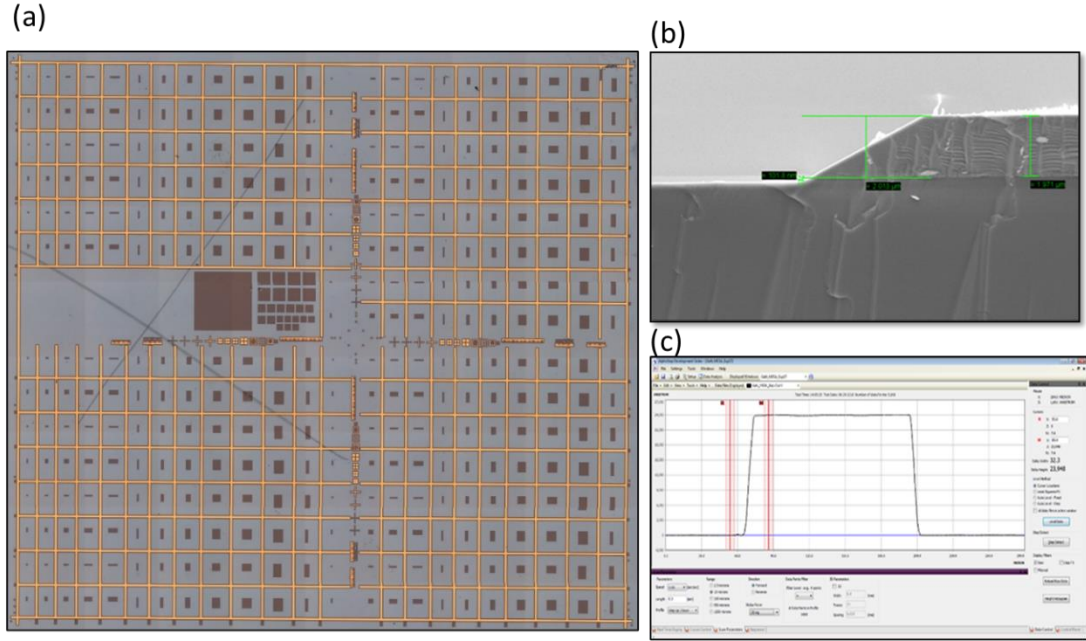


Figure 5.10: (a) Top view of etched mesa structures taken using confocal microscope on 1"x1" sample, (b) Cross-sectional SEM image of etched mesa structure and (c) Etch depth measurement using stylus profiler

5.1.4 Ohmic Contact Fabrication

The AlGaIn/GaN based heterostructure with AlN as spacer layer has exhibited promising DC and RF performance for HEMT due to reduction in alloy disorder scattering [95-99]. However, in AlGaIn/AlN/GaN based HEMTs, insertion of AlN spacer layer results in increase in potential barrier height in ohmic contact region which leads to a significant increase in the contact resistance (R_c). [100, 101] Increase in contact resistance impacts current flow from source to drain electrodes through GaN channel.

Chemical inertness and thermal stability of AlGaIn/AlN/GaN also stimulate difficulties in ohmic contact formation. To achieve high current densities and high extrinsic gains, which are required to obtain high thermal stability and high DC and RF performance of HEMTs, low-resistance ohmic contacts are essential. [102, 103] Ohmic properties of contacts are mainly governed by reactions at metal/semiconductor interface. These interfacial reactions explicate ohmic contact mechanism and give

insight for optimizing contacts for device performance. In order to obtain low R_c for AlGaIn/GaN HEMTs, researchers have reported various processing techniques such as n^+ GaN layer [100], recess-ohmic etching [104-106], surface plasma treatment [107-109] and Si ion-implantation doping [110]. Contact resistance on AlN/GaN based heterostructure is reported as $0.67 \Omega \cdot \text{mm}$ using rapid thermal annealing and $0.65 \Omega \cdot \text{mm}$ using Microwave Annealing technique [111]. Recess etching in ohmic region is experimented on AlGaIn/AlN/GaN based heterostructures and lowest reported contact resistance is $0.27 \Omega \cdot \text{mm}$ [105].

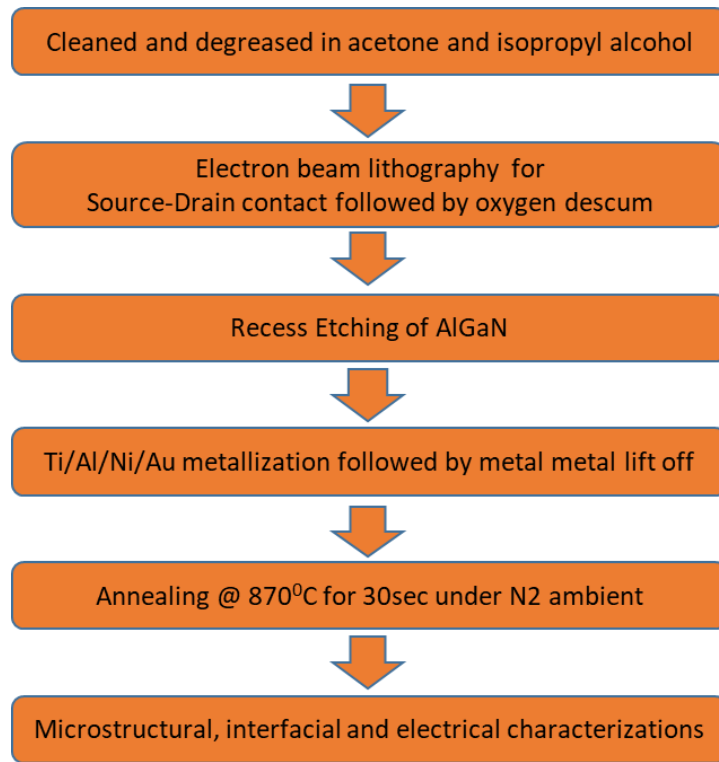


Figure 5.11: Flowchart showing process flow for ohmic contact fabrication

Herewith, recess etching technique is explored in order to obtain good ohmic contact performance. Ti/Al/Ni/Au based metallic system is used that forms ohmic contacts under optimized annealing conditions. This can provide a reliable solution for AlGaIn/AlN/GaN HEMT applications with superior electrical, morphological, and microstructural properties. Atomic Force Microscopy (AFM), High Resolution-Transmission Electron Microscopy (HRTEM), Scanning Electron Microscopy (SEM), X-ray Photoelectron Spectroscopy (XPS) measurements are used to investigate

structural, microstructural and surface properties of ohmic contact stack and TLM is used for electrical characterization. Figure 5.11 flowchart is briefing the involved process flow for ohmic contact fabrication.

5.1.4.1 Electron beam Lithography for Ohmic contact

Once mesa isolation process is completed, the next step in the fabrication sequence is Ohmic Contact (Source-Drain) fabrication. Electron beam lithography-based lift off process is selected for ohmic contact due to its precise operation and better alignment accuracy. The alignment of source/drain layer is critical with the next layer i.e. gate fabrication as gate terminal is to be positioned in the gap between source and drain contact and any misalignment can lead to shorting of gate finger either with source or drain. In order to resolve this issue, kept a set of markers in source-drain layer, which is used as reference for gate fabrication. The distance between source and drain terminal is kept $3.0\text{ }\mu\text{m}$.

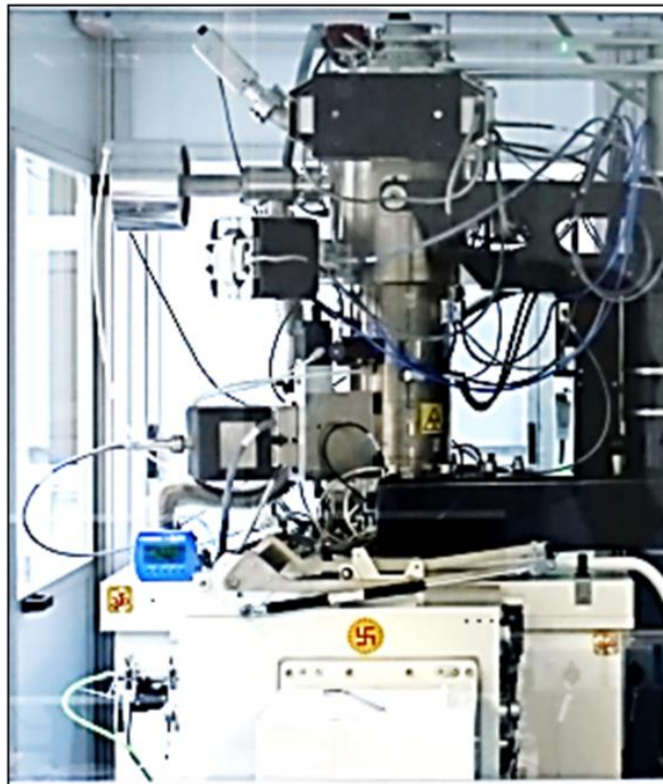


Figure 5.12: Raith Electron Beam Patter Generation (EBPG) 5200 system

Bilayer electron beam resist combination with PMMA as top and MMA (suitable co-poly of PMMA) as bottom layer is used for ohmic contact lithography. The resist total thickness is kept about 1 μm . The resist combination is required to achieve the desired undercut profile to create discontinuity in deposited metal for smooth lift off operation. After MMA and PMMA resists are coated on sample, a thin chrome layer is deposited in order to get rid of the charging issue engendered by electrons. Raith EBPG 5200 system as shown in Figure 5.12 is used for electron beam lithography process. After removing the conductive coating, electron beam patterned sample is developed using MIBK developer diluted with IPA solution. Figure 5.13 shows the source-drain resist profile after development process. The sample is inspected using laser microscope after development and ready for further processing.

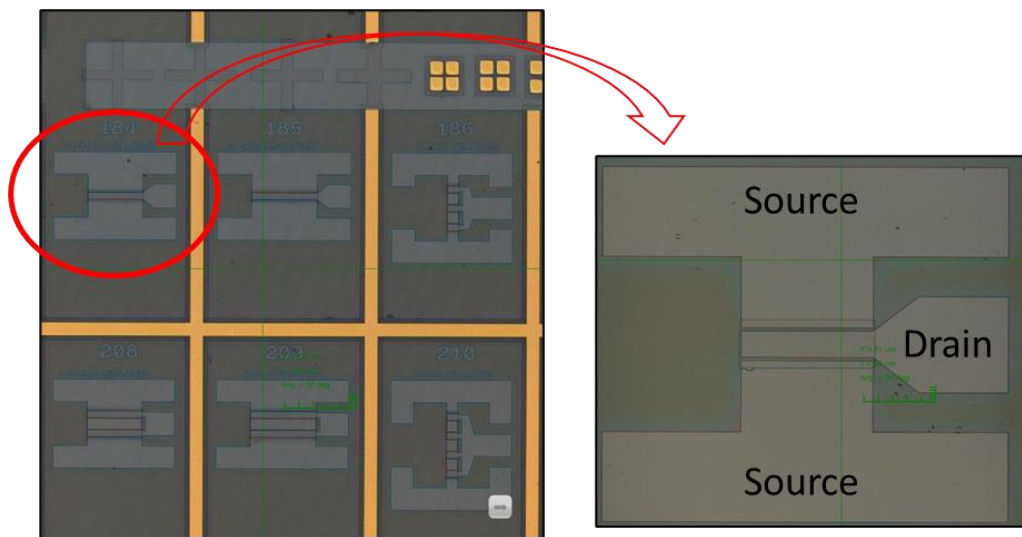


Figure 5.13: Source/Drain Resist Profile after Development Process

5.1.4.2 Recess Etching

The first step of recess etching is oxygen Plasma based descum process which is used to remove the resist residue and active the sample surface for recess etching. An oxygen flow of 30 sccm, and an ICP power of 100 W with 50 W RF bias are used for descum process. The next step is top Si_3N_4 passivation layer of 3 nm needs to be etched.

Fluorine based ICP RIE dry etching is used for this purpose. The third step is etching of AlGaN barrier layer. The chlorine-based chemistry (BCl_3 :15 sccm, Cl_2 :5 sccm and Ar:3 sccm gases) has been used in this process. BCl_3 is very aggressive and removes oxides from surface. Ar plasma is helping in removal of Ga-O and Al-O contents from the surface. It may have additional impact in removing the by-products from surface. In addition, the presence of Cl_2 is found to have positive impact in reducing the oxide to nitride ratio. ICP power of 150 W is applied to produce the plasma along with RF power of 15 W is applied bias the substrate. The plasma is ignited and maintained in the chamber with process pressure of $5.0\text{E-}03$ torr. This low pressure is required to have the anisotropy during etching. The etch rate of this chemistry is 25 nm/min.

5.1.4.3 Metal stack deposition and Annealing process:

After recess etching the sample is dipped in HCl:DI (1:10) for one minute to minimize impact of oxidation on surface. Ti/Al/Ni/Au (20/210/55/45 nm) metallization structure is selected and individual metal thickness is optimized for ohmic contact fabrication. Here Ti and Al participate in the interfacial reactions. Au layer is deposited as an outer layer to prevent the oxidation of metal stack during high temperature annealing process. Ni is deposited as a diffusion barrier layer to prevent or minimize downward diffusion of Au and upward diffusion of Al. This metal stack is deposited by lift-off electron beam evaporation process using Elettrorave dual eb guns system as shown in Figure 5.14. Metalized sample is annealed at $870\text{ }^\circ\text{C}$ for 45 sec under N_2 atmosphere using Annealsys AS-One 150 Rapid Thermal Processing system as shown in Figure 5.15. The fabricated device image of Source-Drain metal deposition after lift-off and annealing process is depicted in Figure 5.16. Schematic cross-section and top view of complete ohmic contact process is shown in Figure 5.17



Figure 5.14: Dual gun Electron Beam evaporation system



Figure 5.15: Annealsys AS-One 150 Rapid Thermal Processing system

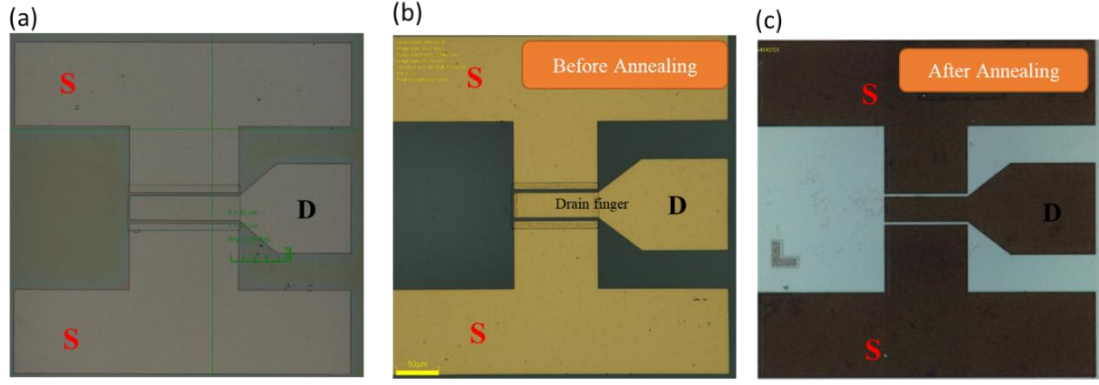


Figure 5.16: Source-Drain (a) resist profile after lithography, (b) metal deposition after lift-off process and (c) ohmic contact after annealing process

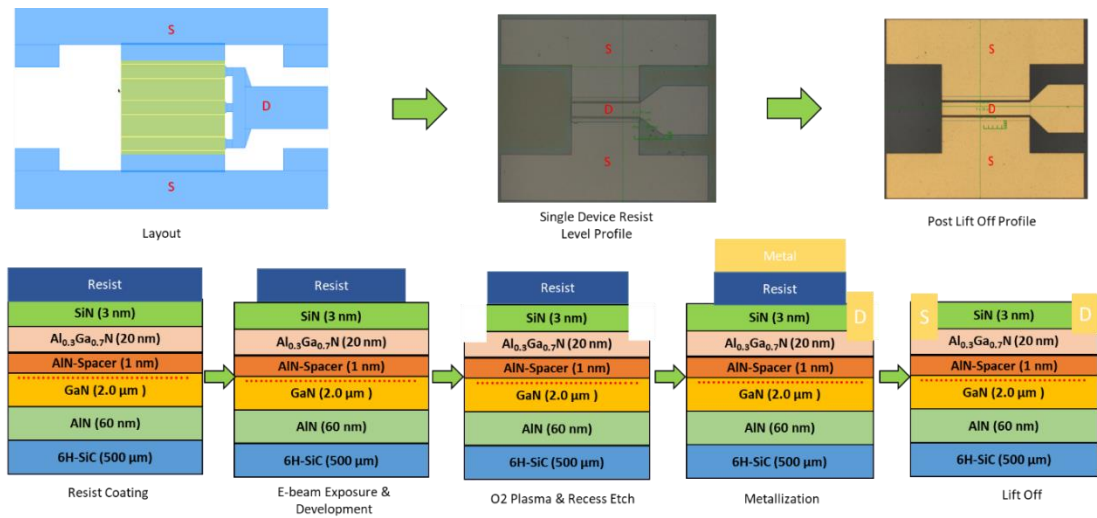


Figure 5.17: Schematic cross-sectional and top view of Ohmic contact fabrication

5.1.4.4 Ohmic Contact Characterization

Surface morphology is characterized using SEM and AFM. High resolution SEM measurement is performed using Ultra 55 SEM equipped with Energy and angle selective Backscattered electron (EsB) detector. Different interface phases are formed after annealing because of diffusion and interfacial reactions at metal/semiconductor interface which is characterized using TEM. High resolution TEM measurements are

performed using Titan Themis 300kV which includes measurement capability in HRTEM and scanning TEM (STEM) mode. The system is equipped with high-angle annular dark-field scanning (HAADF) and bright field (BF) detectors. To determine effect of surface plasma treatment X-ray photoelectron spectroscopy (XPS) characterization is done. High resolution XPS measurements are performed using a Kratos Axis Ultra Spectrometer equipped with a charge neutralization gun. The current-voltage (I-V) characteristics of sample is measured at room temperature using Semiconductor Device Analyzer, Keithly 4200. Contact resistance, specific contact resistance and sheet resistance are computed through Transmission Line Model (TLM) measurements on metal contacts.

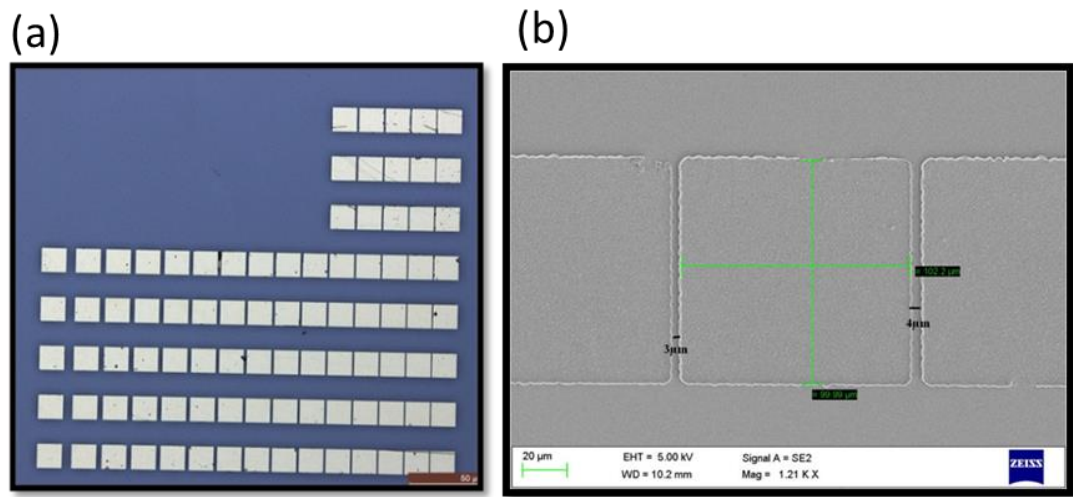


Figure 5.18: (a) Optical image of TLM patterns after metal lift-off and (b) SEM image of TLM pattern

TLM patterns are defined by photo-lithography and characterized by using optical microscope and SEM image. The optical image of TLM patterns and spacing between two TLM pads is depicting in Figure 5.18 (a) and (b) respectively. These patterns are of side length 100 µm and fabricated with separations varying from 3 to 36 µm respectively.

Optimization of metallization stack with individual metal thickness, recess depth and post deposition-annealing conditions after multiple experiments. Further to

it ICP-RIE parameters are also optimized in order to minimize damage and to get required etch depth of AlGaIn layer. Details of surface morphology, metal/semiconductor interface study and electrical characterization results are interpreted below:

Structural and Microstructural Characterization

Surface morphological characterization of bare heterostructure and ohmic contact sample is done using AFM as shown in Figure 5.19. The morphological characterization parameters are briefed in Table 5.1. AFM scan area is kept $5\mu\text{m} \times 5\mu\text{m}$ and measured surface roughness is order of 5.51 and 10.8\AA for bare heterostructure and ohmic contact processed sample respectively. This characterization clearly shows that surface roughness of recess etching treated sample shows increase in surface roughness due to etching.

Table 5.1: Summary of AFM characterization of Ohmic contact

Parameters	Bare Heterostructure	Ohmic contact
Scan Area (μm^2)	5x5	5x5
Roughness Ra (\AA)	5.51	10.8
Roughness Rq (\AA)	7.28	17.8

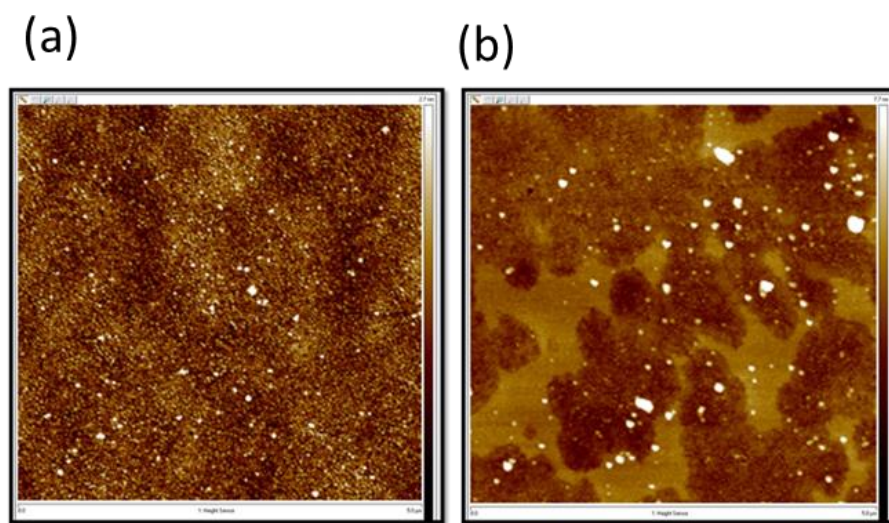


Figure 5.19: (a) AFM image of Bare Heterostructure and (b) Ohmic Contact Sample

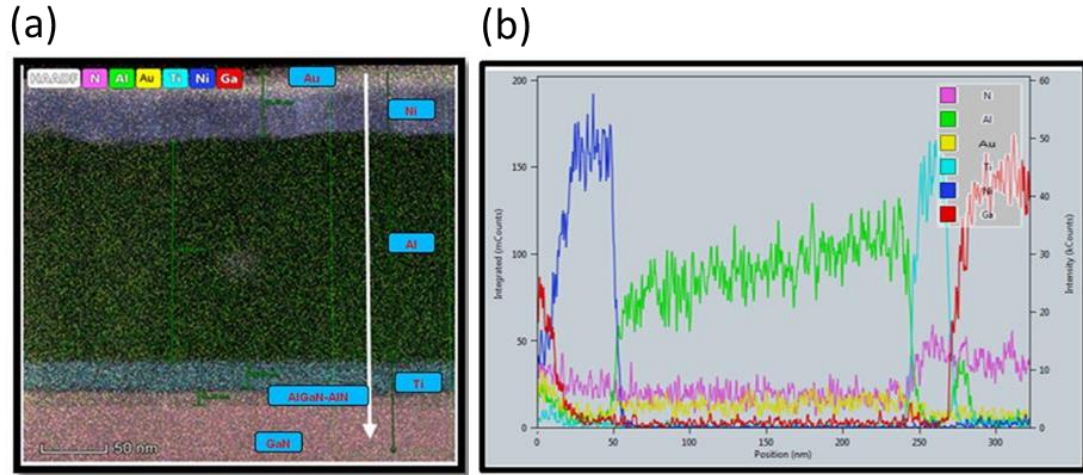


Figure 5.20: (a)HAADF TEM image of metal/semiconductor interface before annealing, (b) EDS analysis across white line shown in Figure 5.20 (a) a before annealing

Similarly, ohmic contact sample is subjected to TEM characterization. The image as shown in Figure 5.20 (a) clearly depicts sharp interfaces before annealing and confirms continuity with no interdiffusion. Elemental analysis using Energy Dispersive Spectroscopy (EDS) along with TEM as shown in Figure 5.20 (b) also indicates pure phase formation and elements in compliance with the arrow shown from top to bottom in TEM Figure 5.20 (a). Surface roughness of ohmic contact sample is characterized after annealing using AFM as shown in Figure 5.21 (a). Surface roughness value of order of nm is good and suitable for formation of sharp metal/semiconductor interface. Post annealing, metal/semiconductor interface study is done using cross sectional TEM as shown in Figure 5.21 (b). It clearly indicates diffusion of Ti to AlGaIn layer because of annealing process to create N vacancies. Ti is observed to simultaneously react with N which leads to formation of TiN at the interface and it is not in form of continuous layer but in the form of protrusion. Removal of native oxide layer by dipping sample in HCl solution is considered a helpful factor for protrusion of TiN in AlGaIn barrier layer. These TiN spikes are very efficient in the formation of low-resistance ohmic contacts by creating direct contact path to the 2DEG [100]

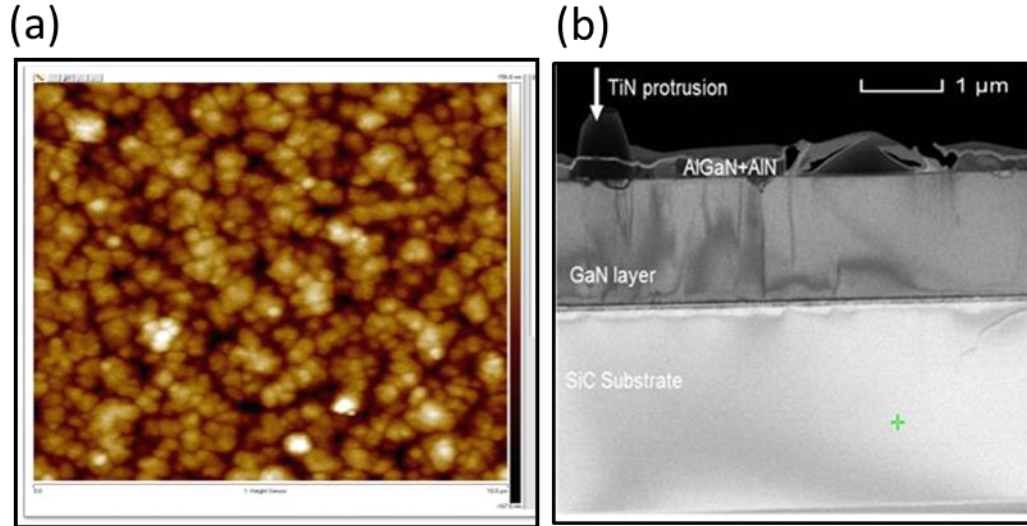


Figure 5.21: Post annealing (a) AFM image of ohmic contact sample and (b) HRTEM image of metal/semiconductor interface of ohmic contact sample

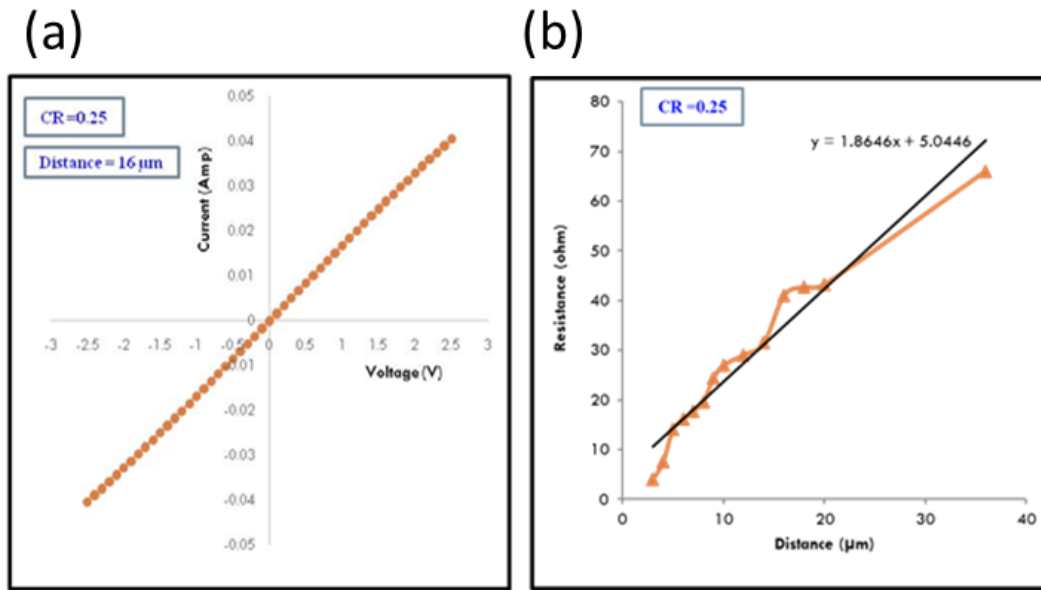


Figure 5.22: (a) I-V measurement of ohmic contact sample and (b) Total resistance vs. pad spacing for ohmic contact sample

Electrical Characterization

I-V measurements on ohmic contact sample is carried out as shown in Figure 5.22 (a). Linear nature of the graphs shows ohmic behavior of the Ti/Al/Ni/Au contacts on the sample. Extracted total resistance vs. pad spacing is shown in Figure 5.22 (b). Contact resistance, sheet resistance and specific contact resistance are extracted from Figure

5.22 are $0.25 \Omega \cdot \text{mm}$, $186 \Omega/\square$ and $3.41 \times 10^{-6} \Omega \cdot \text{cm}^2$ respectively. Based on characterization results, it is evident that recess etching process followed by HCl dip is having good potential for getting optimized contact resistance for better device performance needed for high power applications in microwave systems.

5.1.5 Schottky Contact Fabrication

The stable Schottky contacts with sufficient high barrier height and low leakage current are critical factors for realization of GaN HEMT.

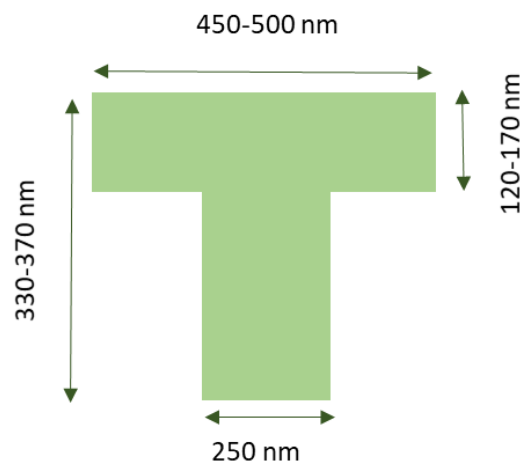


Figure 5.23: Cross Sectional View of T-gate

Schottky contact (Gate) is considered the heart of HEMTs as it governs the device performance. T-shaped or mushroom shaped gate structure with shorter gate lengths is preferred in HEMTs. This enables HEMT to operate at high frequency needed for today's high-speed microwave and millimetre-wave applications.

Table 5.2: Schottky contact geometry parameters

S.N.	Parameters	Values
1.	Gate Length	$\geq 100 \text{ nm}$
2.	Gate Width	$50\text{-}300 \mu\text{m}$
3.	No. of Fingers	2 to 12
4.	Gate Height (Metal Thickness)	$330\text{-}370\text{nm}$
5.	Shape	Mushroom (T)

In terms of fabrication process technology, f_T and f_{Max} can be significantly improved with a T-shaped gate structure. The advantage of T-gate is the shorter gate length L_g along with maximizing the area of the gate. 100 nm length (L_g) mushroom shaped gate is planned to be fabricated with multiple fingers up to 12 numbers to increase the output power of device. The typical cross-sectional view of T gate along with dimension and Schottky contact geometry parameters are listed in Figure 5.23 and Table 5.2 respectively.

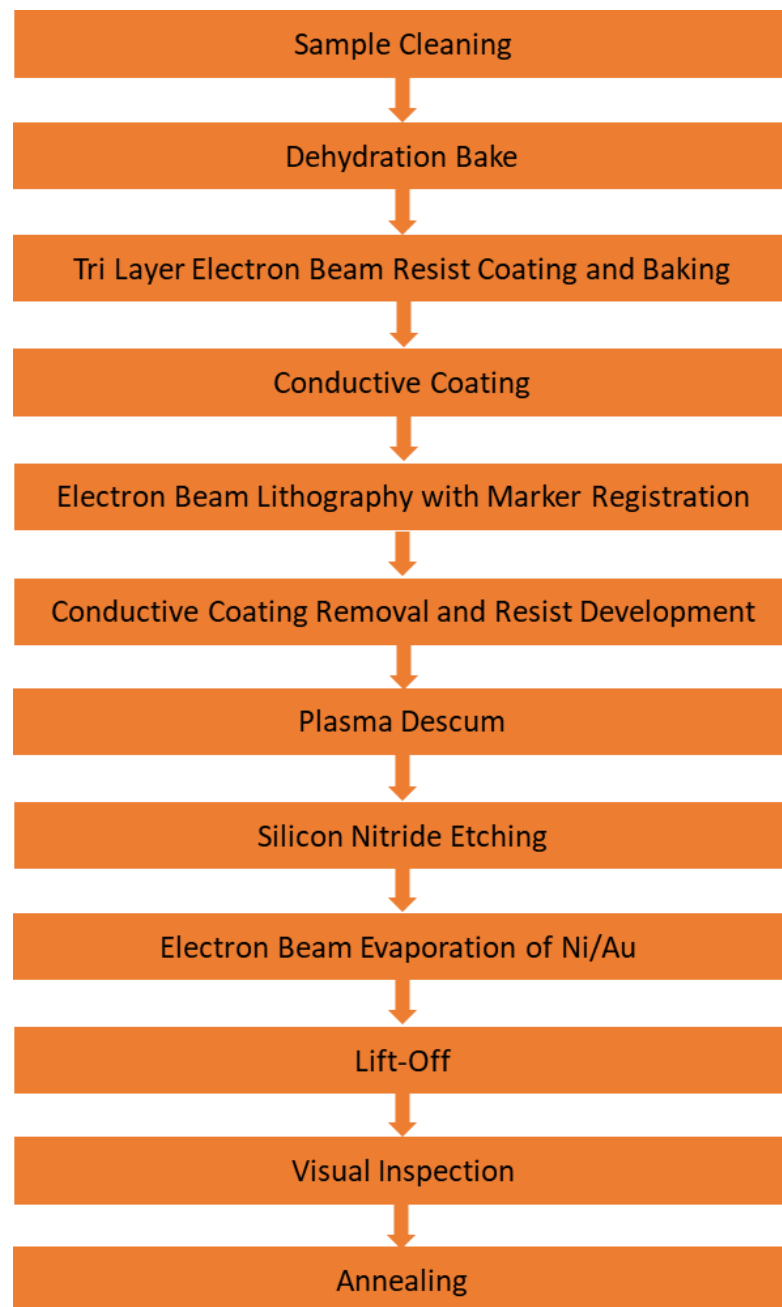


Figure 5.24: Flowchart showing process steps for Fabrication of Gate Contact

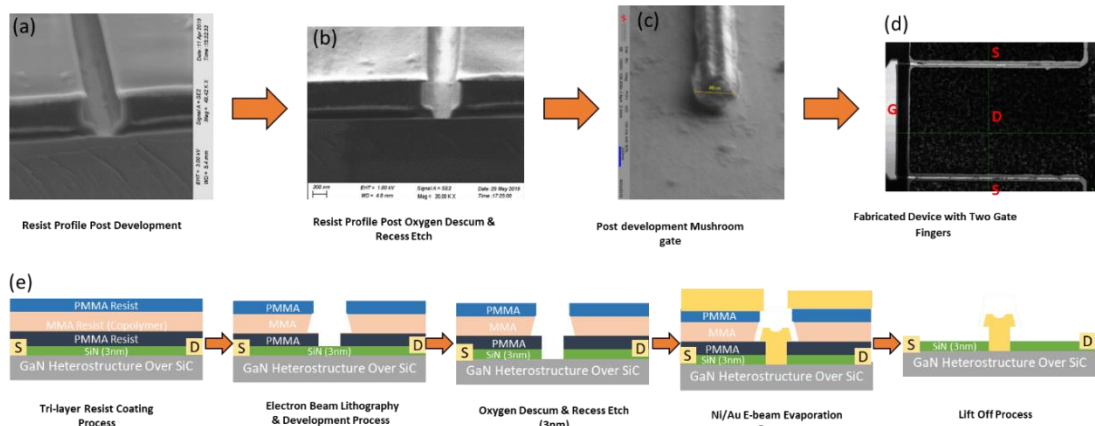


Figure 5.25: (a) Resist profile for mushroom gate, (b) Resist profile after SiN etching (c) Fabricated Mushroom gate, (d) 2 finger device and (e) cross sectional schematic of Gate fabrication Schematic cross-sectional view of Gate fabrication

Electron beam lithography-based lift off Ni/Au deposition process is developed for Schottky contact. Optimizing a process for Schottky contact fabrication on GaN heterostructure using Ni/Au metal scheme which reduction of seven to eight orders of magnitude in reverse leakage current. Figure 5.24 shows the process steps for fabrication of Schottky gate contact. The process begins with sample cleaning. It is cleaned with solvents like acetone and IPA with sonication followed by forced dry nitrogen to remove contaminants, which can affect the fabrication process. After cleaning of the sample, dehydration baking is done using hot plate. A tri-layer electron beam resist is coated in sequential manner using the spinner to achieve the required thickness with uniformity over the substrate. After resist coating the sample is baked using hot plate to evaporate the remaining solvent in the resist. A thin layer of chrome metal is coated over the substrate in order to get rid of the charging issue engendered by electrons due to high resistivity of the GaN heterostructure on SiC substrate. The next fabrication step is electron beam lithography with marker registration. This is the most critical step in the fabrication chain as the gate contact is defined in this step. Before carrying out the electron beam writing, the data received in the GDS format must be processed in the machine-readable format (GPF). Setting acceleration voltage, Proximity Effect Correction (PEC), development-loading factor, application of process

bias, resolution value, write field size, healing operation, Coarse/fine division selection of field and its size etc. are the major parameter in the data processing. After data processing, it is transferred into the control computer and the CJOB file is prepared. Dose (energy), writing current (spot size), writing strategy etc. are the important parameters for eb lithography. Before starting the writing process, markers are registered so that gate can be placed at desired location i.e. in centre of Source and Drain. Conductive chrome coating is removed using prepared Ceric Ammonium Nitride (CAN) based etchant and resist development process is carried out in class-10 environment. Developer concentration, development time etc. are the important parameter in this process. The oxygen plasma cleaning is an important process for removing resist residues. Top passivation layer Si_3N_4 of 3 nm on the heterostructure is etched using ICP-RIE with SF_6 plasma. After etching sample is dipped in HCl:DI (1:2) for one minute to minimize impact of oxidation on surface. Ni/Au (30/300 nm) metal stack is deposited by electron beam evaporation and patterned by the lift-off process. The Ni is deposited as a high work function metal to make efficient Schottky contact with $\text{Al}_{0.3}\text{Ga}_{0.7}\text{N}$ layer, while Au layer of metal is deposited as an outer layer to prevent the oxidation of metal stack during high temperature annealing process. After metallization, sample is taken for lift off operation. The metallized substrate is immersed into acetone and mild sonication is provided. Once the device is ready, it is thoroughly inspected using optical/confocal laser microscopes Olympus OLS 4100 which decide the device usability. The sample is annealed at 450 °C for 120 s under N_2 atmosphere in Rapid thermal annealing system after deposition. The process sequence picture of fabricated mushroom gate along with cross-sectional schematic of GaN HEMT gate fab is shown in Figure 5.25.

Schottky contact characterization

Two elemental metals (Ni and Au) with different metal work functions (5.15 eV and 5.1 eV) are selected for fabricating thermally stable Schottky contacts for high temperature operation devices. I-V and C-V characteristics of Ni/Au Schottky contact are investigated at room temperature. The electrical parameters such as ideality factor, barrier height and saturation current have been evaluated from I-V data. 2DEG carrier density and threshold voltage parameters have been extracted using C-V data.

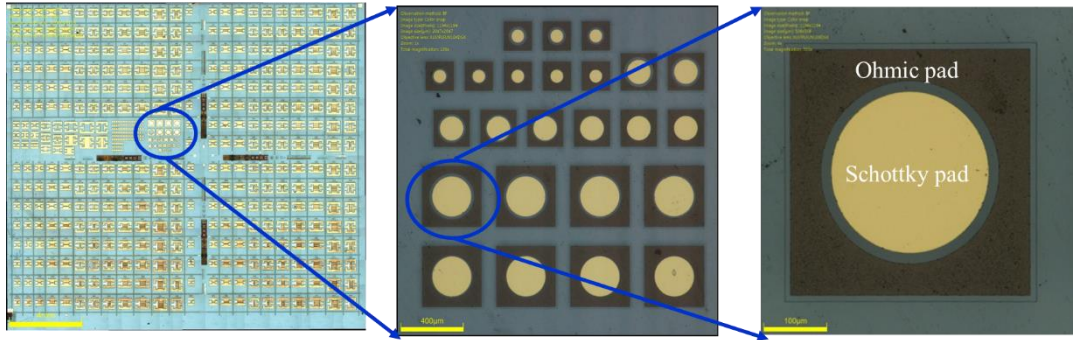


Figure 5.26: Optical image of Schottky test patterns after metal lift-off

The circular transmission line method (CTLTM) pattern has been fabricated as Schottky contact test structure as depicted in Figure 5.26. I-V and C-V characteristics of sample are measured at room temperature using Keithley's Semiconductor Device Analyzer, 4200A. Schottky contact fabrication process is optimized on $\text{Al}_{0.3}\text{Ga}_{0.7}\text{N}/\text{AlN}/\text{GaN}$ based heterostructure for GaN HEMTs. After multiple experiments, individual metal thickness in Ni/Au Schottky metal stack, is optimized. Further to it annealing temperature and time are also optimized for RTA (Rapid Thermal Annealing) process in order to get high SBH and to avoid any oxidation during process. Details of surface morphology and electrical characterization results for fabricated sample are interpreted below:

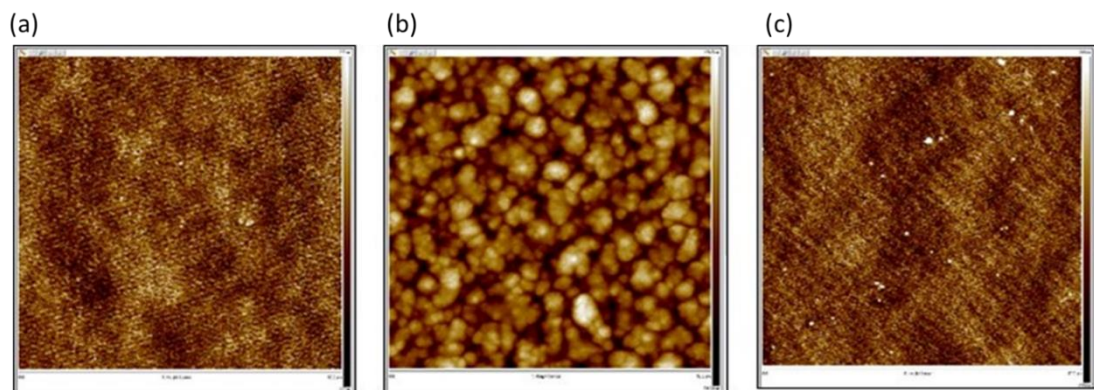


Figure 5.27: AFM image of (a) Bare Heterostructure, (b) Ohmic contact and (c) Schottky contact

Structural and Microstructural Characterization

Surface morphological characterization at bare heterostructure, ohmic contact surface and Schottky contact surface is done using Atomic Force Microscope (AFM). AFM images are shown in Figure 5.27 and morphological characterization parameters are briefed in Table 5.3. AFM scan area is $10\mu\text{m} \times 10\mu\text{m}$ and measured surface roughness is of order 0.77, 41.4 & 1.03 nm on bare heterostructure, ohmic contact surface and Schottky contact surfaces respectively. It shows, Schottky contact surface roughness is relatively good and suitable for formation of sharp metal/semiconductor interface. It further suggests formation of Al-Ni intermetallic, which can improve the contact's surface morphology with little increment in barrier height.

Table 5.3: Summary of AFM characterization of Schottky contact

Parameters	Bare Heterostructure	Ohmic contact	Schottky contact
Scan Area (μm^2)	10x10	10x10	10x10
Roughness Rq (nm)	0.77	41.4	1.03

Electrical Characterization

Ideality factor, SBH, saturation current density has been evaluated before and after annealing. Summary of these extracted parameters is mentioned in Table 5.4. For better control of the channel by the gate defined on top of the AlGaIn, 3nm of Si_3N_4 passivation layer is etched using ICP-RIE. It has already been reported that it will inevitably cause plasma-induced damage to the AlGaIn surface. These damages may exist as defects or dislocations in the lattice, vacancy complexes, recombination centers, formation of dangling bonds on the surface, implanted etch ions etc. which can lead to degrading device performance. These trapping centers act as defect charges and affect strain and surface states of AlGaIn layer and increase the electric field at the AlGaIn layer beneath the gate electrode, which leads to narrowing and reduction of the effective SBH, as shown in Table 5.4 Thus, the Schottky barrier tunnelling of charge carriers will significantly increase after etching. Sample with the annealing treatment partially recovers these defects, which leads to reduction of traps and surface states in the AlGaIn

layer. Accordingly, the SBH after annealing is higher than before annealing. As shown by calculations, the ideality factor before annealing is higher than after annealing. In one word, the annealing process after the metal deposition can remove or mitigate etching-induced damages and suppress the leakage current related to damages, thus, reducing the ideality factor.

Table 5.4: Summary of extracted parameters from I-V data

Parameters	Before Annealing	After Annealing
Saturation Current (Amp)	-1.62×10^{-10}	-3.47×10^{-10}
Barrier Height (eV)	0.64	0.72
Ideality Factor	2.3	1.8

Figure 5.28 (a) shows the comparison of the reverse biased Schottky diode characteristics of before (blue curve) and after annealing (red curve). It can be concluded that the annealing step after the metal deposition is effective for suppressing the leakage current. C-V measurement has been carried out before and after annealing at 1MHz as shown in Figure 5.28 (b), in order to get better insight of fabricated Schottky diodes. It is observed that post annealing the threshold voltage is shifted towards positive direction of the x-axis.

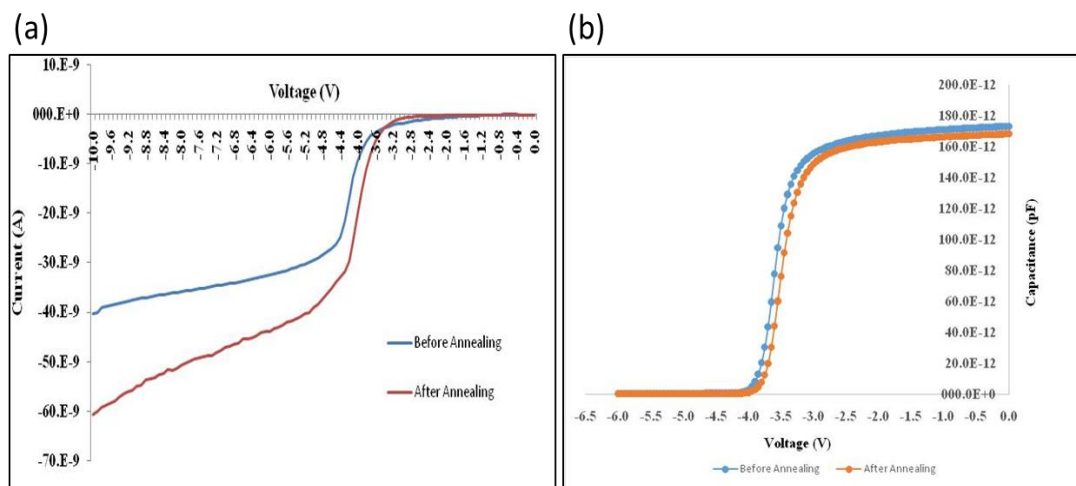


Figure 5.28: (a) Reverse biased Schottky diode characteristics and (b) C-V characteristics before and after annealing

As depicted in Figure 5.28 (b), there is slight reduction in the 2DEG carrier density after annealing. This reduction clearly indicates more depletion of channel under the gate contact after annealing due to increase in SBH. The positive shift in the threshold voltage in C-V is of great importance; as HEMT devices are depletion mode devices and this positive shift makes annealed Schottky contacts more energy efficient as a lower negative voltage is required to turn off the device. Using C-V data, 2DEG density and threshold voltage before and after annealing are extracted and summarized below Table 5.5.

Table 5.5: Summary of extracted parameters from C-V data

Parameters	Before Annealing	After Annealing
2DEG density(cm-2)	1.35 E+13	1.30 E+13
Threshold voltage (V)	- 4.2	- 3.7

In summary, Ni/Au gated contacts on Al_{0.3}Ga_{0.7}N/AlN/GaN heterostructure have been optimized, and characterized. Annealing process for Schottky contact fabrication has also been optimized to improve Schottky contact characteristics. Thermal annealing of the gate recess after metal deposition is found to be an effective method to improve the gate performance of GaN HEMTs. Plasma-induced damages due to Si₃N₄ etching are reduced after annealing and helpful for suppressing the gate leakage current of AlGaIn/GaN HEMTs. Decrease in gate leakage results in decreasing the ideality factor and increasing SBH. The C-V measurement results are also analyzed and it is concluded that thermal annealing post metal deposition can increase the Schottky barrier height in AlGaIn/AlN/GaN based Schottky contacts, thus effectively suppressing the etching/trap assisted tunnelling which leads to decrease in gate leakage.

5.1.6 Device Passivation Process

A surface passivation layer is needed to neutralize surface charges/traps available on the AlGaIn/GaN surface. Silicon Nitride (Si₃N₄) is deposited as the surface passivation layer providing positive charges at AlGaIn surface great enough to neutralize surface

charges. Silicon Nitride passivation generates internal stresses in the deposition and due to the neutralization of surface charges, 2DEG charge density increases at AlGaIn/GaN interface. In complete GaN HEMT fabrication, passivation process at different stages is very much essential in order to protect small dimensional features like nanometric gate etc.

5.1.6.1 Passivation Layer Deposition

GaN devices suffer from surface-related problems such as current degradation, transconductance dispersion, excess gate leakage current through Schottky interfaces and aging of ohmic-schottky contacts. It has not only inhibited device performance but also degrades reliability of GaN based devices [112–114]. III-V materials are sensitive to various influences on the surface potential and affects device performance [115, 116]. Researchers from a couple of laboratories have reported that surface traps have been present in virtually all devices, and leads to the problem of significant dispersion in DC and RF characteristics [117-119]. Efforts have been directed to effectively reduce surface-related issues using surface passivation necessitating low-damage surface treatment and high-quality SiN_x deposition [112, 120, 121]. Nevertheless, influence of Si₃N₄ passivation on small signal RF performance of the AlGaIn/GaN HEMTs has been controversial. A decrease [122, 123] as well as an increase [124] of F_t and F_{max} after passivation is founded. Moreover, after Si₃N₄ passivation a significant increase in the gate and drain leakage currents has also been reported. It is also well acknowledged that increased gate leakage current is associated with Si₃N₄/AlGaIn interface [125, 126].

Table 5.6: SiN passivation experiments details

Sr No	Process Experiments	P1 (Without passivation)	P2 (SiN passivation)	P3 (NP SiN passivation)
1	Passivation Exp 1	√	√	√
2	Passivation Exp 2	√	√	√
3	Passivation Exp 3	√	√	√
4	Passivation Exp 4	√	√	√
5	Passivation Exp 4 (repeat1)	√	√	√
6	Passivation Exp 4 (repeat2)	√	√	√
7	Passivation Exp 4 (repeat3)	√	√	√

Table 5.7: Optimized process parameters for SiN deposition

Sr No	Process parameters	Exp 1 Values	Exp 2 Values	Exp 3 Values	Exp 4 Values
1	Electrode temperature (°C)	350	350	350	350
2	Ultimate vacuum (torr)	1.0E-05	1.0E-05	1.0E-05	1.0E-05
3	Process vacuum (torr)	1.0E-03	1.0E-03	1.0E-03	1.0E-03
4	RF Power (Watt)	50	50	50	50
5	SiH ₄ Flow (SCCM)	20	20	20	20
6	NH ₃ Flow (SCCM)	40	40	40	40
7	N ₂ Flow (SCCM)	980	980	980	980
8	Si ₃ N ₄ thickness (nm)	50	100	200	120

The Silicon Nitride deposition is carried out in Plasma Enhanced Chemical Vapor Deposition (PECVD) system. In this process, the precursors are selected as Silane (SiH₄), Ammonia (NH₃) and Nitrogen (N₂). The various combinations for the process conditions on total 7 samples during SiN passivation are shown in Table 5.6. The best result founded experiment (Experiments 4) is repeated additional three times to confirm the process stability, repeatability and reproducibility. The experiment 4 results presented in this thesis is almost reproducible in all experiment with 2% device-to-device variation (within 1''x1' sample) and 3.5 % sample to sample variation (among different experiments). One sample (P1), before passivation is subjected to DC/RF measurement; second sample (P2) is passivated without nitrogen pre-treated (NP) process and third sample (P3) is passivated using NP. Each experiments process parameters for Si₃N₄ deposition are mentioned in Table 5.7. In this process, the precursors are Silane (SiH₄), Ammonia (NH₃) and Nitrogen (N₂) and prior to loading, the samples (P2 & P3) are cleaned using regular cleaning procedure in acetone and isopropyl alcohol. Further, prior to loading, samples (P2 & P3) are dipped in NH₄OH solution for 30 sec to remove native oxides and carbon contamination and processed one after another in Oxford make Plasma Pro-100 Nano PECVD system. Si₃N₄ film of 120nm is deposited on P2 using process parameters in Table 5.7, while an in-situ N₂ plasma pre-treatment is done at 210°C for 2 min at 10 W power followed by Si₃N₄ deposition on P3 as per the process parameters mentioned in Table 5.7. Typical image of wafer taken by confocal microscopy before and after SiN deposition is shown in Figure 5.29

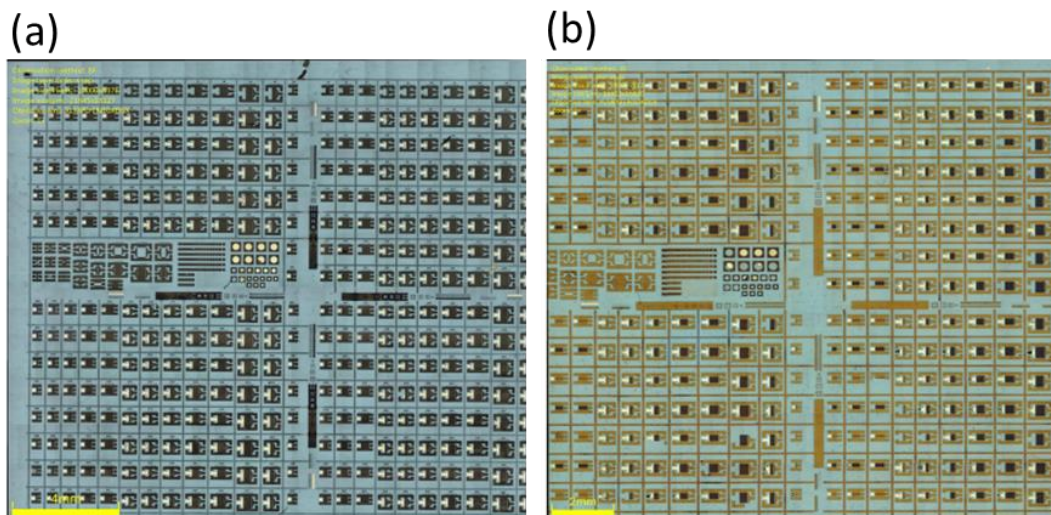


Figure 5.29: Typical image of wafer taken by confocal microscopy (a) before SiN and (b) after SiN deposition

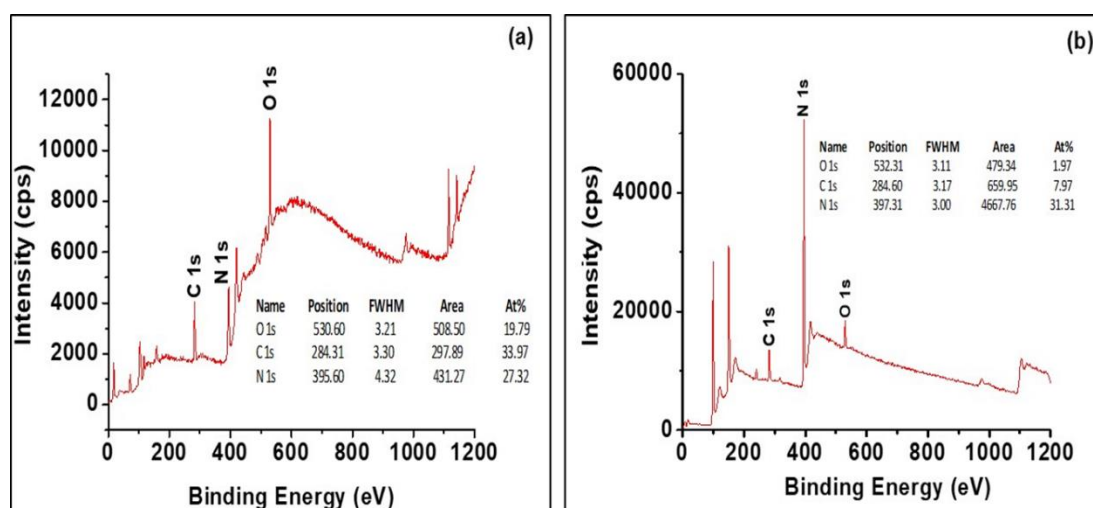


Figure 5.30: (a) XPS spectra before wet chemical & N₂ Plasma treatment and (b) XPS spectra after wet chemical & N₂ Plasma treatment

XPS: Sample is characterized by XPS to study impact of NH₄OH wet chemical treatment followed by in-situ N₂ plasma treatment in order to prepare Al_{0.3}Ga_{0.7}N surface for Si₃N₄ deposition as well as to ascertain chemical bonding of deposited Si₃N₄ film. XPS measurements are performed using a Kratos Axis Ultra Spectrometer at 45° take-off angle with respect to the vertical direction to the sample surface. Spectra is

measured using a monochromatic Al K α X-ray (1486.6 eV). Binding energies are referenced to the C 1s peak at 284.6 eV derived from the abundant carbon contamination. XPS spectra are measured before wet chemical treatment and N₂ plasma treatment as shown in Figure 5.30 (a). O 1s peak at 530.60 eV with atomic concentration of 19.79%, C 1s peak at 284.31 eV with atomic concentration of 33.97%

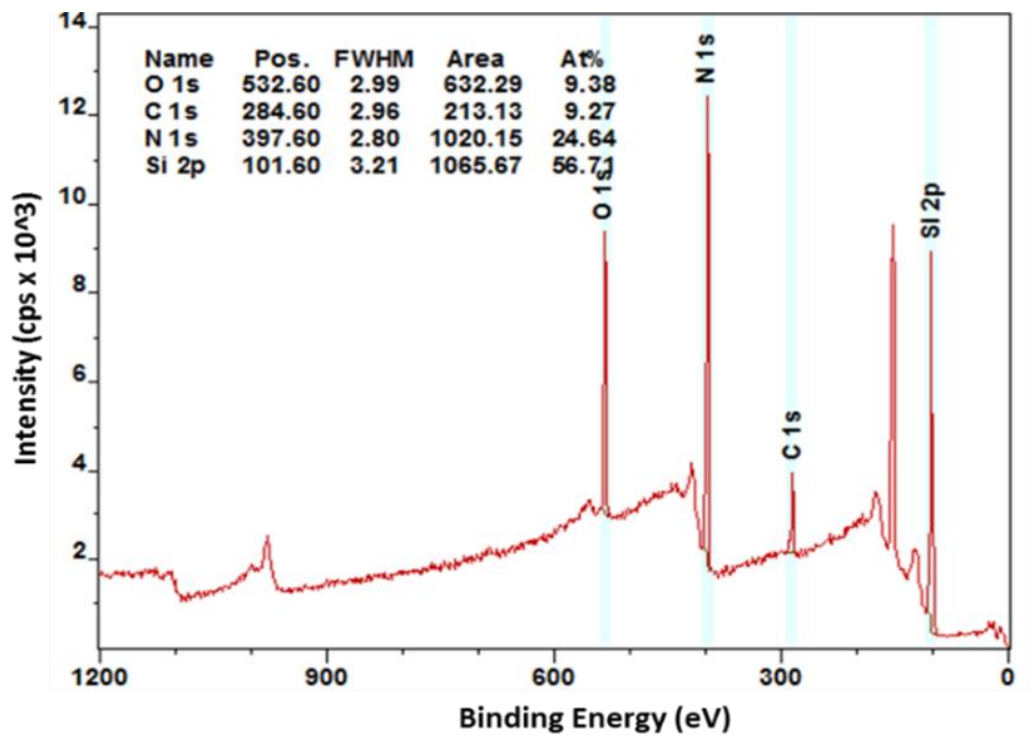


Figure 5.31: XPS spectra post NP Si₃N₄ deposition

and N 1s peak at 395.6 eV with atomic concentration of 27.32%. However, after wet chemical treatment and N₂ plasma treatment as shown in Figure 5.30 (b), XPS spectra show O 1s peak at 532.31 eV with atomic concentration of 1.97%, C 1s peak at 284.6 eV with atomic concentration of 7.97% and N 1s peak at 397.31 eV with atomic concentration of 31.31%. This clearly explains reduction in oxygen and carbon contamination on AlGaN surface, which is considered to significantly contribute in surface defects. After Si₃N₄ thin film deposition, XPS spectra measured are shown in Figure 5.31. It depicts Si 2p peak at 101.6 eV and N 1s peak at 397.6 eV, which confirms Si₃N₄ species [127].

HR-XRD: HR-XRD is used to analyze the stress applied to AlGaIn layer in GaN heterostructure by Si₃N₄ deposition. As reported, it is observed that there is an increase in sheet carrier density at the hetero-interface due to the increase of piezoelectric polarization in the strained AlGaIn layer, if the deposited passivation film produces tensile stress on AlGaIn layer [128]. Figure 5.32 shows changes of HRXRD spectra of GaN heterostructure before and after NP passivation. The inset shows the AlGaIn (0002) diffraction. After NP passivation, AlGaIn (0002) peak shifted toward the high diffraction angle. In 120 nm thick Si₃N₄ deposited sample, the position of the AlGaIn (0002) reflection are increased from 35.1° to 35.11°. It indicates that the lattice constant along the c axis of AlGaIn layer decreased from 5.106 to 5.104 Å. This further indicates increase in biaxial tensile stress applied to the AlGaIn layer which leads to increase in piezoelectric polarization.

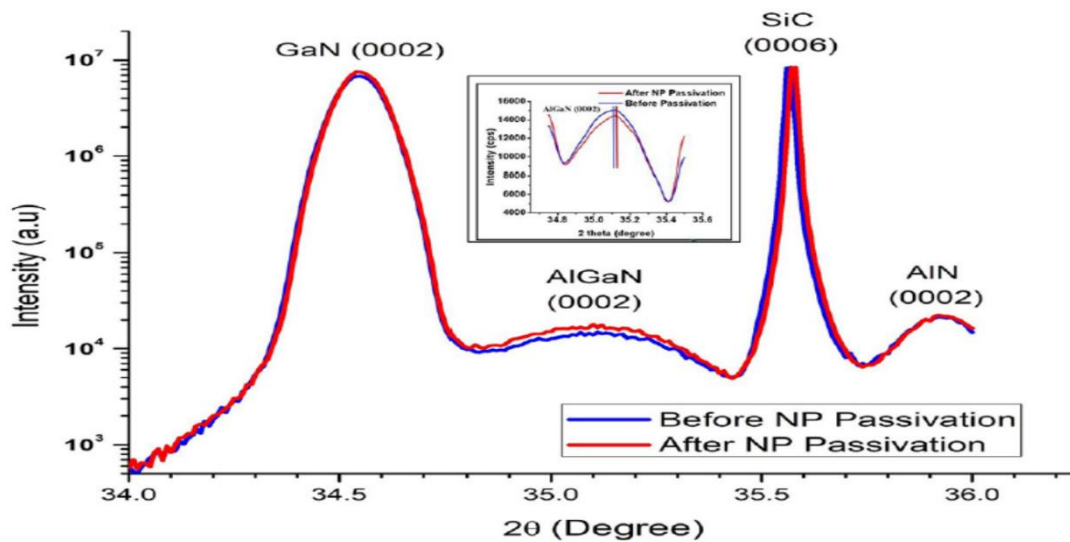


Figure 5.32: HR-XRD pattern before and after NP Si₃N₄ deposition

Ellipsometry: The optical properties and thickness of deposited Si₃N₄ film on P2 and P3 are obtained by spectroscopic ellipsometry using J. A. Wollam variable-angle spectroscopic ellipsometer. Wavelengths from 250 to 1000 nm are used at angles of incidence of 65°, 70°, and 75°. The measured data are fitted by a dispersion law based on the Forouhi-Bloomer model for amorphous semiconducting and insulating materials [129] which determines refractive index n , and the layer thicknesses. Extracted values

of film thickness and refractive index @ 632.8 nm are 119.04 ± 0.032 nm & 2.05; 119.10 ± 0.029 nm & 1.92 on P2 and P3 respectively.

Si_3N_4 films with refractive index > 2.03 are Si rich films, which leads to high dielectric constant and higher capacitance values. In this case, achieved refractive index value for P2 is 2.05 and for P3 is 1.92 and hence suggesting lower capacitance values. The difference in refractive index could be explained by the incorporation of voids in the film microstructure [130]. This further indicates dense and good compositional homogeneity of NP Si_3N_4 film.

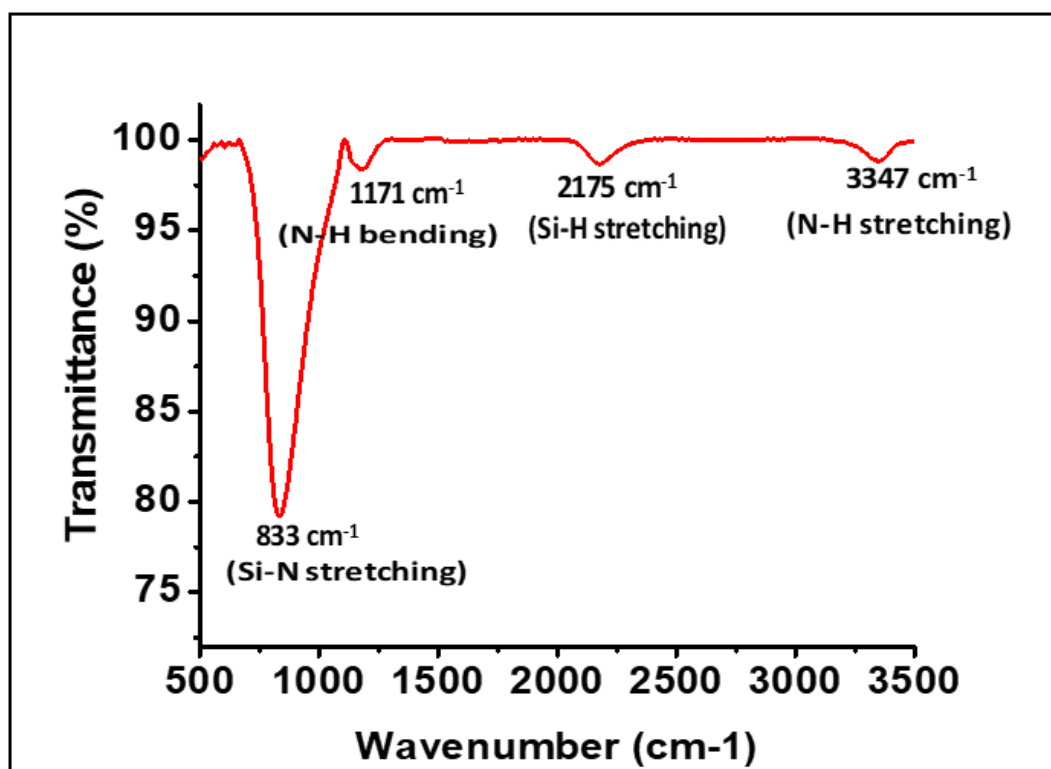


Figure 5.33: FTIR spectra of NP Si_3N_4 film

FTIR: FTIR measurements using High Tech Detection System, working in the range $400 - 4000 \text{ cm}^{-1}$, have been performed on NP Si_3N_4 film in transmission mode. FTIR measurements provide information about the configuration and type of bonding in SiN films, which can be used to determine the deposition regime. Plasma deposition from

SiH₄, NH₃ and N₂ precursors yields SiN films, which can contain Si-N, Si-H, N-H bonds etc. Figure 5.33 shows FTIR spectra of SiN film deposited at 350°C with dominant peak at 833cm⁻¹ corresponding to stretching vibration mode of Si-N bond, the peak at 1171 cm⁻¹ is associated with N-H bending motion, peak at 2175 cm⁻¹ and 3347 cm⁻¹ are associated with Si-H and N-H stretching vibration mode respectively [131]. It clearly depicts the absence of Si-O, Si-H bonds etc., which is a clear indication of the absence of O contamination at the interface between the AlGaN layer and the SiNx layer and confirms thermally stable and dense film. Moreover, optimized NP passivation process shows the deposited film has less N-H and Si-H stretching modes, which leads to hydrogen free film and thus improving the quality of the film

5.1.6.2 Passivation Layer Etching

The passivation layer is useful to avoid the current slump, degradation of properties of fabricated devices and to increase the performance. As explained in the previous section, a Si₃N₄ layer of 120 nm is deposited by PECVD Process. The deposited Si₃N₄ film conformally covered the complete sample. It is essential to open the contact pads to do further processing on sample by the photolithography and dry etching processes. The details of lithography and opening of the passivation layer by dry etching process are discussed below.

Photolithography for Patterning of Passivation Layer:

The mask-based contact photolithography process is used for patterning of the passivation layer. A chrome coated fused quartz mask is used for photolithography. AZ 4620 resist is coated on the substrate using spin coating. The soft bake at 100 °C for 3 minutes is required to bake the resist after spin coating. The alignment between mask and sample is done using alignment marks on the mask and the sample. Mask-aligner system is used for UV exposer.

Dry Etching using ICP RIE:

Dry etching process for SiN passivation layer is started Oxygen plasma to remove the resist residue on etched portion. An oxygen flow of 30 sccm and ICP power of 100 W

along with 10 W RF biasing is used in process. The recipe cannot etch Si_3N_4 while it is having an etch rate of 35 nm/min for AZ 4620 resist. The recipe is run for 1 min for removing resist residue. The SF_6 fluorine gas-based chemistry is used for etching of Si_3N_4 . The process is optimized with several trial runs. The finalized process parameters are 60 sccm SF_6 flow rate and ICP power of 200 W along with 20W RF bias to sample. The etch rate for Si_3N_4 is measured ~ 75 nm/min in this process without affecting the metallic source, drain and gate pads.

5.1.7 Contact Thickening and Air Bridge Fabrication

The metal thickening in pad and finger area is required to further reduce the resistance in pad and electrodes. Contact thickening is done by photolithography followed by TiW/Au metal deposition. AZ 4620 positive photoresist is selected and coated using spin coating process. The mask-based photolithography process is conducted on sample after soft baked. AZ 400k developer is chosen for the resist development process. Descum process in O_2 Plasma is first done on the patterned wafer to remove residue and activate the surface. TiW-Au is deposited using lift-off DC magnetron sputtering system. 200-300Å thick adhesive layer of TiW is deposited and followed by ~ 0.8 μm thick Gold (Au) layer is deposited for contact pad thickening.

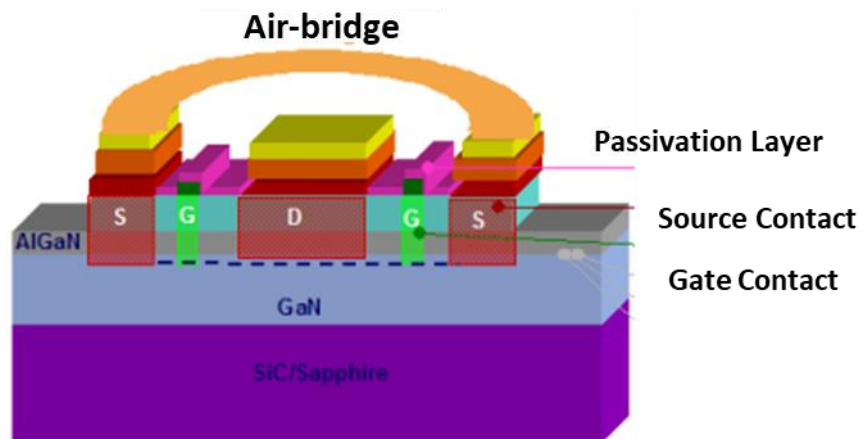


Figure 5.34: Part of Air Bridge connecting Source Terminals

Multi-finger devices having higher number of gate fingers are needed to increase output current and power of device. Up to 12 gate fingers GaN HEMT devices

are fabricated. For multi-finger gates devices air bridges are used to interconnect multiple source terminals. The schematic of air bridge pass over drain and gate terminals is shown in Figure 5.34. It is required to develop a lithography process in which resist structure possesses a rounded profile that will define the shape of the bridge. Two-step mask-based contact photolithography process is selected for air-bridge fabrication. The cross-sectional view of Air Bridge fabrication along with process flow is shown in Figure 5.35.

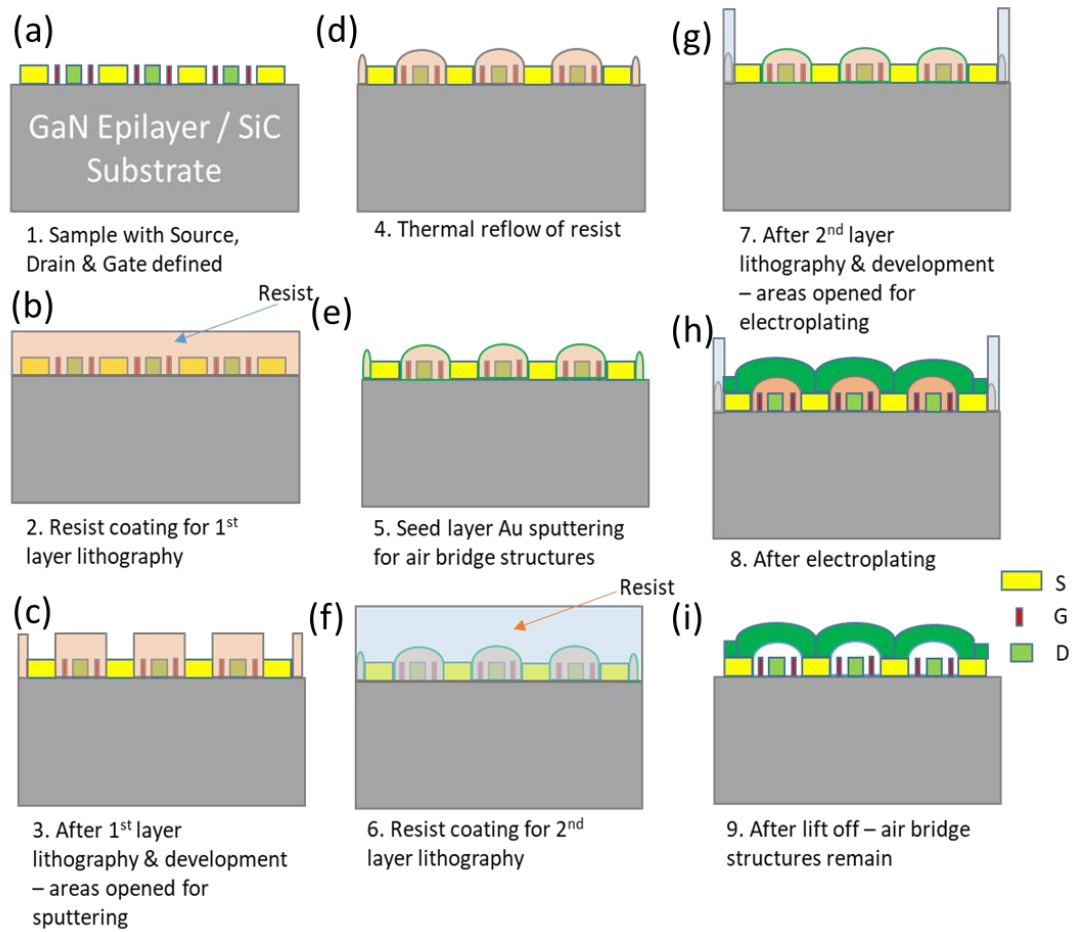


Figure 5.35: Cross sectional view of Air Bridge fabrication process flow

GaN sample is cleaned using Acetone and IPA with sonication to remove the contaminants subsequently sample is placed on the hot plate for the dehydration bake. AZ 4620 positive photoresist is selected and coated using spin coating process. The mask-based photolithography process is conducted on sample after soft baked. AZ 400k developer is chosen for the resist development process. The sample is inspected using microscope for the square profile as shown in Figure 5.35 (c). In order to modify the

shape of resist structure, thermal treatment process is developed. In this process, the sample is heated on the hot plate to alter the resist profile from square to rounded one as depicted in Figure 5.35 (d). The sample is again inspected for the desired rounded sidewall profile and measurements are done using confocal microscope. Descum process in O₂ Plasma is first done on the patterned (resist mold) wafer. The descum process is essential to remove unwanted resist residues left over the area where metallization is required. TiW-Au is deposited using lift-off DC magnetron Sputtering process is used for seed layer deposition. First 200-300Å thick adhesive layer of TiW is deposited and followed by ~0.6 μm thick Gold (Au) layer is deposited.

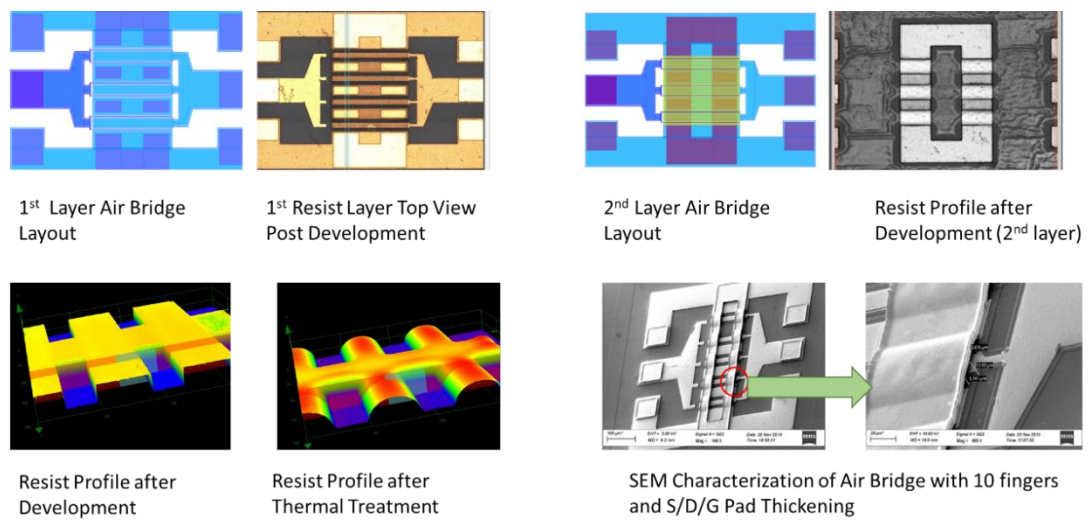


Figure 5.36: Air Bridge Fabrication Process Steps

After the seed layer deposition, again AZ 4620 resist is coating, mask-based photolithography, resist development followed by plating and lift-off are performed as a part of air-bridge fabrication. In second lithography, the span of the air bridge is defined and source, drain, gate pads are also opened for further thickening as shown in Figure 5.35 (e). After mask-based lithography, the sample is developed using AZ 400k developer. The sample is inspected and achieved profile is shown in Figure 5.35 (f). The descum O₂ Plasma followed by electroplating process is conducted on sample. The Au-Ni-Au metal scheme is selected for electroplating process. The total electroplated thickness is 4-6 μm. The final step for air bridge fabrication is metal lift off. However, it is not a conventional lift off process where an undercut is provided in the resist by lithography process.

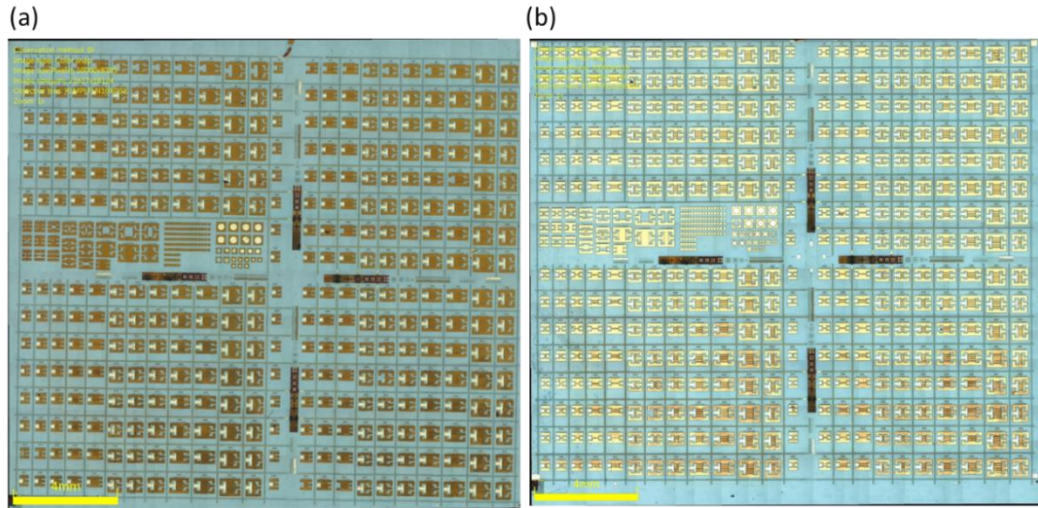


Figure 5.37: Typical image of wafer taken by confocal microscopy (a) before air-bridge fabrication and (b) after air-bridge fabrication

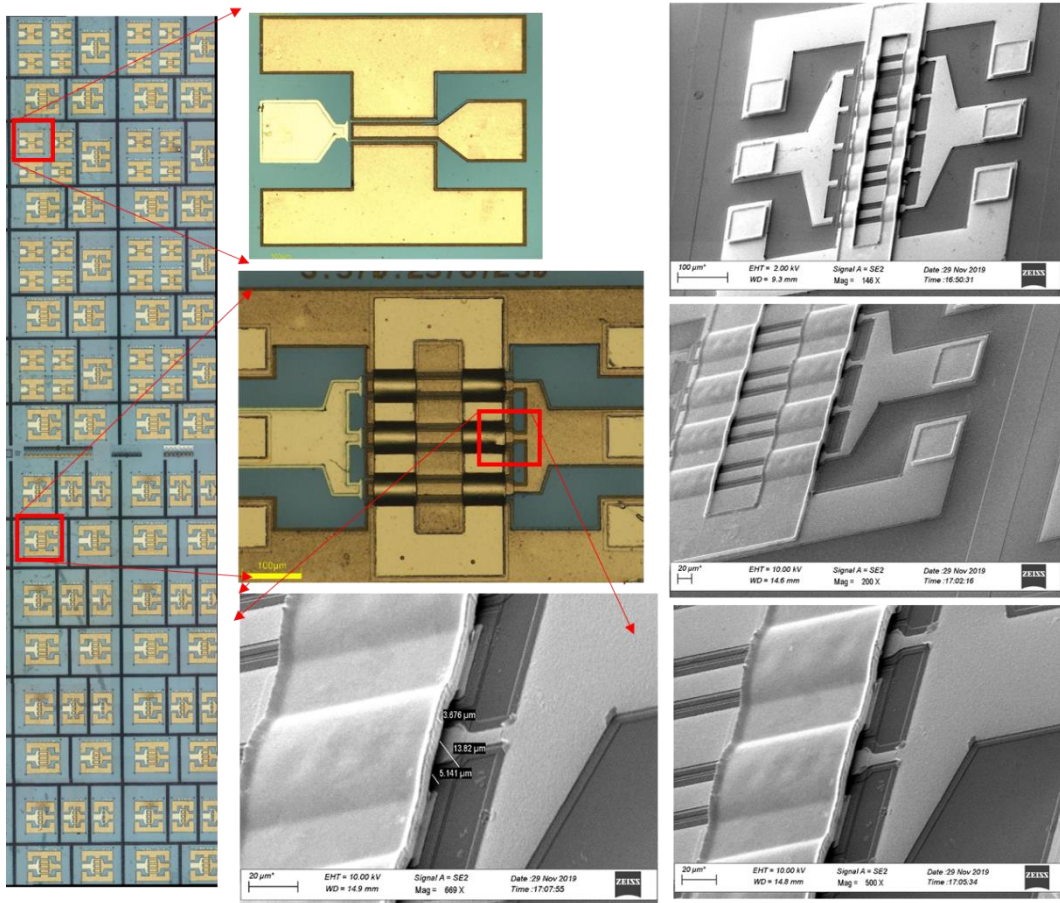


Figure 5.38: Typical portion of fabricated wafer along with zoom image of two finger and multi-finger GaN HEMT devices

In the air bridge development, the resist has got hardened due to various thermal treatments. Hence, the sample is kept in the resist remover i.e. acetone overnight and then intense ultra-sonication is provided for metal layer to break from unwanted areas. The complete air Bridge fabrication process flow along with sample images is shown in Figure 5.36. Typical image of wafer taken by confocal microscopy before and after air-bridge fabrication is shown in Figure 5.37. The zoom SEM images of few two-finger as well as multi-finger devices is depicted in Figure 5.38.

Device DC, RF and Power Measurements

In this part of the work, DC, RF, Breakdown and Power measurement of GaN HEMT will be presented. After the GaN HEMTs are realized, an investigation of device conventional performance in terms of DC, RF, breakdown and Power characteristics is discussed. Influence of fabrication processes on the device performance is analyzed. Optimization of auxiliary processes like passivation and pad thickening process and its influence on device performance is discussed in detail.

6.1 DC Measurement

Current-Voltage (IV) measurements on the fabricated sample are performed using a highly accurate and precise Keithley 4200 source measurement unit (SMU) inside a vacuum chamber equipped with a Janis probe station and Lakeshore temperature controller. The integrated measurement setup is shown in Figure 6.1 which is used for DC and breakdown voltage measurement. The surface traps have been present in GaN HEMT devices and lead to significant degrades DC and RF performance. High quality Si_3N_4 surface passivation deposition is used to effectively reduce surface traps. Contact pad thickening is essential to reduce resistive loss. As the Si_3N_4 passivation and contact pad thickening drastically change the device performance, the DC and RF performance of GaN HEMT device is measured before & after passivation as well as after contact thickening.

The variation of the drain current with respect to applied drain (V_d) and gate (V_g) biasing voltage is plotted in Figure 6.2. The measured output characteristics (I_d - V_d) and transfer characteristics (I_d - V_g) are shown in Figures 6.1 (a) and (b) respectively. The extracted transconductance is $> 350 \text{ mS/mm}$ as shown in Figure 6.1 (c).

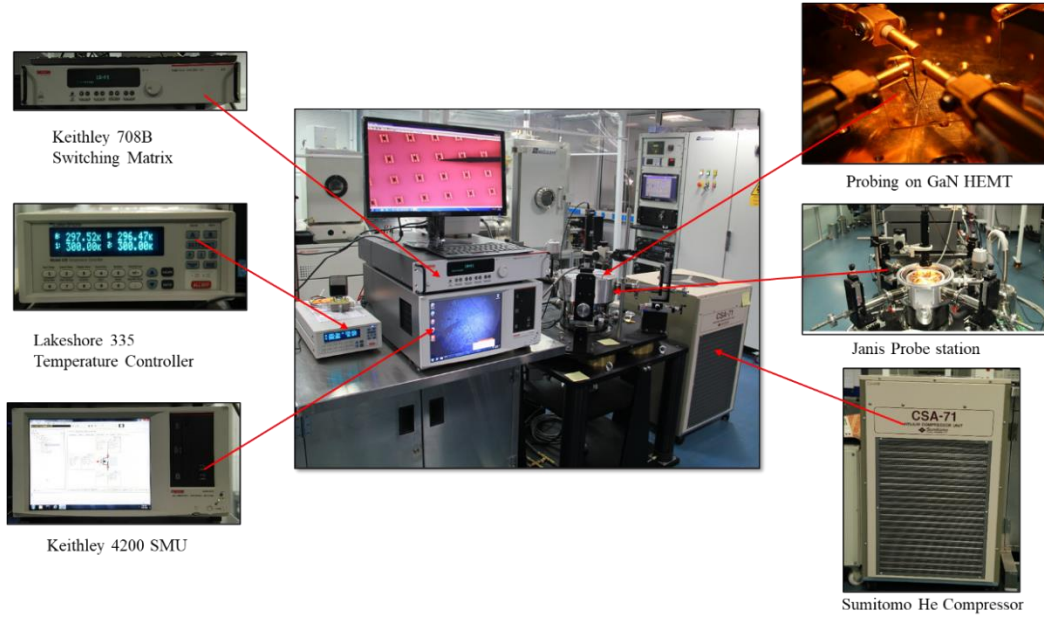


Figure 6.1: Semiconductor Device characterization set up for GaN HEMT DC and Breakdown measurement

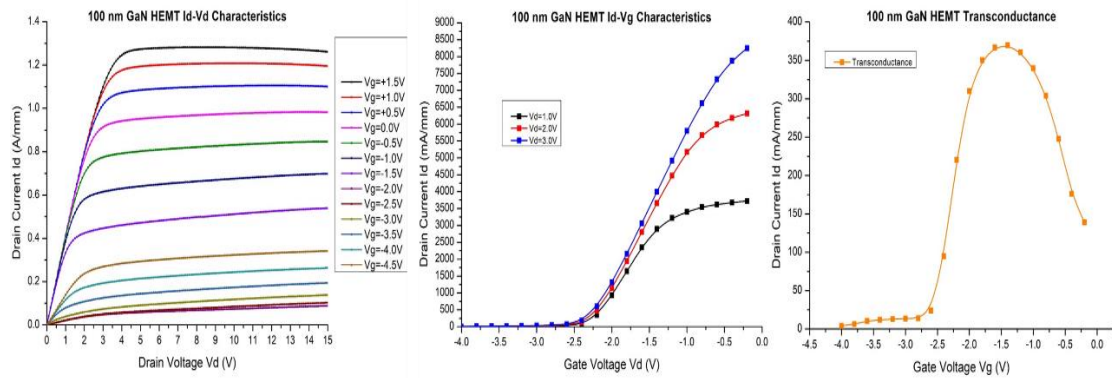


Figure 6.2: Measured 100 nm GaN HEMT (a) output characteristics (I_d - V_d), (b) transfer characteristics (I_d - V_g) and (c) transconductance

6.2 Breakdown Voltage Measurement

The breakdown (BD) voltage of GaN devices is much larger than those of conventional III-V semiconductors. Increased power handling capability is a direct result of large breakdown voltage and thermal conductivity and the fact that higher junction temperatures can be tolerated. Power devices operated at high drain voltages may show important breakdown processes. Breakdown consists in a rapid increase in drain

current, which occurs in the off-state when the drain voltage reaches a critical value. In order to tackle the breakdown issue of HEMT many investigations are carried out to understand its physical origin. Some of the relevant breakdown mechanisms in HEMT devices are as follows:

1. Source-drain breakdown: due to short-channel effects, and/or punch-through.
2. Gate-drain breakdown: due to the presence of relatively high breakdown current components at the gate, which can be either related to the leakage through the Schottky junction or to surface related conduction.
3. Vertical breakdown: due to heterostructure fabrication defects and trap related problems and can be limited by the adoption of suitable back barrier or heterostructure configurations.
4. Impact ionization: that may induce a significant increase in drain current due to the generation of electron-hole pairs close to the gate.

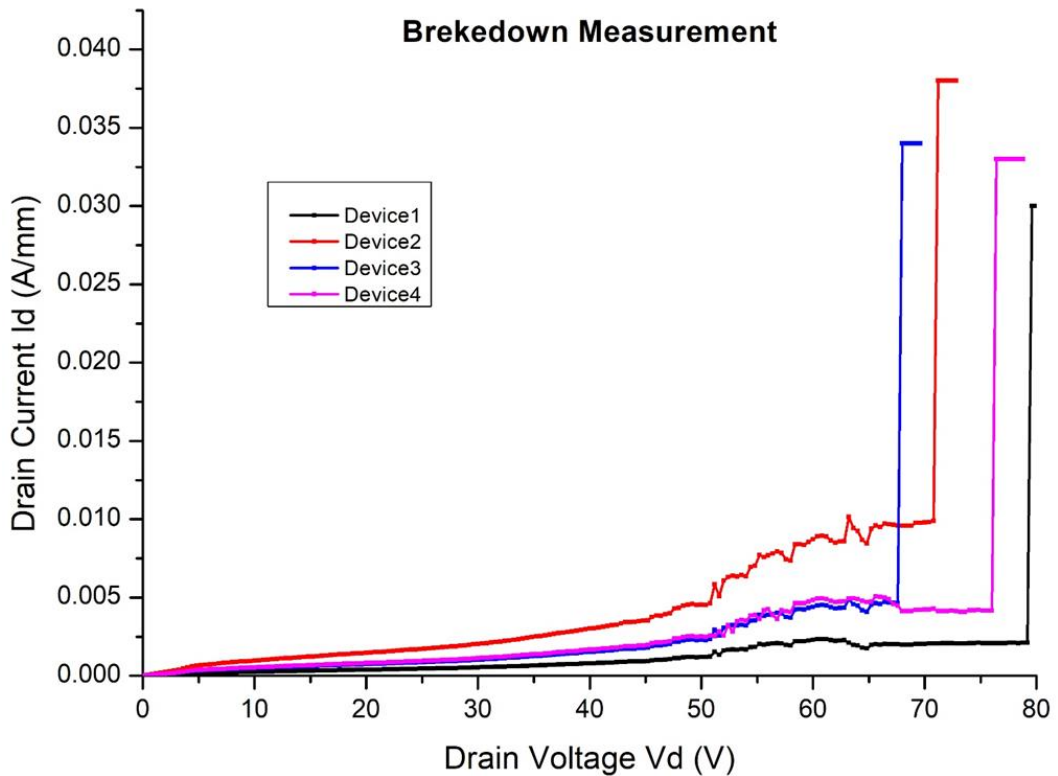


Figure 6.3: Breakdown voltage measurement on 100 nm GaN HEMT devices

Measurement Methodology

Four (04) geometrically different HEMT devices with the source-drain distance L_{SD} is $3.0\text{ }\mu\text{m}$ and the gate length of 100 nm are tested for breakdown measurement. The methodology for breakdown measurement is briefly described following.

The source of the HEMT device is grounded, while the compliance to drain current is set to 0.1 A and is forced to flow at a present level corresponding to off-state breakdown conditions. At the same time the gate-source is biased below pinch-off channel condition. Drain-source voltage was swept from 0 to 100 V . The measured drain-source voltage is used to evaluate the drain source breakdown voltage. The drain current is sharply increased as drain-source voltage reached to breakdown.

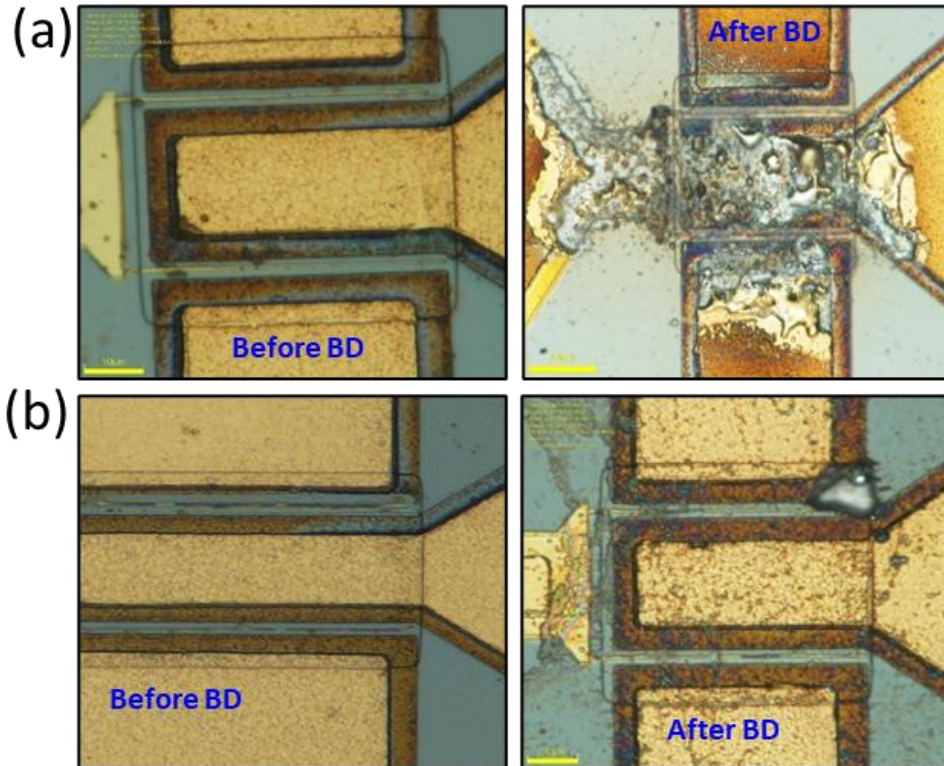


Figure 6.4: Optical image of HEMT before and after destructive breakdown of (a) Device 1 and (b) Device 4.

The breakdown measurement plot on four (04) GaN HEMT devices is shown in Figure 6.3. The measurement results are summarized in Table 6.1. The optical image of HEMT after destructive breakdown is shown in Figure 6.4 for device # 1 and #4.

Table 6.1: Summary of breakdown voltage measurement on 100 nm GaN HEMT devices

Sr No	Device Id	Breakdown voltage (V)
1	Device 1	81.2
2	Device 2	72.8
3	Device 3	69.6
4	Device 4	78.8

6.3 RF Measurement

The RF measurement of GaN HEMT devices is measured using the on-wafer measurement set -up. The setup includes the semi-automatic probe station, gate and drain prober and PNA (parametric network analyser) as shown in Figure 6.5. Extensive calibration and verifications of the setup are performed before each RF measurement to capture reliable measurement. On-Wafer S-parameter calibration is performed up to 80 GHz on the measurement setup. The calibration is done using two methods,

- Calibration using VNA (vector network analyser) calibration wizard – Short, Open, Load, Through, calibration on an ISS is performed in this method.
- Calibration using WinCal Software – WinCal software is used in conjunction semi-automatic probe station, to perform automated calibration. The calibration is then verified against known standards.

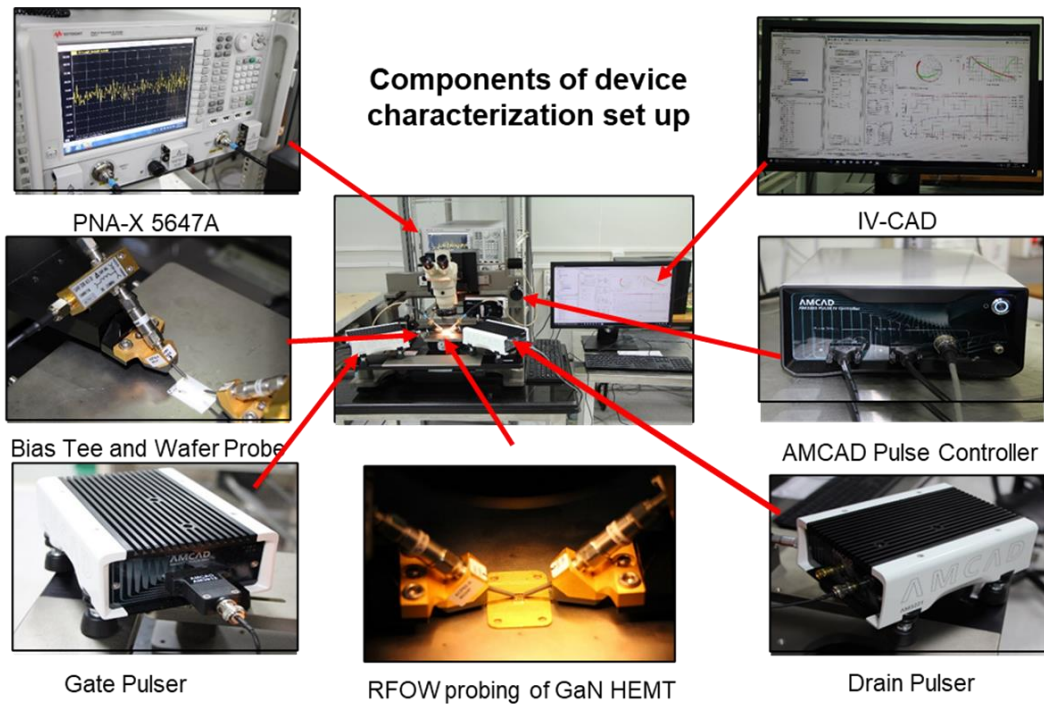


Figure 6.5: GaN HEMT RF and power measurement set-up

The V_g range varied from -4 to 0 V and V_d varied from 0 to 20 V in all DC measurements. RF frequency analysis of the GaN HEMT devices is based on the measurement and evaluation of scattering parameters (S-parameters). The S-parameters are related to traveling waves that are scattered or reflected when an n-port network is inserted into a transmission line. GaN HEMT is measured as a two-port network as shown in Figure 6.6 where the input port corresponds to gate-source and the output port to drain-source.

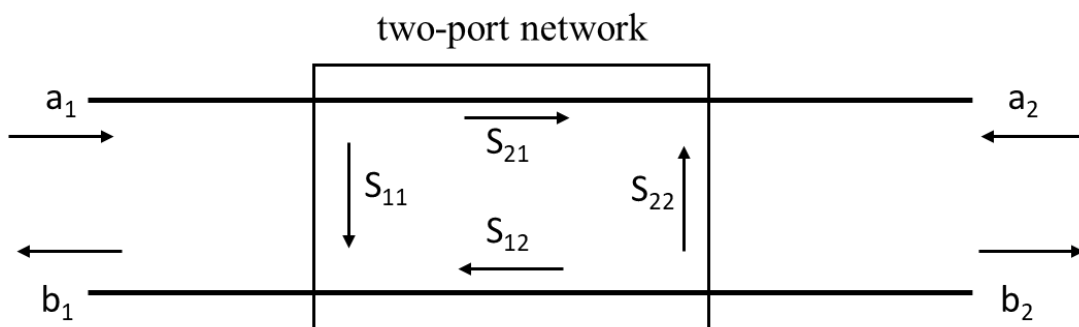


Figure 6.6: The two-port network indicating the incident and reflected voltages at the input and output, reflection coefficients at the input and output port, and s-parameters

S-parameters of two-port network at different conditions are given by [132],

$$\text{Reflection Coefficient at port 1: } s_{11} = \left. \frac{b_1}{a_1} \right|_{a_2=0} \quad (6.1)$$

$$\text{Forward voltage transfer ratio from port 1 to port 2: } s_{21} = \left. \frac{b_2}{a_2} \right|_{a_1=0} \quad (6.2)$$

$$\text{Reflection Coefficient at port 2: } s_{22} = \left. \frac{b_2}{a_2} \right|_{a_1=0} \quad (6.3)$$

$$\text{Reverse transfer ratio from port 2 to port 1: } s_{12} = \left. \frac{b_1}{a_2} \right|_{a_1=0} \quad (6.4)$$

Where, $a_{1,2}$ and $b_{1,2}$ is incident and reflected waves at input and output of the HEMT respectively. S-parameters are used to measure as the function of the frequency. As shown in eq (6.1) to (6.4), the S_{11} is called the input reflection coefficient, S_{12} the reverse transmission coefficient, S_{21} the forward transmission coefficient and S_{22} the output reflection coefficient.

The current gain (h_{21}) is calculated using the measured s-parameter by [132],

$$h_{21} = \frac{-2 s_{21}}{(1 - s_{11})(1 + s_{22}) + s_{21}s_{12}} \quad (6.5)$$

The current gain defines the extrapolation of $|h_{21}|^2$ versus frequency. The frequency corresponds to 0 dB current gain value leading to the current gain cutoff frequency f_T .

The Maximum unilateral gain (MUG) is extracted by using the measured s-parameter as follows [132],

$$G_{MUG} = |S_{21}|^2 \frac{1}{(1 - |s_{11}|^2)(1 - |s_{22}|^2)} \quad (6.6)$$

The first term in Equation 6.6 i.e. $|S_{21}|^2$ is related to the transistor forward transfer ratio and represents the power gain provided by the device. The $(1 - |S_{11}|^2)$ term is the power gain provided by the input circuit and represents the degree of mismatch between the characteristic impedance of the source and the input reflection coefficient. The $(1 - |S_{22}|^2)$ term represents the power gain provided by the output circuit and represents the degree of mismatch between the characteristic impedance of the drain and the output reflection coefficient. The maximum unilateral gain is reduced to $|S_{21}|^2$ by matching the power gain provided by the input and output circuit.

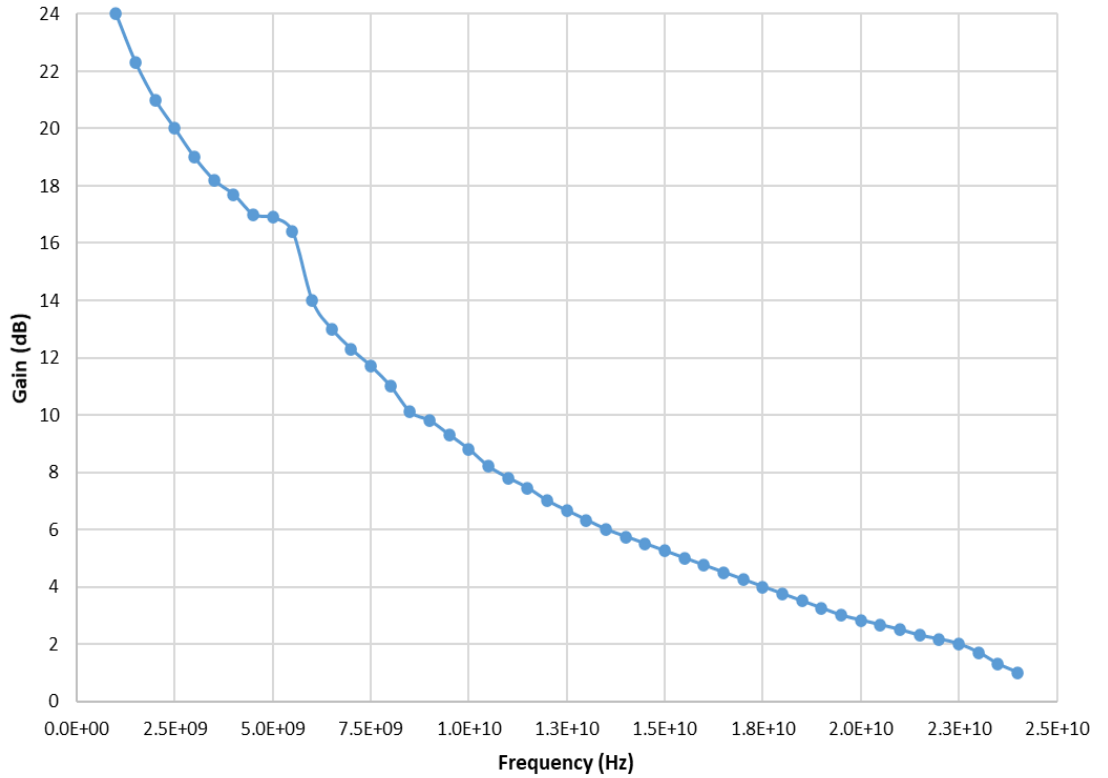


Figure 6.7: Measured current gain h_{21} parameters at different biasing conditions

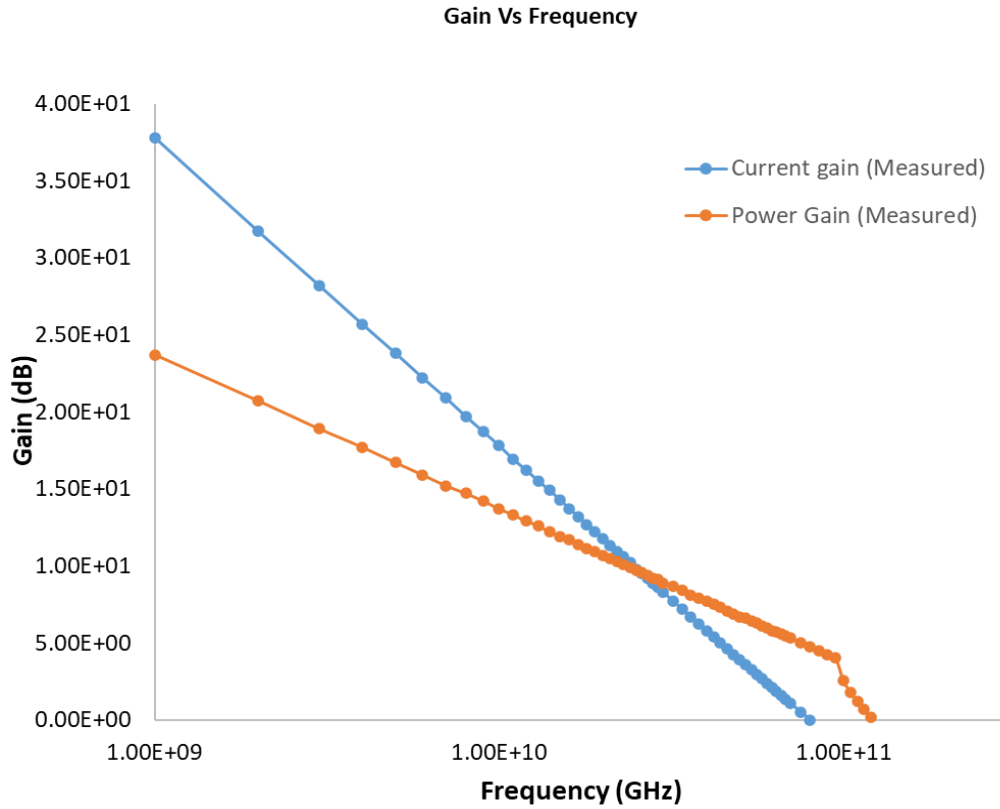


Figure 6.8: Measured current gain and power gain

Figure 6.7 shows the measured S-parameter at different frequency. Figure 6.8 shows the measured current gain and power gain plot against frequency. As discussed in chapter-5, device passivation and contact pad thickening make a significant influence on device DC and RF properties. Table 6.2 summarized the DC and RF parameters of the device before passivation, after passivation and after pad thickening of the device.

Table 6.2: Summary of DC and RF properties of device before passivation, after passivation and after pad thickening

Sr No	Process	Idss (A/mm)	Gm (mS/mm)	Ft (GHz)	Fmax (GHz)	MAG (dB) @ 15 GHz
1	Before passivation	825	283	81.8	115.2	10.43
2	After passivation	979	337	97.7	142.4	12.55
3	After thickening	1050	363	105	160	14.10

6.3 Power Measurement

GaN HEMTs are intended primarily for high power applications at high frequencies. The maximum power that can be expected from the drain circuit of device is given by [132]

$$P_{max} = \frac{I_{DSS}(v_{br} - v_{knee})}{8} \quad (6.7)$$

where I_{DSS} is the maximum drain current, V_{br} is the drain breakdown voltage and V_{knee} is the knee voltage.

The on-wafer power measurement has been done using the load-pull setup. The load-pull setup includes the source and load tuners to vary the input and output impedances for matching, DC power supply, vector network analyser and semi-automatic probe station as shown in Figure 6.5.

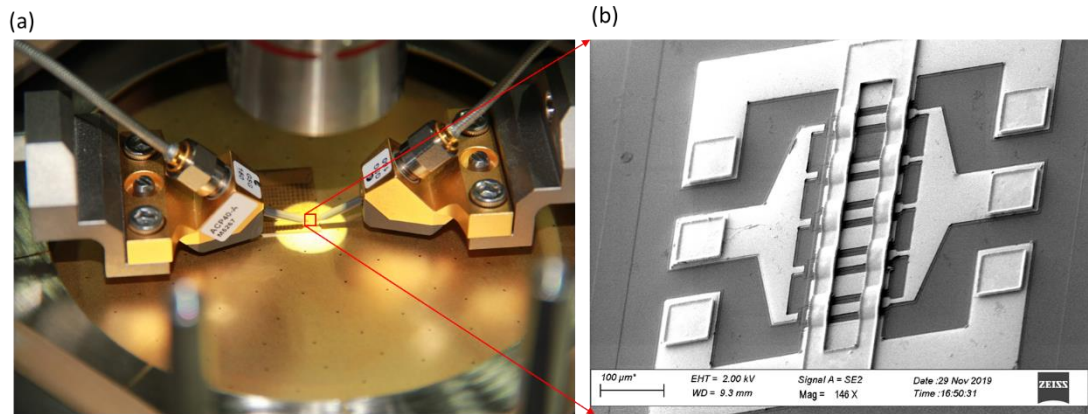


Figure 6.9: (a) GaN HEMT 1"x1" wafer mounted on measurement setup and (b) 10x100 GaN HEMT Device

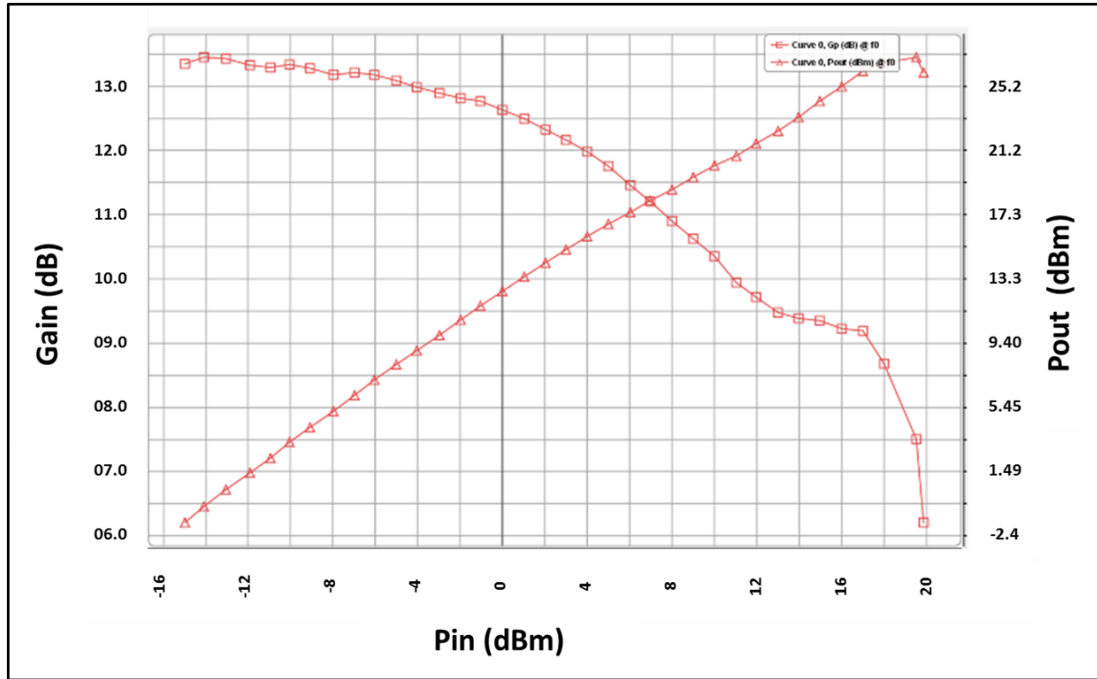


Figure 6.10: On device large signal gain and power measurement

Table 6.3: 100nm GaN HEMTs Power measurement Results (Two-fingers devices)

Sr No	Device Id	Device configuration	Idss (mA/mm) @ Vd=10V	Small signal Gain @ 15 GHz (dB)	Large signal linear Gain @ 15 GHz (dB)	Pout (mW)	Power Handling capability (W/mm)
1	145	2X50 (0.1 mm)	1200	11	10.2	128	1.28
2	229	2X50 (0.1 mm)	1180	11	10.7	140	1.4
3	265	2X50 (0.1 mm)	1190	14	13.3	130	1.3
4	97	2X50 (0.1 mm)	1150	10	9.3	110	1.1
5	218	2X100 (0.2 mm)	1250	11	10.2	240	1.2

Active Load pull and Source pull measurement is also performed on the devices, with second harmonic tuning, to generate power and PAE, contours over the entire unit radius Smith chart. Figure 6.9 (a) shows a fabricated GaN HEMT 1”x1” wafer mounted on a measurement setup. Figure 6.9 (b) shows the magnified view of a fabricated 10 fingers 10X100 GaN HEMT device. The large signal power measurement result of 10x100 GaN HEMT device at 15 GHz frequency appears in Figure 6.10. The

measurement results of different two-finger and multi-finger devices are listed in Table 6.4 and 6.5 respectively.

Table 6.4: 100nm GaN HEMTs Power measurement Results (Multi-fingers devices)

Sr. No	Device Id	Device configuration	Idss (mA/mm) @ Vd=15V	Small signal Gain @ 15 GHz (dB)	Large signal linear Gain @ 15 GHz (dB)	Pout (mW)	Power Density (W/mm)
1	222	6X50 (0.3 mm)	1257	12.1	11.5	456	1.52
2	247	8X100 (0.8 mm)	1125	13.65	12.9	1240	1.55
3	252	10X100 (1 mm)	1050	13.3	14.1	1610	1.61
4	272	6X150 (0.9 mm)	1111	12.8	12.9	1458	1.62
5	246	8X50 (0.4 mm)	1100	13.7	14.0	657	1.64

Table 6.5: Summary Simulated and measured DC, breakdown, RF and power device parameters

Sr No	Device Parameters	Simulated	Measured
1	Idss (A/mm)	0.995	1.05
2	Vknee (V)	5	5.3
3	Ron (ohm*mm)	3.5	3.5
4	Vth (V)	-3.0	-2.9
5	gm (mS/mm)	384	363
6	Breakdown voltage (V)	97.9	81.2
7	ft (GHz)	110	105
8	fmax (GHz)	180	160
9	Power Gain @ 15 GHz (dB)	15.8	14.1
10	Power Density (W/mm)	1.8	1.61

The DC, breakdown, RF and Power measurement device results along with simulated results are listed in Table 6.5 which are closely matching with the corresponding process design kit (PDK) datasheet of renowned international GaN foundries [11].

Terahertz Intersubband Transition Measurement

This chapter introduces ISB transition at ambient temperature as a potential mechanism for terahertz response of the GaN HEMT device. ISBT is demonstrated using IV measurement of GaN HEMT device under dark and illumination base conditions. Usually, it is highly difficult to claim ISBT in HEMT by studying IV characteristics. It is very difficult to distinguish the defects or traps assisted transitions, thermal transitions and ISBTs in the IV characteristics of FET. To confirm the transition is solely dependent upon the bandgap phenomenon, low-temperature photoluminescence (PL) and IV measurements of GaN HEMT are also carried out. Furthermore, to extract the true signatures of intersubband energy levels, non-destructive low temperature photoluminescence (PL) method is used. The temperature and excitation power dependent PL measurement make it easily identify the transitions from 2DEG subbands to valence bands.

7.1 Introduction

FET is showing the response towards terahertz beyond its cutoff frequency even at room temperature irrespective of semiconductor materials systems [13, 15-19]. Dyakonov–Shur plasma wave theory [13, 14] classically explained the terahertz behavior of the device starting from conventional semiconductor Si, GaAs, GaN to recently developed 2D materials system like Graphene, MoS₂, WS₂, black phosphor, etc. We proposed in this chapter, other than plasma wave, ISB transition at ambient temperature as another potential mechanism for terahertz response of the GaN HEMT device. ISBT is demonstrated using IV measurement of GaN HEMT device under dark and illumination base conditions. Usually, IV characteristics are the combination of all possible phenomenon in the FET. It is very difficult to distinguish the defects or traps assisted transitions, thermal transitions and ISBTs in the IV characteristics of FET. The

electrical tuning of ISBT in GaAs HEMT has been demonstrated [133]. There are three following key challenges involved to support the ambient ISBT mechanism in FET/HEMT.

1. Rule out Plasma wave mechanism
2. Defects/traps-based transitions
3. Thermal energy assisted transitions

7.2 Rule out Plasma wave mechanism

The basic physics involved in plasma wave theory is the 2DEG instability in short channel HEMTs has a resonant response to incident electromagnetic radiation. The resonance frequency is governed by the size and shape of the channel, i.e., the geometrical plasmon frequency. Tuning the plasmon resonant frequency to the incident THz wave is used for detectors, mixers and multipliers types of devices. As the carrier resonance happens in terahertz frequency range only. It is not possible to generate plasma wave inside the FET channel, if the incident radiation is having a frequency other than terahertz. In other words, if we are using the source other than terahertz radiation source which is capable to induce the ISBT, the generation of plasma waves can be ruled out inside the FET/HEMT.

7.3 Defects/traps-based transitions

The deep level traps or defects assisted transitions have been well reported since the invention of heterostructure [134]. The traps energy level and density depend upon several parameters like heterostructure growth condition, materials system, etc. Especially in GaN based wide bandgap semiconductor materials, the domination of the deep level traps is even more significant than GaAs semiconductor material [135]. It is highly difficult to prevent the transitions through these traps. However, control over traps-based transition is possible as it is showing the different responses toward the incident radiations. If we are selecting the illumination source that has the least

significant for trap excitation and most significant for ISBT, then defects/traps assisted transitions can also be ruled out.

7.4 Thermal energy assisted transitions

The thermal energy associated at room temperature is ~ 25 meV (~ 6 THz) which is much higher than the spacing between the subband in quantum well. It is very difficult to neglect the thermal energy contribution. Thermal occupation of electrons in higher subband may prevent the observation of ISB transition at ambient temperature [133]. Control over thermal transitions, measurement is done at ambient as well as low temperature in vacuum condition with very high precise and accurate temperature controller. Furthermore, Source-Measurement units (SMUs) are very accurate to detect very small changes in measurement for dark and illumination conditions. As the background thermal energy contribution in transitions are equally present in dark and illumination mode which clearly indicates the presence of ISBT in the measurement.

Table 7.1: Measurement methods and excitation sources used to confirm ISBT

Sr No.	Discrimination ISBT from other mechanism	Used excitation source/methods
1	Plasma wave mechanism	Non terahertz radiation source
2	Defects/traps induced transition	Blue LED
3	Thermal energy contribution	Measurement in vacuum, precise temperature control with highly accurate SMUs Confirm with low temperature IV and PL
4	ISBT	SWIR (1.7-2.1 μm) source

To confirm the transitions, solely happen due to ISB inside the triangular quantum well of the heterostructure, 1 mW SWIR light emitted diode (LED) is used as it is least significant for traps excitation [136, 137], while found most significant for ISBT. Moreover, the use of a SWIR source that is not in the terahertz frequency range ensures that the generation of plasma wave inside the channel is not possible. Blue LED

is selected for traps assisted transitions measurement. Table 7.1 summarized the key challenges involved with its possible solution to confirm the room temperature ISBT in GaN HEMT.

To excite the deep levels traps in GaN heterostructure, 1 mW blue, yellow and red LEDs, as well as 300W halogen lamp-based perpendicular illumination have been used. It is well proven that as move from NIR to UV radiations, the traps excitation becomes more efficient. The excitation of traps in GaN heterostructure above 870 nm is highly difficult [136, 137]. In our experiments also, blue LED is founded more efficient among all used light sources to excite the deep level traps. 90° angle of incident (AOI) for 10-minutes blue LED illumination condition is kept to extract the trap assisted transitions. The Id-Vd characteristics and change in drain current (ΔId) of 100 nm GaN HEMT without and with illumination are shown in Figure 7.1 (a). Deep level traps assisted transitions raised the drain current approximately up to 24 mA/mm as shown in Figure 7.1 (b). It is founded that after 10 minute illumination, there is no further significant increase in drain current which confirms that the majority of traps are saturated and equilibrium condition has reached.

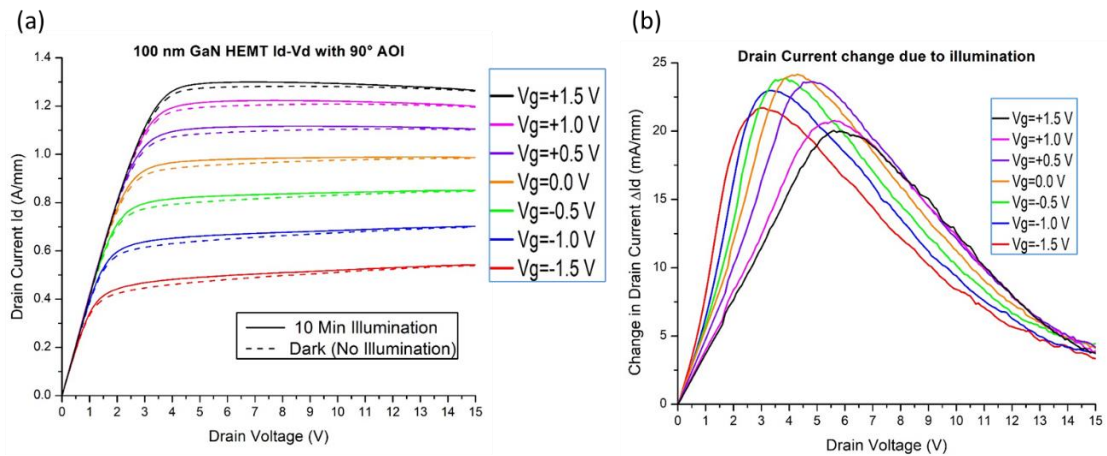


Figure 7.1: Effect of 90° AOI illumination with Blue LED (a) on Id-Vd characteristics of 100 nm GaN HEMT Device (b) change in drain current

Red laser (630-690 nm), NIR LED (650-850 nm) and SWIR LED (1.7-2.1 micron) broadband infrared sources are used in experiment to investigate other physical

phenomena than plasma wave at ambient temperature. It is noted that the ISB absorption characteristics are founded identical for all used IR sources (red laser, NIR and SWIR LEDs) with the highest absorption found for SWIR LED. Hence, for ISBT experiments, 1 mW SWIR LED is selected as it is least significant for traps excitation [136, 137], while most significant for ISBT. GaN heterostructure materials having a wide bandgap with lower cut-off wavelengths than the wavelength of IR light source, ensuring the transition of the carriers from valance band to the conduction band is forbidden.

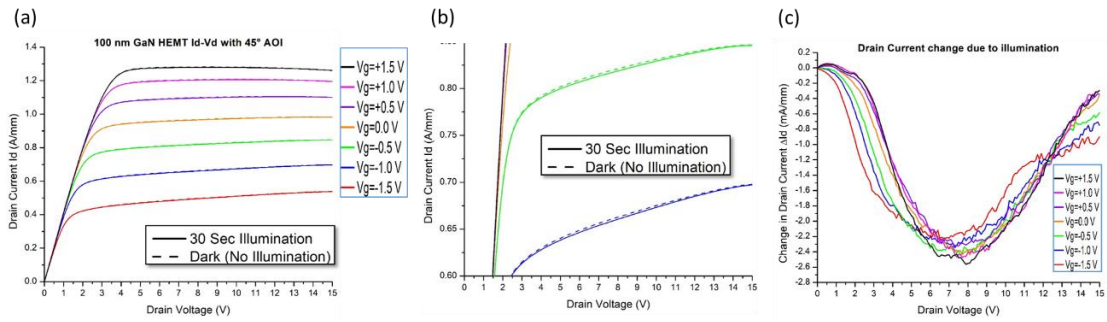


Figure 7.2: Effect of 45° AOI illumination with SWIR led (a) on I_d - V_d characteristics of 100 nm GaN HEMT Device (b) zoom portion of I_d - V_d characteristics for drain current change visualization and (c) change in drain current

As we discussed in chapters 2 and 3, when light is incident perpendicular to the sample surface ISBT cannot be induced, as the electric field has component only in the quantum well plane [67, 138]. The sample is illuminated at an oblique angle of incidence in order to discriminate ISBT with other transitions. When the sample is illuminated with oblique angle, IR radiation interacts with carriers inside the subband of triangular quantum well and transitions happened within the conduction band. The I_d - V_d characteristics and change in drain current (ΔI_d) of 100 nm GaN HEMT without and with 30 sec 45° AOI SWIR LED illumination is shown in Figure 7.2 (a) and 7.2 (c). A zoom portion of the I_d - V_d curve for -0.5 and -1.0 gate voltage is shown in Figure 7.2 (b) for visualization purposes, as the change in drain current is very small due to illumination. Infrared lamp-assisted photoinduced ISBT in doped and undoped multiple quantum well is reported by Olszakier et al. in series of experiments [139-143]. It was concluded that the ISBT involves free electrons as well as excitons. The exciton-based

transitions have higher frequency and oscillator strength than those of the bare electrons.

Triangular quantum well band diagram along with the two E_0 and E_1 subband inside the well involves free electrons transition and excitons based transition as shown in Figure 7.3 (a). In the asymmetrical (triangular) quantum well, inversion symmetry with respect to the quantum well center is broken which leads to a relaxation of the selection rules i.e., transitions between all subband are allowed [138]. The spacing between subband and quantum well width is depending upon gate biasing. Let us consider only two subband E_0 and E_1 inside well having N_0 and N_1 electrons respectively as shown in Figure 7.3 (b). The gate voltage is selected in such a way where ground state E_0 is situated below the fermi level as shown in Figure 7.3 (a). The 2DEG carriers below the Fermi energy level are extracted as a drain current by applying a potential between source and drain. When the sample is illuminated, the electrons in a ground state E_0 interacts with an external electromagnetic field. The electrons pick up photons from the illuminating field, which allows it to enter an excited energy state E_1 within the subband as shown in Figure 7.3 (c). These excited electrons are in the energy level E_1 that is above the Fermi level. As these electrons are not contributed to conduction, the drain current I_d is decreased. It is possible to tune subbands inside the quantum well by external electrical field in HEMT device. Free electrons-based ISBT (0.5 to 10 THz) and excitons-assisted ISBT (for higher frequency) can be exploited as potential tunable source and detector for the entire terahertz range.

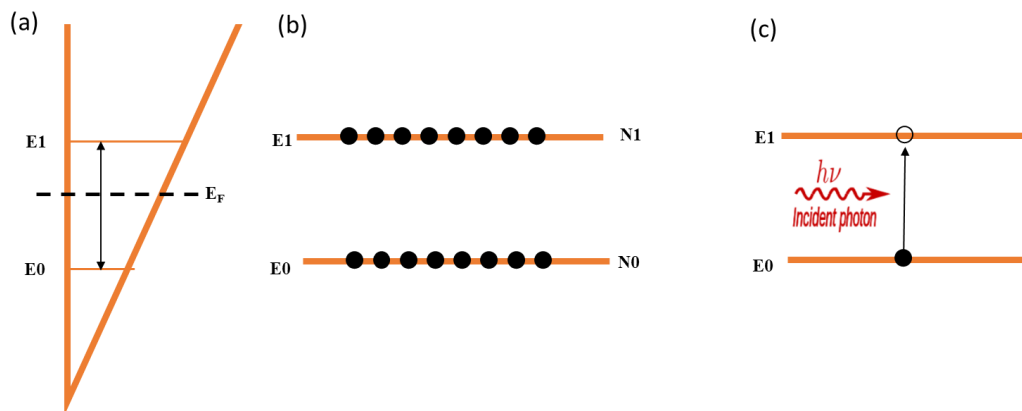


Figure 7.3: (a) Band-schematic of the first two subbands in a 2DEG with respect to the Fermi level (b) carrier distribution in two subband and (c) absorption in the subband.

This mechanism is clearly observed in Figure 7.2 (c) in terms of decrease in drain current due to illumination which shows ISB absorption. The amount of absorption is strictly depending upon the distribution of electrons in the subband, spacing between subband and width of well. To rule out thermal energy contribution in IV characteristics, measurement is done in vacuum conditions with ambient and low temperature environment. The precise and accurate temperature controller and SMUs are used in measurement which able to detect a very small change in drain current in dark and illumination conditions.

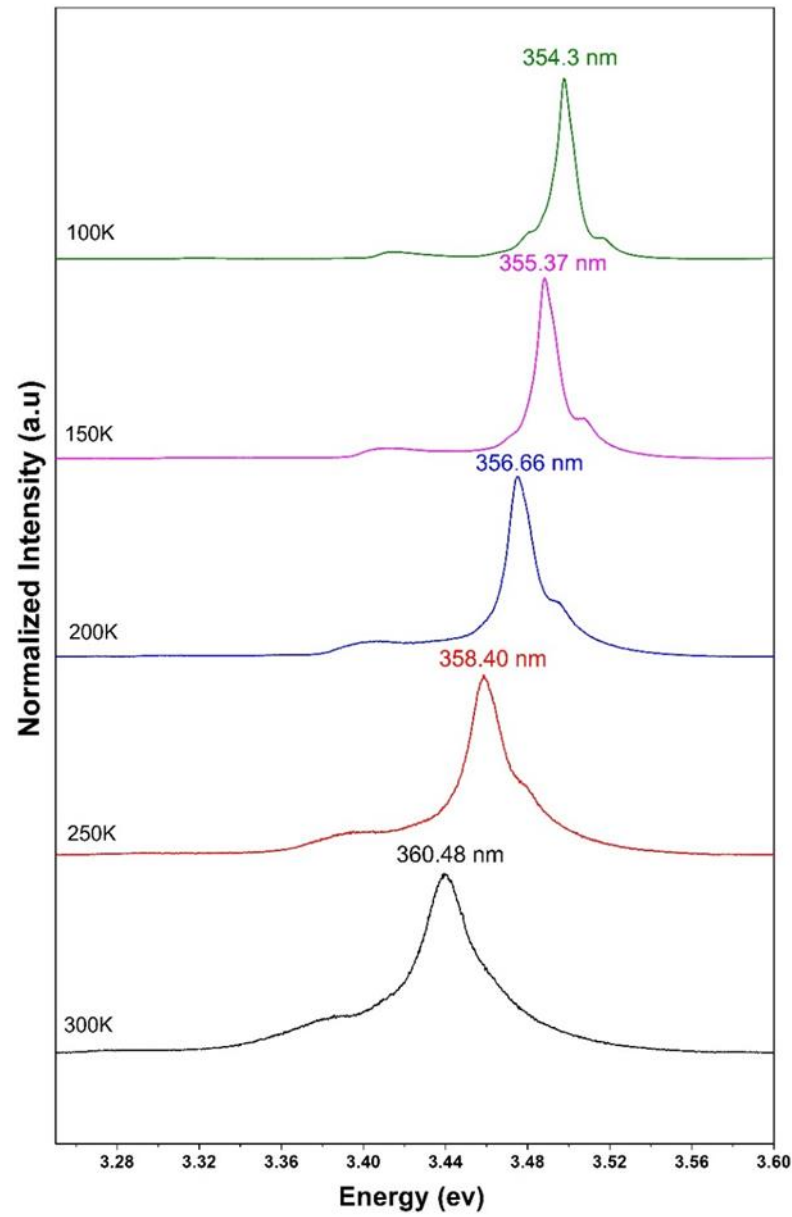


Figure 7.4: Low-temperature PL measurement of GaN heterostructure

Moreover, in order to confirm the transition is solely dependent upon the bandgap phenomenon, low-temperature PL and IV measurements are carried out. The temperature dependent bandgap shifting in GaN found in PL measurement as shown in Figure 7.4 and was matching with previously published result [144].

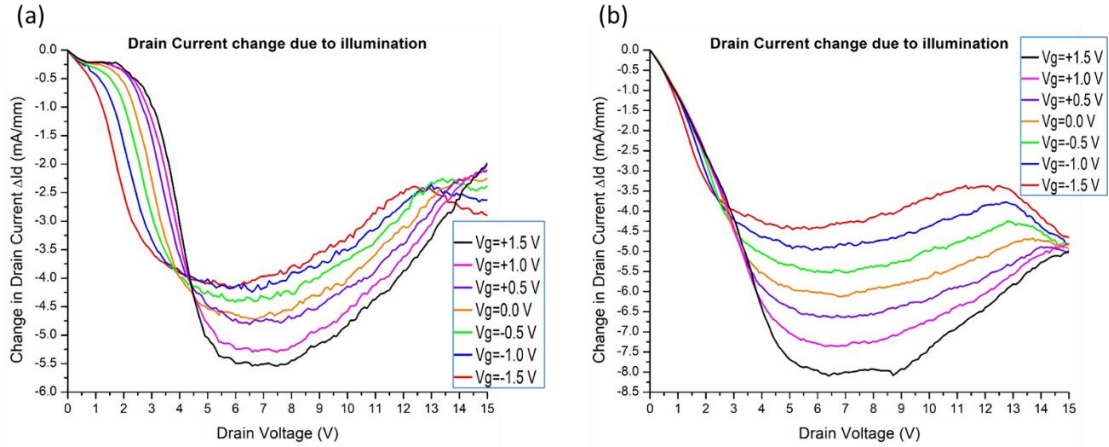


Figure 7.5: Change in drain current due to 45° AOI and 30 second illumination with SWIR LED at temperature (a) 200 K and (b) 100 K

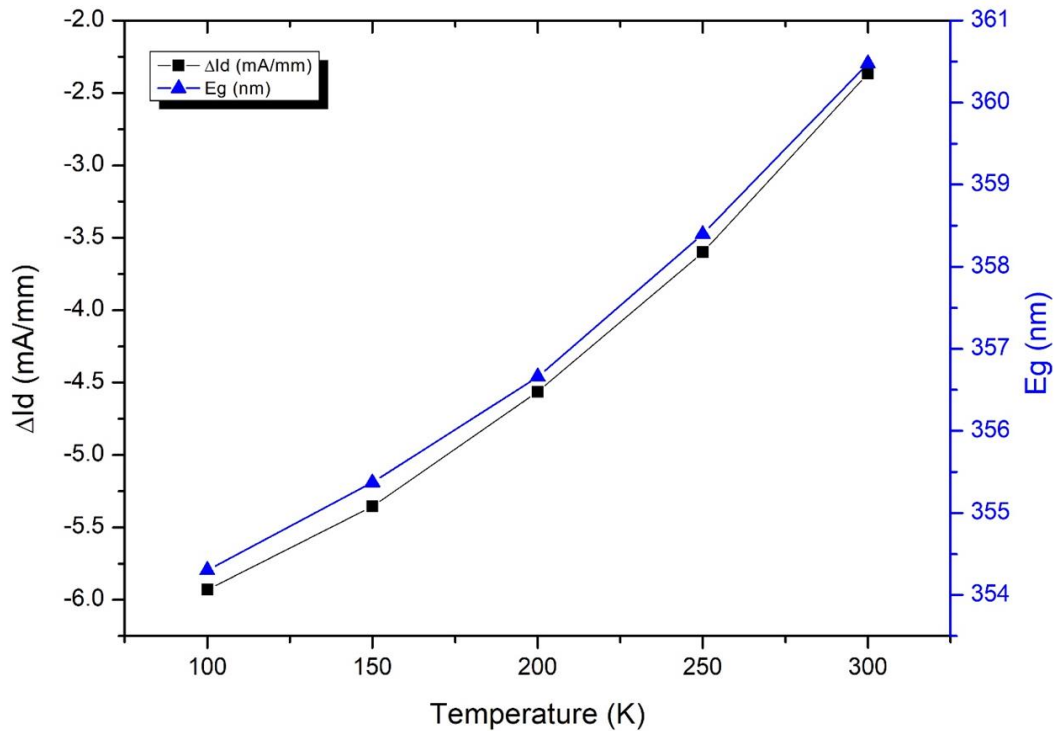


Figure 7.6: Temperature dependent GaN bandgap and change in drain current ($V_g=0$ V and $V_{ds}=8$ V) due to illumination

Low temperature 200K and 100K ISB absorption measurements are also carried out. It is found that the intensity of absorption increases as the temperature decreases as shown in Figure 7.5 (a) and (b). It indicates that thermal energy contribution decreases with a decrease in temperature. The temperature dependent bandgap variation in GaN is perfectly matching with ISB absorption ($V_g=0V$, $V_{ds}=8V$) as depicted in Figure 7.6.

In conclusion, low temperature and angle-dependent illumination-based measurements are used to confirm the ISB transition in GaN HEMT. We have experimentally explored electrical tuning of ISB resonance phenomena inside the triangular quantum well for GaN HEMT device which shows the potential of GaN HEMT technology to realized room temperature terahertz source and detector.

7.5 Optical transitions in GaN

Optical transitions in semiconductors can be classified into two categories, intrinsic and extrinsic transitions. Intrinsic transitions are those that are associated with semiconductors void of impurities and defects. Free excitons and their phonon replicas and free-to-free band transitions represent intrinsic transitions. Impurity-bound excitons, transitions involving impurities such as free-to-bound and bound-to-bound, and defects constitute extrinsic transitions.

Excitonic transitions in GaN

Excitons are classified into free and bound excitons. Wurtzite (Wz) structures are more interesting because of the splitting of the valence band by the crystal field and spin-orbit interactions. Bulk wurtzite band structure of GaN having three free excitons, A, B, and C as shown in Figure 7.7. In high-quality samples with low impurity concentrations, the free excitons can also exhibit excited states, in addition to their ground-state transitions.

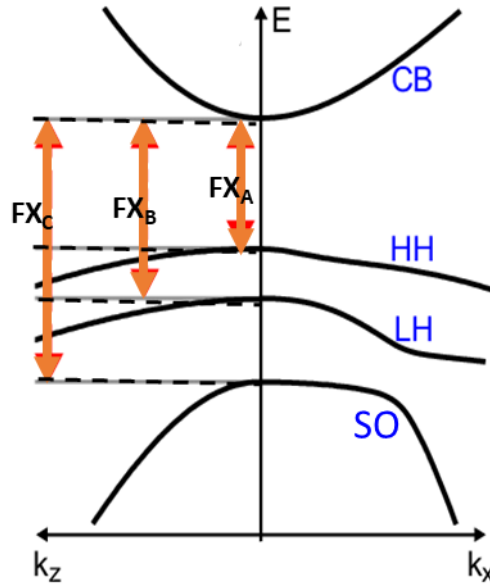


Figure 7.7: Band structure for wurtzite (WZ) bulk semiconductor with Conduction band (CB), heavy-hole (HH), light-hole (LH) and crystal field split off band (SO)

The three emerging states of valance band are termed heavy-hole (HH), light-hole (LH) and crystal field split off band (SO). The related free exciton transitions from the conduction band to these three valence bands are termed FX_A , FX_B , and FX_C excitons. They are FX_A referred to as the heavy-hole state, FX_B the second one referred to as the light-hole state and FX_C the lower one referred to as the crystal field split band.

A bound exciton (BE) is defined as an excited multiparticle state of a defect. Extensive literature on studies of bound excitons in semiconductors is founded. [145-147]. The electronic structure of neutral donor-bound excitons (DBEs) and acceptor-bound excitons (ABEs), is schematically shown in Figure 7.8. The DBE has three interacting particles consist of two electrons and one hole, while ABE has two holes and one electron. The neutral donor-bound excitons (DBEs) and acceptor-bound excitons (ABEs) is denoted by D^0X and A^0X respectively. These two classes of BEs are the most important cases for direct bandgap materials. A different class of BEs are those bound to neutral, where the excited state has two particles (one electron and one hole). The latter BEs are less prominent in direct bandgap materials. The schematic representation of Intrinsic and extrinsic optical transitions that occur in response to an above bandgap excitation in GaN is shown in Figure 7.9.

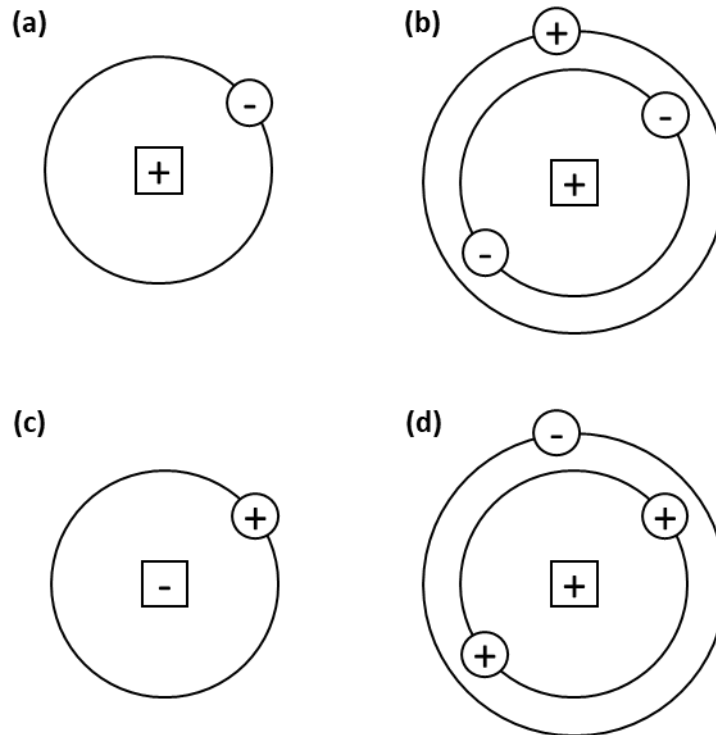


Figure 7.8: Schematic of (a) the neutral donor ground state, (b) neutral donor bound exciton state, (c) the neutral acceptor ground state and (d) the neutral acceptor bound exciton state. (Reprinted with permission from Semiconductors and Semimetals. Vol 50 (1998) Academic Press, Inc)

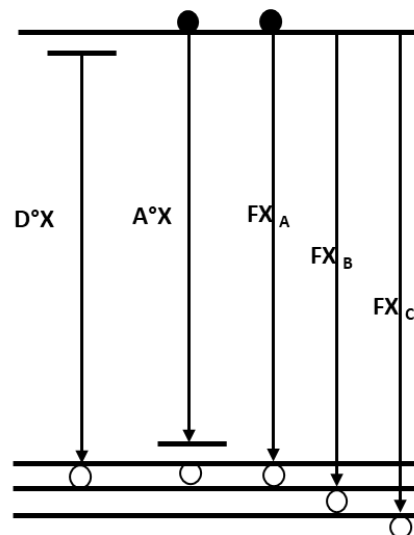


Figure 7.9: Intrinsic and extrinsic optical transitions that occur in response to an above bandgap excitation in GaN.

For the PL measurements, the GaN sample is mounted in a continuous close cycle He-flow cryostat. The temperature is varied from ambient to 5 K and He–Cd ultraviolet laser operating at 325 nm is used for the optical excitation. The luminescence light is detected through a 500 mm monochromator equipped with a cooled charge-coupled device Andor IDUS CCD detector (Model: DU 420BV) using the conventional lock-in technique.

Figure 7.10 shows the Photoluminescence spectra of only GaN buffer layer grown on SiC wafer. The luminescence is dominated by donor bound-exciton line (D^0X), the free excitons transitions (FX_A) and (FX_B). Such assignments of peaks are based on a prior work [148, 149].

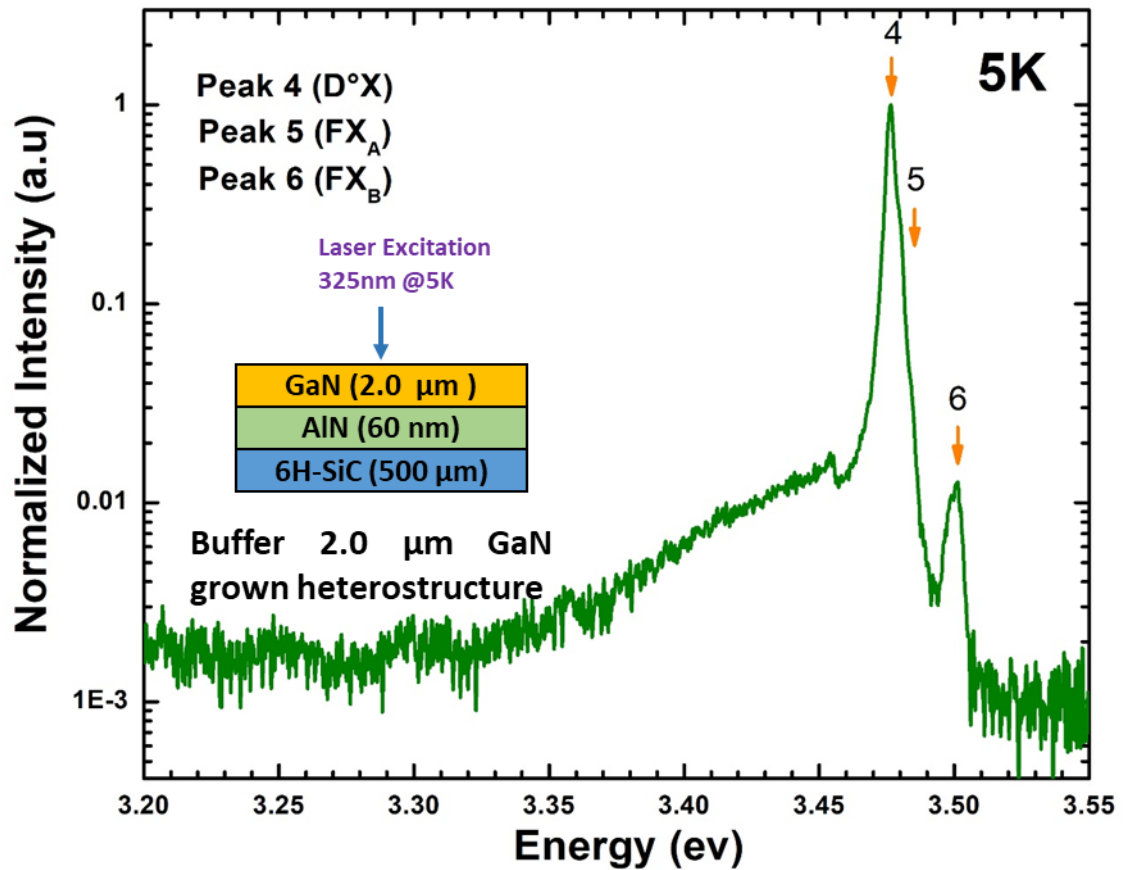


Figure 7.10: Low temperature (5K) PL measurement of 2.0 micron GaN buffer layer grown on SiC wafer

7.5 Optical transitions in GaN Heterostructure

GaN heterostructures are widely used in high-performance devices, like optical emitters and detectors or electronic devices such as HEMTs and HBTs. The band discontinuities, dopant and carrier redistribution are the salient parameters in the traditional compound semiconductors heterostructures. In the GaN heterostructure, an additional parameter polarization comes into play. Furthermore, carrier localization due to potential fluctuations plays an important role in carrier dynamics and eventual the device operation.

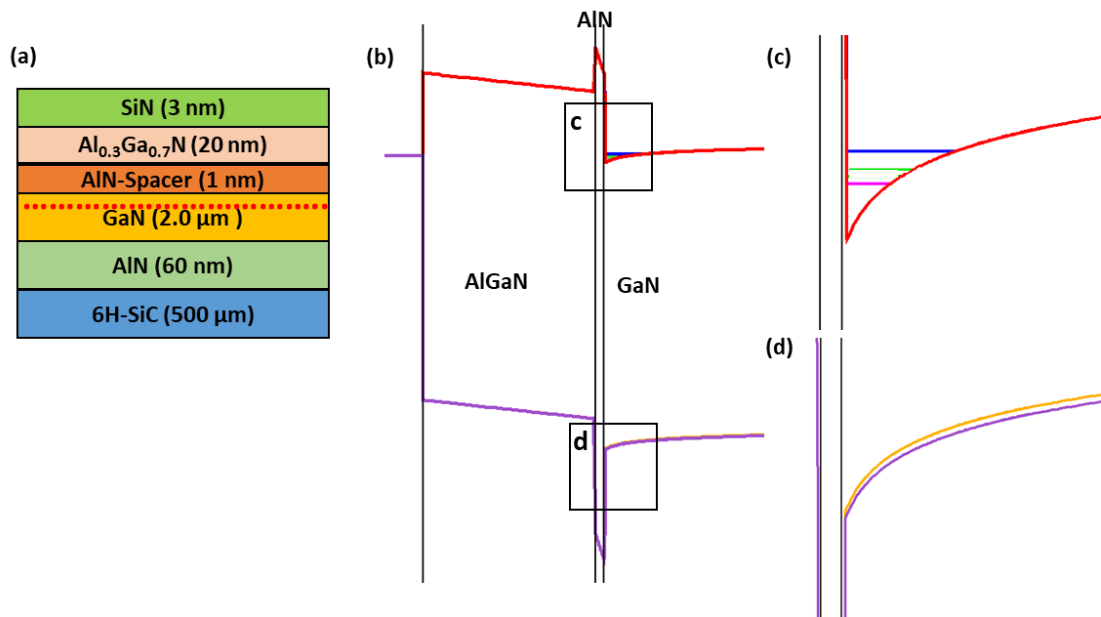


Figure 7.11: (a) GaN heterostructure, (b) Simulated Band structure of AlGaN/AlN/GaN heterostructure, (c) zoom portion of triangular quantum well in conduction band and (d) zoom portion of valance band with light & heavy holes (HH, LH) splitting

The schematic of GaN heterostructures along with layer sequence, thickness and composition is depicted in Figure 7.11 (a). The entire AlGaN/AlN/GaN heterostructure is simulated by solving self-consistent equations of physical processes at every grid point using Advance Silvaco Atlas TCAD device simulation software. The key models employed in the device simulation include polarization models, Caughey

Thomas mobility models, continuity equations and transport equations. In order to precisely calculate the Hamiltonian of the system, calculation started with the formulation of band structure based on the k·p method for wurtzite semiconductor for the conduction band nonparabolicity. The strain effect on the dispersion relation of direct gap semiconductors is considered through multiband k·p model for every material of heterostructure. Developed k·p model is applied to heterostructures structures particularly triangular quantum well via envelope function approximation method. The finite element method is used to solve the coupled multiband Schrödinger Poisson's equation. In the calculation electron effective mass is kept 0.23 m_e which is extracted through measured SdH oscillation in high magnetic field measurement, a conduction band offset kept 2.09 eV between GaN and AlN. The concentration of the electrons in the 2DEG is kept experimentally measured 1.09×10^{13} . Simulated band diagram for the heterostructure is shown in Figure 7.11 (b). The band bending zoom portion at interface for conduction band and valance band are shown in Figure 7.11 (c) and (d) respectively. The extracted three sub-band energy levels inside the triangular quantum well are also depicted in Figure 7.11 (c).

Figure 7.12 shows the temperature dependent PL spectra of GaN heterostructure from ambient temperature to 5K. The luminescence is dominated by donor bound-exciton line (D^0X) at low temperatures, while the free excitons FX_A and FX_B are dominated at higher temperature [150].

The low temperature (5K) PL spectra along with expected recombination features of the sample is depicted in Figure 7.13. The PL spectra are dominated by donor bound excitonic transition (D^0X) at 3.454 eV label as peak #4, which is generally observed in the low temperature PL spectra of GaN epitaxial layers [151, 152]. The free excitons feature label as Peak #5 (FX_A) and peak #6 (FX_B) are also observed as shown in Figure 7.13 [143, 144]. Peak labeled as #4, #5 and #6 corresponds to donor bound-exciton line (D^0X), the free excitons transitions (FX_A) and (FX_B) are identical with buffer GaN layer PL spectra as shown in Figure 7.10. The free A excitons (FX_A) and free B excitons (FX_B) are located at 3.471 eV and 3.492 eV respectively about 17 and

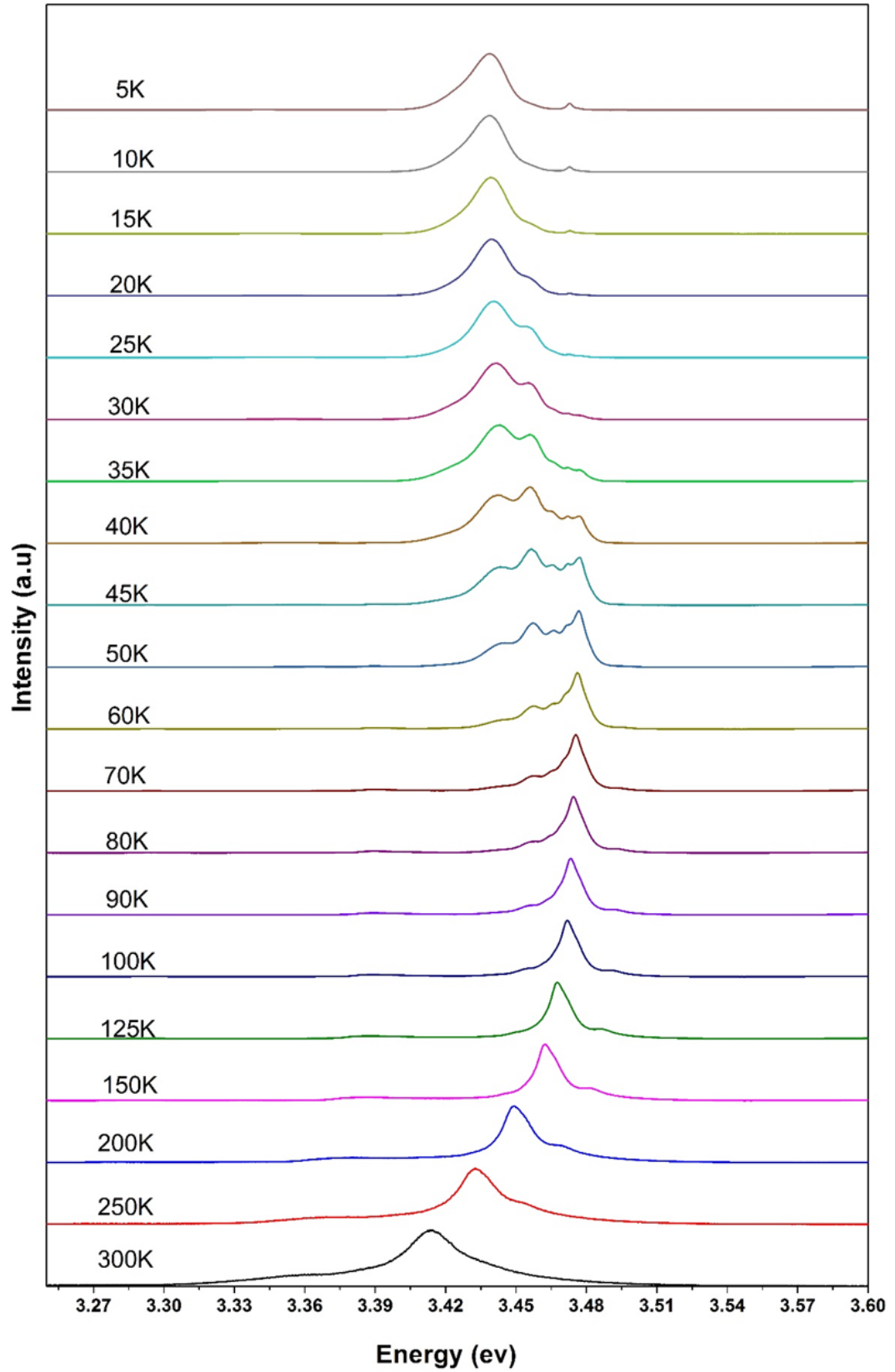


Figure 7.12: Temperature dependent PL spectra of GaN heterostructure from ambient to 5K

38 meV above the (D^0X). In addition to these excitonic features, a broad PL features (peak #1 to #3) located at 3.269 eV, 3.356 eV and 3.438 eV are also observed which tentatively assign as 2DEG peaks feature.

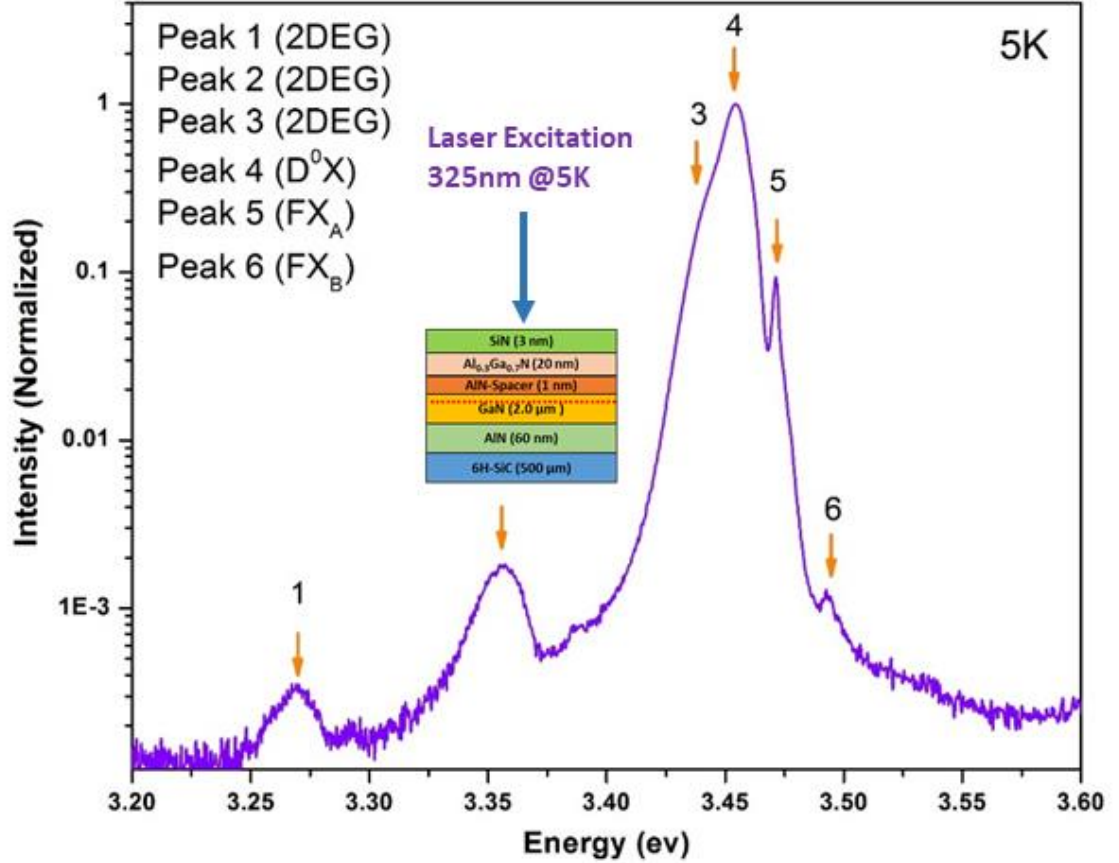


Figure 7.13: Low temperature (5K) PL spectra of AlGaIn/GaN heterostructure on SiC wafer

Figure 7.14 (a) and (b) depict the possible optical transitions corresponding to Peak #1, #2 and #3 by analyzing the simulated band diagram of AlGaIn/GaN heterostructure. The clearly resolved three peaks labeled Peak #1, #2 and #3 become evident just below the donor bound exciton, which may exhibit 2DEG PL features.

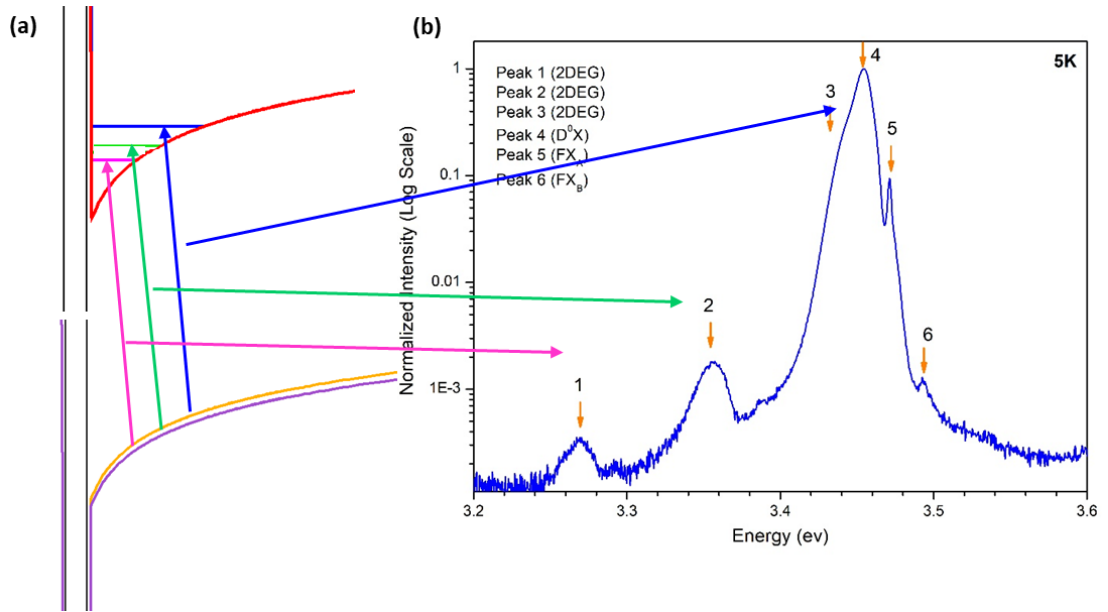


Figure 7.14: (a) triangular quantum well of CB & VB and (b) 5K PL spectra of GaN HEMT structures as well as corresponding D°X, FX and 2DEG band structure

The simplest procedure for identifying 2DEG PL features is to perform PL measurements on the GaN heterostructure sample before and after etching. [153-155] The top barrier layer of GaN heterostructure is etched the by using the reactive ion etching (RIE) system. Total ~ 220 nm thickness is etched which comprised 20 nm AlGaN barrier, 0.8 nm AlN spacer and ~200 nm GaN layer thickness. Atomic level flat etching is very difficult and there is a high possibility to present etching defects on heterostructure. Used recipe is optimized using low energy BCl₃/Cl₂/Ar plasma process to control the etching defect. Further the etching process quality is verifying by comparing Photoluminescence spectra of etched and non-etched sample. Figure 7.15 (a) and (b) shows the Photoluminescence spectra of only GaN buffer layer and barrier etched GaN heterostructure at 5K low temperature respectively which show the etching defects do not much influence the PL spectra.

Three peaks corresponding to D°X, FX_A and FX_B are observed in PL measurements for the only buffer GaN grown sample (Figure 7.15 (a)) as well as barrier etched sample (Figure 7.15 (b)). The PL features associated with peaks #1, #2 and #3 of GaN heterostructure (Figure 7.13) completely vanish in both only buffer GaN grown and etched samples. The PL of GaN heterostructure (Figure 7.13) and the PL of barrier

etched sample and without AlGaN barrier layer grown sample (Figure 7.15), clearly indicate that the origin of broad PL features (peak #1, peak #2 and peak #3) exist near the AlGaN/AlN/GaN heterointerface. Note that the AlGaN barrier is transparent to the excitation laser beam ($\lambda = 325$ nm) hence the possibility of these features as defect related transitions due to AlGaN barrier layer can easily be ruled out. Therefore, the broad PL features are related to either from the 2DEG states or some defect/trap states related to AlGaN/GaN heterointerface.

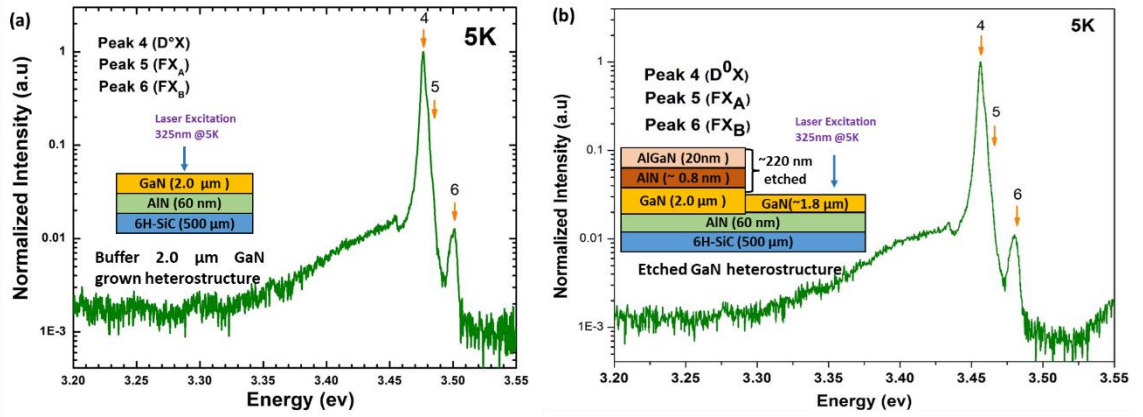


Figure 7.15: Low temperature (5K) PL measurement of (a) only buffer GaN layer grown heterostructure and (b) top etched (~220 nm) GaN heterostructure on SiC wafer

Peak #1, #2 and #3 PL features can be interpreted in terms of the quasi-2D exciton model, in which the Coulomb interaction between the electrons confined in triangular quantum well and the free holes in the valence bands. As shown in Figure 7.16, some of the photogenerated electrons and holes fill the space charge potential at the interface, which drives the electron towards the triangular well and the hole towards the GaN flat-band region. Thus, the photoexcited excitons evolve into quasi-2D excitons. Subsequently recombine, leading to the emission Peak #1, #2 and #3. The recombination related to the 2DEG is known to be strongly dependent on the band bending [156-159]. Such a spatially indirect radiative recombination of electrons confined in the triangular single quantum well with free holes in the valence band indicates that the particular PL feature is related to the 2DEG states [160]. A few researchers have reported that the 2DEG related PL features might also exist at energies

higher than the bandgap of GaN. Such a PL transition had been associated with the recombination of 2DEG electrons with traps lying at the AlGaIn/GaN heterointerface [161, 162].

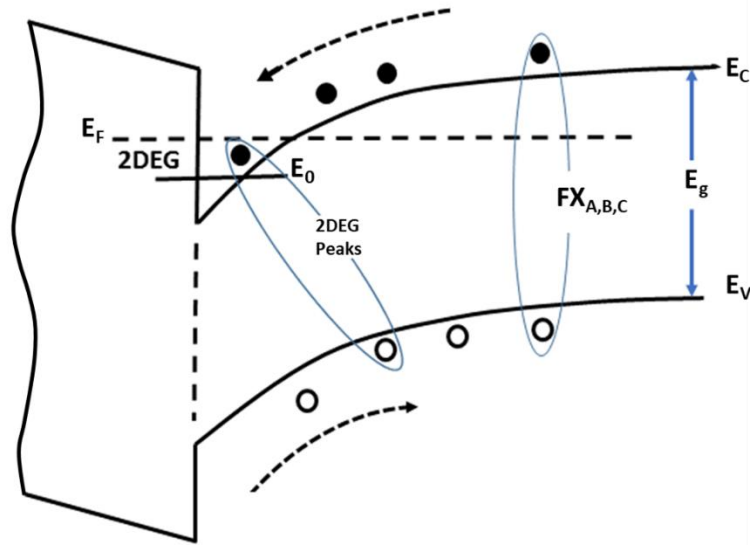


Figure 7.16: Electrons and holes are separated near the interface to form the quasi-two-dimensional excitons

In order to observe such a PL feature, the energy of excitation laser source needs to be greater than the bandgap of the top AlGaIn barrier layer which actually leads to a high possibility of transferring the holes from the AlGaIn barrier layer to the interface traps. However, this possibility is ruled out in present case since the energy of excitation laser source ($\lambda = 325$ nm) in PL experiments is much lower than the bandgap of the AlGaIn barrier layer. Hence, peak #1 to #3 PL features are identified as transitions related to 2DEG lying at the AlGaIn/GaN heterointerface. Here as moved from peak 1 to 3, the corresponding PL emission intensity founded gradually increased. In other words, the higher PL emission intensity founded in excited electron states (E_1 and E_2) in the 2DEG, as compare to the emission associated to ground state (E_0) which can be understood from the overlap of hole and electron wavefunctions [157, 158]. The recombination of the 2D electrons from the higher subbands is much more effective due to the stronger overlap of these electron wavefunction with the wavefunction of holes. The photoexcited holes are near to flat band region, due to the band bending of valance band. The electrons in the ground state are strongly localized to the notch

region, while electrons in excited states (E_1 and E_2) penetrate further into flat band region. This gives the higher recombination probability and hence a stronger PL intensity for the emission corresponding to excited states electrons.

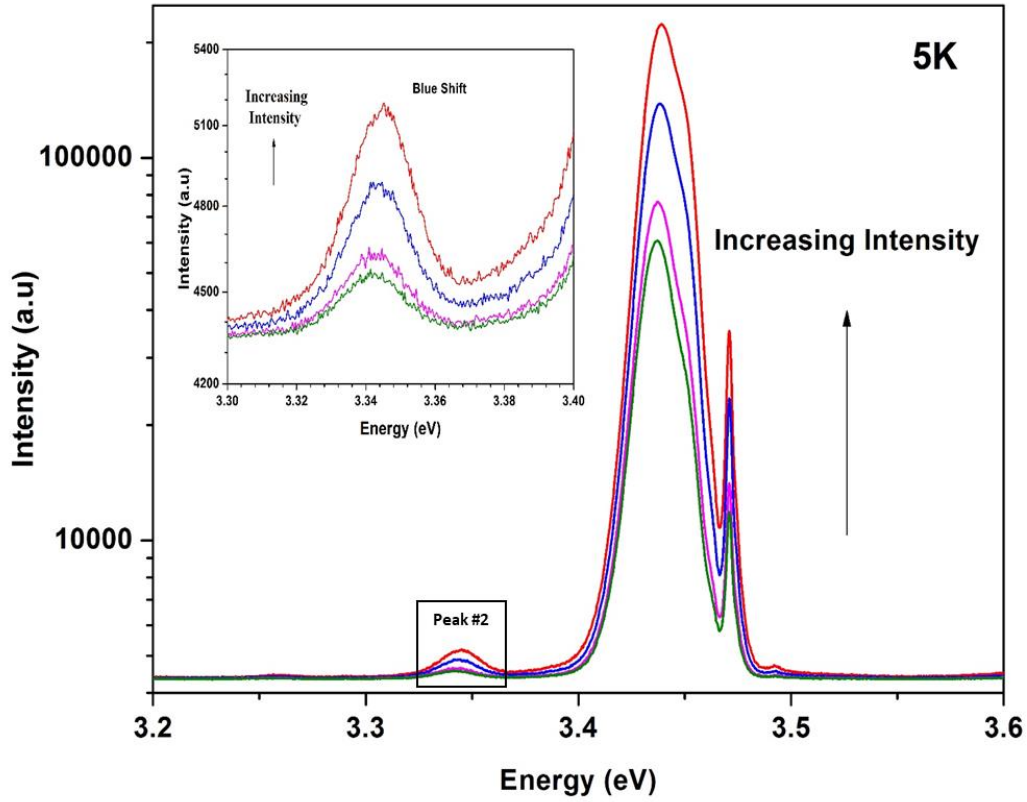


Figure 7.17: 5K PL spectra of GaN HEMT structures with increase of excitation power (inset zoom portion of Peak #2 showing blue shift and stronger PL intensity as increase the excitation laser power)

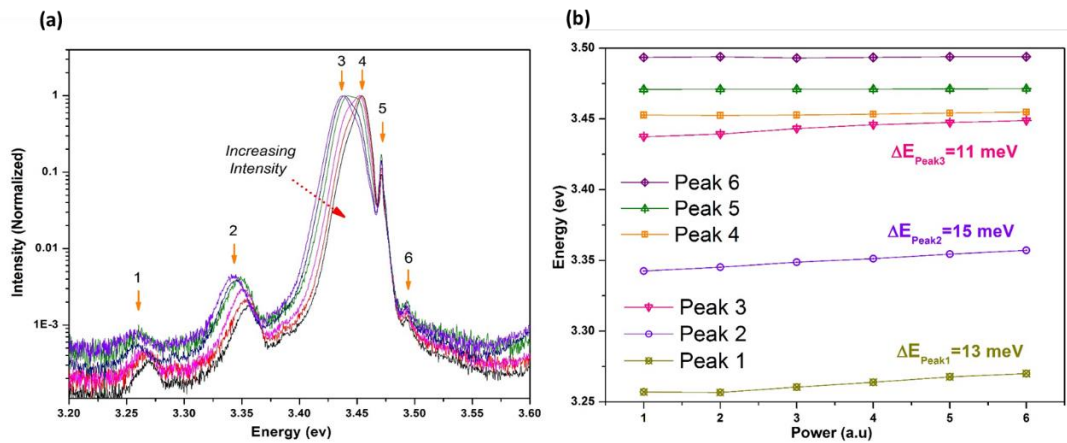


Figure 7.18: (a) 5K PL spectra of GaN HEMT structures with increase of excitation power and (b) Excitation intensity dependent peak shift for peak 1 to peak 6

Further in order to get the confirmatory evidence for the identification of 2DEG PL features can be obtained by studying the effect of temperature and excitation power on the peak energy of 2DEG features [153, 154, 163-165]. The excitonic power dependent PL measurement at 5K temperature is shown in Figure 7.17. In order to study the excitation laser power influence on the weak and strong PL peak simultaneously, normalized the Figure 7.17 plot on a logarithmic scale as shown in Figure 7.18 (a). To identify the correct nature of these emission lines, each spectrum in Figure 7.18 (a) analyzed by means of the standard multiple fitting technique to find out the exact peak positions. A strong blueshift is observed with increased of laser power for the Peak #1, #2 and #3 corresponding to 2DEG feature as shown in Figure 7.18 (a). There is no shifting for peaks #4, #5 and #6 correspond to donor bound-exciton line (D^0X), the free excitons transitions (FX_A) and (FX_B) respectively are clearly observed in the PL spectrum with varying in excitation power of incident laser. The excitation power dependent peaks shift in PL spectra of GaN heterostructure is shown in Figure 7.18 (b). All these blue shifted transitions might be the excitonic recombination of localized electrons at the interface and photoexcited holes in the valence band.

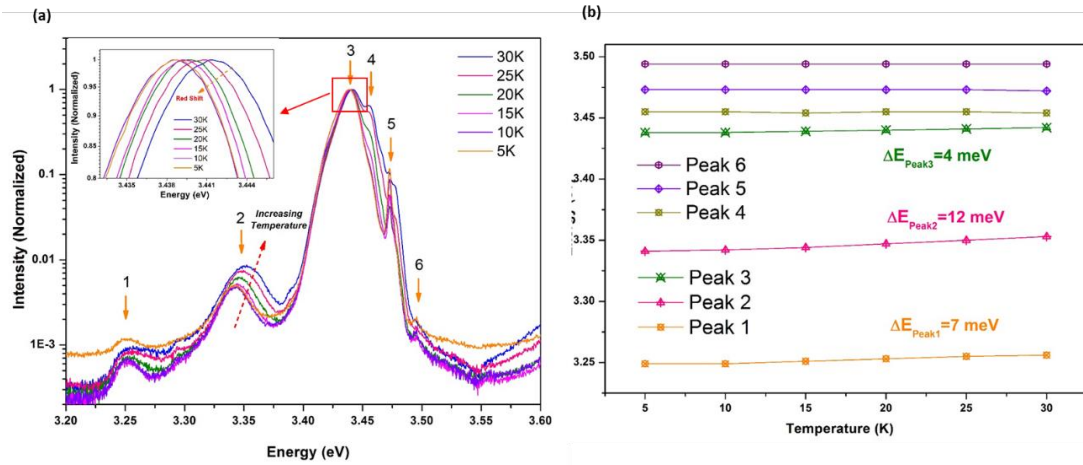
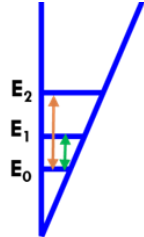


Figure 7.19: (a) PL spectra of AlGaIn/GaN Heterostructure with increase of temperature and (b) temperature dependent peak shift for peak 1 to peak 6

Similarly, the PL spectra of GaN heterostructure for various temperature is shown in Figure 7.19 (a). A redshift is observed as temperature decreased for the Peak #1, #2 and #3 corresponding to 2DEG feature as shown in Figure 7.19 (b). There are no

shifting for peaks #4, #5 and #6 correspond to donor bound-exciton line (D^0X), the free excitons transitions (FX_A) and (FX_B) respectively are clearly observed in the PL spectrum with varying in measurement temperature. The summary of simulated and experimental measured subband energy levels is depicted in Table 7.2.

Table 7.2: Simulated and measured Energy subband levels inside triangular quantum well

Sr No	Energy Subbands	Simulated (meV)	Experimental (meV)	
1	$\Delta E_1 = E_0 - E_1$	91	87	
2	$\Delta E_2 = E_0 - E_2$	186	178	

In summary, experimental demonstration of electrical tuning of ISBT in GaN HEMT device at room temperature has not only provided a new alternate mechanism, but also discriminates ISBT from other transitions induced by deep-level traps and defects in 100 nm GaN HEMT device. Photonics ISBT phenomenon is explored in electronics GaN HEMT device for external biasing depends tuning of the subband. The clear signatures of the 2DEG features are observed in the 5K PL spectrum of the AlGaIn/GaN HEMT sample using excitation laser beam ($\lambda = 325\text{nm}$) source. It is noticed that the broad PL peaks associated with the 2DEG states disappear after etching of AlGaIn barrier layer and GaN buffer layer samples. Furthermore, a large blueshift and red shift corresponding to excitation power and temperature dependence PL measurements confirm the existence of true signatures of ground as well as excited 2DEG states. The intersubband energy levels are measured and emission peaks data are also supported by a simulation. External bias dependent tuning of the subband inside triangular quantum well of GaN HEMT is responded toward incident terahertz radiation. A novel approach for ISBT in GaN HEMT helps to overcome the THz gap in the electromagnetic spectrum at ambient temperature.

Conclusion and Future Work

The results presented in this thesis cover a wide variety of applications with a common background: light matter interaction in triangular quantum well. The interaction of terahertz radiation with HEMT structure is partially unexplored and thus, they still offer extensive research possibilities. This work contributes to both theoretical and experimental areas. The experimental novel ISBT phenomenon in GaN HEMT is demonstrated for potential ambient applications in THz range as well as refined theoretical models mainly based on plasmonic metamaterials assisted ISBT in GaN HEMT. A summary of the main results is described subsequently

We have proposed following original contributions under the framework of Intersubband transition in GaN HEMT:

- We investigated the possibility of extending classic RF GaN HEMT device to the terahertz band with ISBT phenomena.
- We developed theoretical models for electrically tunable ISBT in GaN HEMT. Two other aggregate effects contributions also presented as a metamaterial embedded and plasmonic assisted ISBT in GaN HEMT.
- We fabricated and measured electrical tuning of ISBT in GaN HEMT device at room temperature. We discriminated ISBT from other transitions induced by deep-level traps/defects and thermal transitions in GaN HEMT.
- We extracted the subband energy levels inside triangular quantum well in GaN heterostructure by using photoluminescence PL spectra at low temperature.

Concluding Remarks

We have developed theoretical models for electrically tunable plasmonic metamaterials assisted ISBT in GaN HEMT. Experimental demonstration of electrical tuning of ISBT in GaN HEMT device at room temperature has not only provided a new alternate mechanism, but also discriminates ISBT from other transitions induced by deep-level traps and defects in 100 nm GaN HEMT device. The intersubband energy levels are extracted and PL emission peaks data are also supported by a simulation. Photonics ISBT phenomenon is explored in electronics GaN HEMT device for external biasing depends tuning of the subband. A novel approach for ISBT in GaN HEMT has helped to overcome the THz gap in the electromagnetic spectrum at ambient temperature.

Future work

Following are the research lines in the thesis assure future works and further investigation.

- **Antenna coupled HEMT device**

It is difficult to couple the THz radiation efficiently to the active part of the device. When the dimension of the device is the order of the illuminated terahertz radiation wavelength, it is act as antenna. The usage of antenna increases the efficiency of the device. At THz frequencies, antenna should be integrated lithographically with the device, coupling should be done quasi-optically. Antenna coupling leads to converse the radiation toward the active region between source and drain. The resultant electric field intensity inside the active channel is greatly enhanced. The enhancement of the field due to illumination is strongly depends on the device dimension as well frequency of incident radiation. Dimension and geometry depended antenna couple terahertz source and detector showing great enhance in the performance of devices.

- **Split gate Plasmonic structure**

To address the low-quantum efficiency limitation of conventional terahertz devices, plasmonic split gate contact configuration offers high quantum efficiency and ultrafast operation simultaneously. By using nanoscale plasmonic gate structure significantly enhancing efficiency of device.

- **HEMT on Superlattice structure**

In the present thesis, ISBT in single quantum well of GaN HEMT structure has been discussed. Multiple quantum wells superlattice structure became one of the most widely used approaches for THz devices. Integration of superlattice multiple quantum wells in the GaN HEMT structure gives roof for more versatile effective THz devices.

- **Nitride semiconductor/superconductor heterostructure**

Superconductors based terahertz devices are prime contenders for advanced terahertz electronics systems including space hardware due to their outstanding material properties. The seamless integration of superconductor materials with nitride heterostructure is promising technology for realization of high-power sources and efficient and sensitive detectors in THz range on a single platform.

REFERENCES

- [1] Tonouchi M, Cutting-edge THz technology, *Nat Photonics* **2007**, 1, 97–105, doi: 10.1038/nphoton.2007.3.
- [2] Yang X, Zhao X, Yang K, Liu Y, Liu Y, Fu W, Luo Y, Biomedical applications of terahertz spectroscopy and imaging. *Trends in Biotechnology* **2016**, 34 (10), 810-824
- [3] Mittleman DM, Twenty years of terahertz imaging, *Optical Express* **2018**, 26, 9417–9431.
- [4] Rahman A, Rahman AK, Rao B, Early detection of skin cancer via terahertz spectral profiling and 3D imaging, *Biosensors & Bioelectronics* **2016**, 82, 64–70.
- [5] Nagai N, Sumitomo M, Imaizumi M, Fukasawa R, Characterization of electron- or proton irradiated Si space solar cells by THz spectroscopy, *Semicond. Sci. Technol.* **2006**, 21, 201–209.
- [6] Nagai N, Imai T, Fukasawa R, Kato K, Yamauchi K, Analysis of the intermolecular interaction of nanocomposites by THz spectroscopy, *Appl. Phys. Lett.* **2004**, 85, 4010–4012.
- [7] Siegel P, THz Instruments for Space, *IEEE Transaction on Antennas and Propagation*, **2007**, 8, 55 (11)
- [8] Siegel P, THz for Space: The Golden Age, *IEEE MTT-S International Microwave Symposium*, Anaheim, CA, **2010**, pp. 816-819, doi: 10.1109/MWSYM.2010.5515761
- [9] Ferguson B and Zhang XC, Materials for terahertz science and technology, *Nature Materials* **2002**, 1 26–33, <https://doi.org/10.1038/nmat708>.
- [10] Khanal S, Zhao L, Reno JL, Kumar S, Temperature performance of terahertz quantum-cascade lasers with resonant-phonon active-regions, *Journal of Optics*, **2014**, 16, 094001; DOI: 10.1088/2040-8978/16/9/094001

- [11] Lerude G, Survey of RF GaN Fab: successful commercialization and global supply, *Microwave Journal*, **2021**, 64, 6
- [12] Yue Y, Hu Z, Guo J, Rodriguez BS, Li G, Wang R, Faria F, Fang T, Song B, Gao X, Guo S, Kosel T, Snider G, Fay P, Jena D, Xing H, InAlN/AlN/GaN HEMTs with regrown ohmic contacts and f_T of 370 GHz, *IEEE Electron Device Letters*, **2012**, 33 7 988-990, doi: 10.1109/LED.2012.2196751.
- [13] Dyakonov M, Shur M, Shallow Water Analogy for a Ballistic Field Effect Transistor: New Mechanism of Plasma Wave Generation by dc Current, *Physical Review Letter*, **1993**, 71 15 2465-2468, <https://doi.org/10.1103/PhysRevLett.71.2465>.
- [14] Dyakonov M and Shur M, Detection, Mixing, and Frequency Multiplication of Terahertz Radiation by Two-Dimensional Electronic Fluid, *IEEE Transactions on Electron Devices*, **1996**, 43 3 380-387, doi:10.1109/16.485650.
- [15] Nahar S, Shafee M, Blin S, Penarier A, Nouvel P, Coquillat D, Safwa A, Knap W and Hella M, Wide modulation bandwidth terahertz detection in 130 nm CMOS technology *Eur. Phys. J. Appl. Phys*, **2016**, 76 20101, doi: 10.1051/epjap/2016160302.
- [16] Hou HW, Liu Z, Teng JH, Palacios T, Chua SJ, High Temperature Terahertz Detectors Realized by a GaN High Electron Mobility Transistor *Scientific Report*, **2017**, 7 46664, doi: 10.1038/srep46664.
- [17] Kurita Y, Ducournau G, Coquillat D, Satou A, Kobayashi K, Tombet SB, Meziani YM, Popov VV, Knap W, Suemitsu T, Otsuji T, Ultrahigh sensitive sub-terahertz detection by InP-based asymmetric dual-grating-gate high-electron-mobility transistors and their broadband characteristics *Applied Physics Letters*, **2014**, 104 251114, doi: 10.1063/1.4885499.

- [18] Lucas A, An exotic quantum fluid in graphene under the right conditions, electrons can move as fluids in graphene, *Science*, **2019**, 364, 6436.
- [19] Viti L, Hu J, Coquillat D, Politano A, Knap W, Vitiello MS, Efficient terahertz detection in black-phosphorus nanotransistors with selective and controllable plasma-wave, bolometric and thermoelectric response, *Scientific Reports*, **2016**, 6:20474. DOI: 10.1038/srep20474
- [20] Sun JD, Sun YF, Wu DM, Cai Y, Qin H, Zhang BS, High-responsivity, low-noise, room-temperature, selfmixing terahertz detector realized using floating antennas on a GaN-based field effect transistor, *Applied Physics Letters*, **2012**, 100:013506. DOI: 10.1063/1.3673617.
- [21] Javadi E, Delgado-Notario JA, NMasoumi MS, Elazquez-Perez VJE, Meziani YM, Continuous wave terahertz sensing using GaN HEMTs, *Physica Status Solidi (a)*, **2018**, 215 1700607.
- [22] Hou HW, Liu Z, Teng JH, Palacios T, Chua SJ, A sub-terahertz broadband detector based on a GaN high-electron-mobility transistor with nanoantennas, *Applied Physics Express*, **2017**, 10 014101, <https://doi.org/10.7567/APEX.10.014101>.
- [23] Fatimy A, Dyakonova N, Meziani Y, Otsuji T, Knap W, Vandenbrouk S, Madjour K, Théron D, Gaquiere C, Poisson M, Delage S, Prystawko P, Skierbiszewski C, AlGaIn/GaN high electron mobility transistors as a voltage-tunable room temperature terahertz sources *Journal of Applied Physics*, **2010**, 107 024504, doi:10.1063/1.3291101.
- [24] Bernardini F, Fiorentini V, Vanderbilt D, Spontaneous polarization and piezoelectric constants of III-V nitride. *Physical Review B*. **1997**, 56, 10024
- [25] Denton AR, Ashcroft NW, Vegard's law, *Physical Review A*, **1991**, 43 6 1361
- [26] Ambacher O, Foutz B, Smart J, Shealy JR, Weimann NG, Chu K, Murphy M, Sierakowski AJ, Schaff WJ, Eastman LF, Dimitrov R, Mitchell A,

- Stutzmann M, Two dimensional electron gases induced by spontaneous and piezoelectric polarization in undoped and doped AlGaIn/GaN heterostructures, *Journal of Applied Physics*, **2000**, 87, 334
- [27] Padilla WJ, Basov DN, Smith DR, Negative refractive index metamaterials, *Material Today*, **2006**, 09, 7-8, 28-35
- [28] Jackson JD, Classical Electrodynamics, Wiley, 1998.
- [29] Maier SA, Plasmonics, Fundamentals and Applications, Springer, 2004.
- [30] Wood RW, On a remarkable case of uneven distribution of light in a diffraction grating spectrum, *Philos. Mag.*, **1902**, 4, 396-402.
- [31] Ishimaru, Electromagnetic Wave Propagation, Radiation, and Scattering, Prentice Hall, 1990.
- [32] Pendry JB, Martín-Moreno L, García-Vidal FJ, Mimicking surface plasmons with structured surfaces, *Science*, **2004**, 305, 847
- [33] Scalari G, Maissen C, Hagenmüller D, De Liberato S, Ciuti C, Reichl C, Wegscheider W, Schuh D, Beck M, Faist J, Ultrastrong light-matter coupling at terahertz frequencies with split ring resonators and inter-Landau level transitions, *Journal of Applied Physics*, **2013**, 113 136510
- [34] Benz A, Montañó I, Klem JF, Brener I, Tunable metamaterials based on voltage controlled strong coupling, *Appl. Phys. Lett.*, **2013**, 103, 263116
- [35] Scalari G, Maissen C, Turcinková D, Hagenmüller D, De Liberato S, Ciuti C, Reichl C, Schuh D, Wegscheider W, Beck M, Faist J, Ultrastrong Coupling of the Cyclotron Transition of a 2D Electron Gas to a THz Metamaterial, *Science*, **2012**, 335 1323
- [36] Gabbay A, Brener I, Theory and modeling of electrically tunable metamaterial devices using intersubband transitions in semiconductor quantum wells, *Optical Express*, **2012**, 20 6 6548

- [37] Benz A, Campione S, Liu S, Montano I, Klem JF, Sinclair MB, Capolino F, Brener I, Monolithic metallic nanocavities for strong light matter interaction to quantum-well intersubband excitations, *Optical Express*, **2013**, 21 (26) 32572
- [38] Shrekenhamer D, Rout S, Strikwerda A, Bingham C, Averitt RD, Sonkusale S, Padilla WJ, High speed terahertz modulation from metamaterials with embedded high electron mobility transistors, *Optical Express*, **2011**, 19 10 9968
- [39] Zhang Y, Zhao Y, Liang S, Zhang B, Wang L, Zhou T, Kou W, Lan F, Zeng H, Han J, Feng Z, Chen Q, Mazumder P, Yang Z, Large phase modulation of THz wave via an enhanced resonant active HEMT metasurface, *Nanophotonics*, **2018**, 8 1 153
- [40] Karmakar S, Kumar D, Varshney R, Chowdhury DB, Magneto spectroscopy of terahertz surface plasmons in subwavelength perforated superlattice thin-films, *J. Appl. Phys.*, **2022**, 131, 223102
- [41] Devi KM, Jana A, Punjal A, Acharyya N, Prabhu S, Chowdhury DB, Polarization-independent tunable terahertz slow light with electromagnetically induced transparency metasurface, *New J. Phys.* **2022**, 24, 093004
- [42] Kaur S, Karmakar S, Jana A, Rane S, Varshney R, Chowdhury DB, Hybrid resonant cavities: A route towards phase engineered THz metasurfaces, *iScience*, **2022**, 25, 104024
- [43] Rao SM, Srivastava Y, Kumar G, Chowdhury DB, Modulating Fundamental Resonance in Capacitive Coupled Asymmetric Terahertz Metamaterials, *Scientific Report*, **2018**, 8, 16773
- [44] Devi KM, Jana A, Chowdhury DB, Topological edge states in an all-dielectric terahertz photonic crystal, *Optical Materials Express*, **2021**, 11, 8, 2445.

- [45] Vicarelli L, Vitiello MS, Coquillat D, Lombardo A, Ferrari AC, Knap W, Polini M, Pellegrini V, Tredicucci A, Graphene field-effect transistors as room-temperature THz detectors, *Nature Materials*, **2012**, 11 865
- [46] Zak A, Andersson M, Bauer M, Matukas J, Lisauskas A, Roskos H, Stake J, Antenna-Integrated 0.6 THz FET Direct Detectors Based on CVD Graphene, *Nano Letter*, **2014**, 14 10 5834
- [47] Tong J, Muthee M, Chen S, Yngvesson S, Yan J, Antenna Enhanced Graphene THz Emitter and Detector, *Nano Lett.* **2015**, 15 8 5295
- [48] Viti L, Hu J, Coquillat D, Politano A, Knap W, Vitiello MS. Efficient terahertz detection in black-phosphorus nanotransistors with selective and controllable plasma-wave, bolometric and thermoelectric response, *Scientific Reports*, **2016**, 6, 20474
- [49] Berry C, Wang N, Hashemi M, Unlu M, Jarrahi M, Significant performance enhancement in photoconductive terahertz optoelectronics by incorporating plasmonic contact electrodes. *Nature Communications*, **2016**, 4 1622
- [50] Tanoto H, Teng J, Wu Q, Sun M, Chen Z, Maier S, Wang B, Chum C, Si G, Danner A, Chua S, Greatly enhanced continuous-wave terahertz emission by nano-electrodes in a photoconductive photomixer, *Nature Photonics*, **2012**, 6 121
- [51] Hou H, Liu Z, Teng J, Palacios T, Chua S, A sub-terahertz broadband detector based on a GaN high electron mobility transistor with nanoantennas, *Applied Physics Express*, **2017**, 10 014101
- [52] Wang N, Cakmakyapan S, Lin Y, Javadi H, Jarrahi M, Room-temperature heterodyne terahertz detection with quantum-level sensitivity, *Nature Astronomy*, **2019**, 3 977

- [53] Yu N, Wang Q, Kats M, Fan J, Khanna S, Li L, Davies A, Linfield E, Capasso F, Designer spoof surface plasmon structures collimate terahertz laser beams, *Nature Materials*, **2010**, 9 730
- [54] Smorchkova P, Chen L, Mates T, Shen L, Heikman S, Moran B, Keller S, DenBaars SP, Speck JS, Mishra UK, AlN/GaN and (Al,Ga)N/AlN/GaN two-dimensional electron gas structures grown by plasma-assisted molecular-beam epitaxy, *J. Appl. Phys.*, **2001**, 90, 5196
- [55] Shen L, Heikman S, Moran B, Coffie R, Zhang NQ, Buttari D, Smorchkova RP, Keller S, DenBaars SP, Mishra UK, AlGaIn/AlN/GaN high-power microwave HEMT, *IEEE Electron Device Letters*, **2001**, 22, 10
- [56] Weiwei K, TCAD simulation and modeling of AlGaIn/GaN HFETs, Ph.D. thesis, North Carolina State University, 2011.
- [57] Silvaco® Application note, State of the art 2D and 3D process and device simulation of GaN-based devices, A Journal for Process and Device Engineers, **2013**, 23 (3).
- [58] Silvaco® Application note, “State of the art 2D and 3D process and device simulation of GaN based-devices, Simulation Standard, July, August, September, 2013.
- [59] Albrecht JD, Wang RP, Ruden PP, Farahmand M, Brennan KF, Electron transport characteristics of GaN for high temperature device modeling. *Journal of Applied Physics*, **1998**, 83(9), 4777–4781. <https://doi.org/10.1063/1.367269>
- [60] Chuang SL, Physics of optoelectronic devices, New York John Wiley and Sons 1995.
- [61] Chuang SL, Physics of photonics devices, New York: John Wiley and Sons 2009.
- [62] Bradley AF, Envelope-function formalism for electrons in abrupt heterostructures with material-dependent basis functions. *Physical Review B*, **1996**, 54, 1909–1921.

- [63] Eissfeller T, Vogl P, Real-space multiband envelope-function approach without spurious solutions, *Physical Review B*, **2011**, 84(19), 195122. <https://doi.org/10.1103/PhysRevB.84.195122>
- [64] Foreman BA, Effective mass Hamiltonian and boundary conditions for the valence bands of semiconductor microstructures, *Physical Review B*, **1993**, 48(7), 4964–4967. <https://doi.org/10.1103/PhysRevB.48.4964>
- [65] Wieck AD, Thiele F, Merkt U, Ploog K, Weimann G, Schlapp W, Subband-landau-level coupling in GaAs/Ga_{1-x}Al_x as heterojunctions, *Physical Review B*, **1989**, 39(6), 3785–3794. doi.org/10.1103/PhysRevB.39.3785
- [66] Ando T, Fowler AB, Stern F, Electronics properties of two dimensional systems, *Reviews of Modern Physics*, **1982**, 54(2), 437–672. <https://doi.org/10.1103/RevModPhys.54.437>
- [67] Helm M, The Basic Physics of Intersubband Transitions, in: edited by Liu H, Capasso F, Intersubband Transitions in Quantum Wells: Physics and Device Applications I, Semiconductors and Semimetals, Academic Press, 1999 Vol. 62 pg. 20 and 26.
- [68] Nakano H, Low-profile Natural and Metamaterial Antennas: Analysis Methods and Applications. Hoboken, NJ, USA: Wiley, 2016
- [69] Reshchikov MA, Morkoç H, Defects in GaN: optical signature, *Journal of Applied Physics Review*, **2005**, 97, 061301- 1–061301-95. Also, in the April 2005 issue of Virtual Journal of Ultrafast Science, which can be accessed via <http://www.vjultrafast.org>.
- [70] Pankove JI, Optical Processes in Semiconductors, Prentice-Hall, Englewood Cliffs, NJ 1971.
- [71] Sze SM, Ng KK, Physics of Semiconductor Devices, John Wiley and Sons, 2012.

- [72] Qu DX, Hor YS, Xiong J, Cava RJ, Ong NP, Quantum oscillations and Hall anomaly of surface states in the topological insulator Bi₂Te₃, *Science* 329, 821 (2010).
- [73] Tan YW, Zhu J, Stormer HL, Pfeiffer LN, Baldwin KW, West KW, Measurements of the Density- Dependent Many-Body Electron Mass in Two Dimensional GaAs/AlGaAs Heterostructures, *Phys. Rev. Lett.* **2005**, 94, 016405
- [74] Caviglia D, Gariglio S, Cancellieri C, Sacepe B, Fête A, Reyren N, Gabay M, Morpurgo AF, Triscone JM, Two-Dimensional Quantum Oscillations of the Conductance at LaAlO₃/SrTiO₃ Interfaces, *Phys. Rev. Lett.* **2010**, 105, 236802
- [75] Cao H, Tian J, Miotkowski I, Shen T, Hu J, Qiao S, Chen YP, Quantized Hall Effect and Shubnikov–de Haas Oscillations in Highly Doped Bi₂Se₃: Evidence for Layered Transport of Bulk Carriers, *Phys. Rev. Lett.* **2012**, 108, 216803
- [76] Shalom MB, Ron A, Palevski A, Dagan Y, Shubnikov-De Haas Oscillations in SrTiO₃/LaAlO₃ Interface, *Phys. Rev. Lett.* **2010**, 105, 206401
- [77] Choi S, Heller E, Dorsey D, Vetury R, Graham S, Analysis of the residual stress distribution in AlGa_N/Ga_N high electron mobility transistors, *J. Appl. Phys.* **2013**, 113, 093510
- [78] Moram MA, Vickers ME, X-ray diffraction of III-nitrides, *Rep. Prog. Phys.* **2009**, 72, 036502
- [79] Kuball M, Raman spectroscopy of Ga_N, AlGa_N and Al_N for process and growth monitoring/control. *Surf. Interface Anal.* **2001**, 31, 987
- [80] Edgar JH, Properties of Group III Nitrides, INSPEC, Institute of Electrical Engineers, London UK, 1994 p. 30-35
- [81] Polian A, Grimsditch M, Grzegory I, Elastic constant of Gallium Nitride, *J Appl. Phys.*, **1996**, 79: 3343

- [82] Davydov VY, Averkiev NS, Goncharuk IN, Nelson DK, Nikitina IP, Semchinova OK, Raman and Photoluminescence studies of biaxial strain in GaN epitaxial layers grown on 6H-SiC, *J. Appl. Phys.*, **1997**, 82, 5097
- [83] Wagner JM, Bechstedt F, Phonon deformation potentials of α -GaN and -AlN: An ab initio calculation, *Applied Physics Letters*, **2000**, 77, 346
- [84] Zhao DG, Xu, SJ, Xie MH, Tong SY, Yang H, Stress and its effect on optical properties of GaN epilayers grown on Si(111), 6H-SiC(0001), and c-plane sapphire, *Applied Physics Letters*, **2003**, 83, 4
- [85] Jamil M, Grandusky JR, Jindal V, Shahedipour-Sandvik F, Guha S, Arif M, Development of strain reduced GaN on Si (111) by substrate engineering, *Applied Physics Letters*, **2005**, 87, 082103
- [86] Tripathy S, Chua SJ, Chen P, Miao ML, Micro-Raman investigation of strain in GaN and $\text{Al}_x\text{Ga}_{1-x}\text{N}/\text{GaN}/\text{Al}_x\text{Ga}_{1-x}\text{N}/\text{GaN}$ heterostructures grown on Si(111), *J. Appl. Phys.*, **2002**, 92, 3503
- [87] Jena D, Polarization induced electron populations in III-V nitride semiconductors Transport, growth, and device applications, Ph.D. thesis, University of California, Santa Barbara, 2003
- [88] C Kisielowski, Kruger J, Ruvimov S, Suski T, Ager JW, Jones E, Liliental-Weber Z, Rubin M, Weber ER, Bremser MD, Davis RF, Strain related phenomena in GaN thin films, *Phys. Rev. B*, **1996**, 54 24, 17745
- [89] Ikejiri K, Hiroyama Y, Kasahara K, Hirooka C, Osada T, Tanaka M, Takada T, Egawa T, Mass production ready characteristic of AlGaN/AlN/GaN HEMT structures grown on 200 mm diameter Si substrates using MOCVD, *Semicond. Sci. Technol.* **2021**, 36 014004
- [90] Li H, Mazumder B, Bonef B, Keller S, Wienecke S, Speck JS, Denbaars SP, Mishra UK, Characterization of N-polar AlN in GaN/AlN/(Al,Ga)N heterostructures grown by metal-organic chemical vapor deposition, *Semicond. Sci. Technol.* **2017**, 32 115004

- [91] Rastogi G, Kaneriyaa RK, Sinha S, Upadhyay RB, Optimization of Ohmic Contact Fabrication for $\text{Al}_{0.3}\text{Ga}_{0.7}\text{N}/\text{AlN}/\text{GaN}$ HEMTs on 6H-SiC Using Recess Etching and Surface Plasma Treatment Processes, *J Nanomater Mol Nanotechnol*, **2019**, 8 2, doi: 10.4172/2324-8777.1000267.
- [92] Heikman S, Keller S, Wu Y, Speck JS, DenBaars SP, Mishra UK, Polarization effects in $\text{AlGaIn}/\text{GaIn}$ and $\text{GaIn}/\text{AlGaIn}/\text{GaIn}$ heterostructures, *Journal of Applied Physics*, **2003**, 93, 10114
- [93] Rastogi G, Chaitanya MK, Khare S, Yadav E, Kaneriyaa RK, Upadhyay RB, Kumar PP, Bhattacharya AN, Performance improvement of $\text{Al}_{0.3}\text{Ga}_{0.7}\text{N}/\text{AlN}/\text{GaIn}$ HEMTs using Nitrogen pre-treated Si_3N_4 passivation, *Microelectronic Engineering*, **2021**, 249, 111617
- [94] Ambacher O, Smart J, Shealy JR, Weimann NG, Chu K, Murphy M, Schaff WJ, Eastman LF, Dimitrov R, Wittmer L, Stutzmann M, Rieger W, Hilsenbeck J, Two-dimensional electron gases induced by spontaneous and piezoelectric polarization charges in N- and Ga-face $\text{AlGaIn}/\text{GaIn}$ heterostructures, *Journal of Applied Physics*, **1999**, 85, 6
- [95] Parish G, Umana-Membreno GA, Jolley SM, Buttari D, Keller S, Nener BD, Mishra UK, $\text{AlGaIn}/\text{AlN}/\text{GaIn}$ HEMT with improved carrier transport, Conference on Optoelectronics and Microelectronic Materials and Device, **2004**, 10.1109/COMMAD.2004.1577484
- [96] Arulkumaran S, Vicknesh S, Ng GI, Liu GH, Bryan M, Lee CH, Low specific on-resistance $\text{AlGaIn}/\text{AlN}/\text{GaIn}$ high electron mobility transistors on high resistivity silicon substrate, *Electrochemical and Solid-State Letters*, **2010**, 13 (5) H169.
- [97] Felbinger JG, Fagerlind M, Axelsson O, Rorsman N, Gao X, Guo S, Schaff WJ, Eastman LF, Fabrication and Characterization of Thin-Barrier $\text{Al}_{0.5}\text{Ga}_{0.5}\text{N}/\text{AlN}/\text{GaIn}$ HEMTs, *IEEE Electron Device Letters*, **2011**, 32(7), 889.

- [98] Shen L, Heikman S, Moran B, Coffie R, Zhang NQ, Buttari D, Smorchkova IP, Keller S, DenBaars SP, Mishra UK, AlGa_N/AlN/GaN high-power microwave HEMT, *IEEE Electron Device Letters*, **2001**, 22, 10, 457
- [99] Wang X, Hu G, Ma Z, Ran J, Wang C, Xiao H, Tang J, Li J, Wang J, Zeng Y, Li J, Wang Z, AlGa_N/AlN/GaN/SiC HEMT structure with high mobility GaN thin layer as channel grown by MOCVD, *Journal of Crystal Growth*, **2007**, 298, 835.
- [100] Wang L, Mohammed FM, Ofuonye B, Adesida I, Ohmic contacts to n^{++} -GaN/ n^{++} -GaN capped AlGa_N/AlN/GaN high electron mobility transistors, *Appl. Phys. Lett.*, **2007**, 91, 012113.
- [101] Nanjo T, Suita M, Oishi T, Abe Y, Yagyu E, Yoshiara K, Tokuda Y, Drivability Enhancement for AlGa_N/GaN High-Electron Mobility Transistors with AlN Spacer Layer Using Si Ion Implantation Doping, *Appl. Phys. Express*, **2009**, 2, 031003
- [102] Wang L, Mohammed FM, Adesida I, Differences in the reaction kinetics and contact formation mechanisms of annealed Ti/AlMo/Au Ohmic contacts on n -GaN and AlGa_N/GaN epilayers, *J. Appl. Phys.*, **2007**, 101, 013702.
- [103] Chiu YS, Lin TM, Nguyen HQ, Weng YC, Nguyen CL, Lin YC, Yu HW, Chang EY, Lee CT, Ti/Al/Ni/Au ohmic contacts on AlGa_N/GaN HEMT with improved surface morphology and low contact resistance, *J. Vac. Sci. Technol. B*, **2014**, 32, 011216.
- [104] Miyoshi M, Imanishi A, Egawa T, Ishikawa H, Asai KI, Shibata T, Tanaka M, Oda O, DC Characteristics in High-Quality AlGa_N/AlN/GaN High-Electron-Mobility Transistors Grown on AlN/Sapphire Templates, *Jpn. J. Appl. Phys.*, Part 1, **2005**, 44, 6490.
- [105] Buttari, D, Chini A, Meneghesso G, Zanoni E, Moran B, Heikman S, Zhang NQ, Shen L, Coffie R, DenBaars SP, Mishra UK, Systematic

- characterization of Cl₂ reactive ion etching for improved ohmics in AlGa_N/Ga_N HEMTs, *IEEE Electron Device Lett.*, **2002**, 23,76
- [106] Wang C, Cho SJ, Kim NY, Optimization of Ohmic Contact Metallization Process for AlGa_N/Ga_N High Electron Mobility Transistor, *Transactions on Electrical and Electronic Materials*, **2013**, 14(1), 32.
- [107] Fujishima T, Joglekar S, Piedra D, Lee HS, Zhang Y, Uedono A, Palacios T, Formation of low resistance ohmic contacts in Ga_N-based high electron mobility transistors with BCl₃ surface plasma treatment, *Appl. Phys. Express*, **2013**, 103, 083508.
- [108] Upadhyay BB, Takhar K, Jha J, Ganguly S, Saha D, Surface stoichiometry modification and improved DC/RF characteristics by plasma treated and annealed AlGa_N/Ga_N HEMTs, *Solid State Electronics*, **2018**, 141, 1.
- [109] Cao XA, Piao H, Le Boeuf SF, Li J, Lin JY, Jiang HX, Effects of plasma treatment on the Ohmic characteristics of Ti/Al/Ni/Au contact to n-AlGa_N, *Appl. Phys. Lett.*, **2006**, 89, 082109.
- [110] Nanjo T, Suita M, Oishi T, Abe Y, Yagyu E, Yoshiara K, Tokuda Y, Drivability Enhancement for AlGa_N/Ga_N High-Electron Mobility Transistors with AlN Spacer Layer Using Si Ion Implantation Doping, *Appl. Phys. Express*, **2009**, 2, 031003.
- [111] Zhang LQ, Liu Z, Zhao S, Lin Mz, Wang PF, Low-Temperature Ohmic Contact Formation in AlN/Ga_N HEMT Using Microwave Annealing, *IEEE Transactions on Electron Devices*, **2017**, 64, 3.
- [112] Hashizume T, Ootomo S, Inagaki T, Hasegawa H, Surface passivation of Ga_N and Ga_N/AlGa_N heterostructures by dielectric films and its application to insulated-gate heterostructure transistors, *J. Vac. Sci.Technol.* **2003**, B 21, 1828

- [113] Kim H, Thompson RM, Tilak V, Prunty TR, Shealy JR, Eastman LF, Effects of SiN passivation and high-electric field on AlGaIn-GaN HFET degradation, *IEEE Electron Device Lett.*, **2003**, 24, 421
- [114] Kim H, Schuette M, Jung H, Song J, Lee J, Lu W, Mabon JC, Passivation effects in Ni/AlGaIn/GaN Schottky diodes by annealing, *Appl. Phys. Lett.*, **2006**, 89, 053516
- [115] Bermudez VM, Koleske DD, Wickenden AE, The dependence of the structure and electronic properties of wurtzite GaN surfaces on the method of preparation, *Appl. Surf. Sci.*, **1998**, 126, 69
- [116] Eller BS, Yang J, Nemanich RJ, Electronic surface and dielectric interface states on GaN and AlGaIn, *J. Vac. Sci. Technol. A*, **2013**, 31, 050807
- [117] Keller S, Wu YF, Parish G, Ziang N, Xu JJ, Keller BP, Denbaars SP, Mishra UK, Gallium nitride based power heterojunction field effect transistors: Process development and present status at UCSB, *IEEE Trans Electron Dev*, **2001**, 48, 552–529.
- [118] Ventury R, Zhang NQ, Keller S, Mishra UK, The impact of surface states on the DC and RF characteristics of AlGaIn/GaN HFETs, *IEEE Trans Electron Dev*, **2001**, 48, 560–566.
- [119] Turkuletsand Y, Shalisha I, Surface states in AlGaIn/GaN high electron mobility transistors: Quantitative energetic profiles and dynamics of the surface Fermi level, *Appl. Phys. Lett.*, **2019**, 115, 023502
- [120] Hasegawa H, Inagaki T, Ootomo S, Hashizume T, Mechanisms of current collapse and gate leakage currents in AlGaIn/GaN heterostructure field effect transistors, *J. Vac. Sci. Technol. B*, **2003**, 21, 1844
- [121] Her JC, Cho HJ, Yoo CS, Cha HY, Oh JE, Seo KS, SiNx Prepassivation of AlGaIn/GaN High-Electron-Mobility Transistors Using Remote-Mode Plasma-Enhanced Chemical Vapor Deposition, *Jpn. J. Appl. Phys.*, **2010**, 49, 041002

- [122] Greene BM, Chu KK, Chumbes EM, Smart JA, Shealy JR, Eastman LF, The effect of surface passivation on the microwave characteristics of undoped AlGaIn/GaN HEMTs, *IEEE Electron Dev Lett*, **2000**, 21 268–270.
- [123] Lu W, Kumar V, Schwindt R, Piner E, Adesida I, A comparative study of surface passivation on AlGaIn/GaN HEMTs, *Solid-State Electro*, **2002**, 46 1441–1444.
- [124] Harrison I, Clayton NW, Jeffs NJ, High temperature RF characterization of SiN passivated and unpassivated AlGaIn/GaN HFETs, *Phys Stat Solidi (a)*, **2001**, 188 275–278.
- [125] Ansell BJ, Harrison I, Foxon CT, The effect of surface passivation and illumination on the device properties of AlGaIn/GaN HFETs, *Phys. Stat. Sol. (a)*, **2001**, 188, 279.
- [126] Tan WS, Houston PA, Parbrook PJ, Hill G, Airey RJ, Comparison of different surface passivation dielectrics in AlGaIn/GaN heterostructure field effect transistors, *Journal of Physics D: Applied Physics*, **2002**, 35 595.
- [127] Benkherourou O, Deville JP, X-ray photoelectron spectroscopy of silicon oxynitride layers obtained by low-energy ion implantation, *Appl. Phys. A*, **1998**, 46 87.
- [128] Jeon M, Lee JL, Effects of tensile stress induced by silicon nitride passivation on electrical characteristics of AlGaIn/GaN heterostructure field-effect transistors, *Appl. Phys. Lett.* **2005**, 86, 172101
- [129] Forouhi AR, Bloomer I, Optical dispersion relations for amorphous semiconductors and amorphous dielectrics. *Phys Rev B* **1986**, 34:7018.
- [130] Vernhes R, Zabeida O, Klemberg-Sapieha JE, Martinu L: Pulsed radio frequency plasma deposition of a-SiNx:H alloys: film properties, growth mechanism, and applications, *J ApplPhys*, **2006**, 100:063308.
- [131] Karouta F, Krämer M, Kwaspen JJ, Grzegorzczak A, Hageman P, Hoex B, Kessels WL, Klotwijk J, Timmeringand E, Smit M, Influence of the

- Structural and Compositional Properties of PECVD Silicon Nitride Layers on the Passivation of AlGaIn/GaN HEMTs. *ECS Transactions*, **2008**, 16 (7) 181-191
- [132] Morkoc H, Handbook of Nitride Semiconductors and Devices Vol. 3: GaN-based Optical and Electronic Devices; Wiley-VCH Verlag GmbH & Co. KGaA, Weinheim 2009
- [133] Pal S, Valentin S, Ludwig A, Wieck A, Quantum Confinement in High Electron Mobility Transistors. IntechOpen, London, UK; 2017. DOI: 10.5772/intechopen.68374
- [134] Mooney PM, Deep donor levels (DX centers) in III-V semiconductors, *Journal of Applied Physics*, **1990**, 67 3, <http://dx.doi.org/10.1063/1.345628>.
- [135] Polyakov AY, Lee IH, Deep traps in GaN-based structures as affecting the performance of GaN devices, *Materials Science and Engineering*, **2015**, 94 1-56, <http://dx.doi.org/10.1016/j.mser.2015.05.001>.
- [136] Liang Y, Jia L, He Z, Fan Z, Zhang Y, Yang F, The study of the contribution of the surface and bulk traps to the dynamic R_{dson} in AlGaIn/GaN HEMT by light illumination, *Appl. Phys. Lett.*, **2016**, 109, 182103; <https://doi.org/10.1063/1.4966536>
- [137] Polyakov A, Smirnov N, Shchemerov I, Lee H, Jang T, Dorofeev A, Gladysheva N, Kondratyev E, Turusova Y, Zinovyev R, Turutin A, Ren F, Pearton SJ, Current relaxation analysis in AlGaIn/GaN high electron mobility transistors, *J. Vac. Sci. Technol. B*, **2017**, 35, 011207; doi: 10.1116/1.4973973
- [138] Bastard G, wave mechanics applied to semiconductor heterostructures, Les editions de physique, Les Ulis, Cedex, France, 1988
- [139] Olszakier M, Ehrenfreund E, Cohen E, Bajaj J, Sullivan GJ, Miller D, Intersubband spectroscopy in GaAs/GaAlAs multi-quantum-well structures: Photoinduced absorption, *Superlattices Microstruct*, **1989**, 5 283, [https://doi.org/10.1016/0749-6036\(89\)90301-7](https://doi.org/10.1016/0749-6036(89)90301-7).

- [140] Olszakier M, Ehrenfreund E, Cohen E, Bajaj J, Sullivan GJ, Photoinduced intersubband absorption in undoped multi-quantum-well structures, *Phys. Rev. Lett.*, **1989**, 62 2997.
- [141] Olszakier M, Ehrenfreund E, Cohen E, Bajaj J, Sullivan GJ, Intersubband absorption by photoinduced excitons in undoped multi quantum wells, *Surface Science*, **1989**, 228 123-126, [https://doi.org/10.1016/0039-6028\(90\)90272-A](https://doi.org/10.1016/0039-6028(90)90272-A).
- [142] Garini Y, Olszakier M, Cohen E, Ehrenfreund E, Ron A, Law KK, Merz JL, Gossard AC, Photoinduced intersubband absorption in barrier doped multi-quantum-wells, *Superlattices Microstruct.*, **1990**, 7 287-290, [https://doi.org/10.1016/0749-6036\(90\)90211-O](https://doi.org/10.1016/0749-6036(90)90211-O).
- [143] Cohen E, Ehrenfreund E, Garini Y, Olszakier M, Ron A, Photo-induced intersubband transitions in quantum wells, in: Edited by E. Rosencher et al., Intersubband Transitions in Quantum Wells, Plenum Press, New York, 1992 pg. 264.
- [144] Romero MF, Feneberg M, Moser P, Berger C, Bläsing J, Dadgar A, Krost A, Sakalauskas E, Goldhahn R, Luminescence from two-dimensional electron gases in InAlN/GaN heterostructures with different In content, *Appl. Phys. Lett.*, **2012**, 100, 212101; doi: 10.1063/1.4720087
- [145] Dean PJ, Herbert DC, Topics in current Physics Vol 14, Excitons, Edited by Cho K, Springer Verlag. Berlin, 1979 p. 165
- [146] Monemar B, Lindefelt U, Chen WM, Electronic structure of bound excitons in semiconductors, *Phys B*, **1987**, 146, 256.
- [147] Monemar B, CRC Critical Reviews in Solid State and Materials Sciences 15, 1988, p. 111.
- [148] Shan W, Hauenstein RJ, Fischer AJ, Song JJ, Perry WG, Bremser MD, Davis RF, Goldenberg B, Strain effects on excitonic transitions in GaN: Deformation potentials, *Phys. Rev. B*, **1996**, 54, 13460

- [149] Viswanath K, Lee JI, Kim D, Lee CR, Leem JY, Exciton-phonon interactions, exciton binding energy, and their importance in the realization of room-temperature semiconductor lasers based on GaN, *Phys. Rev. B*, **1998**, 58, 16333
- [150] Zhang L, Cheng K, Degroote S, Leys M, Germain M, Borghs G, Strain effects in GaN epilayers grown on different substrates by metal organic vapor phase epitaxy, *J Appl. Phys.*, **2010**, 108, 073522
- [151] Leroux M, Beaumont B, Grandjean N, Lorenzini P, Haffouz S, Vennegue P, Massies J, Gibart P, Luminescence and reflectivity studies of undoped, n- and p-doped GaN on (0001) sapphire, *Mater. Sci. Eng., B*, **1997**, 50 97
- [152] Chichibu S, Okumura H, Nakamura S, Feuillet G, Azuhata T, Sota T, Yoshida S, Exciton Spectra of Cubic and Hexagonal GaN Epitaxial Films, *Jpn. J. Appl. Phys., Part 1*, **1997**, 36 1976
- [153] Kwack HS et al Optical properties and carrier dynamics of two-dimensional electrons in AlGaIn/GaN single heterostructures *Appl. Phys. Lett.* **2005**, 87 041909
- [154] Wang T, Bai J, Sakai S, Modulation-doping influence on the photoluminescence from the two-dimensional electron gas of Al_xGa_{1-x}N/GaN heterostructures *Phys. Rev. B*, **2001**, 63 205320
- [155] Kim KW, Kim DS, Im KS, Lee JH, Kwon BJ, Kwack HS, Beck S, Cho YH, Strong luminescence of two dimensional electron gas in tensile-stressed AlGaIn/GaN heterostructures grown on Si substrates, *Appl. Phys. Lett.* **2011**, 98 141917
- [156] Yuan YR, Pudensi MA, Vawter CA, Merz JL, New photoluminescence effects of carrier confinement at an AlGaAs/GaAs heterojunction interface, *J. Appl. Phys.*, **1985**, 58, 397

- [157] Kukushkin V, Klitzing KV, Ploog K, Optical spectroscopy of two-dimensional electrons in GaAs–Al_xGa_{1–x}As single heterojunctions, *Phys. Rev. B*, **1988**, 37,8509
- [158] Zhao QX, Bergman JP, Holtz PO, Monemar B, Hallin C, Sundaram M, Merz JL, Gossard AC, Radiative recombination in doped AlGaAs/GaAs heterostructures, *Semicond. Sci. Technol.*, **1990**, 5, 884
- [159] Bergman JP, Zhao QX, Holtz PO, Monemar P, Sundaram M, Merz JL, Gossard AC, Time-resolved measurements of the radiative recombination in GaAs/Al_xGa_{1–x}As heterostructures *Phys. Rev. B*, **1991**, 43, 4771
- [160] Kwack HS et al 2005 Optical properties and carrier dynamics of two-dimensional electrons in AlGa_N/Ga_N single heterostructures *Appl. Phys. Lett.*, **2005**, 87 041909
- [161] Zhang JP, Sun DZ, Wang XL, Kong MY, Zeng YP, Li JM and Lin LY, Fermi-edge singularity observed in a modulation-doped AlGa_N/Ga_N heterostructures, *Appl. Phys. Lett.*, **1998**, 73 2471
- [162] Akopian N, Vardi A, Bahir G, Garber V, Ehrenfreund E, Gershoni D, Poblenz C, Elsass CR, Smorchkova IP and Speck JS, Fermi edge singularity observed in Ga_N/ AlGa_N heterointerfaces *Appl. Phys. Lett.*, **2009**, 94 223502
- [163] Nam KB, Li J, Nakarmi ML, Lin JY, Jiang HX, Growth and optical studies of two-dimensional electron gas of Al-rich AlGa_N/Ga_N heterostructures *Appl. Phys. Lett.*, **2002**, 81 1809
- [164] Shen B, Someya T, Moriwaki O, Arakawa Y, Effect of carrier confinement on photoluminescence from modulation-doped Al_xGa_{1–x}N/Ga_N heterostructures *Appl. Phys. Lett.*, **2000**, 76 679
- [165] Fang CY, Lin CF, Chang EY, Feng MS, A study of subbands in AlGa_N/Ga_N high-electron-mobility transistor structures using low-temperature photoluminescence spectroscopy, *Appl. Phys. Lett.*, **2002**, 80 4558.

LIST OF PUBLICATIONS BASED ON THESIS

Book Chapter

1. **RK Kaneriya**, Gunjan Rastogi, P K Basu, R B Upadhyay and A N Bhattacharya, “A Novel approach for Room-Temperature Intersubband Transition in GaN HEMT for terahertz Applications; **Terahertz Technology, IntechOpen**, DOI: 10.5772/intechopen.98435 (2021); ISBN 978-1-83962-684-5

Papers in peer reviewed international journals

1. **R K Kaneriya**, Chiranjit Karmakar, Manish Sahu, P K Basu and R B Upadhyay “Low temperature photoluminescence study for identification of Intersubband energy levels inside triangular quantum well of AlGa_N/Ga_N Heterostructure”, **Microelectronics Journal** 131 105660 (2023).
2. **R K Kaneriya**, Chiranjit Karmakar, Gunjan Rastogi, M R Patel, R B Upadhyay, Punam Kumar and A N Bhattacharya “Influence of AlN spacer and GaN cap layer in GaN Heterostructure for RF HEMT Applications”, **Microelectronic Engineering** 255 111724 (2022)
3. **R K Kaneriya**, Gunjan Rastogi, P K Basu, R B Upadhyay and A N Bhattacharya “Room temperature photon induced electrical tuning of intersubband transition in GaN HEMT for terahertz applications”, **Microelectronic Engineering**, 233, 111433 (2020)
4. **R K Kaneriya**, Gunjan Rastogi, P K Basu, R B Upadhyay and A N Bhattacharya “Intersubband Device Modeling of Gallium Nitride High Electron Mobility Transistor for Terahertz Applications” **Journal of Radio Science**, 54, 1172-1180, (2019)
5. Chiranjit Karmakar, **R K Kaneriya**, Gunjan Rastogi, R B Upadhyay Punam Kumar and U S Joshi. “Suppression of weak localization due to AlN spacer in AlGa_N/Ga_N two-dimensional electron gas”, **Physics Letter A**, Elsevier 127693, (2021)
6. Gunjan Rastogi, M Krishna Chaitanya, Sanjeev Khare, Ekta Yadav, **R K Kaneriya**, R B Upadhyay, Punam Pradeep Kumar and A N Bhattacharya “Performance improvement of Al_{0.3}Ga_{0.7}N/AlN/GaN HEMTs using Nitrogen pre-treated Si₃N₄ passivation”, **Microelectronic Engineering** 249, 111617 (2021)
7. Gunjan Rastogi, **R K Kaneriya**, R B Upadhyay and A N Bhattacharya “Optimization of Ni/Au Schottky contacts on Al_{0.3}Ga_{0.7}N/AlN/GaN

heterostructure for RF applications”, **International Journal of Nanotechnology and Nanoscience**, 6, 8-15, 2020.

8. Gunjan Rastogi, **R K Kaneriya**, Santanu Sinha and R B Upadhyay “Optimization of ohmic contact fabrication for $\text{Al}_{0.3}\text{Ga}_{0.7}\text{N}/\text{AlN}/\text{GaN}$ HEMTs on 6H-SiC using recess etching and surface plasma treatment processes” **Journal of Nanomaterials & Molecular Nanotechnology of SciTechnol** 8:2 (2019)
9. Gunjan Rastogi, **R K Kaneriya**, Santanu Sinha, R B Upadhyay and A N Bhattacharya “Physics Based Simulation for Studying the Impact of Contact Resistance on DC and RF Characteristics of $\text{AlGaIn}/\text{AlN}/\text{GaN}$ HEMT” **Journal of Radio Science**, 54, 904-909, (2019)

Conference Proceedings

1. Pragya Kushwaha, Chiranjit Karmakar, Manish Sahu, **R K Kaneriya**, Shantnu Sinha, Punam Tyagi and A N Bhattacharya, “Characterization of GaN HEMT at Cryogenic Temperatures” **IEEE International Microwave and RF Conference 2021, IMArc2021**
2. **R K Kaneriya**, Chiranjit Karmakar, Gunjan Rastogi, R B Upadhyay, Punam Kumar and A N Bhattacharya “Investigation of inherent stress using confocal Micro Raman in GaN Heterostructure for RF HEMT Applications”, **International Raman summit 2020**, WiTec, Germany.
3. **R K Kaneriya**, Gunjan Rastogi, P K Basu, R B Upadhyay and A N Bhattacharya “Modeling of electrically tunable metamaterial embedded intersubband transitions in GaN HEMT for terahertz applications” **URSI RCRS 2020, IEEE Xplore**, DOI: 10.23919/URSIRCRS49211.2020.9113510 (2020)
4. **R K Kaneriya**, Gunjan Rastogi, P K Basu, R B Upadhyay and A N Bhattacharya “Physics based Modeling of Gallium Nitride High Electron Mobility Transistor for Terahertz Applications” **URSI AP-RASC 2019, IEEE Xplore**, DOI: 10.23919/URSIAP-RASC.2019.8738691 (2019).
5. Gunjan Rastogi, **R K Kaneriya**, Santanu Sinha, R B Upadhyay and A N Bhattacharya “Physics Based Simulation for Studying the Impact of Contact Resistance on DC and RF Characteristics of $\text{AlGaIn}/\text{AlN}/\text{GaN}$ HEMT” **URSI AP-RASC 2019, IEEE Xplore**, DOI: 10.23919/URSIAP-RASC.2019.8738496 (2019).